THE UNIVERSITY *of* EDINBURGH

Wireless Optical Backhauling for Optical Attocell Networks

Hossein Kazemi

A thesis submitted for the degree of Doctor of Philosophy.
The University of Edinburgh.
January 2019

Abstract

The backhaul of tens and hundreds of light fidelity (LiFi)-enabled luminaires constitutes a major challenge. The problem of backhauling for optical attocell networks has been approached by a number of wired solutions such as in-building power line communication (PLC), Ethernet and optical fiber. In this work, an alternative solution is proposed based on wireless optical communication in visible light (VL) and infrared (IR) bands. The proposed solution is thoroughly elaborated using a system level methodology. For a multi-user optical attocell network based on direct current biased optical orthogonal frequency division multiplexing (DCO-OFDM) and decode-and-forward (DF) relaying, detailed modeling and analysis of signal-to-interference-plus-noise (SINR) and end-to-end sum rate are presented, taking into account the effects of inter-backhaul and backhaul-to-access interferences.

Inspired by concepts developed for radio frequency (RF) cellular networks, full-reuse visible light (FR-VL) and in-band visible light (IB-VL) bandwidth allocation policies are proposed to realize backhauling in the VL band. The transmission power is opportunistically minimized to enhance the backhaul power efficiency. For a two-tier FR-VL network, there is a technological challenge due to the limited capacity of the bottleneck backhaul link. The IR band is employed to add an extra degree of freedom for the backhaul capacity. For the IR backhaul system, a power-bandwidth tradeoff formulation is presented and closed form analytical expressions are derived for the corresponding power control coefficients. The sum rate performance of the network is studied using extensive Monte Carlo simulations. In addition, the effect of imperfect alignment in backhaul links is studied by using Monte Carlo simulation techniques.

The emission semi-angle of backhaul LEDs is identified as a determining factor for the network performance. With the assumption that the access and backhaul systems share the same propagation medium, a large semi-angle of backhaul LEDs results in a substantial degradation in performance especially under FR-VL backhauling. However, it is shown both theoretically and by simulations that by choosing a sufficiently small semi-angle value, the adverse effect of the backhaul interference is entirely eliminated. By employing a narrow light beam in the backhaul system, the application of wireless optical backhauling is extended to multi-tier optical attocell networks. As a result of multi-hop backhauling with a tree topology, new challenges arise concerning optimal scheduling of finite bandwidth and power resources of the bottleneck backhaul link, i.e., optimal bandwidth sharing and opportunistic power minimization. To tackle the former challenge, optimal user-based and cell-based scheduling algorithms are developed. The latter challenge is addressed by introducing novel adaptive power control (APC) and fixed power control (FPC) schemes. The proposed bandwidth scheduling policies and power control schemes are supported by an analysis of their corresponding power control coefficients.

Furthermore, another possible application of wireless optical backhauling for indoor networks is in downlink base station (BS) cooperation. More specifically, novel cooperative transmission schemes of non-orthogonal DF (NDF) and joint transmission with DF (JDF) in conjunction with fractional frequency reuse (FFR) partitioning are proposed for an optical attocell downlink. Their performance gains over baseline scenarios are assessed using Monte Carlo simulations.

Lay summary

Light fidelity (LiFi) is an emerging technology operating based on visible light communication (VLC). With LiFi, the existing light emitting diode (LED) light fixtures turn into optical access points (APs), enabling high speed wireless data communication by light. A LiFi access network is created by configuring multiple APs inside a building. End-user devices are equipped with light-sensitive detectors that allow them to connect to the LiFi network. A major challenge for designing such networks is to provide a means to connect tens or even hundreds of LiFi-enabled light fixtures to the Internet, which, for example, is distributed to the building by a single optical fiber cable. The links between LiFi APs and the Internet distribution point constitute backhaul, an important part of the network infrastructure.

The problem of backhauling for LiFi networks has been approached by a number of wired solutions such as using the indoor electricity wiring as communication channels, or extending Ethernet cables to deliver both data and electricity to LED luminaires. In this thesis, an alternative solution is proposed to realize backhaul links based on wireless optical communication in visible light (VL) and infrared (IR) bands. The proposed solution is elaborated using a systematic methodology aiming to derive analytical tools in order to assess the overall data rate of the network with multiple connected user equipment (UE) devices.

To realize backhauling in the VL band, inspired by concepts developed for radio frequency (RF) cellular networks, methods for sharing the communication bandwidth between the access and backhaul links are proposed. To enhance the power efficiency of backhaul, the transmission power is minimized while making sure the data rate of end-user devices is not affected. When extending the backhaul coverage by a tree topology to provide backhaul connections to LiFi APs located in farther distances, however, a technological challenge arises due to the limited bandwidth of the VL backhaul system. To overcome this problem, the IR band is employed to increase the backhaul bandwidth. For the IR backhaul system, the tradeoff between power and bandwidth is formulated and studied, and a mechanism is proposed to optimally control the backhaul power. The presented analysis is verified by extensive computer simulations.

It is shown that, to achieve the best performance, the light emission in wireless optical backhaul links needs to be as narrow as possible to avoid causing interference to the environment. By employing a sufficiently narrow light beam, the application of wireless optical backhauling is extended to LiFi networks with a large number of APs. Consequently, new challenges arise concerning the optimal use of finite bandwidth and power resources of the backhaul system. To tackle the former issue, novel bandwidth sharing algorithms are developed. The latter challenge is addressed by introducing novel power control schemes.

Furthermore, downlink cooperation between LiFi APs is considered as another application for indoor wireless optical backhauling. More specifically, novel data transmission schemes are proposed allowing two or three APs to jointly transmit data to UE devices by assigning different operating frequencies to adjacent APs. The effectiveness of these joint transmission schemes on improving the data rate performance is examined using computer simulations.

Declaration of originality

I hereby declare that the research recorded in this thesis and the thesis itself were composed and originated entirely by myself in the Light Fidelity (LiFi) Research and Development (R&D) Center, Institute for Digital Communications, School of Engineering, University of Edinburgh.

Hossein Kazemi

Acknowledgements

This thesis would not have come into being, if it were not for the help and support of many wonderful people. I would like to foremost express my deepest gratitude to my supervisor, Professor Harald Haas, who gave me the opportunity to pursue my Ph.D. on a novel research area. He is an ever sparkling fountain of ideas and enthusiasm. I am thankful to his consistent guidance, support and encouragement for hard work.

Also, I am indebted to Dr. Majid Safari for spending hours in his office, having substantial and constructive discussions. I would also like to acknowledge and thank our principal assistant, Ms. Hannah Brown, for her continuous support and assistance in proofreading my research papers and this thesis.

My Ph.D. journey would not have been possible without the support of my colleagues and all my friends from home and abroad. I will never forget the enjoyable moments we spent together and all the laughter we shared. I am not attempting to write down a list of all past and present friends and colleagues, as I am sure that I will forget someone.

My warmest gratitude goes to my parents and my lovely siblings who have always supported me throughout my life. I will be forever indebted to my family for their endless love and trust. Without them, I would not have been where I am today.

Last, but not least, I would like to express my wholehearted gratitude to my wife, Elham, for her unconditional love, support, encouragement, and patience during my studies. The least I can do is to dedicate this thesis to my beloved ones, Elham and my family.

Contents

Lay summary v
Declaration of originality vii
Acknowledgements ix
Contents x
List of figures xiii
List of tables xv
Acronyms and abbreviations xvii
Nomenclature xxiii

1 Introduction **1**
1.1 Motivation 1
1.1.1 The Emergence of Visible Light Communications 1
1.1.2 LiFi Cellular Networks 2
1.1.3 Backhaul Architecture 3
1.2 Contributions 8
1.3 State-of-the-art 10
1.4 Thesis Layout 12

2 Background **15**
2.1 Optical Attocell Network 15
2.2 Indoor Propagation Characteristics of Light 16
2.3 Bandwidth Limitation 17
2.4 Optical Orthogonal Frequency Division Multiplexing 18
2.5 DCO-OFDM Communication System 19
2.5.1 Principles of Operation 19
2.5.2 Achievable Rate 22
2.6 Summary 24

3 A Wireless Optical Backhaul Solution for Optical Attocell Networks **27**
3.1 System Level Preliminaries 28
3.1.1 Downlink Configuration 28
3.2 Wireless Backhaul System Design 30
3.2.1 Wireless Optical Backhauling 30
3.2.2 Signal-to-Noise-plus-Interference Ratio 32
3.2.3 Sum Rate Analysis 36
3.3 Extension to Two-Tier Network 40
3.3.1 Backhaul Links 41
3.3.2 FR-VL Downlink SINR 42
3.3.3 End-to-End Sum Rate 44
3.4 Power Control for Wireless Backhaul System 47
3.4.1 One-Tier Network 48
3.4.2 Two-Tier Network 52

3.4.3 Average Sum Rate Performance . . . 62
3.4.4 Imperfect Alignment in Backhaul Links . . . 64
3.5 Summary . . . 67

4 Extension to Multi-Tier Networks with Multi-Hop Wireless Optical Backhauling 69
4.1 System-Level Preliminaries . . . 70
4.1.1 Network Configuration . . . 70
4.1.2 Signal-to-Noise-plus-Interference Ratio . . . 71
4.2 Multi-Hop Wireless Backhaul System Design . . . 74
4.2.1 Rate Inequality . . . 76
4.2.2 Full Duplex Relaying . . . 77
4.2.3 Bandwidth Sharing . . . 77
4.2.4 End-to-End Sum Rate . . . 78
4.3 Opportunistic Power Control . . . 79
4.3.1 Proposed Schemes . . . 80
4.3.2 Probability of Backhaul Bottleneck Occurrence . . . 84
4.3.3 Illustrative Numerical Examples . . . 88
4.4 Optimal Bandwidth Scheduling . . . 103
4.4.1 User-based Bandwidth Scheduling . . . 103
4.4.2 Cell-based Bandwidth Scheduling . . . 106
4.4.3 Numerical Results and Discussions . . . 107
4.5 Summary . . . 111

5 Downlink Base Station Cooperation with Wireless Optical Backhauling 113
5.1 Fractional Frequency Reuse . . . 113
5.2 Downlink Base Station Cooperation . . . 115
5.2.1 Cooperative Transmission Using FFR . . . 116
5.2.2 Non-Orthogonal Decode-and-Forward Relaying . . . 117
5.2.3 Joint Transmission with Decode-and-Forward Relaying . . . 119
5.2.4 End-to-End Spectral Efficiency . . . 121
5.3 Numerical Results and Discussions . . . 122
5.4 Summary . . . 126

6 Conclusions and Future Works 127
6.1 Summary and Conclusions . . . 127
6.2 Limitations and Future Directions . . . 130

A Proof of Proposition 1 135

B Monotonicity of $g_1(K_1, K_7, K_8)$ in K_1 139

C A Remark on the Constraint in (3.64) 141

D Minimum Element of the Feasible Set for P3 143

E The Expressions of $\mathcal{I}_{0^\circ}(r)$ and $\mathcal{I}_{30^\circ}(r)$ 145

F Proof of Lemma (4) 147

G Publications **149**
G.1 Conference Papers 149
G.2 Journal Papers 149

List of figures

1.1 The backhaul architecture of indoor LiFi cellular networks based on point-to-point wireless RF/optical communications. 5

2.1 DCO-OFDM system block diagram. 20

3.1 Hexagonal cellular layout for a one-tier optical attocell network. 28
3.2 Downlink geometry in an indoor optical attocell network. 29
3.3 Optical attocell network geometry in a polar coordinate system. 30
3.4 Backhaul interference geometry. 34
3.5 Hexagonal cellular layout for a two-tier optical attocell network. 40
3.6 Optimal power ratios K_1^* for the one-tier FR-VL network, and K_7^* and K_8^* for the two-tier FR-VL network with respect to $\Phi_{\rm b}$. 49
3.7 The minimum power ratio $K_{1,\min}$ against the bandwidth ratio $\frac{B_{\rm b}}{B_{\rm a}}$ for the one-tier network with IR backhaul. 50
3.8 Optimal power ratio K_1^* for the one-tier network with IR backhaul versus $\Phi_{\rm b}$ for different values of $B_{\rm b}$. 51
3.9 An instant illustration of the admissible region for P2 based on the first three constraints for $\Phi_{\rm b} = 20^\circ$. 54
3.10 An instant illustration of the admissible region for P2 based on the first three constraints for $\Phi_{\rm b} = 15^\circ$. 55
3.11 An instant illustration of the admissible region for P2 based on the first three constraints for $\Phi_{\rm b} = 25^\circ$. 55
3.12 An instant illustration of the admissible region for P3 for $\Phi_{\rm b} = 20^\circ$. 56
3.13 The tradeoff between the minimum power ratio $K_{1,\min}$ and the bandwidth ratio $\frac{B_{\rm b}}{B_{\rm a}}$ for the two-tier network with IR backhaul. 59
3.14 The minimum bandwidth ratio $\frac{B_{\rm b}}{B_{\rm a}}\big|_{\min}$ against $\Phi_{\rm b}$ for the two-tier network with IR backhaul for different values of $K_{1,\min}$. 59
3.15 Optimal sum power ratio $K_{\rm sum} = K_1^* + K_7^* + K_8^*$ for the two-tier network with IR backhaul versus $\Phi_{\rm b}$ for different values of $B_{\rm b}$. 60
3.16 Average sum rate performance of the one-tier optical attocell network using FR-VL, IB-VL and IR backhaul systems as a function of $\Phi_{\rm b}$. 61
3.17 Average sum rate performance of the two-tier optical attocell network using FR-VL, IB-VL and IR backhaul systems as a function of $\Phi_{\rm b}$. 63
3.18 Average SINR performance of the VL backhaul system against the misalignment error for the one tier network. 65
3.19 Average SINR performance of the VL backhaul system against the misalignment error for the two tier network. 66

4.1 One branch of a five tier super cell. 75
4.2 The statistics of $K_{1,\min}$ under the APC scheme as a function of the total number of tiers for $M = 30$. 89

4.3 The statistics of $K_{1,\min}$ under the APC scheme for a three-tier super cell with different values of the total number of UEs. 90
4.4 $K_{1,\min}$ under FPC1 and FPC2 schemes as a function of the total number of tiers. 91
4.5 Analytical and simulation results of the average SINR $\bar{\gamma}_{\rm a}$ and the average access rate $\bar{\mathcal{R}}_{\rm a}$. 93
4.6 The RTP performance of APC, FPC1 and FPC2 schemes versus the total number of tiers for $M = 30$. 95
4.7 The RTP performance for a three-tier super cell with APC, FPC1 and FPC2 schemes versus the total number of UEs. 96
4.8 The BBO probability for NPC, APC, FPC1 and FPC2 schemes versus the total number of tiers and the total number of UEs for $B_{\rm b} = B_{\rm a}$. 97
4.9 The BBO probability for NPC, APC, FPC1 and FPC2 schemes versus the total number of tiers and the total number of UEs for $B_{\rm b} = 3B_{\rm a}$. 98
4.10 Analytical and simulation results of the backhaul bottleneck occurrence (BBO) probability as a function of K_1 for different values of $N_{\rm T}$ and M. 99
4.11 The average sum rate performance for NPC, APC, FPC1 and FPC2 schemes versus the total number of tiers and the total number of UEs. 100
4.12 The average sum rate performance for NPC, APC, FPC1 and FPC2 schemes versus the total number of tiers for different values of the backhaul bandwidth. . 102
4.13 An example of running Algorithm 1 (UBS) over 100 instant realizations for $N_{\rm T} = 2$ and $M = 10$. 108
4.14 An example of running Algorithm 2 (CBS) over 100 instant realizations for $N_{\rm T} = 2$ and $M = 10$. 108
4.15 The average sum rate performance for UBS and CBS scheduling policies based on Algorithm 1 and Algorithm 2, respectively, for different values of $N_{\rm T}$. . . . 110

5.1 A one-tier optical attocell network with FFR partitioning. 115
5.2 An example of the cooperative downlink transmission in the cell edge region based on the NODF protocol. 117
5.3 An example of the cooperative downlink transmission in the cell edge region based on the JTDF protocol. 120
5.4 The statistics of the UE SE for FR, FFR, CFFR-NODF and CFFR-JTDF systems. 123
5.5 The average SE performance per ring around $\rm BS_0$ for FR, FFR, CFFR-NODF and CFFR-JTDF systems. 125

A.1 DCO-OFDM frame for the downlink of $\rm BS_0$ under IB-VL backhauling. 136

List of tables

3.1 Simulation Parameters 49

4.1 Attocell Configurations 88

5.1 Average SE improvements for FFR, CFFR-NODF and CFFR-JTDF schemes relative to the FR system. 124

Acronyms and abbreviations

AP	Access Point
AF	Amplify-and-Forward
ACO-OFDM	Asymmetrically Clipped Optical OFDM
AMC	Adaptive Modulation and Coding
APC	Adaptive Power Control
ASE	Area Spectral Efficiency
AWGN	Additive White Gaussian Noise
BBO	Backhaul Bottleneck Occurrence
BPSK	Binary Phase Shift Keying
BS	Base Station
CBS	Cell-based Bandwidth Scheduling
CCDF	Complementary Cumulative Distribution Function
CCI	Co-Channel Interference
CDF	Cumulative Distribution Function
CFFR	Cooperative FFR
CLT	Central Limit Theorem
CoMP	Coordinated Multi-Point
CP	Cyclic Prefix
DAS	Distributed Antenna System
DSL	Digital Subscriber Line

DCO-OFDM	DC-biased Optical OFDM
DF	Decode-and-Forward
EMI	Electromagnetic Interference
eU-OFDM	Enhanced Unipolar Optical OFDM
FDE	Frequency Domain Equalization
FEC	Forward Error Correction
FFR	Fractional Frequency Reuse
FFT	Fast Fourier Transform
FOV	Field Of View
FPC	Fixed Power Control
FR	Full Reuse
FRF	Frequency Reuse Factor
FR-VL	Full Reuse Visible Light
FSO	Free Space Optical
FTTB	Fiber-To-The-Building
FTTH	Fiber-To-The-Home
FTTP	Fiber-To-The-Premises
IB-VL	In-Band Visible Light
ICI	Inter-Cell Interference
IM-DD	Intensity Modulation and Direct Detection
i.i.d.	Independent and Identically Distributed
IFFT	Inverse Fast Fourier Transform
IR	Infrared

ISI	Inter-Symbol Interference
JTDF	Joint Transmission with Decode-and-Forward
LAN	Local Area Network
LED	Light Emitting Diode
LiFi	Light Fidelity
LOS	Line-Of-Sight
LTE	Long-Term Evolution
LTE-A	LTE-Advanced
MAC	Medium Access Control
MC	Multi-Carrier
MIMO	Multiple Input Multiple Output
MSE	Mean Square Error
MMSE	Minimum Mean Square Error
mmW	Millimeter Wave
LAN	Local Area Network
NLOS	Non-Line-Of-Sight
NODF	Non-Orthogonal Decode-and-Forward
OFDM	Orthogonal Frequency Division Multiplexing
OFDMA	Orthogonal Frequency Division Multiple Access
PAM	Pulse Amplitude Modulation
PAPR	Peak-to-Average Power Ratio
PD	Photodiode
PDF	Probability Density Function

PE	Power Efficiency
PHY	Physical Layer
PLC	Power Line Communication
PMF	Probability Mass Function
PoE	Power-over-Ethernet
P-OFDM	Polar OFDM
PON	Passive Optical Network
PPP	Poisson Point Process
PSD	Power Spectral Density
PTP	Point-To-Point
QAM	Quadrature Amplitude Modulation
QoS	Quality of Service
QPSK	Quadrature Phase Shift Keying
RGB	Red-Green-Blue
RF	Radio Frequency
RHS	Right Hand Side
RMS	Root Mean Square
RoF	Radio-over-Fiber
RTP	Relative Total Power
SC	Single Carrier
SE	Spectral Efficiency
SEE-OFDM	Spectral and Energy Efficient OFDM
SINR	Signal-to-Noise-plus-Interference Ratio

SMF	Single Mode Fiber
SNR	Signal-to-Noise Ratio
UB	Unlimited Backhaul
UBS	User-based Bandwidth Scheduling
UE	User Equipment
VL	Visible Light
VLC	Visible Light Communication
WiFi	Wireless Fidelity

Nomenclature

B_{b}	Bandwidth of the backhaul system
N_{b}	Number of subcarriers in the backhaul system
ξ_{b}	Subcarrier utilization factor for the backhaul system
b_i	Backhaul link of BS$_i$
$x_i^{\mathrm{b}},\ X_i^{\mathrm{b}}$	Transmitted signal in the backhaul link of BS$_i$
$y_i^{\mathrm{b}},\ Y_i^{\mathrm{b}}$	Received signal for the backhaul link of BS$_i$
$v_i^{\mathrm{b}},\ V_i^{\mathrm{b}}$	Received noise for the backhaul link of BS$_i$
γ_{b_i}	Received SINR per subcarrier for the backhaul link of BS$_i$
$\mathcal{R}_{\mathrm{b}_i}$	Overall achievable rate for the backhaul link of BS$_i$
B_{a}	Bandwidth of the access system
N_{a}	Number of subcarriers in the access system
ξ_{a}	Subcarrier utilization factor for the access system
$x_i^{\mathrm{a}},\ X_i^{\mathrm{a}}$	Transmitted signal in the access link of BS$_i$
$y_u,\ Y_u$	Received signal for the uth UE
$v_u^{\mathrm{a}},\ V_u^{\mathrm{a}}$	Received noise for the uth UE
γ_u	Received SINR per subcarrier for the uth UE
$\mathcal{R}_u$	Achievable rate of the uth UE
$\mathcal{R}_{\mathrm{a}_i}$	Overall achievable rate for the access link of BS$_i$
$\mathcal{R}_i^{\text{FR-VL}}$	Multi-user sum rate for the end-to-end downlink of BS$_i$ with FR-VL backhaul
$\mathcal{R}_i^{\text{IB-VL}}$	Multi-user sum rate for the end-to-end downlink of BS$_i$ with IB-VL backhaul
$\mathcal{R}_i^{\mathrm{IR}}$	Multi-user sum rate for the end-to-end downlink of BS$_i$ with IR backhaul
$\lvert\ \rvert$	Cardinality of a set
*	Complex conjugate operator
$\mathbb{E}$	Statistical expectation
$\lfloor\ \rfloor$	Floor function returning the largest integer that is smaller than or equal to its input argument
$\lceil\ \rceil$	Ceil function returning the smallest integer that is greater than or equal to its input argument
$\preceq$	Componentwise inequality
$\otimes$	Convolution operator

Chapter 1
Introduction

1.1 Motivation

1.1.1 The Emergence of Visible Light Communications

The advent of light emitting diodes (LEDs) has radically changed the modern way of life due to numerous benefits they offer. They can be found everywhere from home appliances, business intelligence dashboards, smart phones, TV sets and lamp posts to advertising panels, aviation lighting, automotive headlamps, traffic signals, camera flashes and medical devices. Besides, the application of LEDs for indoor illumination purposes is rapidly increasing, primarily because of their high energy efficiency, delivering more than 100 lm/W [1]. In addition to providing energy savings, other benefits include long operational lifetime, a compact form factor, easy maintenance and low cost. For these reasons, inefficient light sources such as incandescent and florescent lamps are replaced by LED light bulbs. It is expected that LED lighting reaches a market share of 84% in the general illumination market by 2030 [2].

The growing popularity of mobile-connected devices in conjunction with ubiquitous Internet access has led to an exponential increase in global mobile data traffic which is anticipated to reach 77.5 exabytes per month by the year 2022 [3]. If this trend continues, fulfilling bandwidth requirements encounters a fundamental challenge due to the scarcity of the radio frequency (RF) spectrum. The coincidence of this trend in parallel to the fast developing trend in LED-based lighting has created a unique opportunity for research and development professionals to consider exploring the visible light (VL) spectrum for high speed wireless communications by using light as medium. In fact, despite the mentioned advantages for LEDs, there is a prominent feature which is not fully exploited: the intensity of their output light can be switched at high frequencies such that the rate of variations is imperceptible to the human eye. This property can be utilized for the deployment of value-added services based on visible light communication (VLC) [4]. The VL spectrum offers a vast amount of bandwidth, i.e., 1000 times greater than the entire 300 GHz RF spectrum. This license-free spectrum can be used synergistically with existing RF technologies to help to alleviate the RF spectrum crisis. As a complementary

solution, VLC offers many other advantages over RF. First, the fact that light does not penetrate through opaque objects makes VLC inherently secure against interception. Second, VLC can be used in electromagnetic interference (EMI)-sensitive environments where the radiation of RF signals is highly restricted. Third, in scenarios where the illumination equipment is already in place such as homes or offices, VLC-based services can be deployed by reusing the existing infrastructure. Finally, VLC is a viable complement to RF communications, in that it can support bandwidth-starving download links. This provides an opportunity to piggyback the wireless communication functionality onto the future lighting networks.

The introduction of VLC dates back to the 1880s when the Scottish-born scientist Alexander Graham Bell invented the photophone [5]. While Bell is famous for the invention of the telephone, he believed the photophone was his most important invention. The photophone is considered as the first official demonstration of light-wave communications. It was a device that allowed the transmission of voice over a distance of 200 m by harnessing the sunlight. More recent work began in 2000 at Nakagawa Laboratory, in Japan, by using LEDs as communication devices to transmit data wirelessly. Since 2006, research in the VLC domain has gained momentum, covering various aspects of the technology from device-level performance optimization to link-level transmission techniques. This was supported by the release of the IEEE $802.15.7$ standard draft with the objective to define and disseminate the physical layer (PHY) and the medium access control (MAC) layer for short-range VLC applications [6]. This standard specifies data rates up to 96 Mbits/s to support audio and video multimedia services. Since then, significant research efforts were devoted to be able to demonstrate multi-Gbits/s data rates by using commercial off-the-shelf red-green-blue (RGB) LEDs, phosphorous white LEDs, and μ-LEDs based on optical orthogonal frequency division multiplexing (OFDM) techniques [7,8].

1.1.2 LiFi Cellular Networks

The application of VLC is not limited only to point-to-point (PTP) communication [9]. The high speed wireless networking variant of VLC is recognized as light fidelity (LiFi). It is principally meant to enable LED luminaires to provide broadband wireless connectivity [10]. Particularly, LiFi aims to perform bidirectional multi-user networking with mobility support and seamless handover. Due to its distinguished features such as cost effective deployment and security, LiFi will be used as a key technology in fifth generation (5G) heterogeneous wireless networks and beyond [10,11]. The fact that more than 70% of the wireless data traffic originates

inside buildings [12], makes LiFi especially advantageous for indoor applications in order to offload the data traffic. As an application scenario within the realm of heterogeneous networks, LiFi can coexist with wireless fidelity (WiFi), in which case LiFi realizes a high-bandwidth, uncongested and unregulated downlink path, while WiFi constitutes the uplink channel where congestion is less likely [13].

A cellular system is a type of infrastructure-based network [14]. In a cellular network, the coverage area is divided into many spatially separated cells and the available spectrum is reused locally in each cell. There is a base station (BS) or access point (AP) which is typically located at the center of each cell and it serves multiple user equipments (UEs) within the cell area. Research in the area of wireless cellular networks shows that cell densification is one of the most effective solutions to improve the area spectral efficiency (ASE) performance of the network [15]. With the advancement of wireless communication technologies, more BSs are densely deployed in response to the rising demand for mobile communication services. This leads to modern small-cell systems.

From a network deployment standpoint, the dense distribution of indoor luminaires lays the groundwork for establishing ultra-dense LiFi networks. This has led to the emergence of optical attocells that describe tiny cells deployed with an extremely high spatial reuse [10]. Such cells have an equivalent circular radius between 1 m and 3 m [16]. This is analogous to cell size reduction in long-term evolution (LTE) femtocells, yet offering a much higher ASE performance [17]. Thus, indoor networks incorporating LiFi BSs are referred to as optical attocell networks. An in-depth study on the downlink performance of optical attocell networks subject to a large number of system parameters is available in [16]. It involves a comparison on the area data rate performance (i.e., the achievable data rate per unit area) of an optical attocell network with respect to those achieved by an RF femtocell system and an indoor millimeter wave (mmW) network, all of which are assumed to be deployed in a typical room of the same size. The study shows that through a judicious configuration of the system parameters and by using adaptive modulation and coding (AMC), the optical attocell network generally outperforms both the femtocell and mmW networks in terms of the area data rate.

1.1.3 Backhaul Architecture

Backhaul is an integral part of the cellular network architecture, providing communication links to connect BSs to the core network. This means that the UEs associated with BSs are granted

access to the core network via the backhaul network. In contrast to ad-hoc wireless networks which have no infrastructure (i.e., no backhaul connections), a centralized control mechanism is performed in cellular systems [14]. This facilitates the implementation of many network functions such as adaptive resource allocation, power control, handover, among others. Therefore, cellular systems more efficiently utilize the network resources to meet the quality of service (QoS) requirements of individual UEs than networks without infrastructure. Additionally, networks with infrastructure are organized so that there is a single-hop route connecting the UEs to a BS, since single-hop routes generally exhibit lower latency, lower path loss and higher transmission rates compared to multi-hop routes. For all these reasons, infrastructure-based networks perform notably better than infrastructure-less networks. However, designing a cost effective backhaul is a major challenge for cellular networks [18].

Furthermore, the backhaul quality has an unavoidable significance and impact on the overall network performance. As such, it is crucial to make adequate preparation for transporting the busy wireless traffic from the APs to the core network and vice versa. To this end, backhaul connections need to provide reliable, high speed and low latency links. The development of ultra-dense and high speed access networks in the future will lead to a substantial increase in the backhaul capacity requirement [19]. One possible solution to tackle the backhaul challenge is to apply optical fiber links, which offers excellent performance, but incurs considerable costs. To achieve multi-Gbits/s connectivity for indoor wireless networks, a fiber-to-the-home (FTTH)/fiber-to-the-premises (FTTP) technology based on a passive optical network (PON) architecture is used [20]. Signal distribution from the FTTH/FTTP hop to individual dwellings within a building is also a major component of multi Gbits/s indoor networks. In-building backhauling can be done wirelessly using mmW communications or radio-over-fiber (RoF) distributed antenna systems (DASs) [21,22]. A cost-effective alternative to complement fiber-based PON, namely G.fast, has been standardized [23]. G.fast is a high speed digital subscriber line (DSL) standard which utilizes copper wires and promises Gbits/s connectivity for a distance up to 250 m. It could be a viable option for in-building backhauling in multi-dwelling scenarios. Alternative backhaul solutions based on Ethernet and power line communication (PLC) have also been considered for indoor wireless networks [24, 25].

When it comes to densely deployed indoor optical attocell networks, designing a cost-effective backhaul network for LiFi APs is more challenging. This is mainly because there are multiple LiFi-enabled luminaires in a single room, making the construction of backhaul connections

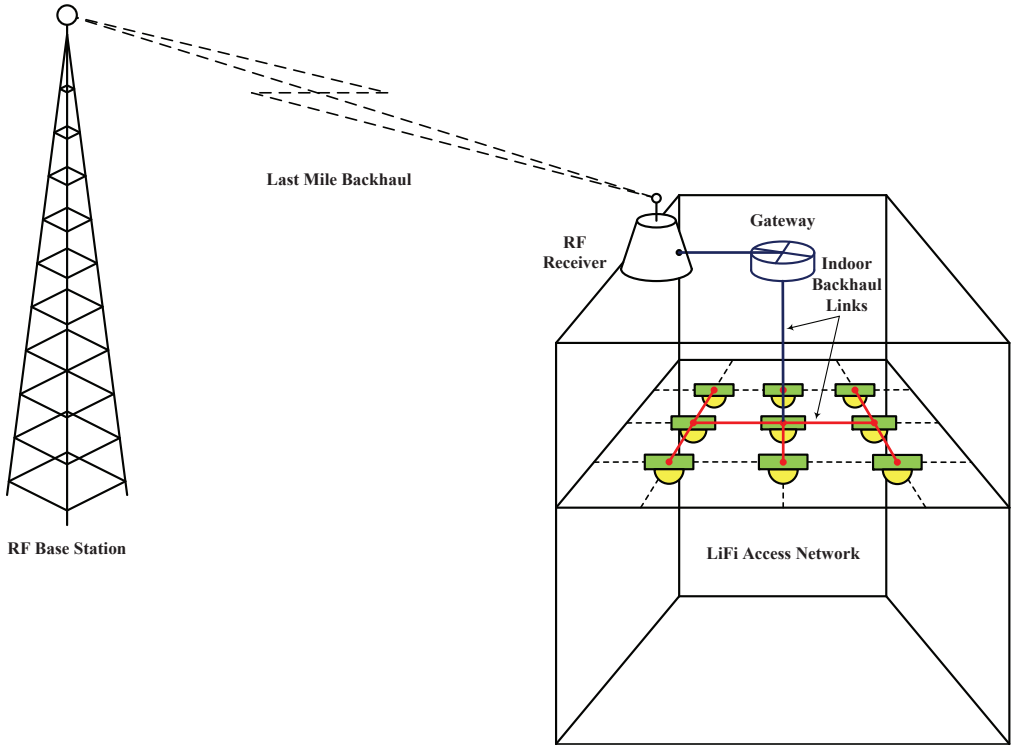

(a) Last mile backhaul connectivity using RF technologies such as LTE or mmW.

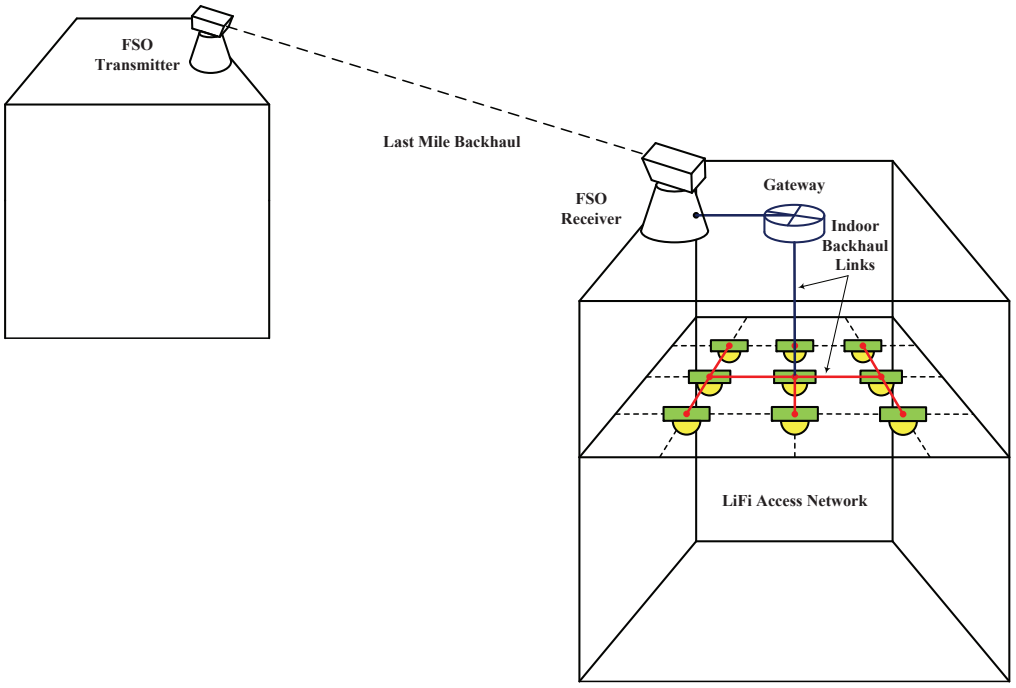

(b) Last mile backhaul connectivity using FSO communications.

Figure 1.1: *The backhaul architecture of indoor LiFi cellular networks based on point-to-point wireless RF/optical communications.*

more complicated. The extent of this issue scales proportionately with the size of the network. Thus, it is important to avoid expensive and complex backhaul designs. From an architectural point of view, the backhaul of indoor optical attocell networks has two main elements: the last mile connectivity and the last meter connectivity, as depicted conceptually in Fig. 1.1.

The first element can be implemented using PTP wireless RF technologies such as LTE or mmW, with an antenna placed at the rooftop, e.g. Fig. 1.1a. It is also possible to realize the last mile connection based on a PTP free space optical (FSO) communication link by installing FSO transceiver equipment on the rooftop, e.g. Fig. 1.1b. Fourth generation (4G) LTE-based networks use LTE-Advanced (LTE-A) small cells/femtocells as an effective means to deliver high speed mobile broadband service by employing carrier aggregation techniques [26]. As a last mile backhaul solution, small cells operating on LTE-A/U bands are able to provide coverage for a whole multi-dwelling unit [22]. The key mmW backhaul solutions leverage the mmW spectrum in 60 GHz and 70–80 GHz bands [27]. The propagation properties of these bands enable the establishment of high capacity, short range links. The attenuation of power at 60 GHz is primarily caused by oxygen or even dry air. For radiation in 70–80 GHz, the power loss is mainly due to absorption by water molecules in the atmosphere.

An mmW backhaul system with highly directive narrow bandwidth antennas can cover up to 3–4 km [22]. However, the line-of-sight (LOS) link between the macro BS and the small cell BS needs to be physically clear and unobstructed as shown in Fig.1.1a. This makes mmW backhaul communications vulnerable to wind-induced misalignments. Ensuring a precise alignment setup constitutes a technical challenge in practice, as it requires strategic placement of mmW transceiver equipment. In addition to RF backhaul solutions, the last mile connection can be built by using laser-based FSO communications. Such a wireless optical communication system can supply substantial transmission capacities comparable to optical fiber links using compact transceiver equipment that can arguably be installed in less than a day, while no license fees are payable [28]. Despite these advantages, the deployment of FSO links is hampered by three major challenges [28]: 1) the need for precise alignment of the LOS link under the building sway; 2) overcoming the signal attenuation caused by adverse weather conditions including haze, fog, cloud and turbulence; and 3) fulfilling the requirement to restrict optical power levels within eye safety limits. The principal shortcoming of urban FSO is the downtime as a result of adverse weather effects. Scattering particles in the free space medium with radii in the same range as laser wavelengths lead to severe attenuation and distortion of the transmitted signal.

The signal power can heavily be attenuated in detrimental weather circumstances, on the order of hundreds of decibels per kilometer. For this reason, FSO links are often augmented by a complementary RF/mmW link as backup in order to be able to maintain the *five nines* availability grade, a criterion to make sure the FSO backhaul remains reliably operational for 99.999% of the time in long run [29].

In scenarios where a fiber-to-the-building (FTTB) link is deployed for last mile connectivity, an optical fiber cable is available up to the building premise and the active node (i.e., the fiber distribution node) may be located in a cabinet at the basement of a multi-dwelling unit. While the employment of optical fibers offers massive bandwidth advantage, laying down optical fiber cables in order to reach individual premises can be extremely expensive and time consuming especially in rural areas. Also, trenching optical fibers to each household in densely populated urban areas demands unfavorable and difficult efforts. Nonetheless, the carrier-grade reliability and supreme capacity of optical fibers cannot be simply overlooked.

Apart from the last mile connectivity, signal distribution from the main hub to individual households is an important component of multi-Gbits/s indoor networks. As such, the communication traffic from the distribution point is run throughout the building via the last meter connectivity. Available options for this part of backhauling in indoor optical attocell networks include optical fiber, Ethernet and PLC. When using a PTP optical fiber system with a passive star topology, many fiber cables need to be installed between the branch node and every BS in the network. This option offers the maximum capacity for backhauling, but at very high cost. The Ethernet option follows a similar cabling approach as in the case of optical fiber in order to establish the indoor distribution network. However, based on the power-over-ethernet (PoE) standard, both data and electricity can be delivered to each light fixture by a single Ethernet cable. Finally, the PLC technique uses the electricity wiring infrastructure as a means to interface the LiFi BSs with the distribution point. Specifically, the backhaul communication is coupled into electrical cables by using a proper hardware interface which requires additional equipment to be installed.

The aforementioned backhauling approaches are all wired. A major drawback of wired solutions is that they highly depend on the wiring infrastructure where any failure directly translates into a loss on the overall network performance. In addition, it is necessary to redesign the wiring infrastructure in order to distribute additional cables to every single luminaire especially for optical fiber and PoE cases. This is subject to extra costs which are hardly justifiable for large networks with densely deployed BSs. To the best of the author' knowledge, wireless op-

tical backhauling has never been considered as an option for indoor optical attocell networks. The wireless optical backhaul solution proposed in this work makes the backhaul network independent of the wiring infrastructure, thus eliminating the cost of modifying the structure of wiring. The required transceivers to establish inter-BS links are built by adding a number of low-cost LEDs and photodiodes (PDs) to LiFi BS units. This thesis puts forward a novel proposal and paves the way for advancing the architecture of optical attocell networks. Since there is a lack of a directly related work in literature, the principal incentive of this research is to lay the groundwork for wireless optical backhauling in optical attocell networks.

1.2 Contributions

This thesis focuses on devising wireless optical backhaul methods for indoor optical attocell networks using a system-level approach. In a systematic way, the aim is to address four objectives:

- Establishing a detailed model for signal transmission through wireless optical backhaul and access systems.
- Evaluating and optimizing the end-to-end downlink performance of optical attocell networks with wireless optical backhauling.
- Examining the scalability of the proposed solution when applied to larger networks.
- Identifying other application scenarios based on the presented approach.

By following these objectives, several contributions have been made.

With regard to the first objective, the aim is to devise a wireless backhaul system for indoor optical attocell networks, based on wireless optical communications in either VL or infrared (IR) bands. A major concern when wireless optical access and backhaul systems are operated on a common propagation medium is to identify the interference that backhaul links cause on each other or on the access system. To this end, for a one-tier hexagonal network model with a star topology, the end-to-end signal transmission from the gateway to UEs with decode-and-forward (DF) relaying is thoroughly analyzed. The effects of inter-backhaul and backhaul-to-access interferences are carefully taken into account and calculated using a geometric modeling methodology. The presented methodology is subsequently extended to a two-tier network with

a tree topology. Based on a DC-biased optical OFDM (DCO-OFDM) modulation scheme, novel analytical signal-to-noise-plus-interference ratio (SINR) expressions are derived for both the access and backhaul systems by considering the aforementioned interference effects. Also, novel bandwidth allocation methods are proposed to realize wireless backhauling in the VL band consisting of full reuse visible light (FR-VL) and in-band visible light (IB-VL) systems. For IB-VL backhauling, the optimal design of the bandwidth allocation ratio is also derived. The mathematical modelings and analytical derivations for the VL backhaul system are published in [30].

Following the second objective leads to the second contribution of this thesis: performance evaluation and optimization for the end-to-end network. To study the effect of load in the network, a multi-user scenario is considered where a number of UEs are randomly distributed over the coverage region. Based on the combination of multi-hop DF relaying and DCO-OFDM, the detailed derivation of the end-to-end sum rate of the UEs is presented. Also, an optimization framework for backhaul power control with the aim to minimize the transmission power of the backhaul system is proposed. The corresponding optimization problems for one-tier and two-tier cases are solved and exact closed form power control coefficients are derived and expressed in terms of system parameters. In addition, a power-bandwidth tradeoff analysis is expounded for a two-tier network with IR backhauling so as to characterize the interplay between the allocated power and the required bandwidth. Separate case studies are considered to evaluate the performance of the optimized backhaul systems, offering illuminating insights into the performance of different backhauling schemes. The effect that the semi-angle of backhaul LEDs cause on the network performance is highlighted through computer simulations. Furthermore, a question that naturally arises is that if there is a misalignment in backhaul links, to what extent does it affect the performance of the backhaul system? To address this question, imperfect alignment errors between adjacent BSs are implemented and studied using simulations. The work conducted on the extended analysis and optimization of VL and IR backhaul systems has led to the publication of [31].

Regarding the third objective, the use of wireless optical backhaul solution is extended to multi-tier networks through introducing the new concept of super cells. Consequently, new challenges arise for backhaul power control and bandwidth scheduling. In an opportunistic approach, three schemes are proposed for controlling the power of the backhaul system based on the availability of the downlink channel information. Particularly, adaptive power control (APC) and fixed

power control (FPC) schemes are designed and their corresponding power control coefficients are analytically derived. Performance improvements are evaluated in terms of the backhaul power efficiency and the probability of backhaul bottleneck. In addition, an analysis of the end-to-end sum rate of the network is performed for the general case of multiple tier networks by taking the effect of bandwidth sharing at the bottleneck link into consideration. Moreover, the presence of multiple flows in the bottleneck link of a single backhaul branch necessitates optimal scheduling of the bandwidth resource. To this end, cell-based bandwidth scheduling (CBS) and user-based bandwidth scheduling (UBS) policies are proposed and novel algorithms are developed to implement them by formulating and solving bandwidth allocation optimization problems. The effectiveness of the proposed algorithms on the end-to-end network performance is investigated by studying the sum rate performance. Part of the research conducted on the derivation of power control coefficients and the evaluation of sub-optimal bandwidth scheduling policies for a two-tier network model has led to the publication of [32], and the rest is under preparation for publication.

In relation to the fourth objective, wireless optical backhauling is used to devise novel cooperative downlink transmission techniques for optical attocell networks. These techniques combine the use of DF relaying with fractional frequency reuse (FFR) partitioning. In particular, by exploiting the opportunity of transmitting on free sub-bands that exist between the neighboring BSs because of FFR planning, two cooperative FFR (CFFR) protocols are proposed, including non-orthogonal decode-and-forward (NODF) and joint transmission with decode-and-forward (JTDF). The proposed schemes are shown to improve upon FFR. This gives rise to a new use case for the proposed wireless optical backhaul systems. For each CFFR scheme, analytical expressions of the downlink SINR and the system spectral efficiency (SE) are derived. Performance gains of the designed systems relative to full reuse (FR) and non-cooperative FFR systems are studied in terms of the average SE. The research conducted on the modeling and analysis of the proposed CFFR transmission techniques has led to the publication of [33, 34].

1.3 State-of-the-art

This section provide a concise review of the state-of-the-art in the domain of backhauling for VLC systems and other related topics. Prior studies have approached the problem of backhauling for indoor VLC systems by three main solutions: in-building PLC, Ethernet and optical fiber. In [35], Komine and Nakagawa initially proposed the idea of exploiting the existing elec-

tricity wiring within buildings for the purpose of backhauling, leading to an integrated PLC and VLC system. Their initial proposal targeted a low data rate of 1 Mbits/s using single carrier (SC) binary phase shift keying (BPSK) modulation. Later in [36], Komine *et al.* considered employing a narrowband quadrature phase shift keying (QPSK)-OFDM system to combat the multipath effect in the VLC channel so as to achieve higher data rates with the integrated PLC and VLC system. The authors in [37] proposed and experimentally demonstrated a deeply integrated PLC and VLC system based on quadrature amplitude modulation (QAM)-OFDM signaling for indoor broadband broadcasting where amplify-and-forward (AF) relaying was used to bridge the PLC and VLC channels with the aim to realize a single frequency network. Moreover, in [38], Ma *et al.* considered further optimization of the performance of the hybrid PLC-VLC system using AF and DF relaying for signal transmission in PLC and VLC hops.

As an alternative option for wired backhauling in VLC systems, the Ethernet technology is employed. By using a single CAT cable, both data and electricity can be distributed to LED luminaires based on the PoE standard. In [39], Mark designed and implemented a cascaded system of PoE and VLC using a dual-hop AF relaying transmission over Ethernet and VLC hops. In addition, in [40], Delgado *et al.* designed an Ethernet-VLC interface to realize indoor broadcasting from an Ethernet-based local area network (LAN) using VLC.

As an alternative to Ethernet, backhauling for VLC systems is also possible with optical fiber. In [41], Wang *et al.* proposed an indoor VLC-based LAN architecture where optical BSs are connected to the core network via standard single mode fiber (SMF) links. To enable multi-Gbits/s connectivity based on deploying SMF, the integration of a multi-band PON architecture and indoor VLC system was proposed and experimentally demonstrated [42, 43].

For indoor optical attocell networks, most theoretical studies focus only on the access part, making the implicit assumption that every BS is separately equipped with an infinite capacity backhaul link to connect to the gateway, e.g., [16, 44, 45], while others use the assumption that the backhaul links are ideal (i.e., lossless and noiseless), albeit they imply a wired backhauling approach, e.g., [46, 47]. This is in contrast to this work where the effect of wireless optical backhaul links on the system functionality is carefully taken into consideration and reflected as a limiting factor in the end-to-end network performance.

For cooperative VLC systems, relay-assisted transmission based on DCO-OFDM for a PTP VLC system is studied in [48], and the end-to-end performance of a dual-hop link with AF

relaying is studied in terms of the bit error probability. Also, the feasible rate regions of a system with two interfering DCO-OFDM transmitters and two receivers is investigated in [49], using a coordinated interference management method based on orthogonal transmission and joint power control. However, the approaches in these studies are not directly applicable to optical attocell networks which essentially include multiple LiFi base stations BSs and UEs. In [47], a coordinated broadcasting scheme was proposed for indoor multi-user VLC applications, similar to coordinated multi-point (CoMP) transmission in RF cellular networks. Furthermore, CoMP joint transmission schemes were investigated for the optical attocell downlink system in [50, 51]. In these works, it was assumed that there is a backhaul network to support the coordination among multiple optical attocells. However, the limiting effect of the backhaul system on the overall system performance was not taken into account. Different from the mentioned works, the work presented in this thesis incorporates the model of the wireless optical backhaul system into the network model and takes advantage of FFR planning to devise cooperative transmission schemes based on DF relaying for optical attocell networks.

1.4 Thesis Layout

The remainder of this thesis is organized as follows: Chapter 2 provides the relevant background for understanding the operation principles of optical attocell networks. First, the concept of optical attocell is presented. This is followed by introducing different phenomena related to indoor propagation of light such as LOS and non-line-of-sight (NLOS) components of the free space channel model and the implication of multipath fading in the context of indoor wireless optical channels. Then, the limitation of bandwidth in VLC systems is explained and the role of front-end elements of the system, i.e., LEDs and PDs, in this respect are described. In addition, the fundamental concepts and different variants of optical OFDM are discussed. Also, the building blocks of a DCO-OFDM communication system, which involves the main modulation scheme in this work, are detailed. Finally, the achievable rate of a DCO-OFDM link is established.

In Chapter 3, the wireless optical backhaul solution is introduced. The end-to-end signal model is described and the geometric modeling of the backhaul interference is presented. In addition, the full design of FR-VL, IB-VL and IR backhaul systems is given. The SINR and sum rate derivations for one tier and two tier network models are explicated. Furthermore, the power optimization formulation and its solution for FR-VL and IR cases are given. The analysis of the bandwidth-power tradeoff for a two-tier network with IR backhauling is presented. The

imperfect alignment of backhaul links is also discussed in this chapter.

In Chapter 4, by employing a sufficiently focused light beam in backhaul links, the application of wireless optical backhauling is extended to multi-tier networks. The derivation of the generalized end-to-end sum rate is given. Then, the criteria for deriving APC and FPC schemes are introduced and the analysis of their power control coefficients are presented. Moreover, bandwidth scheduling based on CBS and UBS algorithms is given in detail. Various performance metrics are considered to shed light on different aspects of the proposed power control schemes and bandwidth scheduling polices. More specifically, relative total power (RTP) and backhaul bottleneck occurrence (BBO) are defined for evaluating power control mechanisms, while the average multi-user sum rate is used to assess bandwidth scheduling policies.

In Chapter 5, CFFR downlink transmission techniques are discussed. The proposed NODF and JTDF protocols are presented. The derivation of their SE expressions is given and the downlink SE performance is studied.

In Chapter 6, a concise summary of the key findings of this thesis is presented, and a number of concluding remarks are provided. Finally, the limitations of the presented work are discussed along with identifying a number of possible directions for future research.

Chapter 2
Background

2.1 Optical Attocell Network

Optical attocell networks lie on top of the indoor lighting infrastructure to enable broadband wireless access by means of light [52]. To this end, the existing light emitting diode (LED)-based luminaires are augmented with the light fidelity (LiFi) technology to be utilized as optical base stations (BSs), with each BS providing coverage for a number of user equipment (UE) devices. An *optical attocell* refers to the area on the receiver plane that a single BS covers. In this work, an optical attocell network with a hexagonal tessellation is considered. In comparison to other potential network models including a square network and a random poisson point process (PPP)-distributed network, the hexagonal cell deployment model leads to the upper bound performance for practical optical attocell networks in terms of the received signal-to-noise-plus-interference ratio (SINR) and cell data rate [16]. Throughout the thesis, the term access point (AP) is used interchangeably for BS.

The realization of LiFi networking relies on inexpensive devices, i.e., LEDs embedded in light fixtures and photodiodes (PDs) that need to be integrated into UEs. Commercial white LEDs generate incoherent light over a broad electromagnetic spectrum covering almost the entire visible light (VL) range. The most viable approach to exploit such devices for wireless communications is intensity modulation and direct detection (IM-DD). In an IM-DD system, the desired waveform is modulated onto the instantaneous power of the optical carrier, and a photodetector transduces the optical signal into an electrical current proportional to the instantaneous received power.

This work primarily focuses on the downlink performance. To realize bidirectional networking in optical attocell networks, the uplink connection is established by using communications in the infrared (IR) band e.g. [9, 53, 54], or in the radio frequency (RF) band e.g. [13, 55, 56]. Nonetheless, by employing a transmission spectrum that does not overlap with the VL band, the uplink problem is considered independent of the downlink.

2.2 Indoor Propagation Characteristics of Light

The characterization and modeling of indoor light propagation have been the subject of many studies for both wireless IR [54, 57–61] and VL [16, 62–66] channels. In essence, an indoor wireless optical channel is identified by line-of-sight (LOS) and non-line-of-sight (NLOS) propagation paths. This work mainly involves directed LOS and non-directed LOS link configurations as described in [54]. For such scenarios, the LOS path is intrinsically the dominating factor when considering the aggregate power of LOS and NLOS components [54]. Besides, incorporating NLOS paths in the channel model significantly increases the computational complexity, albeit with a marginal contribution to the received power. This is especially pronounced for indoor optical attocell networks. In particular, an in-depth study in [16] confirms that NLOS paths have an insignificant effect on the attocells located at a sufficient distance away from the network boundaries. Except in small regions near the walls and corners, the LOS component solely constitutes more than 90% of the overall power contribution [16, 44]. In this work, a LOS light propagation model is used. In addition to simplifying the channel model, it facilitates mathematical tractability for system-level analyses. For the sake of completeness, the implication of multipath propagation in indoor wireless optical and wireless RF channels is underlined through a brief discussion.

For wireless RF channels, the notion of *multipath fading* relates to the phenomenon in which the transmitted signal undergoes several reflections as it propagates and, in consequence, multiple copies of the signal with random magnitudes and phases are superimposed at the receiver. This causes random fluctuations in the instantaneous received power [14]. Different from multipath-induced fading, in indoor wireless optical channels based on IM-DD, the reflected components of the transmitted signal always add up constructively at the receiver, and the short wavelength of optical carriers in conjunction with a large detector area[1] create efficient spatial diversity that neutralizes the fading effect [54]. Equivalently, the concept of spatial diversity is explained by interpreting the detector as a two-dimensional array of many antenna elements whose receptions are squared, low-pass filtered and summed [54]. Therefore, there is no fading for indoor wireless optical channels, provided that the network environment is stationary. For a given link setup, the channel impulse response simply represents a *deterministic* power delay profile rather than a stochastic process.

[1] Typical detector areas are several orders of magnitude greater than square optical wavelengths [54].

2.3 Bandwidth Limitation

Frequency domain characteristics of visible light communication (VLC) systems depend upon two principal elements: the free space channel and the front-end devices. The former element relates to dispersive wireless optical channels in which multipath reflections cause the received signal power to spread out over time. This translates into frequency selectivity in the channel frequency response. For indoor wireless IR channels, it is known that the flatness of the channel gain is strongly dependent on the strength of the LOS component [60]. With a stronger LOS gain, the overall channel gain is more flat. In a similar way, for indoor optical attocell networks, the normalized channel gain (i.e., the ratio of the channel gain to its value at zero frequency) is monotonically decreasing for frequencies less than 20 MHz with a minimum level occurring at about 20 MHz [16]. For frequencies higher than 20 MHz, the normalized channel gain exhibits a damped oscillation around the LOS gain [16]. By using a judicious configuration for the cell radius and the half-power semi-angle of LEDs, the proportion of the LOS component to the total received power is above 90%. That way the maximum loss in the normalized channel gain is kept below 2.5 dB, and hence the channel frequency response is nearly flat around the DC. In such a case, the channel is principally characterized by the DC gain which is almost equal to the LOS gain. The DC gain of the channel is defined as the ratio between the average optical power of the received signal and that of the transmitted signal [54].

The overall frequency response of VLC systems is largely influenced by the front-end device filtering phenomenon [16]. It originates from the finite cut-off frequency of LEDs and PDs, also known as the *modulation bandwidth* [8, 67]. In practice, the bandwidth limitation is imposed at the transmitter side due to the maximum permissible switching speed of the LED, as the responsivity of the PD typically has a wider bandwidth. Low-cost white LEDs are built on blue LED elements faced with a yellow phosphorous coating [68]. As a result of the slow response time of the phosphor layer, the modulation frequency of the device does not exceed several MHz. With a blue filter applied at the receiver, the modulation frequency is improved to few tens of MHz [69]. In comparison to the frequency response of the free space channel, the LED modulation bandwidth is predominant, effectively restricting the VLC bandwidth [16]. In this work, a flat VLC channel with a total bandwidth of B is considered.

For band-limited VLC systems, from a communication engineering perspective, high data rates in the order of multiple hundreds of Mbits/s are often attained by using various techniques such as frequency domain equalization [70,71], multiple input multiple output (MIMO) [72–74], and

rate-adaptive multi-carrier (MC) modulation [69, 75]. From a device engineering standpoint, it is possible to further push the data rate to unlock Gbits/s transmissions based on high bandwidth Gallium-Nitride μ-LEDs [8, 76]. The need for optimizing the performance of LED devices for high speed communication purposes has been the incentive to recent significant research efforts [77, 78]. Yet, the emerging devices are not fully adopted in the interior lighting equipment. This work employs a MC modulation scheme based on optical orthogonal frequency division multiplexing (OFDM) for multi-user data transmission, as discussed next.

2.4 Optical Orthogonal Frequency Division Multiplexing

Optical OFDM has been a candidate modulation scheme for high speed communications through optical channels [79]. The application of OFDM for indoor wireless optical communications offers many advantages, among which the most important ones include: 1) The power spectral density (PSD) of an OFDM signal has sharp transition bands if the number of subcarriers $N \geq 64$ [79]. Therefore, for a band-limited channel, it can approach the maximum signaling rate, i.e., the Nyquist rate, without the need to use filters with sharp cutoff frequencies [80]. As a result, the transmitter can be matched with the low-pass frequency response of the LED, allowing one to maximally utilize the limited bandwidth of the system; 2) The use of OFDM multiplies the symbol period by a factor equal to the total number of subcarriers, which is a large number in most practical cases. Hence, the symbol duration becomes appreciably longer than the root mean square (RMS) delay spread of typical dispersive indoor wireless optical channels [52]. The long symbol interval in conjunction with a single-tap equalizer create an inherent robustness for the signal against inter-symbol interference (ISI); 3) Baseband signal processing can be efficiently implemented in the digital domain by using an inverse fast Fourier transform (IFFT)-fast Fourier transform (FFT) pair, greatly reducing the system complexity; 4) A large number of subcarriers in combination with a properly designed cyclic prefix (CP) effectively transform the dispersive wireless optical channel into a flat channel over the subcarrier bandwidth [79]. That way the complexity of implementing frequency domain equalization (FDE) at the receiver reduces to a single-tap equalizer and the multipath-induced ISI is eliminated with a small overhead [81]. In fact, maximum delay spreads up to 100 ns are fully compensated by a CP of only two samples with a negligible impact on the electrical signal-to-noise ratio (SNR) requirement and the spectral efficiency (SE) [81]. In this work, the signaling overhead associated with the CP is not considered to simplify the system-level analysis; 5)

The full employment of OFDM in combination with an adaptive modulation based on multi-level quadrature amplitude modulation (QAM) turns out to be a promising scheme to deliver very high data rates [75, 82]; 6) The application of optical OFDM can be easily extended to optical orthogonal frequency division multiple access (OFDMA). It enables flexible time and frequency domain resource management for multi-user LiFi networks [83].

Optical IM-DD systems are essentially baseband communication systems in which the signal waveform is represented by the intensity of light. Applying OFDM to such systems requires the time domain signal to be both real-valued and unipolar (i.e., non-negative). Several variants of optical OFDM have been proposed to meet these requirements, such as DC-biased optical OFDM (DCO-OFDM) [84–86], asymmetrically clipped optical OFDM (ACO-OFDM) [87,88], spectral and energy efficient OFDM (SEE-OFDM) [89], polar OFDM (P-OFDM) [90], and enhanced unipolar optical OFDM (eU-OFDM) [91]. These modulation techniques are tailored to reach a compromise for SE and energy efficiency. Among them, DCO-OFDM yields a superior SE over a wide range of optical SNR [92, 93], and it entails a relatively low implementation complexity. However, the need for a high DC bias adversely affects the power efficiency (PE) of DCO-OFDM. Nevertheless, since the primary functionality of LED luminaires is to provide illumination, a high DC bias is required anyway. For this reason, the application of DCO-OFDM is appealing to optical attocell networks [16, 44].

In this work, DCO-OFDM is employed as the main modulation scheme, so in the following, the principles of operation of a DCO-OFDM communication system are concisely presented.

2.5 DCO-OFDM Communication System

2.5.1 Principles of Operation

Fig. 2.1 depicts the building blocks of a DCO-OFDM communication system with an N-point IFFT/FFT, operating over an indoor wireless optical channel. As the signal progresses through the system, the function of different stages is described one by one. First of all, observe that the transformed subsymbols[2] are directly sent into the channel without any further modulation or up-conversion. In this case, it is only possible to transmit a real signal in the time domain. That is why the output of the IFFT is constrained to be real-valued. A common way to ensure this is

[2]To avoid confusion, the term *subsymbol* indicates QAM subsymbols modulated on individual subcarriers while the term *symbol* is reserved to refer to the OFDM symbol as a whole.

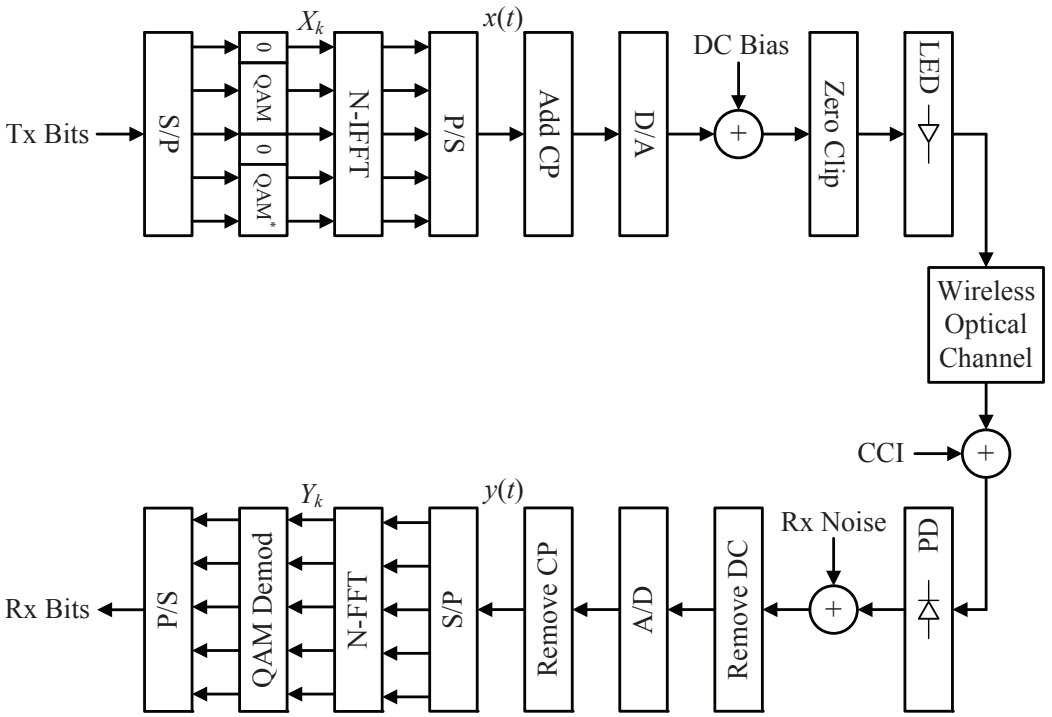

Figure 2.1: *Block diagram of a DCO-OFDM communication system operating in an indoor optical attocell network.*

by using conjugate symmetry [94], also known as *Hermitian symmetry*, for subsymbols. To this end, the baseband bandwidth of the system is divided into N independent parallel subchannels, with each one acquiring an equal bandwidth. Based on a variable-rate QAM modulation [95], with a constellation of size of 2^b, the input binary information sequence is arranged in a parallel format and buffered into blocks of b bits to be loaded onto data-carrying subchannels with a total number of $\tilde{N} = \frac{N}{2} - 1$. The bits assigned to the kth subchannel are mapped to the kth complex QAM subsymbol denoted by X_k. The average power of QAM subsymbols are normalized to unity such that $\mathbb{E}\left[|X_k|^2\right] = 1$. The total number of subsymbols is extended to N by enforcing the Hermitian symmetry so that $X_{N-k} = X_k^*$ for $k = 1, 2, \ldots, \tilde{N}$. In order to maintain conjugate symmetry, it is essential that X_0 and $X_{\frac{N}{2}}$ be real. If the original value of X_0 is zero, then both X_0 and $X_{\frac{N}{2}}$ are set to zero. Otherwise, a new data block may be transmitted by assigning the real part of the corresponding QAM subsymbol to X_0 and its imaginary part to $X_{\frac{N}{2}}$ [94]. Since X_0 is reserved for DC bias, the 0th and the π-shifted subcarriers are left unmodulated by setting $X_0 = X_{\frac{N}{2}} = 0$, as shown in Fig. 2.1. The resulting DCO-OFDM frame has the following structure:

$$\mathbf{X} = \left[0, X_1, X_2, \ldots, X_{\tilde{N}}, 0, X_{\tilde{N}}^*, \ldots, X_2^*, X_1^*\right]^T. \tag{2.1}$$

By applying an N-point IFFT, the N elements of $\mathbf{X}$ in (2.1) are transformed into N purely real samples in the time domain. The IFFT output signal at time sample t, for $t = 0, 1, \cdots, N-1$, is given by:

$$x(t) = \frac{1}{\sqrt{N}} \sum_{k=0}^{N-1} X_k e^{\hat{j}\frac{2\pi kt}{N}} = \frac{2}{\sqrt{N}} \sum_{k=1}^{\tilde{N}} |X_k| \cos\left(\frac{2\pi kt}{N} + \angle X_k\right), \tag{2.2}$$

where $\hat{j} = \sqrt{-1}$; and $|X_k|$ and $\angle X_k$ are magnitude and phase of X_k, respectively. Subsequently, the N samples are converted from the parallel to serial format and a CP is appended to the beginning of the OFDM symbol. For $N \geq 64$, the IFFT output signal in (2.2) follows a zero mean real Gaussian distribution based on the central limit theorem (CLT) [96]. To establish a unit variance at the IFFT output, that is, to normalize the average power of the baseband modulated signal in (2.2) to unity, i.e., $\mathbb{E}\left[|x(t)|^2\right] = 1$, the DCO-OFDM frame is multiplied by a factor of $\sqrt{\frac{N}{N-2}}$, before applying the IFFT [16]. In order to set the average electrical power of the OFDM symbol (i.e., the total transmission power) to P_{elec}, the time domain signal is scaled to $\sqrt{P_{\text{elec}}}x(t)$. Finally, after digital-to-analog conversion, a DC bias is added and the remaining negative samples are clipped at zero. The resulting positive signal is used to drive the forward current of the LED. The output optical signal at time sample t can be written as follows:

$$x_{\text{opt}}(t) = \sqrt{P_{\text{elec}}}x(t) + x_{\text{DC}}, \tag{2.3}$$

where x_{DC} is the DC bias. The DCO-OFDM signal in (2.3) varies the instantaneous intensity of the LED light. This involves an electrical to optical conversion that is subject to nonlinear current-to-power transfer characteristic of the LED. The nonlinear relationship between the LED current and the output optical power can be linearized using predistortion techniques [97]. The modulating signal is still subject to clipping distortion due to the limited dynamic range of the LED. Upon choosing a proper value for the DC bias, signal clipping occurs symmetrically with respect to the average optical power [98], which is given by $P_{\text{opt}} = \mathbb{E}[x_{\text{opt}}(t)] = x_{\text{DC}}$, based on (2.3). A reasonable choice for the DC bias is $x_{\text{DC}} = \alpha\sqrt{P_{\text{elec}}}$ where α is a scaling factor [88]. Then, applying $\alpha = 3$ guarantees that 99.7% of the dynamic swing of the signal envelope remains undistorted according to the three-sigma rule and the clipping noise can be safely discarded [98]. Note that the illumination level depends on the average optical power, which is determined by the DC bias. Also, the total transmission power is related to the average optical power via $P_{\text{elec}} = \frac{P_{\text{opt}}^2}{\alpha^2}$. In addition, P_{elec} is equally divided among data-carrying subcarriers so that each subcarrier acquires the same power of $\frac{P_{\text{opt}}^2}{(N-2)\alpha^2}$.

At the receiver, first a PD detects the instantaneous intensity of the modulated light, then the DC component is subtracted from the detected photocurrent. Followed by perfect sampling, and the removal of CP samples, the resultant N output samples are arranged in a parallel format, and they are converted into $\tilde{N}$ complex values by using an N-point FFT. Finally, the $\tilde{N}$ transmitted subsymbols are individually demodulated according to their respective QAM constellation and the retrieved data blocks are then arranged from the parallel to serial format.

2.5.2 Achievable Rate

To facilitate the rate analysis, a closed form expression of the achievable rate of a DCO-OFDM link is required. To this end, in the following, the achievable rate per subcarrier over a flat wireless optical channel is discussed. Then, the maximum signaling rate for a band-limited and low-pass system with a total bandwidth of B is examined. Consequently, the overall achievable rate and the SE for a DCO-OFDM system are established.

2.5.2.1 Achievable Rate Per Subcarrier

For a dynamic range limited wireless optical system based on DCO-OFDM, the Shannon-Hartley capacity theorem can be applied individually to each subcarrier in between two points: the input of the IFFT at the transmitter and the output of the FFT at the receiver, see Fig. 2.1. Note that for DCO-OFDM, regardless of DC bias addition and removal operations, the information carrying component of the signal is bipolar, i.e., the signal amplitude can be either positive or negative. By contrast, capacity bounds such as those established in [99, 100] are generally based on a pulse amplitude modulation (PAM) scheme, in which case the signal amplitude is restricted to be unipolar, i.e., only positive.

Besides, whatever peak power that the information-carrying part of a DCO-OFDM signal has, it is clipped by the limited dynamic range of the LED. The clipping distortion is modeled by an attenuation coefficient and an additive non-Gaussian noise based on the Bussgang theorem [98]. Nonetheless, such a nonlinear distortion can be avoided by using a sufficiently high value for the DC bias relative to the variance of the DCO-OFDM signal envelope, which leads to a negligible clipping effect [98]. In principle, through a large number of subcarriers, the FFT operation effectively converts any independent and identically distributed (i.i.d.) perturbation term added to the received signal, including clipping noise and co-channel interference (CCI),

into a Gaussian noise according to the CLT [98].

In addition, to achieve the desired peak-to-average power ratio (PAPR) performance, there is an average power constraint, which is directly related to the average optical power constraint as discussed in Section 2.5.1. Therefore, for the aforementioned input-output points *in the electrical domain*, the Shannon-Hartley capacity formula can be used. For a DCO-OFDM transmission system operating over a flat wireless optical channel, the achievable rate on subcarrier k as a function of the received SINR γ is readily obtained as:

$$\mathcal{R}_k = \Delta f \log_2 (1 + \gamma), \tag{2.4}$$

where Δf is the subchannel bandwidth. The value of Δf depends on the symbol rate, which is discussed next.

2.5.2.2 Overall Achievable Rate

For the sake of clarity, the definition of bandwidth for low-pass systems is needed. For a low-pass system whose frequency support spans from zero up to a cutoff frequency, the bandwidth is equal to the cutoff frequency [101]. Such a *single-sided* bandwidth is imposed by the low-pass frequency response of the system, e.g., the VLC system. In this case, only the real dimension associated with the positive frequency axis is usable for signal transmission. In fact, a baseband OFDM transmission with a total number of N subcarriers and a symbol period of T occupies a *double sided* (i.e., null-to-null) bandwidth of $\frac{N}{T}$ in the range between $-\frac{N}{2T}$ and $\frac{N}{2T}$. In the case of DCO-OFDM, the Hermitian symmetry ensures a real-output IFFT by arranging complex conjugate replicas of subsymbols on the negative part of the baseband frequency range. Hence, the Nyquist sampling rate is $f_\mathrm{s} = \frac{N}{T}$ and an N-point FFT is required at the receiver to recover the subsymbols [80].

For a band-limited and low-pass system with a single-sided bandwidth of B, to utilize the whole spectrum, the zero-to-null bandwidth of the DCO-OFDM signal and the system bandwidth are matched so that $B = \frac{N}{2T}$. Thus, the symbol rate (i.e., the subchannel bandwidth) is:

$$\Delta f = \frac{1}{T} = \frac{2B}{N}. \tag{2.5}$$

Alternatively, this can be interpreted as the signal spectrum spans from $-\frac{f_\mathrm{s}}{2} = -B$ to $\frac{f_\mathrm{s}}{2} = B$,

leading to $\Delta f = \frac{f_s}{N} = \frac{2B}{N}$. Substituting this into (2.4) results in:

$$\mathcal{R}_k = \frac{2B}{N} \log_2 (1 + \gamma) . \tag{2.6}$$

Using $\tilde{N} = \frac{N}{2} - 1$, the overall achievable rate becomes:

$$\mathcal{R} = \sum_{k=1}^{\tilde{N}} \mathcal{R}_k = \tilde{N} \times \frac{2B}{N} \log_2 (1 + \gamma) , \tag{2.7a}$$

$$= \xi B \log_2 (1 + \gamma) , \tag{2.7b}$$

where ξ is defined as the *subcarrier utilization factor*:

$$\xi = \frac{2\tilde{N}}{N} = \frac{N - 2}{N}. \tag{2.8}$$

The SE of a DCO-OFDM system with a single-sided bandwidth B is given by:

$$\eta = \frac{\mathcal{R}}{B} = \xi \log_2 (1 + \gamma) \quad \text{bits/s/Hz} \tag{2.9}$$

2.6 Summary

This chapter serves as the basis for subsequent technical chapters by providing the required background information. Important concepts involved in understanding the operation of optical attocell networks are highlighted using a top-down approach. The chapter starts with an overview of how a LiFi attocell is formed and continues with discussions about light undergoing various propagation phenomena over indoor wireless optical channels. The implications of path loss and fading for the modeling of these channels are reviewed. First, LOS and NLOS propagation models are introduced. It is clarified that excluding small regions in proximity to the network boundaries where the NLOS effect is manifested most, in the rest of areas under coverage, more than 90% of the received optical power comes solely from the LOS component. In addition, the notion of multipath fading for optical IM-DD channels is inspected, concluding that the signal fading is effectively averaged out over the photodetector surface as its area is typically a million times the square wavelength of optical carriers. Furthermore, the frequency domain characteristics of VLC systems are concisely explored, underlining the fact that the end-to-end transmission system is mainly governed by the frequency response of front-end de-

vices. Thus, the bandwidth limitation is attributed to the finite modulation bandwidth of LEDs and PDs.

In view of transmission techniques, optimal OFDM is introduced as a suitable candidate that can deliver high data rates with the limited VLC bandwidth. In LiFi systems, the use of optical OFDM with a very short CP leads to the elimination of multipath-induced ISI. Such a powerful modulation can efficiently run on a baseband processing platform using IFFT/FFT operations. Due to its granular frequency content, it provides flexible access to the operating bandwidth, which is utilized for optimal management of network resources. In order to implement a dual functionality of illumination and communication in a simple yet effective manner, DCO-OFDM is employed. It is considered the principal modulation scheme for optical attocell networks due to its superlative SE performance. A DCO-OFDM communication system is presented in detail to elucidate the role of each building block. In consideration of the constrained dynamic range of LEDs, a major challenge of adopting optical OFDM techniques lies in controlling their PAPR performance. To take advantage of DCO-OFDM, by adjusting the DC bias at $x_{\mathrm{DC}} = 3\sqrt{P_{\mathrm{elec}}}$, only less than 3% of the signal swing is affected by the nonlinear clipping distortion. This restrains the PAPR level by ensuring 97% of the signal swing remains undistorted. Furthermore, to assess the achievable rate of DCO-OFDM links, a simple and tractable expression is established based on the Shannon-Hartley formula. Given a single-sided bandwidth B of the underlying VLC system, the achievable rate is given by $\mathcal{R} = \xi B \log_2(1+\gamma)$ bits/s where ξ is the subcarrier utilization ratio and γ is the link SINR. Such a compact expression constitutes a foundation for data rate evaluation purposes.

Chapter 3
A Wireless Optical Backhaul Solution for Optical Attocell Networks

In this chapter, a wireless backhaul solution is proposed for indoor optical attocell networks, based on wireless optical communications in either visible light (VL) or infrared (IR) bands. The distinct contributions of this chapter are summarized as follows: 1) The proposed backhaul solution is thoroughly analyzed for a one-tier hexagonal network model with a star topology. The application of wireless optical backhauling is then extended to a two-tier network using a tree topology to evaluate the scalability of the proposed solution; 2) Novel analytical signal-to-noise-plus-interference ratio (SINR) and sum rate expressions are derived for end-to-end signal transmission from the gateway to user equipment (UE) with multi-hop decode-and-forward (DF) relaying. To this end, the effects of inter-backhaul and backhaul-to-access interferences are carefully taken into consideration using a geometric modeling approach; 3) To study the effect of load in the network, a multi-user scenario is considered where a number of UEs are randomly distributed over the coverage region; 4) A power control mechanism is proposed, aiming for the optimization of the transmission power in the backhaul system. For one-tier and two-tier cases, the corresponding power allocation coefficients are derived in closed form in terms of system parameters; 5) The full employment of IR communications is shown to deliver a superior performance for wireless optical backhauling. Supported by a power-bandwidth tradeoff analysis for a two-tier network, it is shown that a properly designed IR backhaul system can achieve the performance of an unlimited backhaul (UB) network; 6) The effect of imperfect alignment errors in backhaul links on the system performance is identified using simulations.

The remainder of this chapter is organized as follows: Section 3.1 gives essential preliminaries required for system level analysis, including the channel model of downlink and the achievable rate of DC-biased optical OFDM (DCO-OFDM); Section 3.2 presents the design and modeling of full reuse visible light (FR-VL), in-band visible light (IB-VL) and IR backhaul systems with an emphasis on the one-tier network deployment, followed by SINR and sum rate derivations; Section 3.3 provides an extension of the backhaul solution when applied to a two-tier network;

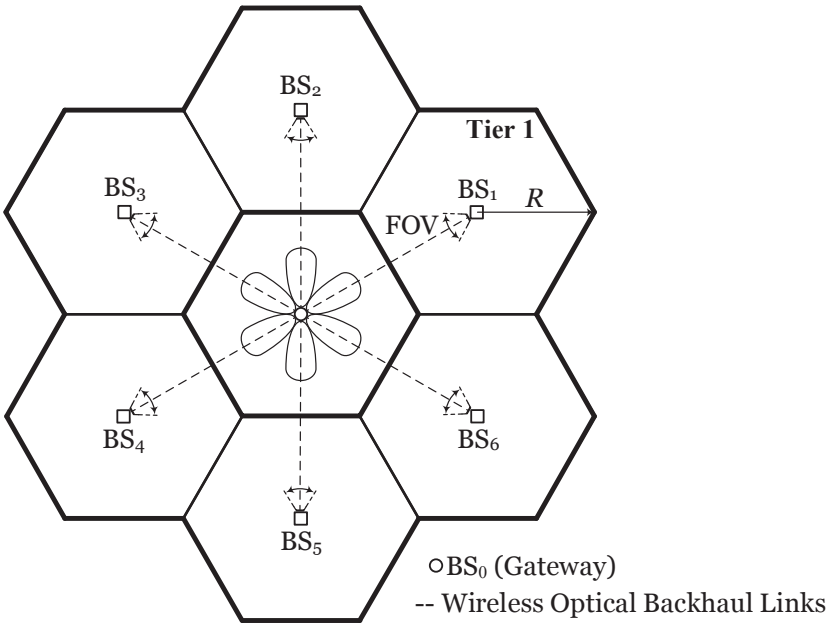

Figure 3.1: *Hexagonal cellular layout for a one-tier optical attocell network, and a plan view of wireless optical backhaul links.*

Section 3.4 expounds an optimization framework proposed to minimize the transmission power for FR-VL and IR backhaul systems. It also presents an exclusive discussion on the effect of misalignment in the backhaul system; Section 3.4 briefly outlines key findings and remarks, concluding the chapter.

3.1 System Level Preliminaries

3.1.1 Downlink Configuration

Fig. 3.1 depicts the hexagonal layout of a one-tier optical attocell network with 7 attocells. Also, Fig. 3.2 illustrates the geometric configuration of the downlink system. The transmitter consists of a white light emitting diode (LED) installed on the ceiling and there is a solid-state photodiode (PD) mounted on the UE receiver. The photosensitive receiver of the UE first converts the incident optical power collected within the field of view (FOV) to an electrical current then decodes the desired information. It is assumed that the LEDs are oriented vertically downward and the UE devices have a vertically upward orientation. The receiver FOV is assumed to be sufficiently wide to allow simultaneous detection of optical signals from all base stations (BSs).

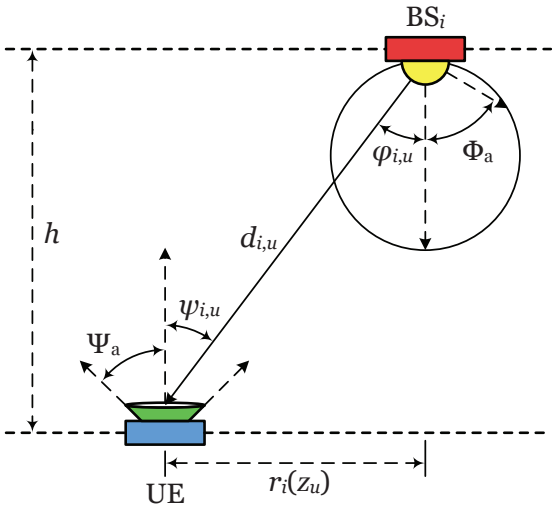

Figure 3.2: *Downlink geometry in an indoor optical attocell network using these parameters: Φ_a is the semi-angle at half-power of the Lambertian pattern; $d_{i,u}$ is the Euclidean distance between the UE and BS$_i$; $\varphi_{i,u}$ is the light radiance angle with respect to the normal vector of the ceiling; $\psi_{i,u}$ is the light incidence angle with respect to the normal vector of the receiver plane; Ψ_a is the FOV of the UE receiver; $r_i(z_u)$ is the horizontal distance between the UE and BS$_i$; h is the vertical distance separating the UE from the ceiling.*

By using a Lambertian emission pattern for LEDs, the DC gain of the visible light communication (VLC) channel from BS$_i$ to the uth UE is given as follows [54, Eq. (10)]:

$$H_{i,u}^{a} = \frac{(m+1)A_{PD}}{2\pi d_{i,u}^2}\cos^m(\varphi_{i,u})\cos(\psi_{i,u})\mathbb{1}_{FOV}(\psi_{i,u}), \tag{3.1}$$

where $m = -\frac{\ln 2}{\ln(\cos\Phi_a)}$ is the Lambertian order and Φ_a is the semi-angle at half-power of the LED emission pattern; A_{PD} is the effective PD area; $d_{i,u}$ is the Euclidean distance between the UE and BS$_i$; $\varphi_{i,u}$ is the light radiance angle with respect to the maximum power direction for BS$_i$; $\psi_{i,u}$ is the light incidence angle with respect to the normal vector of the PD plane; and Ψ_a is the FOV for the UE receiver. These are depicted in Fig. 3.2. The last factor in (3.1) is an indicator function defined as:

$$\mathbb{1}_{FOV}(\psi_{i,u}) = \begin{cases} 1, & 0 \le \psi_{i,u} \le \Psi_a \\ 0, & \psi_{i,u} > \Psi_a \end{cases} \tag{3.2}$$

To elaborate, a polar coordinate system with BS$_0$ at the origin, as shown in Fig. 3.3, is considered. For geometric variables related to BS$_0$, the BS subscript 0 is dropped to simplify notation. More specifically, $z_u = (r_u, \theta_u)$ represents polar coordinates of the UE with respect to BS$_0$.

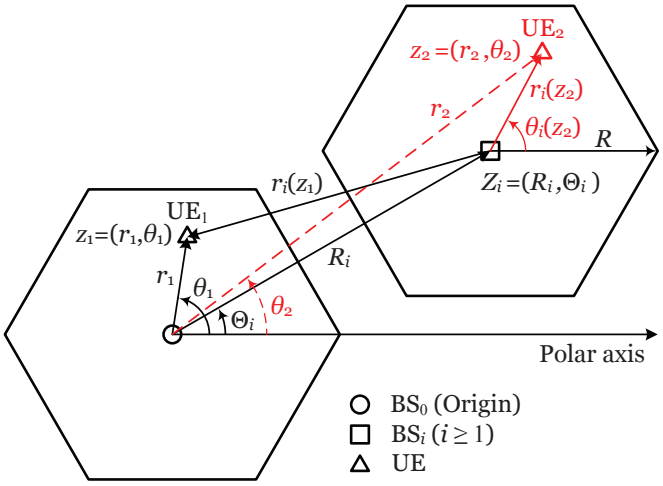

Figure 3.3: *Optical attocell network geometry in a polar coordinate system. An example with two UEs shows relative radial distances and polar angles.*

One can express the variables $d_{i,u}$, $\cos(\varphi_{i,u})$ and $\cos(\psi_{i,u})$ in terms of $z_u = (r_u, \theta_u)$ by using the relations $d_{i,u} = \sqrt{r_i^2(z_u) + h^2}$ and $\cos(\varphi_{i,u}) = \cos(\psi_{i,u}) = \frac{h}{d_{i,u}}$, where $r_i(z_u)$ is the horizontal distance between the UE and BS$_i$. The polar coordinates of BS$_i$ are denoted by (R_i, Θ_i). Assuming $0 \leq \psi_{i,u} \leq \Psi_{\mathrm{a}}$, an alternative representation is obtained for (3.1):

$$H_{i,u}^{\mathrm{a}} = \frac{(m+1)h^{m+1}A_{\mathrm{PD}}}{2\pi}\left(r_i^2(z_u) + h^2\right)^{-\frac{m+3}{2}}, \tag{3.3}$$

where $r_i(z_u) = \sqrt{r_u^2 + R_i^2 - 2R_i r_u \cos(\theta_u - \Theta_i)}$.

3.2 Wireless Backhaul System Design

In the following, first, the modeling and analysis for a one-tier network, as shown in Fig. 3.1, is presented. Subsequently, the presented methodology is extended for a two-tier network.

3.2.1 Wireless Optical Backhauling

The proposed system employs point-to-point wireless optical communication so as to build a wireless backhaul network. To this end, either VL or IR bands in the optical spectrum can be utilized, both of which are considered in this work. There are cost-effective LED and PD devices for both bands that can be used to integrate backhaul transceivers with the BS units.

The wireless backhaul configuration using a star topology for a one-tier network is depicted in Fig. 3.1. As shown, only the central BS is directly connected to the core network. The remaining BSs in the first tier are routed to the core network via wireless backhaul links with the central BS using DF relaying [102]. Therefore, BS_0 is the gateway for BS_i, $\forall i \geq 1$. Relay BSs are permitted to operate in a full duplex mode because of two reasons: 1) there is no direct line-of-sight (LOS) path from the backhaul transmitter to the backhaul receiver at the same relay as they are mounted on two opposite sides of the BS unit; 2) the self-interference caused by the multipath propagation from the transmitter to the receiver on the same relay is not significant for typical indoor environments according to a study in [103]. The aim of this work is to focus on the *end-to-end* performance from the gateway to the UEs, assuming that there is a wired link between the gateway and the core network with an adequate capacity to support the aggregate data flowing in the whole backhaul network plus the downlink data for BS_0. The wireless backhaul links are provided by perfectly aligned VLC or wireless IR links. Such links can be established by adding six auxiliary LEDs on BS_0 allowing each one to point at a BS in the first tier. For each auxiliary LED, a PD is then added to the corresponding BS on the other side of the backhaul link.

The gateway continuously sends a flow of data toward BS_i without interruption. When backhaul links operate in the VL spectrum, the access and backhaul links inevitably share the same frequency band and as a consequence, mutually interfere, assuming they are spatially transparent to each other. Note that there may be a suspended ceiling under the actual ceiling, creating an enclosed space which can physically separate the VLC channels of the access and backhaul parts. However, such a facility is not available everywhere and the purpose of this work is to avoid introducing any change to the existing indoor infrastructure. In order to manage the backhaul-to-access interference, two bandwidth allocation methods are proposed, including FR-VL and IB-VL. In the FR-VL method, the entire bandwidth is fully reused across all the access and backhaul links. In the IB-VL method, two orthogonal sub-bands are allocated to the access and backhaul links and each sub-band may be fully reused by either one. More details are available in Section 3.2.3. For BS_i in the first tier, i.e., $i \in \mathcal{T}_1 = \{1, 2, \ldots, 6\}$, a dual-hop relaying transmission is performed over one backhaul hop and one hop for the access link. For BS_0, the entire bandwidth is fully used for downlink access even in the IB method, since BS_0 is directly connected to the gateway. Note that the access links do not affect the backhaul links based on the LOS propagation.

As an alternative to the VL band, the IR band is considered for wireless optical backhaul design. IR LEDs typically have a much wider modulation bandwidth than white LEDs, with cutoff frequencies in the order of 440 MHz and up to 1.7 GHz [104]. Such high bandwidths are usually produced by reducing the radiative lifetime of the minority carries [68], however at the expense of decreasing the output optical power, since the internal power-bandwidth product is fixed [68]. Most commercial and low-cost IR LEDs emit wavelengths in the range between 780 nm and 950 nm [54]. The principal drawback of radiation in this range relates to eye safety, which is globally governed by international electromechanical commission (IEC) standards. In particular, the IEC Class 1 determines an allowable exposure limit for IR transmitters depending on their wavelength, diameter and emission semi-angle [54]. In addition to eye safety regulations, it is desirable to limit the transmission power for IR backhauling in consideration of the power consumption.

3.2.2 Signal-to-Noise-plus-Interference Ratio

The backhaul link of BS_i, b_i, and the LED on its transmit end are both labeled with the index of the BS on its receive end. For instance, b_1 represents the link that connects BS_0 to BS_1. In the following, signal models are always given in the frequency domain on subcarrier k or in the time domain at time sample t, by assuming perfect sampling and synchronization. Also, it is assumed that the uth UE is associated with BS_i $\forall i \in \{0\} \cup \mathcal{T}_1$. These are not mentioned again in the sequel for the sake of brevity. Moreover, one can see in Fig. 3.1 that the backhaul network topology is symmetric around BS_0. Without loss of generality, the received signal model for the backhaul system is presented in terms of BS_1 and b_1.

3.2.2.1 Backhaul Link

Let $x_i^{\mathrm{b}}(t)$ and $X_i^{\mathrm{b}}(k)$ be the signal transmitted for BS_i through b_i in the time and frequency domains, respectively. For any of the proposed wireless optical backhaul systems, the signal intended for the downlink of BS_1 has to be decoded at BS_1 first. After removing the DC bias, the received photocurrent at BS_1 from b_1 is calculated as:

$$y_1^{\mathrm{b}}(t) = R_{\mathrm{PD}}\sqrt{P_{\mathrm{b}_1}}x_1^{\mathrm{b}}(t) \otimes h_1^{\mathrm{b}}(t) + R_{\mathrm{PD}}\sqrt{P_{\mathrm{b}_1}}\left[x_2^{\mathrm{b}}(t) \otimes h_{1,2}^{\mathrm{b}}(t) + x_6^{\mathrm{b}}(t) \otimes h_{1,6}^{\mathrm{b}}(t)\right] + v_1^{\mathrm{b}}(t), \tag{3.4}$$

where R_{PD} is the PD responsivity; $h_1^{\mathrm{b}}(t)$ is the impulse response of the wireless optical channel for the link b_1; and $v_1^{\mathrm{b}}(t)$ is the receiver generated noise. On the right hand side (RHS) of (3.4), $x_2^{\mathrm{b}}(t)$ and $x_6^{\mathrm{b}}(t)$ are interference terms caused by cross-coupling with b_2 and b_6, see Fig. 3.1. The impulse responses of interference channels from b_2 and b_6 to b_1 are represented by $h_{1,2}^{\mathrm{b}}(t)$ and $h_{1,6}^{\mathrm{b}}(t)$, respectively. In addition, $P_{\mathrm{b}_j} = K_j P_{\mathrm{a}}$ is the power allocated to the backhaul links of the first tier, where K_j is introduced as the power control coefficient for b_j; and P_{a} is the downlink transmission power. An equal power allocation is used so that $P_{\mathrm{b}_j} = K_1 P_{\mathrm{a}}\ \forall j \in \mathcal{T}_1$. Taking an N_{b}-point fast Fourier transform (FFT) of (3.4), the output signal becomes:

$$Y_1^{\mathrm{b}}(k) = \frac{1}{\sqrt{N_{\mathrm{b}}}} \sum_{t=0}^{N_{\mathrm{b}}-1} y_1^{\mathrm{b}}(t) e^{-\hat{\jmath}\frac{2\pi kt}{N_{\mathrm{b}}}}, \tag{3.5a}$$

$$= R_{\mathrm{PD}}\sqrt{P_{\mathrm{b}_1}} X_1^{\mathrm{b}}(k) H_1^{\mathrm{b}}(k) + R_{\mathrm{PD}}\sqrt{P_{\mathrm{b}_1}} \left[X_2^{\mathrm{b}}(k) H_{1,2}^{\mathrm{b}}(k) + X_6^{\mathrm{b}}(k) H_{1,6}^{\mathrm{b}}(k) \right] + V_1^{\mathrm{b}}(k), \tag{3.5b}$$

$$= R_{\mathrm{PD}} G_{\mathrm{b}} \sqrt{P_{\mathrm{b}_1}} X_1^{\mathrm{b}}(k) + R_{\mathrm{PD}} (1/2)^{\ell} G_{\mathrm{b}} \sqrt{P_{\mathrm{b}_1}} \left[X_2^{\mathrm{b}}(k) + X_6^{\mathrm{b}}(k) \right] + V_1^{\mathrm{b}}(k). \tag{3.5c}$$

Based on the geometry of the backhaul links as shown in Fig. 3.1, by assuming a Lambertian emission for the auxiliary LEDs and using [54, Eq. (10)], the DC gain of interference channels are obtained as $H_{1,2}^{\mathrm{b}}(k) = H_{1,6}^{\mathrm{b}}(k) = (1/2)^{\ell} G_{\mathrm{b}} \sqrt{P_{\mathrm{b}_1}}$ where $G_{\mathrm{b}} = \frac{(\ell+1) A_{\mathrm{PD}}}{6\pi R^2}$ is the DC gain of the wireless optical channel for a backhaul link and $\ell = -\frac{\ln 2}{\ln(\cos \Phi_{\mathrm{b}})}$ is the Lambertian order and Φ_{b} is the emission semi-angle of the auxiliary LEDs. Thus, (3.5b) turns into (3.5c). The total noise added at the receiver, $V_1^{\mathrm{b}}(k)$, captures the aggregate effect of signal-independent shot noise induced by the ambient light, and thermal noise of the receiver front-end. It is commonly modeled as a zero mean additive white Gaussian noise (AWGN) [63]. The variance of $V_1^{\mathrm{b}}(k)$ is given by $\sigma_{\mathrm{b}}^2 = N_0 \xi_{\mathrm{b}} f_{\mathrm{s}}^{\mathrm{b}}$, where N_0 denotes the noise power spectral density (PSD); $f_{\mathrm{s}}^{\mathrm{b}}$ is the sampling frequency used in the backhaul system; and $\xi_{\mathrm{b}} = \frac{N_{\mathrm{b}}-2}{N_{\mathrm{b}}}$. According to the Nyquist theorem [105], the minimum sampling frequency is related to the backhaul system bandwidth by $f_{\mathrm{s}}^{\mathrm{b}} = 2B_{\mathrm{b}}$. Due to the geometric symmetry of the network, all the backhaul links have the same SINR. Based on (3.5), the SINR of b_j can be derived as:

$$\gamma_{\mathrm{b}_j} = K_1 \left[2\left(\frac{1}{4}\right)^{\ell} K_1 + \frac{1}{\gamma_{\mathrm{b}}} \right]^{-1},\ \forall j \in \mathcal{T}_1 \tag{3.6}$$

where:

$$\gamma_{\mathrm{b}} = \frac{((\ell+1) A_{\mathrm{PD}} R_{\mathrm{PD}})^2 P_{\mathrm{a}}}{72\pi^2 R^4 N_0 B_{\mathrm{b}} \xi_{\mathrm{b}}^2}. \tag{3.7}$$

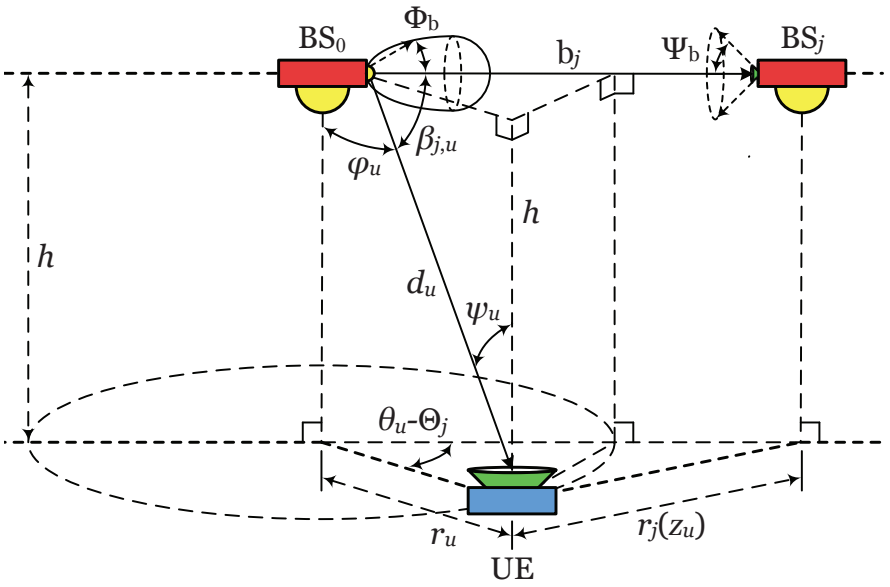

Figure 3.4: *Backhaul interference caused by* b_j, $j \in \mathcal{T}_1$, *on the downlink of the UE associated with BS*$_i$, $i \in \{0\} \cup \mathcal{T}_1$.

For each backhaul system, the analysis of the downlink SINR is separately presented as follows.

3.2.2.2 Full Reuse Visible Light Backhaul

Let $x_i^{\mathrm{a}}(t)$ and $X_i^{\mathrm{a}}(k)$ be the signal transmitted by BS_i in the access system in the time and frequency domains, respectively. After removing the DC component and taking an N_{a}-point FFT, the received signal of the uth UE situated in the attocell of BS_i, $\forall u \in \mathcal{U}_i$ and $\forall i \in \{0\} \cup \mathcal{T}_1$, can be written as:

$$Y_u^{\text{FR-VL}}(k) = R_{\mathrm{PD}} H_{i,u}^{\mathrm{a}} \sqrt{P_{\mathrm{a}}} X_i^{\mathrm{a}}(k) + R_{\mathrm{PD}} \sum_{j \in \mathcal{Q}_i} G_{j,u} \sqrt{P_{\mathrm{b}_j}} X_j^{\mathrm{b}}(k) + R_{\mathrm{PD}} \sum_{j \in \mathcal{J}_i} H_{j,u}^{\mathrm{a}} \sqrt{P_{\mathrm{a}}} X_j^{\mathrm{a}}(k) + V_u^{\mathrm{a}}(k). \tag{3.8}$$

where $\mathcal{J}_i$ is the index set of interfering BSs for BS_i; $\mathcal{Q}_i$ is the index set of interfering backhaul links for BS_i; and $G_{j,u}$ represents the DC gain of the wireless optical channel between b_j and the UE. There are two types of co-channel interference (CCI) on the RHS of (3.8). The second term is the backhaul interference and the third term is the inter-cell interference (ICI). The backhaul interference arises from the links connecting BS_0 to the first tier. Fig. 3.4 illustrates the backhaul interference of b_j affecting the downlink of BS_i, $\forall j \in \mathcal{T}_1$ and $\forall i \in \{0\} \cup \mathcal{T}_1$. Based

on (3.1), one obtains:

$$G_{j,u} = \frac{(\ell+1)A_{\mathrm{PD}}}{2\pi d_u^2}\cos^{\ell}(\beta_{j,u})\cos(\psi_u), \tag{3.9}$$

where $\beta_{j,u}$ is the light radiance angle of the auxiliary LED for b_j relative to the UE receiver. From Fig. 3.4, it can be observed that $\beta_{j,u}$ is related to the complementary angle $\varphi'_u = 90^\circ - \varphi_u$ by a cylindrical rotation of $\theta_u - \Theta_j$, and therefore:

$$\cos(\beta_{j,u}) = \cos(\varphi'_u)\cos(\theta_u - \Theta_j), \tag{3.10a}$$

$$\cos(\varphi'_u) = \frac{r_u}{d_u}. \tag{3.10b}$$

Consequently, $G_{j,u}$ can be expressed as follows:

$$G_{j,u} = \frac{(\ell+1)hA_{\mathrm{PD}}}{2\pi} r_u^{\ell}\cos^{\ell}(\theta_u - \Theta_j)(r_u^2 + h^2)^{-\frac{\ell+3}{2}}. \tag{3.11}$$

In (3.8), the variance of the noise term, $V_u^{\mathrm{a}}(k)$, is $\sigma_{\mathrm{a}}^2 = N_0\xi_{\mathrm{a}}f_{\mathrm{s}}^{\mathrm{a}}$ where $\xi_{\mathrm{a}} = \frac{N_{\mathrm{a}}-2}{N_{\mathrm{a}}}$; and $f_{\mathrm{s}}^{\mathrm{a}} = 2B_{\mathrm{a}}$ is the sampling frequency of the access system. By using (3.8), a unified expression is derived for the received SINR at the UE location:

$$\gamma_u^{\text{FR-VL}} = \frac{\mathcal{S}(z_u)}{\mathcal{F}_{\mathrm{BI}}(z_u) + \mathcal{F}_{\mathrm{ICI}}(z_u) + \Omega}, \tag{3.12}$$

where $\mathcal{S}(z_u)$, $\mathcal{F}_{\mathrm{ICI}}(z_u)$ and $\mathcal{F}_{\mathrm{BI}}(z_u)$ are defined as the desired signal effect, the ICI effect and the backhaul interference effect, respectively. The first two effects are given by:

$$\mathcal{S}(z_u) = \xi_{\mathrm{a}}^{-1}(r_i^2(z_u) + h^2)^{-m-3}, \tag{3.13}$$

$$\mathcal{F}_{\mathrm{ICI}}(z_u) = \sum_{j\in\mathcal{J}_i}(r_j^2(z_u) + h^2)^{-m-3}. \tag{3.14}$$

The parameter Ω in (3.12) is given by:

$$\Omega = \frac{8\pi^2 N_0 B_{\mathrm{a}}\xi_{\mathrm{a}}}{((m+1)h^{m+1}A_{\mathrm{PD}}R_{\mathrm{PD}})^2 P_{\mathrm{a}}}, \tag{3.15}$$

Using (3.11), the backhaul interference effect can be derived as:

$$\mathcal{F}_{\mathrm{BI}}(z_u) = K_1\mathcal{F}_1(z_u;\mathcal{Q}_i), \tag{3.16a}$$

$$\mathcal{F}_1(z_u;\mathcal{Q}_i) = \frac{(\ell+1)^2}{(m+1)^2h^{2m}}\sum_{j\in\mathcal{Q}_i}\frac{r_u^{2\ell}\cos^{2\ell}(\theta_u-\Theta_j)}{(r_u^2+h^2)^{\ell+3}}, \tag{3.16b}$$

where $\mathcal{Q}_i \subset \mathcal{T}_1$.

3.2.2.3 In-Band Visible Light Backhaul

By means of the IB-VL backhaul system, the backhaul interference effect is eliminated. From (3.12), the received SINR of the uth UE is readily given by:

$$\gamma_u^{\text{IB-VL}} = \frac{\xi_{\text{a}}^{-1}(r_i^2(z_u) + h^2)^{-m-3}}{\sum\limits_{j \in \mathcal{J}_i} (r_j^2(z_u) + h^2)^{-m-3} + \Omega}. \tag{3.17}$$

3.2.2.4 Infrared Backhaul

By employing a single IR wavelength that is fully reused across all the backhaul links, the backhaul SINR is identical to that in (3.6). Also, since the backhaul interference effect is perfectly canceled, the downlink SINR denoted by γ_u^{IR} is equal to $\gamma_u^{\text{IB-VL}}$ given by (3.17).

3.2.3 Sum Rate Analysis

3.2.3.1 Access and Backhaul Rates

The access and backhaul systems are assumed to have an equal subchannel bandwidth so that $\frac{2B_{\text{a}}}{N_{\text{a}}} = \frac{2B_{\text{b}}}{N_{\text{b}}}$, implying identical symbol periods for DCO-OFDM frames of the two systems. Suppose there are M UEs in the network in total which are globally numbered from 1 to M. The UEs are uniformly scattered over the exact coverage of the network and they are associated with their nearest BSs according to the maximum received SINR criterion [33, 34]. Let $\mathcal{U}_i$ be the index set of the UEs associated with BS_i such that $|\mathcal{U}_i| = M_i$ and $\sum_{i=0}^{N_{\text{BS}}-1} M_i = M$, where N_{BS} is the total number of BSs. Each UE served by BS_i is equally given a bandwidth of $\frac{2B_{\text{a}}}{M_i}$. Based on (2.7), it follows that:

$$\mathcal{R}_{\text{a}_i} = \frac{\xi_{\text{a}} B_{\text{a}}}{M_i} \sum_{u \in \mathcal{U}_i} \log_2(1 + \gamma_u), \tag{3.18a}$$

$$\mathcal{R}_{\text{b}_i} = \xi_{\text{b}} B_{\text{b}} \log_2(1 + \gamma_{\text{b}_i}). \tag{3.18b}$$

For an ideal case that the backhaul system does not limit the end-to-end performance of the network, the following condition holds:

$$\mathcal{R}_{\mathrm{b}_i} \geq \mathcal{R}_{\mathrm{a}_i},\ \forall i \in \mathcal{T}_1 \tag{3.19}$$

3.2.3.2 FR-VL Backhaul

In this work, *end-to-end sum rate* refers to the sum of the achievable end-to-end rates of UEs. From the definition of FR-VL backhauling, it follows that $B_{\mathrm{a}} = B_{\mathrm{b}} = B$, thus $\xi_{\mathrm{a}} = \xi_{\mathrm{b}} = \xi$. For BS_0, the sum rate of UEs can be calculated as:

$$\mathcal{R}_0^{\text{FR-VL}} = \frac{\xi B}{M_0} \sum_{u \in \mathcal{U}_0} \log_2\left(1 + \gamma_u^{\text{FR-VL}}\right). \tag{3.20}$$

For BS_i in the first tier, by using (3.6) and (3.12), the uth UE $\forall u \in \mathcal{U}_i$ experiences an end-to-end rate of:

$$\mathcal{R}_u = \min\left[\frac{\xi B}{M_i}\log_2(1+\gamma_{\mathrm{b}_i}), \frac{\xi B}{M_i}\log_2\left(1+\gamma_u^{\text{FR-VL}}\right)\right], \tag{3.21a}$$

$$= \frac{\xi B}{M_i}\min\left[\log_2(1+\gamma_{\mathrm{b}_i}), \log_2\left(1+\gamma_u^{\text{FR-VL}}\right)\right], \tag{3.21b}$$

$$= \frac{\xi B}{M_i}\log_2\left(1+\min\left[\gamma_{\mathrm{b}_i}, \gamma_u^{\text{FR-VL}}\right]\right), \tag{3.21c}$$

The derivation of (3.21) is based on [102, Eq. (15)] through setting the direct source-to-destination channel gain to zero. The factor $\frac{1}{2}$ in [102, Eq. (15)] is omitted because the relay BSs operate in full-duplex mode. In (3.21c), $\min\left[\gamma_{\mathrm{b}_i}, \gamma_u^{\text{FR-VL}}\right]$ represents the equivalent SINR of a dual-hop DF relaying transmission for the uth UE associated with BS_i. The end-to-end sum rate is derived as follows:

$$\mathcal{R}_i^{\text{FR-VL}} = \frac{\xi B}{M_i} \sum_{u \in \mathcal{U}_i} \log_2\left(1+\min\left[\gamma_{\mathrm{b}_i}, \gamma_u^{\text{FR-VL}}\right]\right). \tag{3.22}$$

3.2.3.3 IB-VL Backhaul

In this case, B_{a} and B_{b} correspond to two orthogonal sub-bands allocated to the access and backhaul parts. Let δ be the ratio of the bandwidth fraction allocated to the access part relative to the total VLC bandwidth. It follows that $B_{\mathrm{a}} = \delta B$ and $B_{\mathrm{b}} = (1-\delta)B$ for $0 < \delta < 1$.

Considering that BS_0 is directly connected to the gateway, the sum rate of UEs for BS_0 does not contribute into the design of the parameter δ under IB-VL backhauling. That is why BS_0 is allowed to access the full bandwidth for downlink transmission. Also, BS_0 plays a marginal role when considering the average sum rate of the whole network. Nonetheless, for the sake of completeness, an analytical expression is provided by Proposition 1.

Proposition 1. *Under IB-VL backhauling, the sum rate of UEs for BS_0 can be equivalently represented by:*

$$\mathcal{R}_0^{\text{IB-VL}} = \frac{\xi B}{M_0} \sum_{u \in \mathcal{U}_0^{(\delta)}} \log_2\left(1 + \gamma_u^{\text{IB-VL}}\right) + \frac{\xi B}{M_0} \sum_{u \in \mathcal{U}_0^{(1-\delta)}} \log_2\left(1 + \gamma_u^{\text{FR-VL}}\right), \tag{3.23}$$

where $\mathcal{U}_0^{(\delta)}$ and $\mathcal{U}_0^{(1-\delta)}$ are two complementary subsets of $\mathcal{U}_0$ such that $\left|\mathcal{U}_0^{(\delta)}\right| = \delta M_0$ and $\left|\mathcal{U}_0^{(1-\delta)}\right| = (1-\delta)M_0$, assuming δM_0 is an integer.

The derivation of (3.23) is presented in Appendix A. The detailed design of δ is discussed in Proposition 2.

Proposition 2. *For a one-tier network, the bandwidth allocation criterion is derived as:*

$$\delta = \frac{\log_2(1+\gamma_{\mathrm{b}_1})}{\max\limits_i \left[\frac{1}{M_i} \sum\limits_{u \in \mathcal{U}_i} \log_2(1+\gamma_u^{\text{IB-VL}})\right] + \log_2(1+\gamma_{\mathrm{b}_1})}. \tag{3.24}$$

Proof. Substituting (3.18a) and (3.18b) into (3.19) and simplifying yields:

$$(1-\delta)\log_2\left(1+\gamma_{\mathrm{b}_i}\right) \geq \frac{\delta}{M_i} \sum_{u \in \mathcal{U}_i} \log_2\left(1+\gamma_u^{\text{IB-VL}}\right). \tag{3.25}$$

Rearranging (3.25) to solve in terms of δ results in:

$$\delta \leq \frac{\log_2(1+\gamma_{\mathrm{b}_i})}{\frac{1}{M_i} \sum\limits_{u \in \mathcal{U}_i} \log_2(1+\gamma_u^{\text{IB-VL}}) + \log_2(1+\gamma_{\mathrm{b}_i})}, \ \forall i \in \mathcal{T}_1 \tag{3.26}$$

As the condition in (3.26) holds $\forall i \in \mathcal{T}_1$, among the six backhaul branches, the one with the maximum sum rate is considered to specify the value of δ. This leads to the maximum reliable rate for the dual-hop DF transmission. Note that once the value of δ is determined, it is fixed for the entire network. The backhaul SINR is identical for all six backhaul links, and hence γ_{b_i} can be replaced with γ_{b_1}. In the denominator of the fraction on the RHS of (3.26), only

the first term varies depending on BS_i. Therefore, the fraction is minimized by replacing the mentioned term with its maximum value, resulting in the minimum upper bound for δ which satisfies (3.26) $\forall i \in \mathcal{T}_1$. This concludes the proof for (3.24). ■

Based on (3.17) and (3.24), the sum rate of UEs for BS_i, $\forall i \in \mathcal{T}_1$, is obtained as:

$$\mathcal{R}_i^{\text{IB-VL}} = \frac{\xi \delta B}{M_i} \sum_{u \in \mathcal{U}_i} \log_2 \left(1 + \gamma_u^{\text{IB-VL}}\right). \tag{3.27}$$

Note that the methodology used here to acquire the bandwidth allocation ratio δ is consistent with that for multi-hop wireless networks using orthogonal resources for intermediate hops [106]. For example, the result presented in Lemma 1 in [106] can be derived by substituting the RHS of (3.26) into (3.27) which gives the capacity of the dual-hop system as the harmonic mean of the capacities of the two hops.

3.2.3.4 IR Backhaul

In the IR case, the bandwidth of the backhaul system is greater than that of the access system, i.e., $B_{\mathrm{b}} > B_{\mathrm{a}} = B$ and $\xi_{\mathrm{b}} > \xi_{\mathrm{a}} = \xi$. The sum rate of UEs for BS_0 is readily given by (3.20) provided that $\gamma_u^{\text{FR-VL}}$ is replaced by γ_u^{IR}. For BS_i in the first tier, the uth UE $\forall u \in \mathcal{U}_i$ has an end-to-end rate of:

$$\mathcal{R}_u = \min \left[\frac{\xi_{\mathrm{b}} B_{\mathrm{b}}}{M_i} \log_2(1 + \gamma_{\mathrm{b}_i}), \frac{\xi_{\mathrm{a}} B_{\mathrm{a}}}{M_i} \log_2 \left(1 + \gamma_u^{\text{IR}}\right) \right], \tag{3.28a}$$

$$= \frac{\xi B}{M_i} \min \left[\zeta \log_2(1 + \gamma_{\mathrm{b}_i}), \log_2 \left(1 + \gamma_u^{\text{IR}}\right) \right], \tag{3.28b}$$

where ζ is defined as the effective bandwidth ratio:

$$\zeta = \frac{\xi_{\mathrm{b}} B_{\mathrm{b}}}{\xi_{\mathrm{a}} B_{\mathrm{a}}}. \tag{3.29}$$

The sum rate of UEs for BS_i, $\forall i \in \mathcal{T}_1$, is expressed in the form:

$$\mathcal{R}_i^{\text{IR}} = \frac{\xi B}{M_i} \sum_{u \in \mathcal{U}_i} \min \left[\zeta \log_2(1 + \gamma_{\mathrm{b}_i}), \log_2 \left(1 + \gamma_u^{\text{IR}}\right) \right]. \tag{3.30}$$

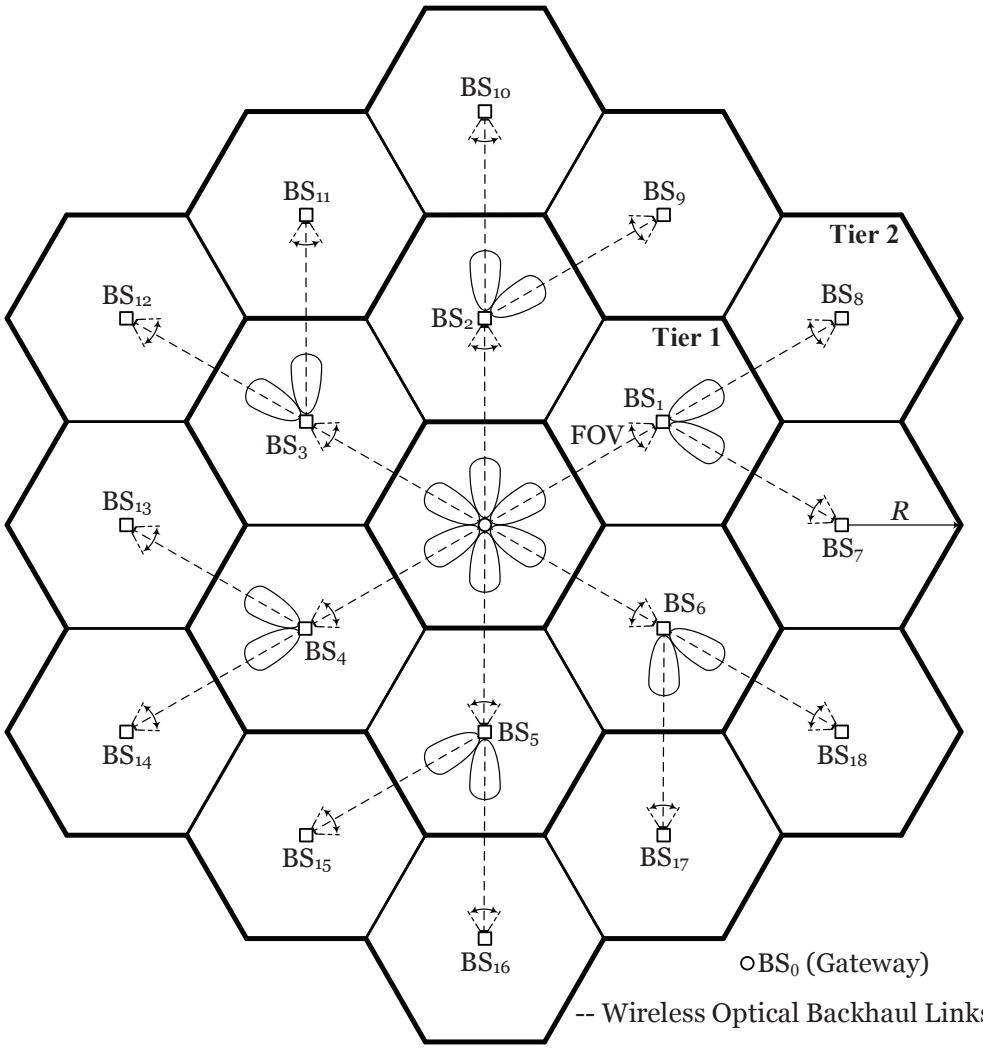

Figure 3.5: *Hexagonal cellular layout for a two-tier optical attocell network, and a plan view of multi-hop wireless optical backhaul links.*

3.3 Extension to Two-Tier Network

The application of wireless optical backhauling is extended for a two-tier hexagonal network. Fig. 3.5 depicts the hexagonal cellular layout of a two tier optical attocell network encompassing 19 attocells. Consequently, a tree topology is used for the backhaul network, as shown in Fig. 3.5. To this end, two extra auxiliary LEDs are added to each BS in the first tier to point at two BSs in the second tier. For BS_i in the second tier, $\forall i \in \mathcal{T}_2 = \{7, 8, \ldots, 18\}$, a triple-hop relaying transmission is performed over two intermediate backhaul hops and another hop for the access link.

Due to the symmetric topology of the network around BS_0, according to Fig. 3.5, any one

of the six backhaul branches in the tree topology is an indicator for the performance of the remaining branches. This observation especially simplifies the presentation of the received signal model for the backhaul system by focusing on BS_1, BS_7 and BS_8. First, the SINR of the backhaul links is established. Moving on, the SINR and sum rate of the downlink under different backhaul systems are individually discussed.

3.3.1 Backhaul Links

The three signals sent for the downlinks of BS_1, BS_7 and BS_8 are fully decoded at BS_1. After taking an N_{b}-point FFT, the signal received by BS_1 through b_1 is calculated as:

$$\begin{aligned} Y_1^{\mathrm{b}}(k) = R_{\mathrm{PD}} G_{\mathrm{b}} \sqrt{P_{\mathrm{b}_1}} X_1^{\mathrm{b}}(k) + R_{\mathrm{PD}} (1/2)^{\ell} G_{\mathrm{b}} \sqrt{P_{\mathrm{b}_1}} \left[X_2^{\mathrm{b}}(k) + X_6^{\mathrm{b}}(k) \right] + \\ R_{\mathrm{PD}} (1/2)^{\ell+1} G_{\mathrm{b}} \sqrt{P_{\mathrm{b}_7}} X_9^{\mathrm{b}}(k) + V_1^{\mathrm{b}}(k). \end{aligned} \tag{3.31}$$

The signals received by BS_7 and BS_8 from b_7 and b_8, respectively, are derived as follows:

$$\begin{aligned} Y_7^{\mathrm{b}}(k) = & R_{\mathrm{PD}} G_{\mathrm{b}} \sqrt{P_{\mathrm{b}_7}} X_7^{\mathrm{b}}(k) + R_{\mathrm{PD}} (1/3) \big(\sqrt{3}/2\big)^{\ell+1} G_{\mathrm{b}} \sqrt{P_{\mathrm{b}_1}} \left[X_1^{\mathrm{b}}(n) + X_6^{\mathrm{b}}(k) \right] + \\ & R_{\mathrm{PD}} (1/2)^{\ell} G_{\mathrm{b}} \sqrt{P_{\mathrm{b}_8}} X_8^{\mathrm{b}}(k) + R_{\mathrm{PD}} (1/2)^{\ell+1} G_{\mathrm{b}} \sqrt{P_{\mathrm{b}_8}} X_{18}^{\mathrm{b}}(k) + V_7^{\mathrm{b}}(k). \end{aligned} \tag{3.32}$$

$$\begin{aligned} & Y_8^{\mathrm{b}}(k) = R_{\mathrm{PD}} G_{\mathrm{b}} \sqrt{P_{\mathrm{b}_8}} X_8^{\mathrm{b}}(k) + R_{\mathrm{PD}} (1/2)^{\ell} G_{\mathrm{b}} \sqrt{P_{\mathrm{b}_7}} X_7^{\mathrm{b}}(k) + \\ & R_{\mathrm{PD}} (1/3) \big(\sqrt{3}/2\big)^{\ell+1} G_{\mathrm{b}} \sqrt{P_{\mathrm{b}_7}} X_9^{\mathrm{b}}(k) + R_{\mathrm{PD}} (5/7) \big(1/2\sqrt{7}\big)^{\ell+1} G_{\mathrm{b}} \sqrt{P_{\mathrm{b}_7}} X_{11}^{\mathrm{b}}(k) + V_8^{\mathrm{b}}(k). \end{aligned} \tag{3.33}$$

In (3.31)–(3.33), $P_{\mathrm{b}_j} = K_j P_{\mathrm{a}}$ is the power allocated to b_j, with K_j as the corresponding power control coefficient. An equal power is assigned to the backhaul links of the first tier. The backhaul links of the second tier are divided into two groups of odd and even-numbered, with a different power allocated to each group. This is primarily because of the asymmetric spatial distribution of the received SINR on the attocells of odd and even-numbered BSs in the second tier. The SINR of b_j can be derived and expressed as:

$$\gamma_{\mathrm{b}_j} = K_1 \left[2 \left(\frac{1}{4} \right)^{\ell} K_1 + \left(\frac{1}{4} \right)^{\ell+1} K_7 + \frac{1}{\gamma_{\mathrm{b}}} \right]^{-1}, \ \forall j \in \mathcal{T}_1 \tag{3.34}$$

$$\gamma_{\mathrm{b}_j} = K_7 \left[\frac{2}{9} \left(\frac{3}{4} \right)^{\ell+1} K_1 + 5 \left(\frac{1}{4} \right)^{\ell+1} K_8 + \frac{1}{\gamma_{\mathrm{b}}} \right]^{-1}, \ \forall j \in \mathcal{T}_2^{\mathrm{odd}} \tag{3.35}$$

$$\gamma_{\mathrm{b}_j} = \frac{K_8}{K_7}\left[\left(\frac{1}{4}\right)^{\ell} + \frac{1}{9}\left(\frac{3}{4}\right)^{\ell+1} + \frac{25}{49}\left(\frac{1}{28}\right)^{\ell+1} + \frac{1}{K_7\gamma_{\mathrm{b}}}\right]^{-1}, \ \forall j \in \mathcal{T}_2^{\mathrm{even}} \tag{3.36}$$

where $\mathcal{T}_2^{\mathrm{odd}} = \{7, 9, \ldots, 17\}$ and $\mathcal{T}_2^{\mathrm{even}} = \{8, 10, \ldots, 18\}$ are the index sets of odd and even-numbered BSs in the second tier, respectively; and γ_{b} is given by (3.7).

3.3.2 FR-VL Downlink SINR

In a two-tier network, the downlink experiences the backhaul interference caused by both the links connecting BS_0 to the first tier and those lying in between the first and the second tiers. For the first tier, the DC gain of the interference channel, $G_{j,u}$, corresponding to b_j, $\forall j \in \mathcal{T}_1$, is given by (3.11). For the second tier, the calculation of $G_{j,u}$ for the downlink interference channel for b_j, $\forall j \in \mathcal{T}_2$, is similar in principle to that of (3.11). By contrast, the only difference comes from the need to shift the origin of the coordinate system to the coordinates of the BS in the first tier to which the transmit end of b_j is connected. Nevertheless, this is omitted here to avoid duplication. Consequently, the downlink SINR is readily available in (3.12) with a total backhaul interference of the form:

$$\mathcal{F}_{\mathrm{BI}}(z_u) = K_1\mathcal{F}_1(z_u; \mathcal{Q}_i) + K_7\mathcal{F}_2(z_u; \mathcal{O}_i) + K_8\mathcal{F}_2(z_u; \mathcal{E}_i), \tag{3.37}$$

where $\mathcal{F}_1(z_u; \mathcal{Q}_i)$ is given by (3.16b); $\mathcal{O}_i \subset \mathcal{T}_2^{\mathrm{odd}}$ and $\mathcal{E}_i \subset \mathcal{T}_2^{\mathrm{even}}$ are the index sets of interfering odd and even-numbered backhaul links of the second tier, respectively; and:

$$\mathcal{F}_2(z_u; \mathcal{A}_i) = \frac{(\ell+1)^2}{(m+1)^2 h^{2m}} \sum_{j \in \mathcal{A}_i} \frac{r_s^{2\ell}(z_u)\cos^{2\ell}\left(\theta_s - \Theta_{\mathrm{b}_j}\right)}{\left(r_s^2(z_i) + h^2\right)^{\ell+3}}, \tag{3.38}$$

for $\mathcal{A}_i = \mathcal{O}_i, \mathcal{E}_i$. In (3.38), (r_s, θ_s) are the relative coordinates of z_u, and Θ_{b_j} is the relative angle of b_j, with respect to the polar axis of BS_s for $s = \lfloor \frac{j-5}{2} \rfloor$.

In [30], the backhaul LED semi-angle Φ_{b} is identified as a key determinant of the performance for a VL backhaul system. A special case of interest for the downlink SINR is to evaluate an asymptotic behavior of the backhaul interference effect when the wireless backhaul links are extremely directive. Such a case is used in the following as a theoretical bound for the system performance. This is established in Theorem 1.

Theorem 1. *For the FR-VL backhaul system, in the limit as Φ_{b} tends to zero, the backhaul interference effect on the downlink approaches zero at any location in the network, for either a*

one-tier or a two-tier network.

Proof. The analysis is performed for the limit $\ell \to \infty$ which is equivalent to $\Phi_{\mathrm{b}} \to 0$. Based on (3.16) and (3.38), a unified expression is obtained for the backhaul interference effect as follows:

$$\mathcal{F}_{\mathrm{BI}}(z_u) = \frac{(\ell+1)^2}{(m+1)^2 h^{2m}} \sum_{j \in \mathcal{Q}_i} \frac{K_j r_s^{2\ell}(z_u) \cos^{2\ell}\big(\theta_s - \Theta_{\mathrm{b}_j}\big)}{\big(r_s^2(z_u) + h^2\big)^{\ell+3}}. \tag{3.39}$$

Rearranging (3.39), and taking the limit $\ell \to \infty$, the asymptotic backhaul interference effect can be evaluated as:

$$\lim_{\ell\to\infty} \mathcal{F}_{\mathrm{BI}}(z_u) = \frac{1}{(m+1)^2 h^{2m} (r_s^2 + h^2)^3} \lim_{\ell\to\infty} \sum_{j \in \mathcal{Q}_i} K_j (\ell+1)^2 \left[\frac{r_s^2 \cos^2\big(\theta_s - \Theta_{\mathrm{b}_j}\big)}{r_s^2 + h^2} \right]^{\ell}. \tag{3.40}$$

In (3.40), the fraction inside the bracket is bounded as follows:

$$0 \leq \frac{r_s^2 \cos^2\big(\theta_s - \Theta_{\mathrm{b}_j}\big)}{r_s^2 + h^2} < 1. \tag{3.41}$$

Using (3.41), the limit of the two product terms that depend on ℓ under the summation in (3.40) can be calculated as:

$$\lim_{\ell\to\infty} (\ell+1)^2 \left[\frac{r_s^2 \cos^2\big(\theta_s - \Theta_{\mathrm{b}_j}\big)}{r_s^2 + h^2} \right]^{\ell} = 0, \tag{3.42}$$

because, as $\ell \to \infty$, the term $[\,]^{\ell}$ decays much faster than the term $(\ell+1)^2$ grows. Considering that K_j is a finite value under the summation in (3.40), substituting (3.42) into (3.40) yields:

$$\lim_{\ell\to\infty} \mathcal{F}_{\mathrm{BI}}(z_u) = 0, \ \forall u, \tag{3.43}$$

hence the proof is complete. ■

3.3.3 End-to-End Sum Rate

3.3.3.1 Rate Inequalities for Unlimited Backhaul

For a two-tier network, to avoid the backhaul capacity from restricting the end-to-end data rate, there are three backhaul-access rate constraints of:

$$\mathcal{R}_{\mathrm{b}_1} \geq \mathcal{R}_{\mathrm{a}_1} + \mathcal{R}_{\mathrm{a}_7} + \mathcal{R}_{\mathrm{a}_8}, \tag{3.44a}$$

$$\mathcal{R}_{\mathrm{b}_7} \geq \mathcal{R}_{\mathrm{a}_7}, \tag{3.44b}$$

$$\mathcal{R}_{\mathrm{b}_8} \geq \mathcal{R}_{\mathrm{a}_8}. \tag{3.44c}$$

Among (3.44a)–(3.44c), (3.44a) is the dominant constraint, meaning that the capacity of b_1 has to be sufficiently high to support the aggregate rate demanded by BS_1, BS_7 and BS_8. Otherwise, the limited capacity of b_1 turns into a *backhaul bottleneck*.

The six backhaul links branched from the gateway carry most of the data traffic in the network, and each one has to accommodate three downstream data flows. In order to fairly apportion the backhaul capacity, an equally weighted fair scheduling method is employed [107], by which every data flow in a shared backhaul link is allocated an equal proportion of the available capacity. The allocated resources are orthogonal so that b_1 is effectively decomposed into three independent parallel channels, each one having an achievable rate of $\mu_j \mathcal{R}_{\mathrm{b}_1}$, where $\mu_j = \frac{1}{3}$ is the weight assigned to the jth data flow. The capacity of b_1 can be decomposed in the frequency domain. According to μ_j, the DCO-OFDM frame is divided into three parts and each one is independently loaded with an information block from the jth data flow. At BS_1, different sub-bands are separated in the frequency domain based on the FFT of the received signal. Once the symbols encapsulated in the three sub-bands are individually decoded, each group is modulated with a distinct orthogonal frequency division multiplexing (OFDM) frame which is retransmitted in the corresponding direction.

3.3.3.2 FR-VL Backhaul

For BS_0, the sum rate of UEs is given by (3.20). For the first and the second tiers, the end-to-end rate of UEs cannot be higher than the allocated capacity of each intermediate hop based on the maximum flow–minimum cut theorem [108]. By using (3.34)–(3.36) and (3.12), for BS_i in

the first tier, the uth UE $\forall u \in \mathcal{U}_i$ achieves an end-to-end rate of:

$$\mathcal{R}_u = \min\left[\frac{\mu_i \xi B}{M_i}\log_2(1+\gamma_{\mathrm{b}_i}), \frac{\xi B}{M_i}\log_2\left(1+\gamma_u^{\text{FR-VL}}\right)\right], \tag{3.45a}$$

$$= \frac{\xi B}{M_i}\min\left[\mu_i \log_2(1+\gamma_{\mathrm{b}_i}), \log_2\left(1+\gamma_u^{\text{FR-VL}}\right)\right]. \tag{3.45b}$$

The sum rate of UEs for BS_i is derived as:

$$\mathcal{R}_i^{\text{FR-VL}} = \frac{\xi B}{M_i}\sum_{u\in\mathcal{U}_i}\min\left[\mu_i \log_2\left(1+\gamma_{\mathrm{b}_i}\right), \log_2\left(1+\gamma_u^{\text{FR-VL}}\right)\right],\ \forall i \in \mathcal{T}_1 \tag{3.46}$$

For BS_i in the second tier, the uth UE $\forall u \in \mathcal{U}_i$ acquires an end-to-end rate of:

$$\mathcal{R}_u = \min\left[\frac{\mu_i \xi B}{M_i}\log_2(1+\gamma_{\mathrm{b}_s}), \frac{\xi B}{M_i}\log_2(1+\gamma_{\mathrm{b}_i}), \frac{\xi B}{M_i}\log_2\left(1+\gamma_u^{\text{FR-VL}}\right)\right], \tag{3.47a}$$

$$= \frac{\xi B}{M_i}\min\left[\mu_i \log_2(1+\gamma_{\mathrm{b}_s}), \log_2(1+\gamma_{\mathrm{b}_i}), \log_2\left(1+\gamma_u^{\text{FR-VL}}\right)\right], \tag{3.47b}$$

where $s = \left\lfloor \frac{i-5}{2} \right\rfloor$ returns the index of the corresponding bottleneck link. The end-to-end sum rate is:

$$\mathcal{R}_i^{\text{FR-VL}} = \frac{\xi B}{M_i}\sum_{u\in\mathcal{U}_i}\min\left[\mu_i \log_2\left(1+\gamma_{\mathrm{b}_s}\right), \log_2\left(1+\gamma_{\mathrm{b}_i}\right), \log_2\left(1+\gamma_u^{\text{FR-VL}}\right)\right],\ \forall i \in \mathcal{T}_2 \tag{3.48}$$

3.3.3.3 IB-VL Backhaul

The criterion for designing the bandwidth allocation ratio δ for a two-tier network is expounded in Proposition 3.

Proposition 3. *For a two-tier network, the value of the bandwidth allocation ratio δ is fixed to be:*

$$\delta = \frac{\log_2(1+\gamma_{\mathrm{b}_1})}{\max\limits_i\left[\sum\limits_{j\in\mathcal{L}_i}\frac{1}{M_j}\sum\limits_{u\in\mathcal{U}_j}\log_2(1+\gamma_u^{\text{IB-VL}})\right] + \log_2(1+\gamma_{\mathrm{b}_1})}. \tag{3.49}$$

Proof. According to the three rate constraints in (3.44), (3.44a) corresponds to the bottleneck backhaul link and is the most challenging one. Therefore, a bandwidth allocation ratio δ that satisfies (3.44a) makes the other two constraints automatically fulfilled. For this reason, the

focus is on (3.44a) to derive the expression of δ. The general form for (3.44a) is given by:

$$\mathcal{R}_{\mathrm{b}_i} \geq \sum_{j \in \mathcal{L}_i} \mathcal{R}_{\mathrm{a}_j}, \tag{3.50}$$

where $\mathcal{L}_i = \{i, 2i+5, 2i+6\}\ \forall i \in \mathcal{T}_1$, containing the indexes of all three BSs for the backhaul branch corresponding to $\mathrm{BS}_i\ \forall i \in \mathcal{T}_1$. Inserting (3.18a) and (3.18b) in (3.50) and simplifying gives:

$$(1-\delta)\log_2\left(1+\gamma_{\mathrm{b}_i}\right) \geq \delta \sum_{j \in \mathcal{L}_i} \frac{1}{M_i} \sum_{u \in \mathcal{U}_i} \log_2\left(1+\gamma_u^{\text{IB-VL}}\right). \tag{3.51}$$

Solving the above inequality for δ yields an upper bounded for the bandwidth allocation ratio δ as follows:

$$\delta \leq \frac{\log_2(1+\gamma_{\mathrm{b}_i})}{\sum\limits_{j \in \mathcal{L}_i} \frac{1}{M_j} \sum\limits_{u \in \mathcal{U}_j} \log_2(1+\gamma_u^{\text{IB-VL}}) + \log_2(1+\gamma_{\mathrm{b}_i})},\ \forall i \in \mathcal{T}_1 \tag{3.52}$$

The minimum value for δ is obtained by taking the maximum sum rate over the six possible triples on the RHS of (3.52), corresponding to the six backhaul branches. One can deduce the minimum upper bound for δ as presented in (3.49), and this completes the proof. ■

Based on (3.49), the sum rate of UEs for BS_i, $\forall i \in \mathcal{T}_1 \cup \mathcal{T}_2$, is readily given by (3.27).

Note that the number of orthogonal resources in this work (i.e., sub-bands) is always two, unlike the case in [106] where the number of orthogonal resources is equal to the number of hops in the network (i.e., half-duplex). In particular, there are only two orthogonal sub-bands for a two-tier network in which three hops are involved for downlink transmission in the second tier.

3.3.3.4 IR Backhaul

Under the assumption of a single IR wavelength being fully reused over all the backhaul links, the sum rate analysis is similar to the FR-VL case except for involving the effective bandwidth ratio in the IR case. The end-to-end sum rate for BS_i is derived as:

$$\mathcal{R}_i^{\mathrm{IR}} = \frac{\xi B}{M_i} \sum_{u \in \mathcal{U}_i} \min\left[\mu_i \zeta \log_2\left(1+\gamma_{\mathrm{b}_i}\right), \log_2\left(1+\gamma_u^{\mathrm{IR}}\right)\right],\ \forall i \in \mathcal{T}_1 \tag{3.53}$$

$$\mathcal{R}_i^{\mathrm{IR}} = \frac{\xi B}{M_i} \sum_{u \in \mathcal{U}_i} \min\left[\mu_i \zeta \log_2\left(1+\gamma_{\mathrm{b}_s}\right), \zeta \log_2\left(1+\gamma_{\mathrm{b}_i}\right), \log_2\left(1+\gamma_u^{\mathrm{IR}}\right)\right],\ \forall i \in \mathcal{T}_2 \tag{3.54}$$

where ζ is given by (3.29); and $s = \left\lfloor \frac{i-5}{2} \right\rfloor$.

3.4 Power Control for Wireless Backhaul System

A power optimization framework is presented for wireless optical backhaul systems discussed in Sections 3.2 and 3.3. This is particularly motivated by the fact that backhaul LEDs do not need to provide illumination for the environment, and their optical power can therefore be minimized to enhance the power efficiency (PE). However, reducing the power in the backhaul links adversely affects their capacity, and thus the network performance may be compromised. Finding the minimum power for the backhaul system while maintaining the network performance at a desired level is formulated as an optimization problem. Note that P_{a} is already fixed. As a result, the minimization of P_{b_j} is equivalent to the minimization of $K_j = \frac{P_{\mathrm{b}_j}}{P_{\mathrm{a}}}$. Due to eye safety considerations, the allowed peak power for all wireless optical backhaul systems is limited to be no more than the power of the access system, as the backhaul LEDs may have narrow emission semi-angles. This means $P_{\mathrm{b}_j} \leq P_{\mathrm{a}}$, and hence $0 < K_j \leq 1 \; \forall j$. Note that $K_j = 1$ represents the case where no power control is applied to b_j.

In order to adjust the backhaul power, the network controller requires the instantaneous channel state information for each UE individually. However, for large networks with a large number of UEs, fulfilling such a requirement is cumbersome and practically infeasible. Hence, a scenario in which every BS experiences the highest sum rate from the associated UEs is considered, implying the highest load on the backhaul system. In a given attocell, the maximum achievable rate coincides with the unique point where the peak SINR occurs. Obviously, the sum rate of multiple UEs all of which are colocated at such a point is equal to the achievable rate of a single UE located at the same point, assuming a uniform bandwidth allocation to UEs. Therefore, it is sufficient to focus on the point that corresponds to the peak SINR for the purpose of optimization, and the UE index u is dropped. Although the described scenario might be the worst case, the advantages include: 1) no need for the knowledge of the instantaneous downlink channel; 2) the power optimization is done only once for a given network configuration.

In the following, the backhaul power optimization is presented first for a one-tier network and then for a two-tier network. To elaborate, let z_i represent an arbitrary point within the attocell of BS_i with γ_i denoting the downlink SINR at z_i and let $z_{i,\max} = (r_{i,\max}, \theta_{i,\max})$ be the point of the maximum downlink SINR.

3.4.1 One-Tier Network

3.4.1.1 FR-VL Backhaul

For a one tier FR-VL network, it is sufficient to present the problem formulation for the first branch involving BS_1 and its backhaul link b_1, because of the symmetric arrangement of BSs around BS_0 as shown in Fig. 3.1. The optimization problem is stated as follows:

$$\begin{aligned} \mathrm{P1}: \underset{K_1}{\text{minimize}} \quad & K_1 && \text{(3.55a)} \\ \text{subject to} \quad & \log\left(1+\gamma_{\mathrm{b}_1}\right) - \log\left(1+\gamma_1^{\text{FR-VL}}\right) \geq 0, && \text{(3.55b)} \\ & 0 < K_1 \leq 1. && \text{(3.55c)} \end{aligned}$$

The first constraint is due to (3.19). The second constraint is to limit the backhaul power to be always less than or equal to the access power. The first constraint can be equivalently written as $\gamma_{\mathrm{b}_1} \geq \gamma_1^{\text{FR-VL}}$. Using (3.12)–(3.16) for $i = 1$ in place of $\gamma_1^{\text{FR-VL}}$, and solving the inequality for K_1, one obtains:

$$K_1 \geq K_{1,\min}, \tag{3.56}$$

where $K_{1,\min}$ is derived in closed form:

$$\begin{aligned} K_{1,\min} = & \frac{\mathcal{S}(z_1)}{2\mathcal{F}_1(z_1;\mathcal{Q}_1)} \times \\ & \left[-\frac{\mathcal{F}_{\mathrm{ICI}}(z_1)+\Omega}{\mathcal{S}(z_1)} + 2\left(\frac{1}{4}\right)^{\ell} + \sqrt{\left(\frac{\mathcal{F}_{\mathrm{ICI}}(z_1)+\Omega}{\mathcal{S}(z_1)} - 2\left(\frac{1}{4}\right)^{\ell}\right)^2 + \frac{4\mathcal{F}_1(z_1;\mathcal{Q}_1)}{\mathcal{S}(z_1)\gamma_{\mathrm{b}}}} \right]. \end{aligned} \tag{3.57}$$

Note that $K_{1,\min}$ is expressed at $z_1 = (r_1, \theta_1)$ which can be anywhere within the attocell of BS_1. At the same time, finding exact coordinates of $z_{1,\max}$ depends on the value of K_1. One can jointly find the values of $K_{1,\min}$ and $z_{1,\max}$ by using (3.57) and maximizing $\gamma_1^{\text{FR-VL}}$ given by (3.12), in a recursive manner. For infinite size attocell networks, the received SINR peaks exactly at the center of each attocell [16]. It might slightly deviate from the center due to the finite network deployment and the backhaul interference effect. The approximation $z_{1,\max} \approx (0,0)$ is used for simplicity. The solution to P1 can be written in the form:

$$K_1^* = \min[K_{1,\min}, 1]. \tag{3.58}$$

Numerical results are mainly presented in terms of the backhaul LED semi-angle given a fixed

Parameter	Symbol	Value
Downlink LED Optical Power	P_{opt}	10 W
Downlink LED Semi-Angle	Φ_{a}	40°
Vertical Separation	h	2.25 m
Hexagonal Cell Radius	R	2.5 m
Total VLC Bandwidth	B	20 MHz
IFFT/FFT Length	N	1024
Noise Power Spectral Density	N_0	5×10^{-22} A^2/Hz
Receiver Field of View	Ψ_{a}, Ψ_{b}	85°
PD Effective Area	A_{PD}	10^{-4} m^2
PD Responsivity	R_{PD}	0.6 A/W
DC Bias Scaling Factor	α	3

Table 3.1: *Simulation Parameters*

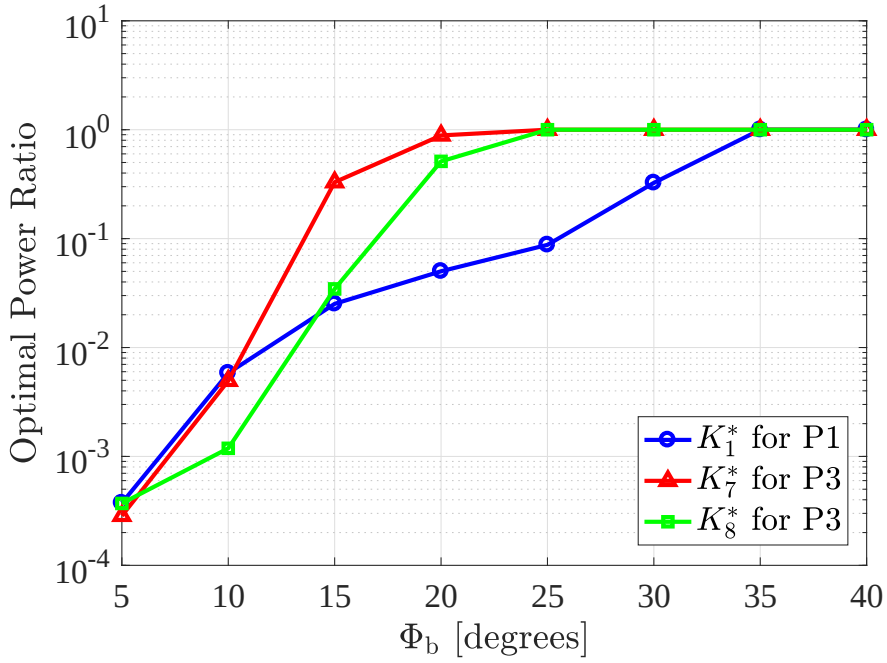

Figure 3.6: *Optimal power ratios K_1^* for the one-tier FR-VL network, and K_7^* and K_8^* for the two-tier FR-VL network with respect to Φ_{b}.* P1 *refers to the optimization problem in* (3.55) *corresponding to the one-tier network as shown in Fig. 3.1.* P3 *indicates the optimization problem in* (3.72) *associated with the two tier network in Fig. 3.5.*

configuration for the downlink system. In optical attocell networks, the downlink parameters such as the LED semi-angle, cell coverage radius and vertical separation are essentially configured to meet the requirements for illumination and SINR quality [16]. Table 3.1 lists the system parameters used for simulations.

Fig. 3.6 shows the optimal solution K_1^* to P1 against Φ_{b}. It can be observed that by increasing

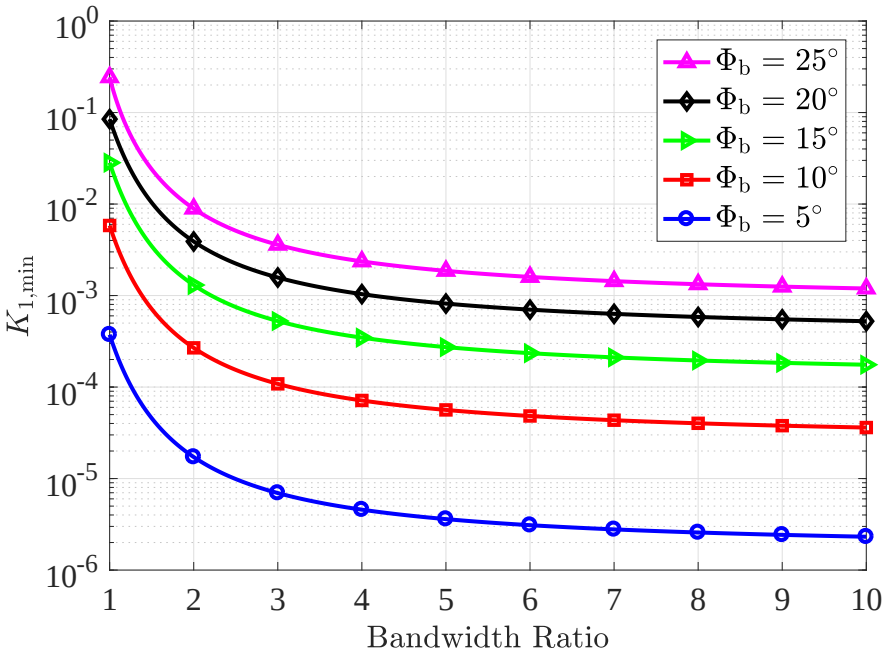

Figure 3.7: *The minimum power ratio $K_{1,\min}$ against the bandwidth ratio $\frac{B_b}{B_a}$ for the one-tier network with IR backhaul.*

Φ_b, the value of K_1^* is saturated at unity for $\Phi_b \geq 35°$. The value of K_1^* stays below 0.1 for $\Phi_b \leq 25°$. In this case, the power allocated to the backhaul links can be less than one tenth of the downlink power which is a remarkable gain for PE of the FR-VL backhaul system.

3.4.1.2 IR Backhaul and Power-Bandwidth Tradeoff

The bandwidth of the IR system is taken as a variable. More specifically, the desired variable is defined as the ratio of the bandwidth of the backhaul system to that of the downlink system, i.e., $\frac{B_b}{B_a}$. The optimization problem statement is similar to the FR-VL case and is omitted to avoid duplication. The minimum power ratio $K_{1,\min}$ satisfies the constraint in (3.19), and it can be derived by substituting $\mathcal{R}_{b_1} = \xi B_b \log_2(1+\gamma_{b_1})$ and $\mathcal{R}_{a_1} = \xi B_a \log_2\left(1+\gamma_1^{IR}\right)$ into (3.19), which gives:

$$K_{1,\min} = \frac{\left[\left(\left(1+\gamma_1^{IR}\right)^{\frac{B_a}{B_b}} - 1\right)^{-1} - 2\left(\frac{1}{4}\right)^{\ell}\right]^{-1}}{\gamma_b}. \tag{3.59}$$

Fig. 3.7 presents $K_{1,\min}$ as a function of $\frac{B_b}{B_a}$ for different values of Φ_b. A tradeoff is observed between the minimum power ratio and the required bandwidth ratio. The tradeoff is improved

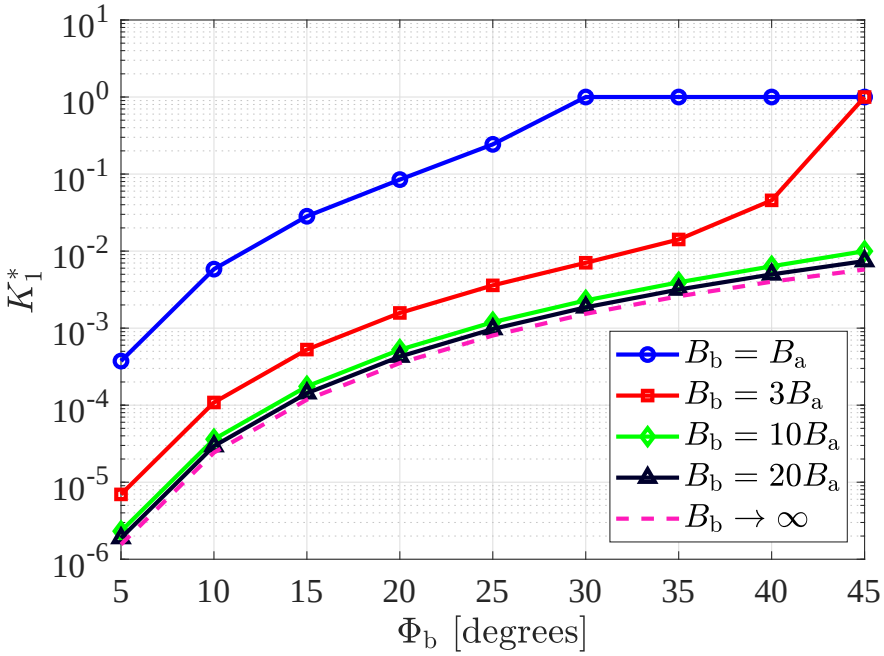

Figure 3.8: *Optimal power ratio K_1^* for the one-tier network with IR backhaul versus Φ_{b} for different values of B_{b}. The asymptotic value of $K_{1,\min}$ when $B_{\mathrm{b}} \to \infty$ is obtained by using* (3.60).

by focusing the light beam in the backhaul links. For $\frac{B_{\mathrm{b}}}{B_{\mathrm{a}}} = 1$, $K_{1,\min} < 1$ for all considered values of Φ_{b}. Fig. 3.8 shows the optimal power ratio, defined as $K_1^* = [K_{1,\min}, 1]$, with respect to Φ_{b} for different values of B_{b}. It can be seen that the optimal power ratio is an increasing function of Φ_{b}. Also, it can be observed that increasing B_{b} provides a higher improvement for the optimal power ratio in lower bandwidths. For example, consider increasing B_{b} from B_{a} to $3B_{\mathrm{a}}$ and that from $10B_{\mathrm{a}}$ to $20B_{\mathrm{a}}$. The justification is that by increasing B_{b}, the reduction rate of $K_{1,\min}$ diminishes for higher values of the bandwidth according to Fig. 3.7. In fact, when the backhaul bandwidth is large enough, $K_{1,\min}$ is saturated. This phenomenon originates from the Shannon's wideband capacity limit [109], whereby the backhaul capacity approaches an asymptotic value as the backhaul bandwidth increases unboundedly. Equivalently, $K_{1,\min}$ converges to a constant level when B_{b} tends to infinity. Based on (3.59) and (3.7), the solution to the following limit can readily be derived with the aid of L'Hôpital's rule, which yields:

$$\lim_{B_{\mathrm{b}} \to \infty} K_{1,\min} = \hat{\gamma}_{\mathrm{b}}^{-1} B_{\mathrm{a}} \log\left(1 + \gamma_1^{\mathrm{IR}}\right), \tag{3.60}$$

where:

$$\hat{\gamma}_{\mathrm{b}} = \frac{((\ell+1) A_{\mathrm{PD}} R_{\mathrm{PD}})^2 P_{\mathrm{a}}}{72\pi^2 R^4 N_0 \xi_{\mathrm{b}}^2}. \tag{3.61}$$

The wideband value of $K_{1,\min}$ is computed by using (3.60) and is included as a benchmark in Fig. 3.8. The asymptotic expression in (3.60) is the lower bound of $K_{1,\min}$, which identifies the minimum amount of operating power for a one-tier backhaul network.

3.4.2 Two-Tier Network

3.4.2.1 FR-VL Backhaul

For a two-tier FR-VL network, without loss of generality, the problem is formulated only for the first branch by focusing on BS_1, BS_7 and BS_8 and their respective backhaul links b_1, b_7 and b_8. This is derived from the symmetric configuration of the six backhaul branches around the gateway as shown in Fig. 3.5. The optimization problem is stated as follows:

$$\mathrm{P2}: \underset{\{K_1,K_7,K_8\}}{\text{minimize}} \quad K_{\text{sum}} = \sum_{j=1,7,8} K_j \tag{3.62a}$$

$$\text{subject to} \quad g_1(K_1, K_7, K_8) \geq 0, \tag{3.62b}$$

$$\log\left(1+\gamma_{\mathrm{b}_7}\right) - \log\left(1+\gamma_7^{\text{FR-VL}}\right) \geq 0, \tag{3.62c}$$

$$\log\left(1+\gamma_{\mathrm{b}_8}\right) - \log\left(1+\gamma_8^{\text{FR-VL}}\right) \geq 0, \tag{3.62d}$$

$$0 < K_j \leq 1. \tag{3.62e}$$

The objective is to minimize the total power allocated to each backhaul branch including three backhaul links. The first three constraints are adopted from (3.44). The function g_1 in the first constraint is given by:

$$g_1(K_1, K_7, K_8) = \log\left(1+\gamma_{\mathrm{b}_1}\right) - \sum_{i=1,7,8} \log\left(1+\gamma_i^{\text{FR-VL}}\right). \tag{3.63}$$

An instant illustration of the admissible region defined by the first three constraints in (3.62) helps to gain insight on the solution space for P2. To this end, note that the function g_1 in (3.63) is monotonically increasing in the direction of K_1. It is shown in Appendix B that the partial derivative of g_1 with respect to K_1 is strictly positive. Therefore, one can rearrange the first constraint in (3.62) and write it as:

$$K_1 \geq K_{1,\min}(K_7, K_8). \tag{3.64}$$

In a similar way, the following alternative forms are obtained for the second and the third constraints in (3.62), respectively:

$$K_7 \geq K_{7,\min}(K_1, K_8), \tag{3.65}$$

$$K_8 \geq K_{8,\min}(K_1, K_7), \tag{3.66}$$

where $K_{7,\min}(K_1, K_8)$ and $K_{8,\min}(K_1, K_7)$ are derived in closed form:

$$\begin{aligned} K_{7,\min}(K_1, K_8) =& \frac{\mathcal{S}(z_7)}{2\mathcal{F}_2(z_7;\mathcal{O}_7)} \times \\ & \Bigg[- \frac{K_1\mathcal{F}_1(z_7;\mathcal{Q}_7) + K_8\mathcal{F}_2(z_7;\mathcal{E}_7) + \mathcal{F}_{\mathrm{ICI}}(z_7) + \Omega}{\mathcal{S}(z_7)} + \\ & \Bigg(\left(\frac{K_1\mathcal{F}_1(z_7;\mathcal{Q}_7) + K_8\mathcal{F}_2(z_7;\mathcal{E}_7) + \mathcal{F}_{\mathrm{ICI}}(z_7) + \Omega}{\mathcal{S}(z_7)} \right)^2 + \\ & \frac{4\mathcal{F}_2(z_7;\mathcal{O}_7)}{\mathcal{S}(z_7)} \left(\frac{2}{9} \left(\frac{3}{4} \right)^{\ell+1} K_1 + 5 \left(\frac{1}{4} \right)^{\ell+1} K_8 + \frac{1}{\gamma_{\mathrm{b}}} \right) \Bigg)^{\frac{1}{2}} \Bigg]. \end{aligned} \tag{3.67}$$

$$\begin{aligned} K_{8,\min}(K_1, K_7) =& \frac{\mathcal{S}(z_8)}{2\mathcal{F}_2(z_8;\mathcal{E}_8)} \times \\ & \Bigg[- \frac{K_1\mathcal{F}_1(z_8;\mathcal{Q}_8) + K_7\mathcal{F}_2(z_8;\mathcal{O}_8) + \mathcal{F}_{\mathrm{ICI}}(z_8) + \Omega}{\mathcal{S}(z_8)} + \\ & \Bigg(\left(\frac{K_1\mathcal{F}_1(z_8;\mathcal{Q}_8) + K_7\mathcal{F}_2(z_8;\mathcal{O}_8) + \mathcal{F}_{\mathrm{ICI}}(z_8) + \Omega}{\mathcal{S}(z_8)} \right)^2 + \\ & \frac{4\mathcal{F}_2(z_8;\mathcal{E}_8)}{\mathcal{S}(z_8)} \left(\left[\left(\frac{1}{4} \right)^{\ell} + \frac{1}{9} \left(\frac{3}{4} \right)^{\ell+1} + \frac{25}{49} \left(\frac{1}{28} \right)^{\ell+1} \right] K_7 + \frac{1}{\gamma_{\mathrm{b}}} \right) \Bigg)^{\frac{1}{2}} \Bigg]. \end{aligned} \tag{3.68}$$

However, $K_{1,\min}$ in (3.64) cannot be explicitly expressed in terms of K_7 and K_8, as the equation $g_1(K_1, K_7, K_8) = 0$ is non-resolvable for K_1. The Newton-Raphson method is used to evaluate $K_{1,\min}(K_7, K_8)$ given the values of K_7 and K_8, according to the following iterative rule:

$$K_{1,\min}^{(n)} = K_{1,\min}^{(n-1)} - \left. \frac{g_1(K_1, K_7, K_8)}{\frac{\partial g_1}{\partial K_1}} \right|_{K_1 = K_{1,\min}^{(n-1)}}, \tag{3.71}$$

where the superscript n indicates the iteration number. Fig. 3.9 illustrates the boundary surfaces for (3.64), (3.65) and (3.66), for $\Phi_{\mathrm{b}} = 20°$. It is observed that the boundary surface of $K_{1,\min}(K_7, K_8)$ stands above the allowed level of $K_1 = 1$. Moreover, when considering the three boundaries, their admissible region has no intersection with the unit cube defined by the

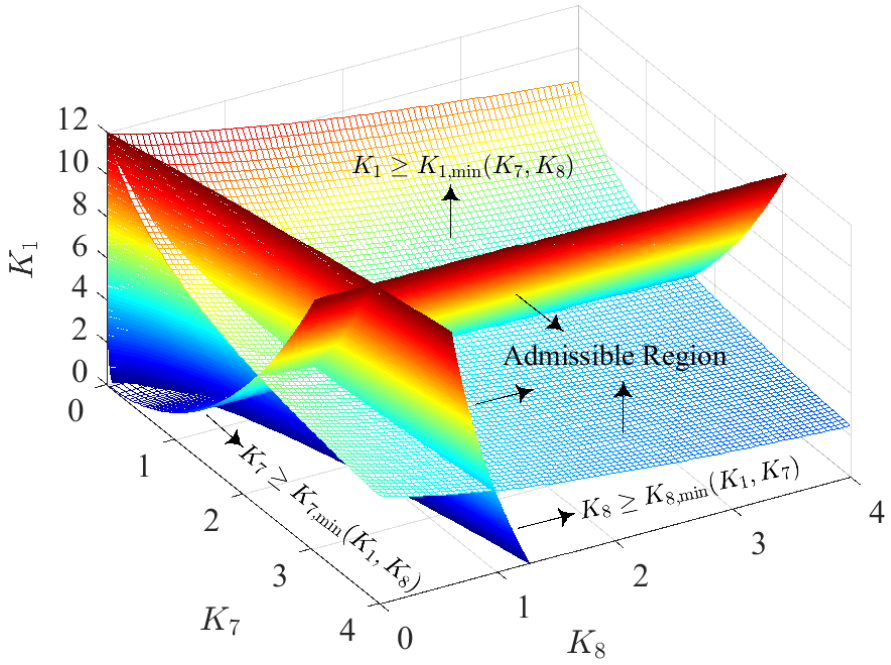

Figure 3.9: *An instant illustration of the admissible region for* P2 *based on the first three constraints for* $\Phi_{\mathrm{b}} = 20°$.

last constraint in (3.62). This reveals a fundamental design challenge for the FR-VL backhaul system since the power in the backhaul links is not practically allowed to exceed the downlink power, and thus the finite capacity of b_i, $i \in \mathcal{T}_1$, determines the upper limit of the downlink data rate in the first and the second tiers.

To evaluate the sensitivity of the admissible region to the backhaul semi-angle Φ_{b}, two more illustrations are provided for $\Phi_{\mathrm{b}} = 15° < 20°$ and $\Phi_{\mathrm{b}} = 25° > 20°$ in Figs. 3.10 and 3.11, respectively. By reducing the semi-angle value to $\Phi_{\mathrm{b}} = 15°$ in Fig. 3.10, relative to Fig. 3.9, the boundary surface of $K_{1,\min}(K_7, K_8)$ moves further away from the allowed level of $K_1 = 1$ and the feasible set is thus empty. In the case where the semi-angle value increases to $\Phi_{\mathrm{b}} = 25$ as shown in Figs. 3.11, all three boundary surfaces evolve in a way that the conditions (3.64) and (3.65) no longer overlap within the shown range of values of K_1, K_7 and K_8. It is also observed from Fig. 3.10 that choosing a smaller value of the semi-angle Φ_{b} causes the two boundary surfaces $K_{7,\min}(K_1, K_8)$ and $K_{8,\min}(K_1, K_7)$ to move toward K_1-K_7 and K_1-K_8 planes, which renders their respective constraints feasible. Hence, the first constraint defined by $K_{1,\min}(K_7, K_8)$ when combined with the last constraint in (3.62) cannot be satisfied. In fact, the feasible set of P2 is empty for most practical cases.

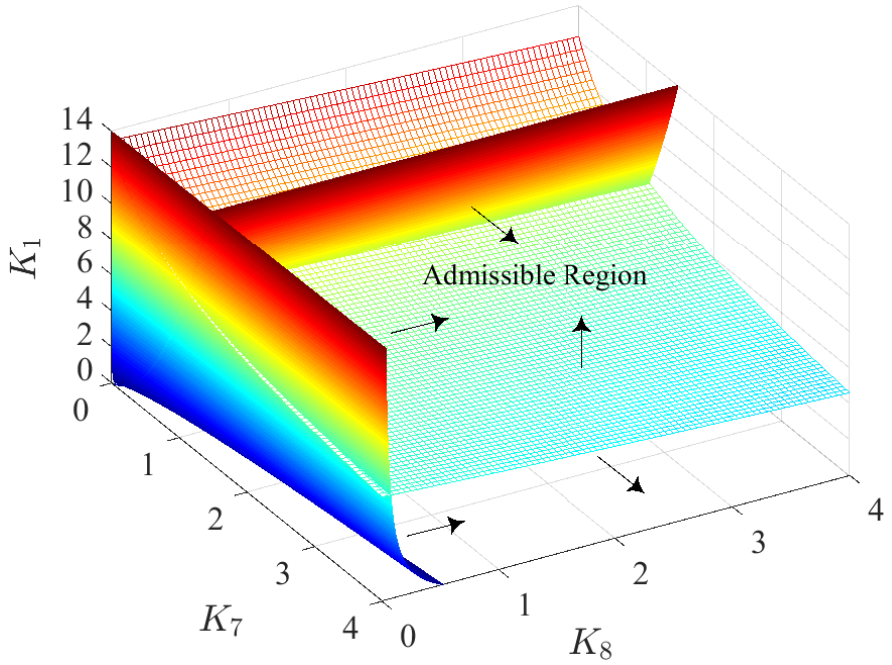

Figure 3.10: *An instant illustration of the admissible region for* P2 *based on the first three constraints for* $\Phi_{\mathrm{b}} = 15°$.

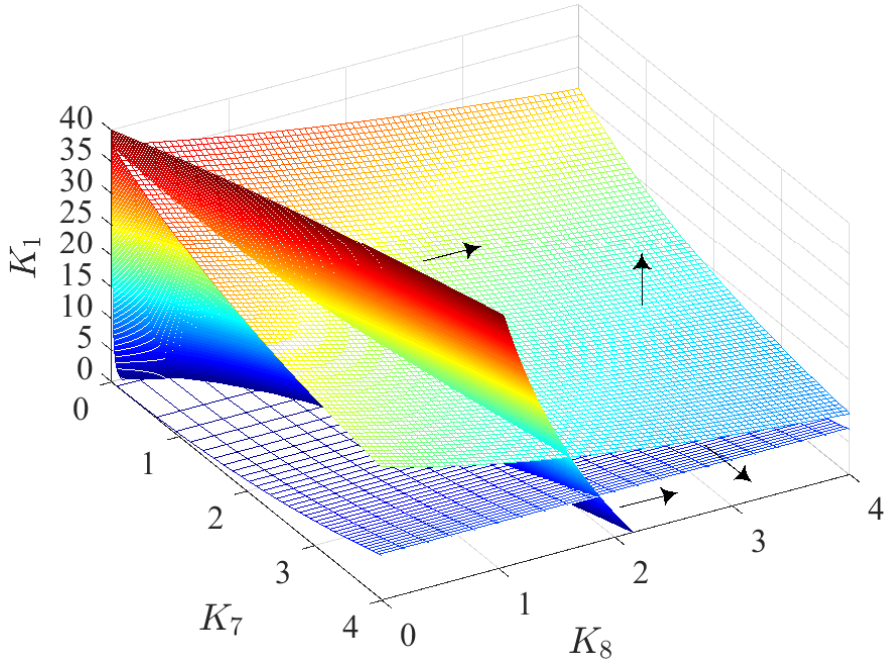

Figure 3.11: *An instant illustration of the admissible region for* P2 *based on the first three constraints for* $\Phi_{\mathrm{b}} = 25°$.

To verify this observation, the feasibility of the constraint in (3.64) is examined analytically. However, the function $K_{1,\min}(K_7, K_8)$ is not available in closed form. Instead, an asymptotic

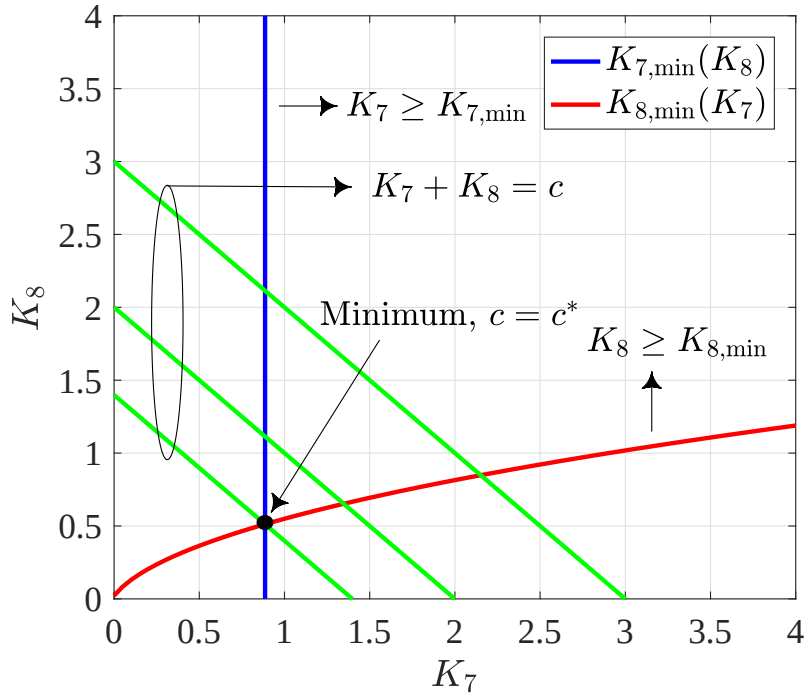

Figure 3.12: *An instant illustration of the admissible region for* P3 *for* $\Phi_{\mathrm{b}} = 20°$. *The objective function is shown as the family of lines* $K_7 + K_8 = c$ *for three values of* c. *The minimum of the objective function is indicated by* $c = c^*$.

bound is derived for small values of Φ_{b} in Appendix C. This bound represents the best scenario under which the backhaul links attain a high capacity by means of focusing the light emission pattern. In practice, this can be realized by using appropriate optical lenses to collimate the LED light in the backhaul links. Based on (C.1), and using the system parameters in Table 3.1, it can be verified that $K_{1,\min} \gg 1$. For example, $K_{1,\min} \approx 189$ for $\Phi_{\mathrm{b}} = 5°$. To move on further, the first constraint is relaxed by fixing K_1 at $K_1 = 1$, which is the maximum possible value for K_1. One can continue to minimize K_7 and K_8 with the new problem stated as follows:

$$\begin{aligned}
\mathrm{P3}: \ \underset{\{K_7,K_8\}}{\text{minimize}} \quad & \sum_{j=7,8} K_j && \text{(3.72a)}\\
\text{subject to} \quad & K_7 \geq K_{7,\min}(K_8), && \text{(3.72b)}\\
& K_8 \geq K_{8,\min}(K_7), && \text{(3.72c)}\\
& 0 < K_j \leq 1. && \text{(3.72d)}
\end{aligned}$$

Fig. 3.12 illustrates the admissible region for P3 for $\Phi_{\rm b} = 20^\circ$ on the K_7-K_8 plane, based on the boundaries given by (3.67) and (3.68) for $K_1 = 1$. It can be verified that the boundary curves $K_{7,\min}(K_8)$ and $K_{8,\min}(K_7)$ are monotonically increasing for $K_7 > 0$ and $K_8 > 0$. They coincide at the unique intersection point represented by $\left(K_{7,\min}^{\dagger}, K_{8,\min}^{\dagger}\right)$ in the positive quadrant $\mathbb{R}_+^2$, which, in fact, is the minimum element of the feasible set. This is proved by using the aforementioned property of the boundary curves; see Appendix D. The projections of the objective function onto the K_7-K_8 plane are the family of lines $K_7 + K_8 = c$ for $c \geq 0$, as shown for different values of c in Fig. 3.12. By decreasing c, the minimum value of the objective function occurs for $c = c^*$ at the intersection point. The solution to P3 can be written as:

$$(K_7^*, K_8^*) = \left(\min\left[K_{7,\min}^{\dagger}, 1\right], \min\left[K_{8,\min}^{\dagger}, 1\right]\right). \tag{3.73}$$

Referring to Fig. 3.6, the optimal solutions (K_7^*, K_8^*) to P3 against $\Phi_{\rm b}$ are shown. It can be observed that by increasing $\Phi_{\rm b}$, the value of K_1^* is saturated at unity for $\Phi_{\rm b} \geq 35^\circ$. It is observed that for $\Phi_{\rm b} \leq 20^\circ$, both K_7^* and K_8^* are less than one. The power minimization for the FR-VL backhaul system in the two-tier case encountered a fundamental limitation due to the inadequate capacity of the bottleneck backhaul link even when using a directive light beam. This challenge is addressed by using the IR band for backhauling.

3.4.2.2 IR Backhaul and Power-Bandwidth Tradeoff

Different from the FR-VL case, the underlying optimization problem for a two-tier network can be solved in the IR case. The reason for this is the downlink SINR $\gamma_1^{\rm IR}$ does not depend on the power ratios unlike in the FR-VL case. Therefore, $\gamma_1^{\rm IR}$ is decoupled from $\gamma_{\rm b_1}$, and this causes the boundary surface defined by (3.44a), i.e., $K_{1,\min}(K_7, K_8)$, to be a flat plane. By considering the other two planes defined by (3.44b) and (3.44c), i.e., $K_{7,\min}(K_1, K_8)$ and $K_{8,\min}(K_1, K_7)$, the solution is at the vertex of the admissible region, which is the intersection of the three planes. Based on (3.44a), $K_{1,\min}$ is derived as:

$$\begin{aligned} K_{1,\min} = \Bigg[\prod_{i=7,8} \left[\left(1+\gamma_i^{\rm IR}\right)^{\frac{B_{\rm a}}{B_{\rm b}}} - 1 \right]^{-1} + \left(\frac{1}{4}\right)^{\ell+1} \left[\left(1+\gamma_8^{\rm IR}\right)^{\frac{B_{\rm a}}{B_{\rm b}}} - 1 \right]^{-1} - \\ 5\left(\frac{1}{4}\right)^{\ell+1} \left[\frac{3}{4}\left(\frac{1}{4}\right)^{\ell} + \frac{1}{9}\left(\frac{3}{4}\right)^{\ell+1} + \frac{25}{49}\left(\frac{1}{28}\right)^{\ell+1} \right] \Bigg] \gamma_{\rm b}^{-1} \Delta^{-1}, \end{aligned} \tag{3.74}$$

where:

$$\Delta = \left(\prod_{i=7,8} \left[\left(1+\gamma_i^{\mathrm{IR}}\right)^{\frac{B_\mathrm{a}}{B_\mathrm{b}}} - 1 \right]^{-1} - 5\left(\frac{1}{4}\right)^{\ell+1} \left[\left(\frac{1}{4}\right)^{\ell} + \frac{1}{9}\left(\frac{3}{4}\right)^{\ell+1} + \frac{25}{49}\left(\frac{1}{28}\right)^{\ell+1} \right] \right) \times \left(\left[\prod_{i=1,7,8} \left(1+\gamma_i^{\mathrm{IR}}\right)^{\frac{B_\mathrm{a}}{B_\mathrm{b}}} - 1 \right]^{-1} - 2\left(\frac{1}{4}\right)^{\ell} \right) - \frac{2}{9}\left(\frac{3}{16}\right)^{\ell+1} \left[\left(1+\gamma_8^{\mathrm{IR}}\right)^{\frac{B_\mathrm{a}}{B_\mathrm{b}}} - 1 \right]^{-1}. \tag{3.75}$$

Based on the other two constraints in (3.44b) and (3.44c), and by using (3.74), the minimum power ratios $K_{7,\min}$ and $K_{8,\min}$ are derived as:

$$K_{7,\min} = \left[\left(\left[\prod_{i=1,7,8} \left(1+\gamma_i^{\mathrm{IR}}\right)^{\frac{B_\mathrm{a}}{B_\mathrm{b}}} - 1 \right]^{-1} - 2\left(\frac{1}{4}\right)^{\ell} \right) \left(\left[\left(1+\gamma_8^{\mathrm{IR}}\right)^{\frac{B_\mathrm{a}}{B_\mathrm{b}}} - 1 \right]^{-1} + 5\left(\frac{1}{4}\right)^{\ell+1} \right) + \frac{2}{9}\left(\frac{3}{4}\right)^{\ell+1} \left[\left(1+\gamma_8^{\mathrm{IR}}\right)^{\frac{B_\mathrm{a}}{B_\mathrm{b}}} - 1 \right]^{-1} \right] \gamma_\mathrm{b}^{-1}\Delta^{-1}. \tag{3.76}$$

$$K_{8,\min} = \left[\left(\left[\prod_{i=1,7,8} \left(1+\gamma_i^{\mathrm{IR}}\right)^{\frac{B_\mathrm{a}}{B_\mathrm{b}}} - 1 \right]^{-1} - 2\left(\frac{1}{4}\right)^{\ell} \right) \left(\left[\left(1+\gamma_7^{\mathrm{IR}}\right)^{\frac{B_\mathrm{a}}{B_\mathrm{b}}} - 1 \right]^{-1} + \left(\frac{1}{4}\right)^{\ell} + \frac{1}{9}\left(\frac{3}{4}\right)^{\ell+1} + \frac{25}{49}\left(\frac{1}{28}\right)^{\ell+1} \right) + \frac{2}{9}\left(\frac{3}{4}\right)^{\ell+1} \left[\frac{3}{4}\left(\frac{1}{4}\right)^{\ell} + \frac{1}{9}\left(\frac{3}{4}\right)^{\ell+1} + \frac{25}{49}\left(\frac{1}{28}\right)^{\ell+1} \right] \right] \gamma_\mathrm{b}^{-1}\Delta^{-1}, \tag{3.77}$$

Among the three power ratios of $K_{1,\min}$, $K_{7,\min}$ and $K_{8,\min}$, $K_{1,\min}$ introduces the most challenging tradeoff as it represents the bottleneck backhaul link.

Fig. 3.13 demonstrates the tradeoff between $K_{1,\min}$ and $\frac{B_\mathrm{b}}{B_\mathrm{a}}$ for the same set of values for Φ_b as used in Fig. 3.7. Compared with Fig. 3.7, the tradeoff curves are shifted to the right. In particular, so as to achieve $K_{1,\min} < 1$, a bandwidth ratio of $\frac{B_\mathrm{b}}{B_\mathrm{a}} > 1$ is required even in the case where Φ_b is as small as 5°. As a design guideline, it is useful to investigate how much bandwidth is needed for the IR backhaul system to ensure a certain minimum power level for the bottleneck backhaul link. This can be acquired using Fig. 3.13. For instance, to allow the power ratio of the bottleneck backhaul link to be equal to $K_{1,\min} = 0.01$ for $\Phi_\mathrm{b} = 5^\circ$, a bandwidth ratio no less than $\frac{B_\mathrm{b}}{B_\mathrm{a}} = 2.1$ is needed. The minimum bandwidth ratio denoted by $\frac{B_\mathrm{b}}{B_\mathrm{a}}\big|_{\min}$ is formally presented in Fig. 3.14 as a function of Φ_b for different values of $K_{1,\min}$. It can be observed that $\frac{B_\mathrm{b}}{B_\mathrm{a}}\big|_{\min}$ is rising with increase in Φ_b. The case of $K_{1,\min} = 1$ gives the lower bound for the minimum bandwidth ratio. For $\Phi_\mathrm{b} = 20^\circ$, $\frac{B_\mathrm{b}}{B_\mathrm{a}}\big|_{\min} = 6, 3.3, 2.4$ for $K_{1,\min} = 0.01, 0.1, 1$.

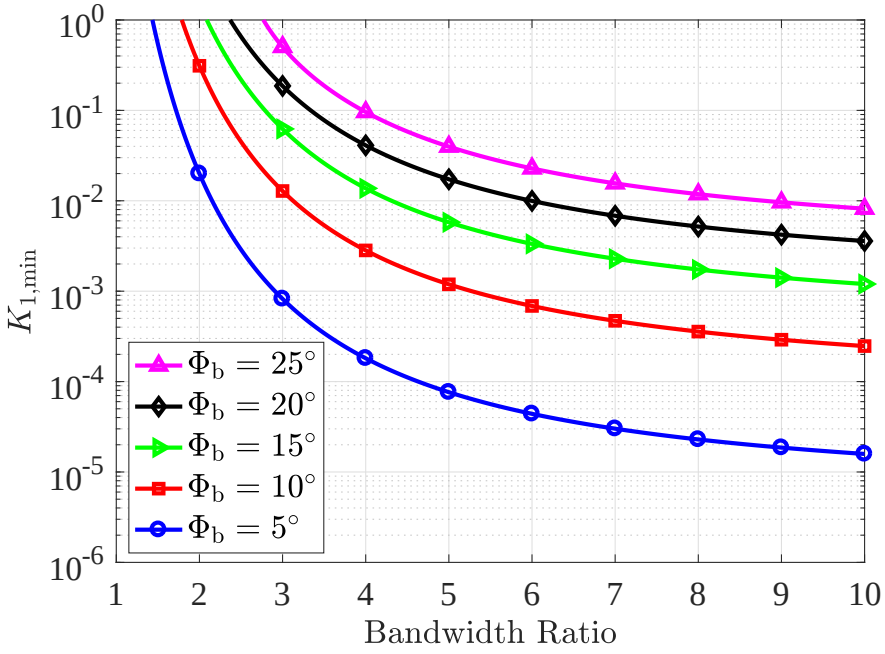

Figure 3.13: *The tradeoff between the minimum power ratio $K_{1,\min}$ and the bandwidth ratio $\frac{B_b}{B_a}$ for the two-tier network with IR backhaul.*

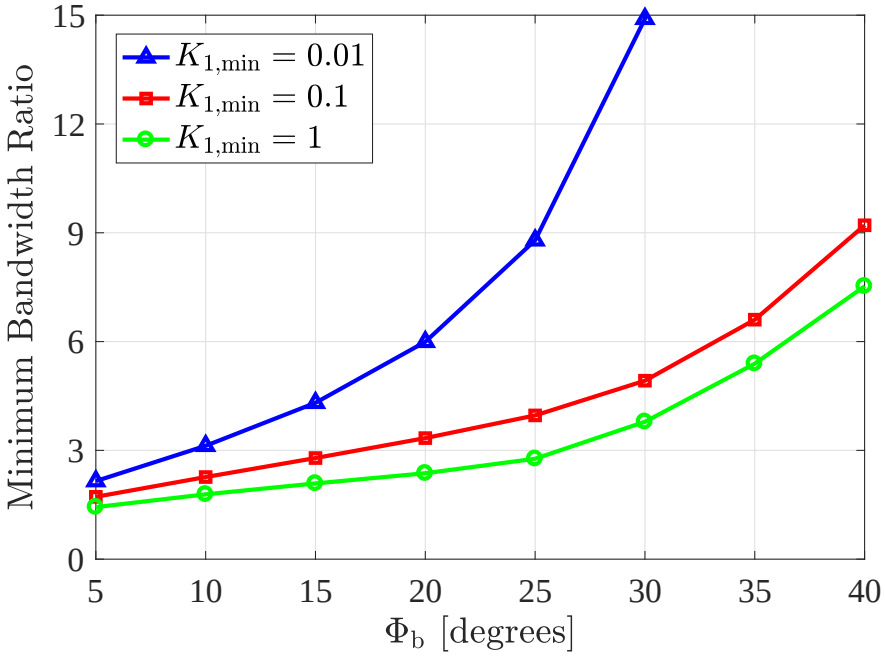

Figure 3.14: *The minimum bandwidth ratio $\frac{B_b}{B_a}\big|_{\min}$ against Φ_b for the two-tier network with IR backhaul for different values of $K_{1,\min}$.*

Fig. 3.15 presents the optimal sum power ratio defined as $K_{\text{sum}} = K_1^* + K_7^* + K_8^*$ against Φ_b for different values of B_b, where $K_j^* = \min[K_{j,\min}, 1]$ for $j = 1, 7, 8$. For the considered

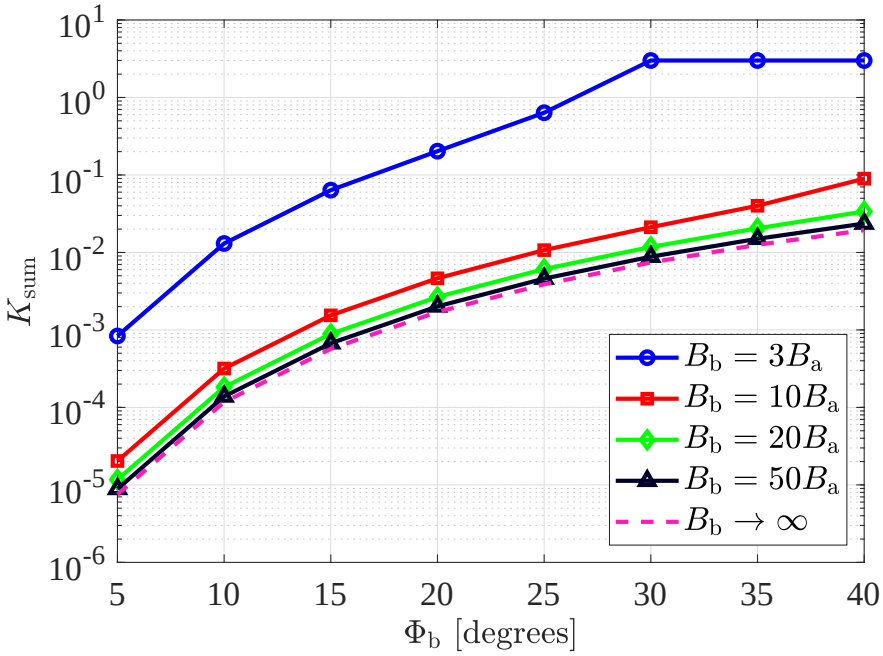

Figure 3.15: *Optimal sum power ratio* $K_{\text{sum}} = K_1^* + K_7^* + K_8^*$ *for the two-tier network with IR backhaul versus* Φ_{b} *for different values of* B_{b}*. The limit of* K_{sum} *for* $B_{\text{b}} \to \infty$ *is based on* (3.78)–(3.80).

branch, this quantity represents the sum of optimal powers of the backhaul links normalized by the transmission power of the access system, i.e., $K_{\text{sum}} = \frac{P_{\text{b}_1}^* + P_{\text{b}_7}^* + P_{\text{b}_8}^*}{P_{\text{a}}}$. Note that the maximum value of K_{sum} is exactly equal to 3, which can be seen in the case of $B_{\text{b}} = 3B_{\text{a}}$ in Fig. 3.15. It can be observed that by further increasing the bandwidth after $B_{\text{b}} = 10B_{\text{a}}$, there is a negligible change in K_{sum}. This can be explained as the values of K_j^* are effectively flattened for $B_{\text{b}} \geq 10B_{\text{a}}$. This flattening effect in Fig. 3.15 is due to the Shannon's wideband capacity limit [109]. Similar to the one tier IR backhaul network, the asymptotic values of power control coefficients can be obtained by evaluating their limit as the backhaul bandwidth approaches infinity. Based on (3.74), (3.76) and (3.77), the desired limits are derived as follows:

$$\lim_{B_{\text{b}} \to \infty} K_{1,\min} = \hat{\gamma}_{\text{b}}^{-1} B_{\text{a}} \sum_{i=1,7,8} \log\left(1 + \gamma_i^{\text{IR}}\right), \tag{3.78}$$

$$\lim_{B_{\text{b}} \to \infty} K_{7,\min} = \hat{\gamma}_{\text{b}}^{-1} B_{\text{a}} \log\left(1 + \gamma_7^{\text{IR}}\right), \tag{3.79}$$

$$\lim_{B_{\text{b}} \to \infty} K_{8,\min} = \hat{\gamma}_{\text{b}}^{-1} B_{\text{a}} \log\left(1 + \gamma_8^{\text{IR}}\right), \tag{3.80}$$

where $\hat{\gamma}_{\text{b}}$ is given by (3.61). The asymptotic value of K_{sum} is equal to the sum of (3.78)–(3.80). This constitutes the lower bound of the sum power ratio as shown in Fig. 3.15.

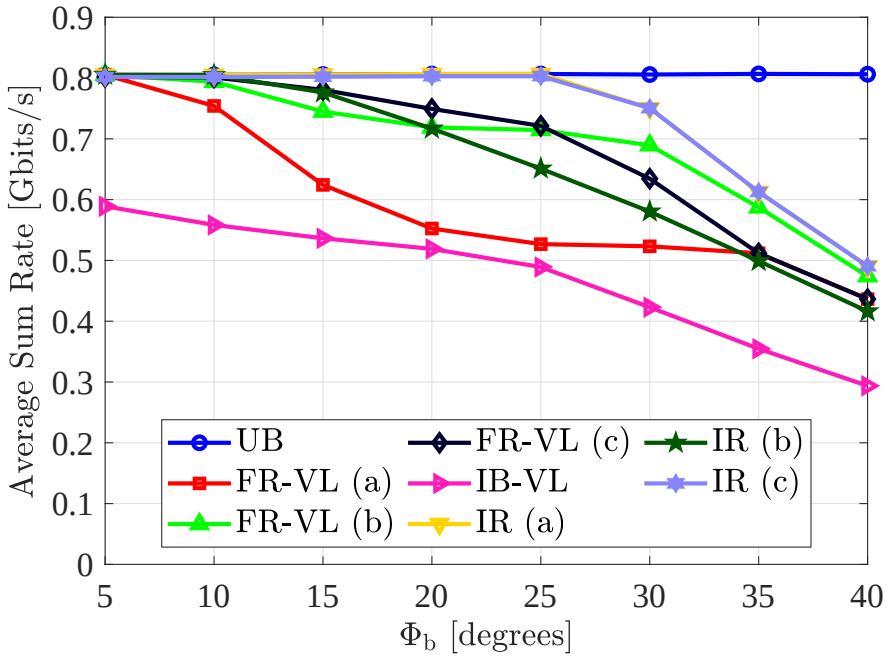

Figure 3.16: *Average sum rate performance of the one-tier optical attocell network using FR-VL, IB-VL and IR backhaul systems as a function of* Φ_b. *For FR-VL (a)* $K_1 = 1$*; (b)* $K_1 = 0.1$*; (c)* $K_1 = K_1^*$. *For IR (a)* $K_1 = 1$*; (b)* $K_1 = 0.01$*; and (c)* $K_1 = K_1^*$. *For IR backhaul,* $B_b = B_a$.

Next, simulation results are presented for the overall average sum rate performance of one-tier and two-tier optical attocell networks using FR-VL, IB-VL and IR backhaul systems based on the sum rate analysis and the backhaul power optimization presented in Sections 3.3 and 3.4. In addition, a UB network is considered as the baseline scenario in which every single BS is individually connected to the core network using a high capacity wired backhaul link. Simulations are conducted based on Monte Carlo averaging over a large number of random realizations for the distribution of UEs in the network, using the parameters given in Table 3.1. To make a fair comparison between a one-tier and a two-tier network, the average UE density (i.e., the average number of UEs per cell) is fixed, by considering $M = 15$ and $M = 40$ for one-tier and two-tier cases, respectively. For FR-VL and IR backhaul systems, both cases including with and without power control are studied using various combinations of power ratios to exemplify the effect of power control on the network performance. Note that the optimization objective is the sum power of the backhaul system and therefore it does not necessarily maximize the sum rate performance. Nevertheless, this may happen in some cases as an extra benefit of the power optimization.

3.4.3 Average Sum Rate Performance

3.4.3.1 One-Tier Network

Fig. 3.16 demonstrates the average performance of the one-tier optical attocell network. First, the focus is on FR-VL and IB-VL backhaul systems. It is observed that general trends for both FR-VL and IB-VL systems are monotonically decreasing with respect to $\Phi_{\rm b}$. For FR-VL, the reason for this is that by widening the light beam, the backhaul interference on the downlink is increased and at the same time, the SINR of the backhaul links is reduced. For IB-VL, on the other hand, an increase in $\Phi_{\rm b}$ causes the sub-band ratio δ to decrease because of the lower SINR of the backhaul links. This has suppressed the overall performance of the first tier since it is directly proportional to δ according to (3.27). Furthermore, it is observed that FR-VL outperforms IB-VL throughout the entire range of $\Phi_{\rm b}$ regardless of the value of K_1, in spite of the fact that FR-VL causes a higher interference. This is achieved as a result of the better utilization of the bandwidth. For $\Phi_{\rm b} = 5^\circ$, the performance of the FR-VL network reaches the upper limit of 806 Mbits/s offered by the UB network. This is attributed in part to a substantial reduction in the backhaul interference for small values of $\Phi_{\rm b}$, in line with Theorem 1.

Fig. 3.16 shows the performance of FR-VL and IR backhaul systems including power control. For FR-VL, by comparing cases (a) and (b), it can be observed that the performance is significantly improved when the backhaul power is reduced by a factor of 10. The improvement is up to 188 Mbits/s for moderate values of $\Phi_{\rm b}$. This is primarily because by reducing the backhaul power, the adverse effect of backhaul interference is alleviated. In comparison to case (b), the FR-VL case (c) that uses the optimal power ratio achieves a better performance until $\Phi_{\rm b} = 25^\circ$, at which $K_1^* = 0.1$. Note that $K_{1,\min} > 0.1$ for $\Phi_{\rm b} > 25^\circ$; see Fig. 3.6. In the case of IR, the bandwidth ratio is equal to one. Fig. 3.16 shows that IR backhauling performs near the UB limit especially for cases (a) and (c) which correspond to $K_1 = 1$ and $K_1 = K_1^*$, for small to moderate values of $\Phi_{\rm b}$. This indicates that the PE of the IR backhaul system can be remarkably improved by using the minimum power control coefficients given by (3.74), (3.76) and (3.77), depending on the value of $\Phi_{\rm b}$. This gain is attained while preserving the average sum rate performance identical to the case when using the full power for the IR backhaul system. In the IR case (b), where the power of the backhaul system is reduced by a factor of 100, no loss in performance is observed for $\Phi_{\rm b} \leq 10^\circ$, and the extent of performance loss is still sustainable for moderate to large values of $\Phi_{\rm b}$.

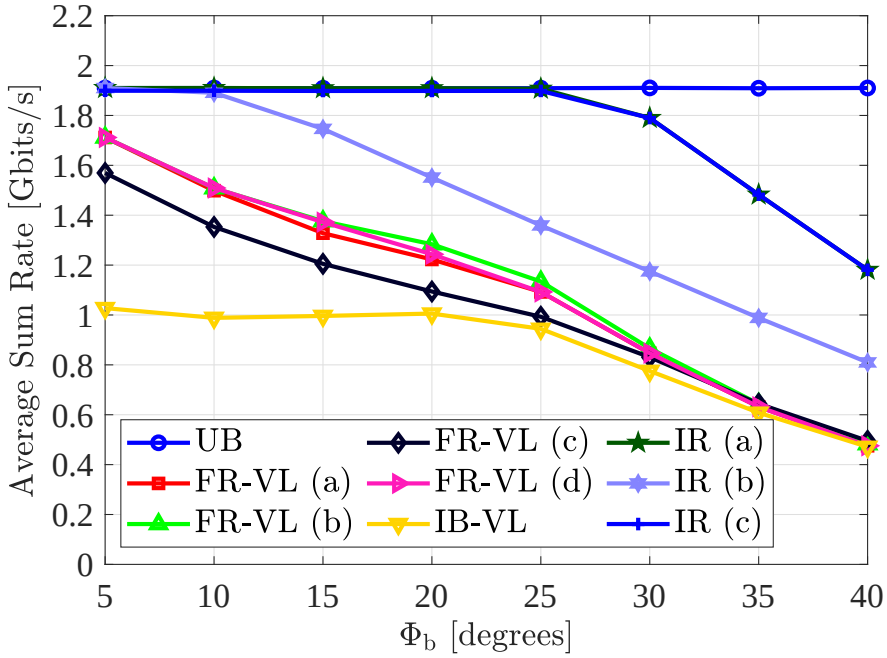

Figure 3.17: *Average sum rate performance of the two-tier optical attocell network using FR-VL, IB-VL and IR backhaul systems as a function of* Φ_b. *For FR-VL case (a)* $K_1 = K_7 = K_8 = 1$*; (b)* $K_1 = 1$*, and* $K_7 = K_8 = 0.1$*; (c)* $K_1 = K_7 = K_8 = 0.1$*; and (d)* $K_1 = 1$*, and* $(K_7, K_8) = (K_7^*, K_8^*)$. *For IR case (a)* $K_1 = K_7 = K_8 = 1$*; (b)* $K_1 = K_7 = K_8 = 0.01$*; and (c)* $K_j = K_j^*$ *for* $j = 1, 7, 8$. *For IR backhaul,* $B_b = 3B_a$.

3.4.3.2 Two-Tier Network

Fig. 3.17 demonstrates the average sum rate performance of the two-tier optical attocell network. The UB network gives the constant upper limit of 1.91 Gbits/s for the network performance. In addition, the IB-VL network globally has the worst performance. Among the FR-VL cases, case (c) using $K_1 = K_7 = K_8 = 0.1$ has the lowest performance. The other three cases take the same value of $K_1 = 1$. The low performance in case (c) is due to a ten times reduction in the power of the bottleneck backhaul link, which directly affects the sum rate performance of the network. The performance of case (d) using the optimal power ratios of (K_7^*, K_8^*) is bounded from below by that of case (a) and from above by that of case (b), where (a) and (b) correspond to $K_7 = K_8 = 1$ and $K_7 = K_8 = 0.1$. Cases (a), (b) and (d) perform slightly better than case (c). Furthermore, in the case of IR, a bandwidth ratio of three is used. It is evident that the performance of case (c) using the minimized power ratios perfectly matches with case (a) that uses the full power for the IR backhaul system, though using the minimum sum power. Likewise, the power of all the backhaul links can be reduced according to the value

of Φ_{b} without degrading the network performance. This is achieved by choosing a sufficient bandwidth for the IR backhaul system, i.e., $B_{\mathrm{b}} = 3B_{\mathrm{a}}$.

3.4.4 Imperfect Alignment in Backhaul Links

So far, the wireless optical backhaul links are assumed to be perfectly aligned, in that every backhaul LED is aimed at its corresponding receiver on the other end of the link. An imperfect alignment between adjacent BSs potentially leads to a degradation in the system performance as it can adversely affect the SINR of backhaul links by reducing their effective channel gain. A question naturally arises, how impactful is the effect of imperfect alignment? To address this issue, a simulation scenario is set up for the backhaul system in which a random misalignment error causes the light radiance angle to deviate from the alignment axis. In practice, such a pointing error is mainly driven by uncertainties inherent in the installation process. A uniform distribution model is employed, allowing the misalignment error to randomly vary within a limited range. The average SINR of backhaul links is demonstrated in Fig. 3.18 for the one tier network, and in Fig. 3.19 for the two tier network. The results are presented for only one branch of the backhaul system due to the network symmetry. In the following, the interplay between the misalignment error and the backhaul LED semi-angle Φ_{b} is highlighted.

Fig. 3.18 shows the average backhaul SINR as a function of Φ_{b} under perfect and imperfect alignment conditions. The magnitude of the angle error varies in an interval $[0, 3^{\circ}]$. It can be observed that the performance with misalignment closely follows the case with perfect alignment especially for moderate to large values of Φ_{b}. There is a discrepancy between the two cases which mostly appears for small values of Φ_{b}. By comparison, the misalignment error leads to a slight degradation in the performance as a result of: 1) a loss in the LOS gain for the backhaul links; 2) an increase in the interference level from neighboring BSs. This is in line with an intuitive observation that the misalignment error is more impactful for narrower light beams. To better illustrate this phenomenon, the average SINR performance is shown in Fig. A.1b as a function of the magnitude of the misalignment error. Although the average SINR exhibits a decreasing behavior with respect to the error magnitude, this is less significant when Φ_{b} increases. More specifically, over the range $[0, 3^{\circ}]$ for the error magnitude, there is a 3 dB loss in the average SINR for $\Phi_{\mathrm{b}} = 2^{\circ}$, while the loss is only 0.65 dB for $\Phi_{\mathrm{b}} = 5^{\circ}$, and there is almost no loss for $\Phi_{\mathrm{b}} = 15^{\circ}$.

Based on these results, a deduction can be made that by using a larger semi-angle for backhaul

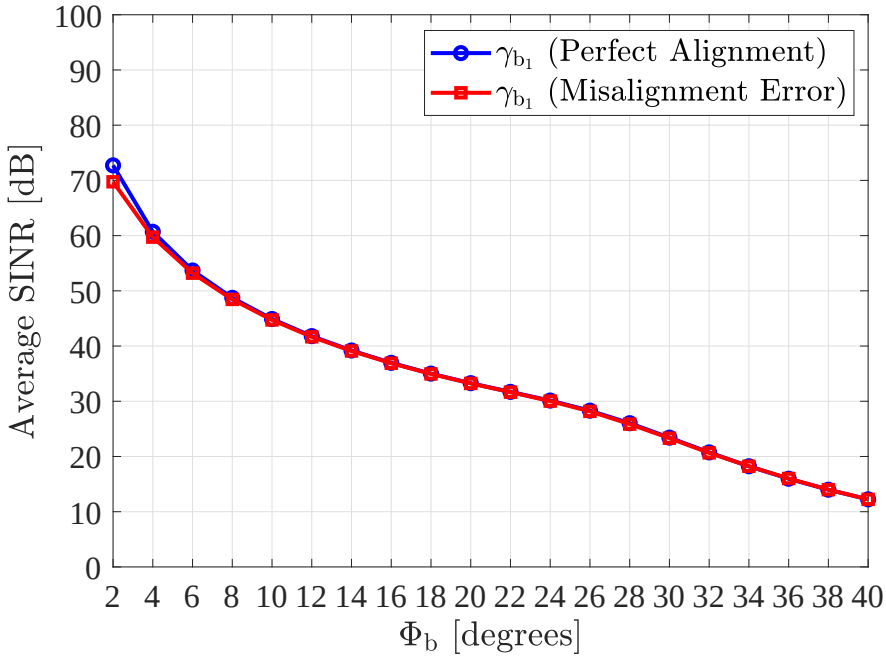

(a) Average backhaul SINR as a function of the LED semi-angle Φ_b under perfect and imperfect alignment. The misalignment error is up to $\pm 3^\circ$ about the alignment axis.

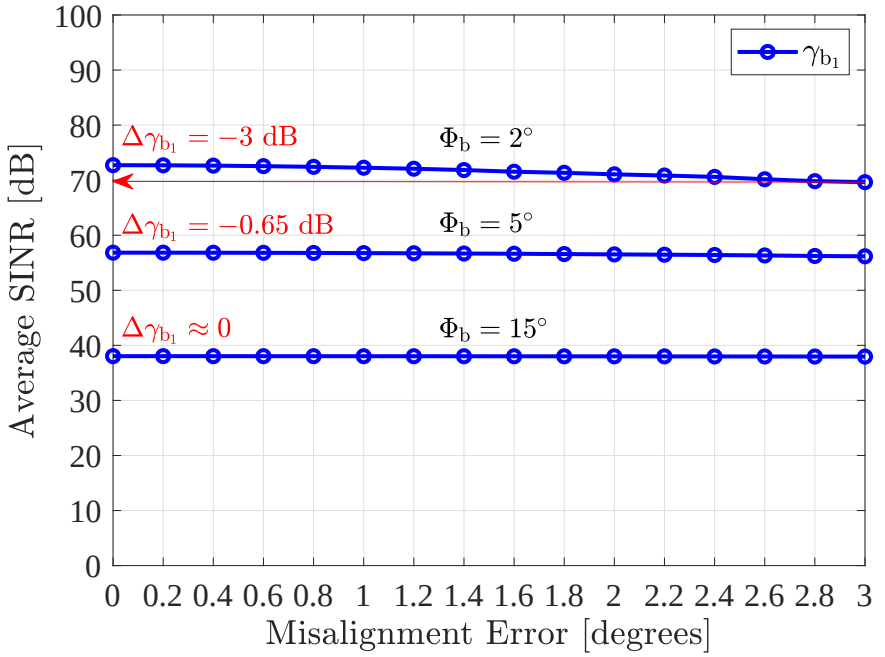

(b) Average backhaul SINR as a function of the misalignment error for different values of the LED semi-angle Φ_b.

Figure 3.18: *Average SINR performance of the VL backhaul system against the misalignment error for the one tier network. In all cases,* $K_1 = 0.1$.

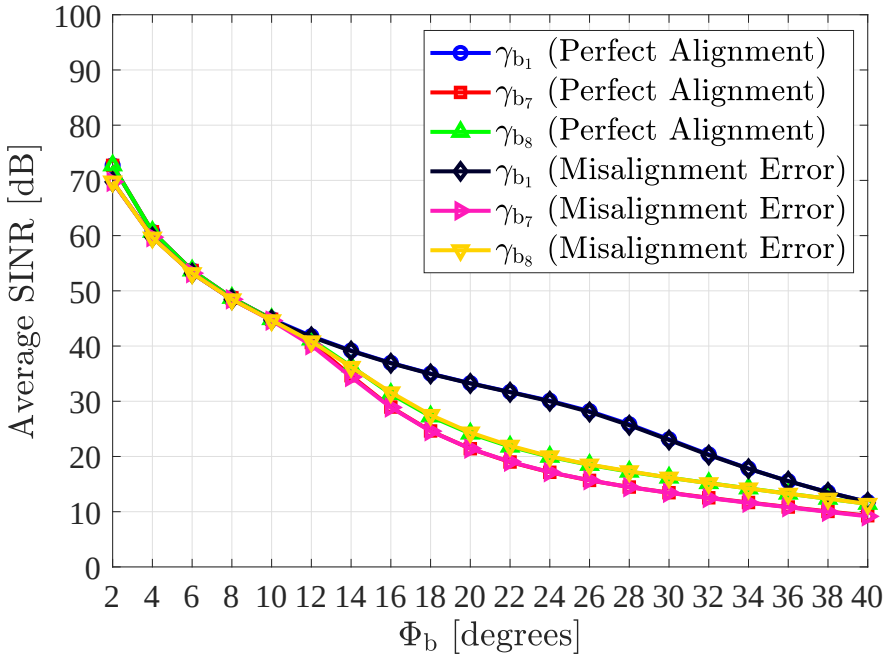

(a) Average backhaul SINR as a function of the LED semi-angle Φ_b under perfect and imperfect alignment. The misalignment error is up to $\pm 3^\circ$ about the alignment axis.

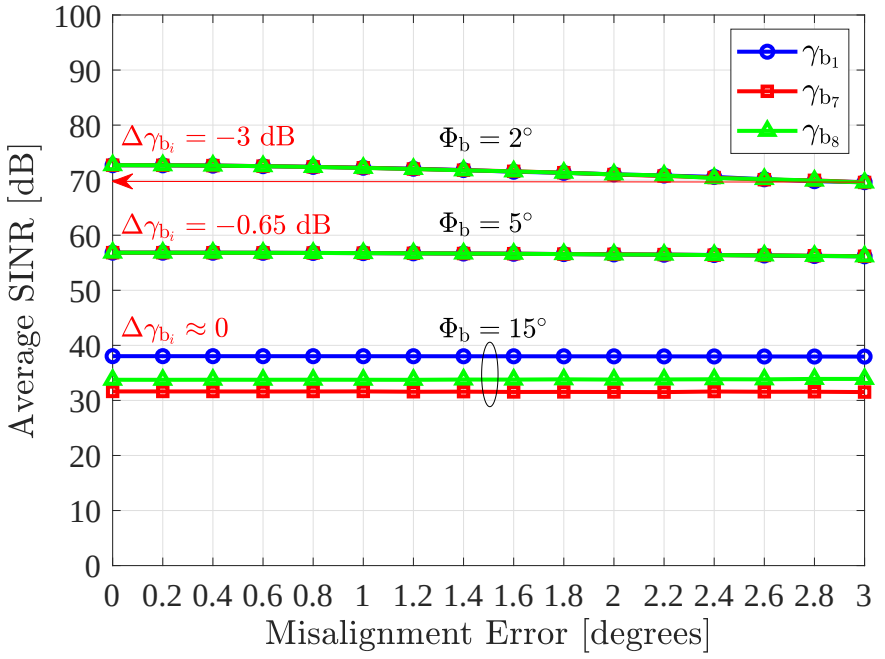

(b) Average backhaul SINR as a function of the misalignment error for different values of the LED semi-angle Φ_b.

Figure 3.19: *Average SINR performance of the VL backhaul system against the misalignment error for the two tier network. In all cases,* $K_1 = K_7 = K_8 = 0.1$.

LEDs, the system becomes more tolerant against the misalignment error. As such, by increasing the semi-angle of backhaul LEDs, the optical power is distributed over a larger spherical solid angle in the propagation space. A larger illuminated spot (i.e., the effective area on the receiver plane containing the optical power transmitted within the LED semi-angle) is created on the receiver plane. Provided that the illuminated spot is sufficiently larger than the photodetector area, the received power does not change for small misalignment errors. Similarly, the same conclusion is drawn by interpreting the results of the two tier network as shown in Fig. 3.19. To sum up, these results suggest that for a wide range of values of Φ_{b} (i.e., $5^{\circ} \leq \Phi_{\mathrm{b}} \leq 40^{\circ}$), the effect of imperfect alignment can be safely assumed insignificant.

3.5 Summary

In this chapter, a novel wireless backhaul solution is proposed for indoor optical attocell networks by which the BSs are connected to the gateway via multi-hop wireless optical links. For both FR-VL and IB-VL backhaul systems, the downlink performance depends upon the directivity of the light beam in the backhaul links. A better performance is achieved for a smaller value of Φ_{b}. In addition, FR-VL gives a significantly better performance than IB-VL, and it enables the network to attain the performance of a benchmark UB network particularly for a one-tier deployment. Following a power optimization for the backhaul system, the results suggest that FR-VL is not an appropriate option for network deployments of more than one tier. Alternatively, the migration of wireless optical backhauling to the IR band is proposed. In this case, after establishing a power-bandwidth tradeoff analysis for a two-tier network, IR backhauling shows the potential that it does not only outperform FR-VL backhauling but its performance is closely matched to that of the UB network in terms of the network sum rate, when using a properly designed divergence angle for the light beam in the backhaul links. For the IR backhaul system, given a modulation bandwidth of only three times that of the downlink VLC system, the backhaul transmission power can be made 100 times lower than the full power operation without influencing the network performance, which is a remarkable gain for PE. Concerning misalignment in backhaul links, the impact of the orientation angle error varying in a given range is not significant as long as the semi-angle of backhaul LEDs is greater than a threshold value depending on the error magnitude. This means an appropriate choice for the semi-angle of backhaul LEDs, which is not too small, makes the entire system immune to possible pointing errors.

Chapter 4
Extension to Multi-Tier Networks: Opportunistic Power Control and Optimal Bandwidth Scheduling for Multi-Hop Wireless Backhauling

In this chapter, the use of wireless optical backhaul solution is extended to multi-tier networks via the introduction of the new concept of super cells. Consequently, new challenges arise for backhaul power control and bandwidth scheduling. The contributions of this chapter include: 1) Novel power control schemes are proposed to limit the backhaul power in an opportunistic approach. In particular, three schemes are proposed to control the power of the backhaul system based on the availability of the downlink channel information, including: adaptive power control (APC) and fixed power control (FPC). The design of each scheme is supported by a thorough analysis and the corresponding power control coefficients are analytically derived; 2) In order to assess the performance of the proposed power control schemes, a new metric called backhaul bottleneck occurrence (BBO) is defined. The BBO probability is analytically evaluated and a simple and tight approximation is derived for it. The approximate expression derived in this chapter is useful for system level design of multi-hop wireless optical backhauling to predict the BBO performance of the network; 3) Performance improvements are evaluated in terms of the total transmission power of the backhaul system. In addition, new insights are provided into the performance of the backhaul system by studying the relative total power (RTP), BBO and the average sum rate performance; 4) An analysis of the end-to-end sum rate of the network is performed for the general case of multiple tier networks by taking the effect of bandwidth sharing at the bottleneck link into consideration; 5) user-based bandwidth scheduling (UBS) and cell-based bandwidth scheduling (CBS) policies are proposed for optimal scheduling of the bandwidth resource. Novel algorithms are developed to implement them by formulating and solving bandwidth allocation optimization problems. The optimization problems are convex with a non-differentiable objective function. The optimal solution is derived for each policy based on the projected subgradient method.

The remainder of this chapter is organized as follows: Section 4.1 provides fundamental tools required for system level analysis, including the statistics of the downlink signal-to-noise-plus-interference ratio (SINR) and the backhaul SINR when the light emission in the backhaul system is assumed to be sufficiently focused; Section 4.2 discusses high level principles related to the design of multi-hop wireless optical backhauling when applied to multi-tier networks: the backhaul-access rate inequality, multi-hop full-duplex relaying, bandwidth sharing and the generalized end-to-end sum rate analysis; Section 4.3 expounds the design, modeling and analysis of the proposed APC and FPC schemes. The BBO probability and the derivation of its analytical approximation are also given in this section. Numerical results for the power control schemes are provided with a variety of examples and case studies; Section 4.4 includes optimal bandwidth scheduling under UBS and CBS policies. The underlying optimization problem and its solution are discussed. The presented analysis is supported by a number of numerical examples; Section 4.5 provides a summary of key findings and concluding remarks.

4.1 System-Level Preliminaries

4.1.1 Network Configuration

An unbounded optical attocell network with a hexagonal tessellation is considered. Such a model is appropriate for network deployments in spacious office environments [16]. The network incorporates multi-tier bundles of hexagonal attocells which are referred to as *super cells* in this work, with each bundle encompassing one, or possibly more than one tiers. The entire network coverage is then *tiled* by multiple super cells. Within every super cell, only the central base station (BS) is directly connected to the gateway while the remaining BSs are connected using a tree topology that extends from a root at the central BS toward the outer tiers. Inter-BS backhaul links employ a wireless optical communication technology operating in visible light (VL) or infrared (IR) optical bands as discussed in Chapter 3. In this chapter, the wireless optical backhaul links are assumed to be perfectly aligned and equipped with directive (i.e., narrow-beam) transmissions so as to avoid causing any interference to colocated links that operate on the same optical band. In Chapter 3, it was shown that by using a sufficiently narrow light beam, the backhaul links cause a negligible interference, i.e., either crosstalk in the backhaul network or backhaul-induced interference on the access network.

A number of user equipment (UE) devices are randomly scattered in the coverage of a super cell

according to a uniform distribution, attempting to obtain a downlink connection from optical BSs. The employment of DC-biased optical OFDM (DCO-OFDM) for data transmission in both access and backhaul systems allows an efficient management of network resources in order to optimize a network-wide utility as presented in Section 4.3. To maintain the generality of presentation, the parameters associated with the access system are denoted with the subscript a and those related to the backhaul system are represented using the subscript b. Specifically, an N_{a}-point (resp. N_{b}-point) inverse fast Fourier transform (IFFT)/fast Fourier transform (FFT) is used for DCO-OFDM transmission in the access (resp. backhaul) system. The rest of the assumptions are similar to those used in Chapter 3.

For completeness, the received SINR is briefly described for both access and backhaul systems, and the statistics of the downlink SINR is derived in detail.

4.1.2 Signal-to-Noise-plus-Interference Ratio

4.1.2.1 Downlink SINR Statistics

With the assumption of the whole bandwidth being fully reused across all attocells, the downlink quality in each attocell is influenced by co-channel interference (CCI) from neighboring BSs. When the number of interfering BSs is large, the aggregate effect of the received CCI signals can be treated as a white Gaussian noise. Also, the received signal of downlink is perturbed by an additive noise comprising signal-independent shot noise and thermal noise, which is modeled by a zero mean Gaussian distribution with a single-sided power spectral density (PSD) of N_0. According to a polar coordinate system with BS_0 at the origin, and after removing the backhaul interference effect from (3.12), the electrical SINR per subcarrier for the uth UE located at the point $z_u = (r_u, \theta_u)$ inside the attocell of BS_i simplifies to:

$$\gamma_u = \frac{\xi_{\mathrm{a}}^{-1}(r_i^2(z_u) + h^2)^{-m-3}}{\sum\limits_{j \in \mathcal{J}_i} (r_j^2(z_u) + h^2)^{-m-3} + \Omega}, \tag{4.1}$$

where Ω is given by (3.15).

The downlink SINR is a function of the UE coordinates, which are distributed uniformly at random over the network. Therefore, the downlink SINR is a random variable. For an unbounded hexagonal attocell network, the cumulative distribution function (CDF) of the downlink SINR is presented in [16]. For the set of assumptions used in this work, a methodology similar to that

in [16] is adopted as follows. To facilitate the analysis, the coverage area of a hexagonal cell of radius R is approximated by an equivalent circular cell of radius R_{e} while preserving the area so that $R_{\mathrm{e}} = \sqrt{\frac{3\sqrt{3}}{2\pi}}R$. The probability density functions (PDFs) of r_u and θ_u are given by:

$$f_{r_u}(r) = \begin{cases} \frac{2r}{R_{\mathrm{e}}^2}, & r \in [0, R_{\mathrm{e}}] \\ 0, & \text{otherwise} \end{cases}, \tag{4.2a}$$

$$f_{\theta_u}(\theta) = \begin{cases} \frac{1}{2\pi}, & \theta \in [0, 2\pi] \\ 0, & \text{otherwise} \end{cases}. \tag{4.2b}$$

To derive an analytical expression for the CDF of γ_u, it is convenient to calculate the conditional probability of $\mathbb{P}\left[\gamma_u < \gamma | r_u = r\right]$, where γ is a given threshold SINR. This can be expressed as:

$$\mathbb{P}\left[\gamma_u < \gamma | r_u = r\right] = \mathbb{P}\left[\sum_{j \in \mathcal{J}_i} (r_j^2(z_u) + h^2)^{-m-3} > \frac{\xi_{\mathrm{a}}^{-1}(r_i^2(z_u) + h^2)^{-m-3}}{\gamma} - \Omega \middle| r_u = r\right]. \tag{4.3}$$

The evaluation of (4.3) requires the statistics of the CCI term $\sum_{j \in \mathcal{J}_i}(r_j^2(z_u) + h^2)^{-m-3}$, which can be expanded as follows:

$$\mathcal{I}(\theta_u | r_u = r) = \sum_{j \in \mathcal{J}_i} \left(r^2 + R_j^2 - 2R_j r \cos(\theta_u - \Theta_j) + h^2\right)^{-m-3}, \tag{4.4}$$

where (R_i, Θ_i) represent the polar coordinates of BS$_j$. The CCI expression in (4.4) involves an intricate transformation of θ_u for $r_u = r$. To alleviate the complexity, a proper simplification can be made by noting that in an unbounded network, the effective inter-cell interference (ICI) range is up to two tiers around the considered attocell [16]. With this simplification, an approach similar in principle to the *flower model* as introduced in [110] is used in [16] to approximate the CCI term with respect to θ_u. Specifically, $\mathcal{I}(\theta_u | r_u = r)$ as a function of θ_u exhibits a sinusoidal oscillation between two bounds with a period of $60°$. As a result:

$$\mathcal{I}(\theta_u | r_u = r) \approx \frac{\mathcal{I}_{0°}(r) + \mathcal{I}_{30°}(r)}{2} + \frac{|\mathcal{I}_{0°}(r) - \mathcal{I}_{30°}(r)|}{2} \cos(6\theta_u). \tag{4.5}$$

The functions $\mathcal{I}_{0°}(r)$ and $\mathcal{I}_{30°}(r)$ appearing in (4.5) are available in closed form in [16]. For clarity, these functions are explicitly given in Appendix E. Substituting (4.5) into (4.3) and rearranging yields:

$$\mathbb{P}\left[\gamma_u < \gamma | r_u = r\right] = \mathbb{P}\left[\cos(6\theta_u) > \mathcal{Z}(r, \gamma)\right], \tag{4.6}$$

where:

$$\mathcal{Z}(r,\gamma)=\frac{2\gamma^{-1}\xi_{\mathrm{a}}^{-1}(r^2+h^2)^{-m-3}-2\Omega}{|\mathcal{I}_{0^\circ}(r)-\mathcal{I}_{30^\circ}(r)|}-\frac{\mathcal{I}_{0^\circ}(r)+\mathcal{I}_{30^\circ}(r)}{|\mathcal{I}_{0^\circ}(r)-\mathcal{I}_{30^\circ}(r)|}. \tag{4.7}$$

To solve (4.6), the interval $[0,2\pi]$ is divided into 12 disjoint subintervals such that the function $\cos(6\theta_u)$ is invertible in each subinterval, then by using the law of total probability:

$$\begin{aligned}&\mathbb{P}\left[\cos(6\theta_u)>\mathcal{Z}(r,\gamma)\right]=\\&\sum_{k=1}^{12}\mathbb{P}\left[\cos(6\theta_u)>\mathcal{Z}(r,\gamma)\,\middle|\,\frac{(k-1)\pi}{6}\leq\theta_u\leq\frac{k\pi}{6}\right]\mathbb{P}\left[\frac{(k-1)\pi}{6}\leq\theta_u\leq\frac{k\pi}{6}\right].\end{aligned} \tag{4.8}$$

The first probability under the summation equals the length of a region for which the condition $\cos(6\theta_u)>\mathcal{Z}(r,\gamma)$ holds divided by $\frac{\pi}{6}$, since θ_u is uniformly distributed according to (4.2b). This is given by:

$$\mathbb{P}\left[\cos(6\theta_u)>\mathcal{Z}(r,\gamma)\,\middle|\,\frac{(k-1)\pi}{6}\leq\theta_u\leq\frac{k\pi}{6}\right]=\frac{1}{2}-\frac{1}{\pi}\arcsin^{\dagger}\left(\mathcal{Z}(r,\gamma)\right), \tag{4.9}$$

where:

$$\arcsin^{\dagger}(x)=\begin{cases}\frac{\pi}{2}, & x>1\\ \arcsin(x), & |x|\leq 1\\ -\frac{\pi}{2}, & x<-1\end{cases}. \tag{4.10}$$

The second probability under the summation in (4.8) is equal to:

$$\mathbb{P}\left[\frac{(k-1)\pi}{6}\leq\theta_u\leq\frac{k\pi}{6}\right]=\frac{1}{12}. \tag{4.11}$$

By combining (4.8), (4.9) and (4.11), the conditional probability in (4.6) is derived as:

$$\mathbb{P}\left[\gamma_u<\gamma|r_u=r\right]=\frac{1}{2}-\frac{1}{\pi}\arcsin^{\dagger}\left(\mathcal{Z}(r,\gamma)\right). \tag{4.12}$$

Finally, the unconditional probability of $\mathbb{P}\left[\gamma_u<\gamma\right]$ can be evaluated by integrating (4.12) over the PDF $f_{r_u}(r)$ in (4.2a), which results in:

$$\mathbb{P}\left[\gamma_u<\gamma\right]=\int_0^{R_{\mathrm{e}}}\mathbb{P}\left[\gamma_u<\gamma|r_u=r\right]\frac{2r}{R_{\mathrm{e}}^2}dr=\frac{1}{2}-\frac{2}{\pi R_{\mathrm{e}}^2}\int_0^{R_{\mathrm{e}}}\arcsin^{\dagger}\left(\mathcal{Z}(r,\gamma)\right)rdr. \tag{4.13}$$

Based on (4.13), the CDF of γ_u can be efficiently computed by numerical integration methods.

Note that γ_u is a bounded random variable such that:

$$\gamma_{\min} \leq \gamma_u \leq \gamma_{\max}, \tag{4.14}$$

where:

$$\gamma_{\min} = \frac{\xi_{\mathrm{a}}^{-1}(R_{\mathrm{e}}^2 + h^2)^{-m-3}}{\mathcal{I}_{30^\circ}(R_{\mathrm{e}}) + \Omega}, \tag{4.15a}$$

$$\gamma_{\max} = \frac{\xi_{\mathrm{a}}^{-1} h^{-2m-6}}{\mathcal{I}_{0^\circ}(0) + \Omega}. \tag{4.15b}$$

4.1.2.2 Backhaul SNR

Since the backhaul links have an equal link distance, and the cross-coupling interference among them is insignificant, they exhibit an identical signal-to-noise ratio (SNR). In addition, the transmission power of the backhaul system can be less than the access system. In fact, because of directive transmissions, the line-of-sight (LOS) channel gain is already high which means the required power to reach a given SNR is lower. By using either (3.6) or (3.34)–(3.36) when $\ell \gg 1$, the received SNR per subcarrier for b_i $\forall i$ is derived as:

$$\gamma_{\mathrm{b}_i} = \frac{((\ell+1) A_{\mathrm{PD}} R_{\mathrm{PD}})^2 P_{\mathrm{b}_i}}{72\pi^2 R^4 N_0 B_{\mathrm{b}} \xi_{\mathrm{b}}^2}, \tag{4.16}$$

where $P_{\mathrm{b}_i} = K_i P_{\mathrm{a}}$ is the transmission power for the link b_i, and K_i is the corresponding power control coefficient and P_{a} is the total power for multi-user transmission in the access system.

4.2 Multi-Hop Wireless Backhaul System Design

This section presents high-level principles of the multi-hop wireless optical backhaul system, including access-backhaul rate inequality, full duplex relaying, bandwidth sharing and effective end-to-end sum rate per cell. This work lays emphasis on the backhaul system performance, and hence multi-user access is simplified by using orthogonal frequency division multiple access (OFDMA) scheduling where the downlink bandwidth is equally allocated to the UEs of each attocell. For flat channels, it turns out that equal bandwidth allocation is the optimal solution for proportionally fair multi-user scheduling. In the following, a super cell with a total number of N_{T} tiers is considered for analysis. For clarity, one branch of a super cell with $N_{\mathrm{T}} = 5$ is illustrated in Fig. 4.1. Note that the picture of the whole super cell is constituted by rotating and

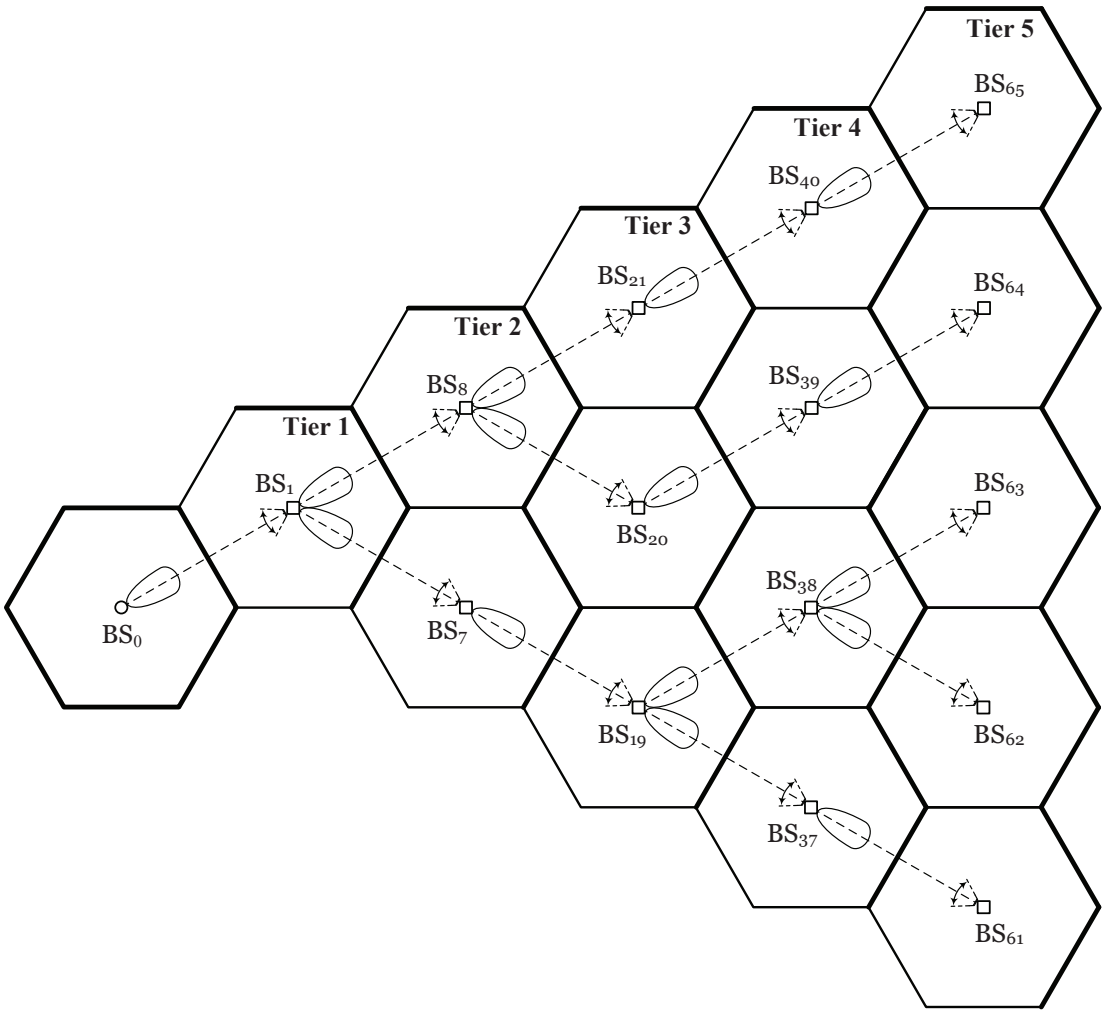

Figure 4.1: *One branch of a five tier super cell with a plan view of multi-hop wireless optical backhaul configuration.*

repeating the shown branch every 60° counterclockwise. Nevertheless, this is just an illustration and the generality of presentation is maintained throughout the chapter by adopting a parametric modeling methodology, i.e., for a general case of the kth branch for $k = 1, 2, \ldots, 6$.

According to Fig. 4.1, a *tree topology* is chosen for the backhaul network since: 1) It guarantees the *shortest path* between the gateway and every BS in the outer tiers; 2) It is matched well with the hexagonal cellular layout due to the circular symmetry of the network around the central BS; and 3) It can be scaled to multi-tier networks with any number of tiers. Albeit, the choice of tree topology with the particular connections as shown in Fig. 4.1 is not a limiting assumption. The aim of this specific choice is to fix the topology and concentrate on the technical aspects of multi-hop wireless optical backhauling. However, the proposed modeling is more general and

is valid as long as there is a *spanning tree* that establishes a route from the gateway to every BS within the same branch. The number of such trees can be large depending on the total number of the deployed tiers and it can be accounted a degree of freedom for practical implementations. To ensure the realization of shortest path spanning trees, making backhaul connections between adjacent BSs in the same tier is avoided. For instance, for BS_{20} in Fig. 4.1, the backhaul link between BS_8 and BS_{20} is considered, instead of which the one connecting BS_{21} to BS_{20} could be used. This would involve one more hop and hence make the backhaul path to BS_{20} longer. Moreover, the rationale behind arranging backhaul connections in the way as shown in Fig. 4.1 is to balance the load of the backhaul links of the second tier, i.e., seven BSs are assigned to the upper sub-branch and seven to the lower sub-branch.

4.2.1 Rate Inequality

The access and backhaul systems have an equal subchannel bandwidth so that $\frac{B_{\mathrm{a}}}{N_{\mathrm{a}}} = \frac{B_{\mathrm{b}}}{N_{\mathrm{b}}}$, leading to the same symbol periods for DCO-OFDM frames of the two systems. Denote by $\mathcal{L}_i$ the index set of BSs that use the link b_i to connect to the gateway and denote by $\mathcal{U}_i$ the index set of UEs associated with BS_i such that $|\mathcal{U}_i| = M_i$. Every UE served by BS_i acquires an equal bandwidth of $\frac{2B_{\mathrm{a}}}{M_i}$. For a unlimited backhaul (UB) network, the following condition holds between the access sum rate for BS_i and the overall achievable rate of b_i:

$$\mathcal{R}_{\mathrm{b}_i} \geq \sum_{j \in \mathcal{L}_i} \mathcal{R}_{\mathrm{a}_j}. \tag{4.17}$$

where $\mathcal{R}_{\mathrm{a}_i}$ and $\mathcal{R}_{\mathrm{b}_i}$ are given by (3.18). This inequality holds for every single backhaul link in the ith branch.

For an N_{T}-tier super cell, the nth tier encompasses $\frac{6n}{n} = n$ BSs in each branch excluding the central BS, with each BS having a proprietary backhaul link. Therefore, the total number of BSs per branch excluding BS_0 is calculated by a partial summation:

$$N_{\mathrm{BS}} = \sum_{n=1}^{N_{\mathrm{T}}} n = \frac{N_{\mathrm{T}}\left(N_{\mathrm{T}}+1\right)}{2}. \tag{4.18}$$

In fact, (4.17) represents N_{BS} conditions for all $i \in \mathcal{T}_n$ such that $|\mathcal{T}_n| = n$ for $n = 1, 2, \ldots, N_{\mathrm{T}}$. Among them, the most challenging one to fulfil is when $i \in \mathcal{T}_1$, which requires sufficient capacity for b_i to respond to the aggregate sum rate of all N_{BS} BSs in the ith branch. However,

this is not always possible in realistic scenarios, in which case the limited capacity of b_i results in a backhaul bottleneck. The link between the gateway and the first tier is referred to as a *bottleneck backhaul link*, or simply a *bottleneck link*. Different from the first tier, satisfying the condition in (4.17) for higher tiers (i.e., for $n \geq 2$) is not challenging if the backhaul power is properly adjusted. This point is further clarified in Section 4.3. In this chapter, it is primarily assumed that there is a backhaul bottleneck that motivates the utilization of finite power and bandwidth resources of the bottleneck link.

4.2.2 Full Duplex Relaying

Full duplex relaying enables intermediate relays to transmit and receive simultaneously on the same frequency band. In wireless systems, a major challenge for full duplex communications is that the radio frequency (RF) transceiver is subject to self-interference because the strong signal generated by the transmit antenna in close proximity to the receive antenna severely degrades the received SINR. In multi-hop relaying systems, concurrent transmissions by relays lead to significant levels of interference due to the broadcasting nature of radio communications. A half duplex signaling protocol allows each relay to transmit only on its preallocated (time or frequency) resource slot to eliminate interference at the expense of a remarkable loss in spectral efficiency (SE). For the multi-hop wireless optical relaying system under consideration, half-duplex relaying results in an unnecessary misutilization of resources and hence relay BSs are permitted to operate in full duplex mode. Because of the narrow-beam and LOS propagation of light in the backhaul links: 1) at each relay, there is zero LOS interference from the backhaul transmitter to the backhaul receiver since they are installed on two opposite sides of the BS unit; 2) by using a sufficiently focused optical beam in the backhaul links, the cross-coupling interference among them is effectively canceled [30].

4.2.3 Bandwidth Sharing

For a multi-tier network, multiple signals intended for BSs in different tiers are transmitted via multi-hop backhaul links based on decode-and-forward (DF) relaying. For each branch of the backhaul network, the downlink data traffic for all N_{BS} BSs is carried by the corresponding bottleneck link. The use of DCO-OFDM in conjunction with DF relaying allows data multiplexing to be realized in the frequency domain. This way the bandwidth of the bottleneck link is divided into N_{BS} orthogonal sub-bands, with each sub-band allocated to an independent

data flow. After the symbols encapsulated in different sub-bands are individually and fully decoded at BS$_i$ in the first tier, they are reassembled into N_{BS} distinct groups. One group alone is modulated with a DCO-OFDM frame and directly retransmitted for the downlink of BS$_i$. The remaining $N_{\mathrm{BS}}-1$ groups are repackaged into separate DCO-OFDM frames and forwarded in their desired directions toward higher tiers.

For the kth branch of the network, orthogonal decomposition of the effective bandwidth $\xi_{\mathrm{b}}B_{\mathrm{b}}$ of the bottleneck link b_k into N_{BS} parts entails a weight coefficient of $\mu_i \in [0,1]$ satisfying $\sum_{i\in\mathcal{L}_k}\mu_i = 1$, thereby allocating a dedicated share of $\mu_i\xi_{\mathrm{b}}B_{\mathrm{b}}$ to BS$_i$ $\forall i \in \mathcal{L}_k$. In other words, the DCO-OFDM frame is fragmented into N_{BS} segments, with each one independently loaded with the downlink data for BS$_i$. Hence, the required signal processing to discriminate between different sub-bands is performed in the frequency domain by using the FFT of the received signal from b_k. Note that in Section 3.3, an equal bandwidth allocation is applied to the considered two-tier network so as to simplify bandwidth sharing. It helps to concentrate on the objectives of Chapter 3. Instead, the optimal design of μ_i for the generalized case of multi-tier networks is available in Section 4.4.

4.2.4 End-to-End Sum Rate

Recall from Section 3.2.3 that the end-to-end sum rate is defined as the sum of the achievable end-to-end rates of individual UEs. The derivation of the end-to-end sum rate follows similar steps as presented in Sections 3.2.3 and 3.3.3 for one-tier and two-tier networks, respectively. To extend the analysis for a multi-tier network, two key principles are used: 1) the end-to-end rate of each UE is predominated by the minimum allocated capacity over all intermediate hops based on the maximum flow–minimum cut theorem [108]; 2) bandwidth sharing introduces a loss factor of μ_i into the end-to-end SE of every UE for BS$_i$.

The signals intended for BSs in the nth tier need to traverse exactly n intermediate hops through backhaul links. The effective spectral efficiencies of all those n intermediate links are input to the $\min$ operator, among which the dominant term is merely posed by the bottleneck link since $0 \le \mu_i \le 1$. Therefore, for BS$_i$ in the nth tier for $n = 1, 2, \ldots, N_{\mathrm{T}}$, the end-to-end rate of the uth UE simplifies to:

$$\mathcal{R}_u = \frac{\xi_{\mathrm{a}}B_{\mathrm{a}}}{M_i}\min\left[\mu_i\zeta\log_2(1+\gamma_{\mathrm{b}_k}), \log_2(1+\gamma_u)\right],\ \forall u \in \mathcal{U}_i \tag{4.19}$$

where ζ is defined as follows:

$$\zeta = \frac{\xi_{\mathrm{b}} B_{\mathrm{b}}}{\xi_{\mathrm{a}} B_{\mathrm{a}}}. \tag{4.20}$$

In (4.19), the index of the bottleneck link is indicated by $k = \left\lfloor \frac{i-(3n-1)(n-1)}{n} \right\rfloor \ \forall i \in \mathcal{L}_k$. As a sanity check, for special cases of $n = 1$ and $n = 2$, this indicator returns $k = i$ and $k = \lfloor \frac{i-5}{2} \rfloor$, respectively, conforming with (3.45) and (3.47). The generalized end-to-end sum rate for BS_i in the nth tier becomes:

$$\mathcal{R}_i^{\mathrm{sum}} = \frac{\xi_{\mathrm{a}} B_{\mathrm{a}}}{M_i} \sum_{u \in \mathcal{U}_i} \min \left[\mu_i \zeta \log_2(1 + \gamma_{\mathrm{b}_k}), \log_2(1 + \gamma_u) \right], \ \forall i \in \mathcal{T}_n \tag{4.21}$$

The N_{BS} members of the kth branch in an N_{T}-tier super cell are identified by the index set:

$$\mathcal{L}_k = \bigcup_{n=1}^{N_{\mathrm{T}}} \mathcal{L}_{k,n}, \ \forall k \in \mathcal{T}_1 \tag{4.22}$$

where $\mathcal{L}_{k,n}$ is a subset of $\mathcal{L}_k$ that enumerates the indexes of BSs involved in the nth tier of the kth branch according to:

$$\mathcal{L}_{k,n} = \{ nk + 3n(n-1) - j |\ j = 0, 1, \ldots, n-1 \}. \tag{4.23}$$

For instance, consider a two-tier super cell, then for $k = 1$, (4.23) reduces to $\mathcal{L}_1 = \{1\} \cup \{7, 8\} = \{1, 7, 8\}$. In a similar way, for the first branch of a three-tier super cell, (4.23) yields $\mathcal{L}_1 = \{1\} \cup \{7, 8\} \cup \{19, 20, 21\} = \{1, 7, 8, 19, 20, 21\}$. These cases are verified by Fig. 4.1.

4.3 Opportunistic Power Control

As discussed in Section 3.4, the primary incentive to minimize the optical power of the backhaul light emitting diodes (LEDs) is that they are not intended to provide illumination for the environment. This opportunity is exploited to establish a power optimization framework with the aim to reach a balance for the power efficiency (PE) of the backhaul system while maintaining the desired sum rate performance. In this section, two main categories of power control schemes are put forward: APC and FPC. With APC, as its name implies, the backhaul power is variably changed in proportion to the current channel conditions in the access system. Alternatively, in FPC, the transmission power in the backhaul branch is fixed at a desired operating point. In Section 3.4, the problem formulation relies upon the maximum downlink SINR to

avoid the need for collecting the instantaneous channel information of all UEs. In fact, such a criterion is required to deal with the backhaul interference effect. Nonetheless, the peak SINR is not the only criterion that could be defined especially when using a narrow light beam in the backhaul links, in which case the backhaul interference is not present. This particularly renders the power control problem more tractable for multi-tier networks. In the following, two more criteria are proposed to fix the backhaul power: the first one is based on the average downlink data rate and the second one uses the average downlink SINR.

4.3.1 Proposed Schemes

4.3.1.1 Adaptive Power Control (APC)

The transmission power of the backhaul system is adaptively adjusted according to the sum rates in the access system. To this end, the condition in (4.17) can be expressed in terms of the power control coefficient K_i:

$$K_i \geq \frac{\exp\left(\frac{\ln 2}{\xi_{\mathrm{b}} B_{\mathrm{b}}} \sum_{j \in \mathcal{L}_i} \mathcal{R}_{\mathrm{a}_j}\right) - 1}{\gamma_{\mathrm{b}}}. \tag{4.24}$$

For each branch of the backhaul network, the corresponding feasible set is defined by (4.24) through the system of inequalities for all the N_{BS} BSs. Based on the boundary of the feasible set, the minimum values of K_i, denoted by $K_{i,\min}$, are derived as:

$$K_{i,\min} = \frac{\exp\left(\zeta^{-1} \sum_{j \in \mathcal{L}_i} \frac{1}{M_j} \sum_{u \in \mathcal{U}_j} \ln\left(1 + \gamma_u\right)\right) - 1}{\gamma_{\mathrm{b}}}. \tag{4.25}$$

4.3.1.2 Fixed Power Control (FPC)

The transmission power of the backhaul system once designed is fixed for the entire network. Two criteria are identified for this purpose. The first criterion is to allocate power so as to satisfy the statistical average of the achievable rate for the access system over the area covered by each attocell. The second criterion takes into account the achievable rate corresponding to the statistical average of the downlink SINR over the area covered by each attocell. The resulting power control schemes are referred to as FPC1 and FPC2, respectively, and the corresponding power control coefficients are given in the following.

The average data rate of the access system is required for FPC1. This is provided in Lemma 1. The optimal power ratio for FPC1 is subsequently derived in Proposition 4.

Lemma 1. *The average achievable rate per attocell for an arbitrary number of UEs is calculated by:*

$$\bar{\mathcal{R}}_{\mathrm{a}} = \frac{\mathcal{R}_{\min} + \mathcal{R}_{\max}}{2} + \frac{2\xi_{\mathrm{a}} B_{\mathrm{a}}}{\pi R_{\mathrm{e}}^2 \ln 2} \int_{\gamma_{\min}}^{\gamma_{\max}} \int_{0}^{R_{\mathrm{e}}} \frac{\arcsin^{\dagger}\left(\mathcal{Z}(r,\gamma)\right) r}{1+\gamma} dr d\gamma. \tag{4.26}$$

Proof. By using (3.18a), the average achievable rate for the attocell of BS_i is given by:

$$\mathbb{E}\left[\mathcal{R}_{\mathrm{a}_i}\right] = \frac{\xi_{\mathrm{a}} B_{\mathrm{a}}}{M_i} \sum_{u \in \mathcal{U}_i} \mathbb{E}\left[\log_2(1+\gamma_u)\right], \tag{4.27a}$$

$$= \xi_{\mathrm{a}} B_{\mathrm{a}}\, \mathbb{E}\left[\log_2(1+\gamma_u)\right], \tag{4.27b}$$

where the second equality is deduced from the fact that $\gamma_u \ \forall u \in \mathcal{U}_i$ are independent and identically distributed (i.i.d.), resulting in $\mathbb{E}\left[\mathcal{R}_{\mathrm{a}_i}\right] = \bar{\mathcal{R}}_{\mathrm{a}} \ \forall i$. For a bounded random variable X such that $x_{\min} \leq X \leq x_{\min}$, the mean of X is related to its complementary cumulative distribution function (CCDF) via:

$$\mathbb{E}[X] = x_{\min} + \int_{x_{\min}}^{x_{\max}} \mathbb{P}[X > x] dx. \tag{4.28}$$

By using the CDF of γ_u in (4.13), the expectation in (4.27b) is therefore expanded as follows:

$$\bar{\mathcal{R}}_{\mathrm{a}} = \mathcal{R}_{\min} + \underbrace{\int_{\mathcal{R}_{\min}}^{\mathcal{R}_{\max}} \mathbb{P}\left[\xi_{\mathrm{a}} B_{\mathrm{a}} \log_2(1+\gamma_u) > x\right] dx}_{I_1}, \tag{4.29}$$

where:

$$I_1 = \frac{\xi_{\mathrm{a}} B_{\mathrm{a}}}{\ln 2} \int_{\gamma_{\min}}^{\gamma_{\max}} \mathbb{P}\left[\gamma_u > \gamma\right] \frac{d\gamma}{1+\gamma}, \tag{4.30a}$$

$$= \frac{\xi_{\mathrm{a}} B_{\mathrm{a}}}{\ln 2} \int_{\gamma_{\min}}^{\gamma_{\max}} \left(1 - \mathbb{P}\left[\gamma_u \leq \gamma\right]\right) \frac{d\gamma}{1+\gamma}, \tag{4.30b}$$

$$= \frac{\xi_{\mathrm{a}} B_{\mathrm{a}}}{\ln 2} \int_{\gamma_{\min}}^{\gamma_{\max}} \left[\frac{1}{2} + \frac{2}{\pi R_{\mathrm{e}}^2} \int_0^{R_{\mathrm{e}}} \arcsin^{\dagger}\left(\mathcal{Z}(r,\gamma)\right) r dr\right] \frac{d\gamma}{1+\gamma}, \tag{4.30c}$$

$$= \frac{\mathcal{R}_{\max} - \mathcal{R}_{\min}}{2} + \frac{2\xi_{\mathrm{a}} B_{\mathrm{a}}}{\pi R_{\mathrm{e}}^2 \ln 2} \int_{\gamma_{\min}}^{\gamma_{\max}} \int_0^{R_{\mathrm{e}}} \frac{\arcsin^{\dagger}\left(\mathcal{Z}(r,\gamma)\right) r}{1+\gamma} dr d\gamma, \tag{4.30d}$$

where the change of variable $x = \xi_{\mathrm{a}} B_{\mathrm{a}} \log_2(1+\gamma)$ is applied in (4.30a), which maintains the inequality under a probability measure as the logarithm is a monotonically increasing function. The last result in (4.30d) is derived by using:

$$\frac{\xi_{\mathrm{a}} B_{\mathrm{a}}}{\ln 2} \int_{\gamma_{\min}}^{\gamma_{\max}} \frac{d\gamma}{1+\gamma} = \frac{\xi_{\mathrm{a}} B_{\mathrm{a}}}{2 \ln 2} \ln\left(\frac{1+\gamma_{\max}}{1+\gamma_{\min}}\right) = \frac{\mathcal{R}_{\max} - \mathcal{R}_{\min}}{2}. \tag{4.31}$$

Replacing I_1 in (4.29) by (4.30d) and simplifying leads to (4.26). ■

Proposition 4. *The minimum power control coefficient for b_i based on FPC1 is given by:*

$$K_{i,\min} = \frac{\exp\left(\frac{\ln 2}{\xi_{\mathrm{b}} B_{\mathrm{b}}} |\mathcal{L}_i| \bar{\mathcal{R}}_{\mathrm{a}}\right) - 1}{\gamma_{\mathrm{b}}}, \tag{4.32}$$

where $\bar{\mathcal{R}}_{\mathrm{a}}$ is the average achievable rate over an attocell, and it is given by Lemma 1.

Proof. According to FPC1, the right hand side (RHS) of (4.17) needs to be modified as follows:

$$\xi_{\mathrm{b}} B_{\mathrm{b}} \log_2(1 + K_i \gamma_{\mathrm{b}}) \geq \mathbb{E}\left[\sum_{j \in \mathcal{L}_i} \mathcal{R}_{\mathrm{a}_j}\right], \tag{4.33}$$

where:

$$\mathbb{E}\left[\sum_{j \in \mathcal{L}_i} \mathcal{R}_{\mathrm{a}_j}\right] = \sum_{j \in \mathcal{L}_i} \mathbb{E}\left[\mathcal{R}_{\mathrm{a}_j}\right] = |\mathcal{L}_i| \bar{\mathcal{R}}_{\mathrm{a}}. \tag{4.34}$$

Combining (4.33) with (4.34) and rearranging the inequality in terms of K_i gives:

$$K_i \geq \frac{\exp\left(\frac{\ln 2}{\xi_{\mathrm{b}} B_{\mathrm{b}}} |\mathcal{L}_i| \bar{\mathcal{R}}_{\mathrm{a}}\right) - 1}{\gamma_{\mathrm{b}}}. \tag{4.35}$$

The RHS of (4.35) represents the minimum allowed value of K_i as denoted by $K_{i,\min}$ in (4.32) and hence the proof is complete. ■

The average SINR of the access system is needed for FPC2. This is given by Lemma 2. The optimal power ratio for FPC2 is then derived in Proposition 5.

Lemma 2. *The average downlink SINR is calculated by:*

$$\bar{\gamma}_{\mathrm{a}} = \frac{\gamma_{\min} + \gamma_{\max}}{2} + \frac{2}{\pi R_{\mathrm{e}}^2} \int_{\gamma_{\min}}^{\gamma_{\max}} \int_{0}^{R_{\mathrm{e}}} \arcsin^{\dagger}\left(\mathcal{Z}(r,\gamma)\right) r dr d\gamma. \tag{4.36}$$

Proof. Note that different UEs reach the same average achievable rate due to the fact that γ_u $\forall u$ are i.i.d. random variables. By using (4.28), the average downlink SINR is derived as:

$$\bar{\gamma}_{\mathrm{a}} = \gamma_{\min} + \underbrace{\int_{\gamma_{\min}}^{\gamma_{\max}} \mathbb{P}\left[\gamma_u > x\right] dx}_{I_2}. \tag{4.37}$$

Referring to the CDF of γ_u in (4.13), I_2 is evaluated as follows:

$$I_2 = \int_{\gamma_{\min}}^{\gamma_{\max}} \left(1 - \mathbb{P}\left[\gamma_u \leq \gamma\right]\right) d\gamma, \tag{4.38a}$$

$$= \int_{\gamma_{\min}}^{\gamma_{\max}} \left[\frac{1}{2} + \frac{2}{\pi R_{\mathrm{e}}^2} \int_{0}^{R_{\mathrm{e}}} \arcsin^{\dagger}\left(\mathcal{Z}(r,\gamma)\right) r dr\right] d\gamma, \tag{4.38b}$$

$$= \frac{\gamma_{\max} - \gamma_{\min}}{2} + \frac{2}{\pi R_{\mathrm{e}}^2} \int_{\gamma_{\min}}^{\gamma_{\max}} \int_{0}^{R_{\mathrm{e}}} \arcsin^{\dagger}\left(\mathcal{Z}(r,\gamma)\right) r dr d\gamma. \tag{4.38c}$$

Substituting I_2 in (4.37) with (4.38c) results in (4.36). ■

Proposition 5. *The minimum power control coefficient for b_i based on FPC2 is given by:*

$$K_{i,\min} = \frac{\left(1 + \bar{\gamma}_{\mathrm{a}}\right)^{\zeta^{-1}|\mathcal{L}_i|} - 1}{\gamma_{\mathrm{b}}}, \tag{4.39}$$

where $\bar{\gamma}_{\mathrm{a}}$ is the average downlink SINR given by Lemma 2.

Proof. In the case of FPC2, the inequality in (4.17) changes to:

$$\xi_{\mathrm{b}} B_{\mathrm{b}} \log_2(1 + K_i \gamma_{\mathrm{b}}) \geq \sum_{j \in \mathcal{L}_i} \xi_{\mathrm{a}} B_{\mathrm{a}} \log_2(1 + \mathbb{E}[\gamma_u]), \tag{4.40}$$

where $\mathbb{E}[\gamma_u] = \bar{\gamma}_{\mathrm{a}}$. It immediately follows that:

$$K_i \geq \frac{(1 + \bar{\gamma}_{\mathrm{a}})^{\zeta^{-1}|\mathcal{L}_i|} - 1}{\gamma_{\mathrm{b}}}. \tag{4.41}$$

The RHS of (4.41) is, in fact, the minimum value that K_i can take and this is denoted by $K_{i,\min}$ in (4.39), concluding the proof. ■

In Proposition 4 and Proposition 5, note that $|\mathcal{L}_i| = N_{\mathrm{BS}}$ when $i \in \mathcal{T}_1$, i.e., for bottleneck links.

4.3.2 Probability of Backhaul Bottleneck Occurrence

To gain insight into the performance of the power control schemes, a metric called BBO is defined as follows.

Definition 1. *The BBO is a metric to measure the probability that the aggregate sum rate of the access system in a backhaul branch exceeds the capacity of the corresponding bottleneck link. Equivalently, it evaluates the probability that the condition in* (4.17) *is violated.*

Mathematically, the BBO probability for the kth branch, for a given $k \in \mathcal{T}_1$, is expressed by:

$$\mathcal{P}_{\mathrm{BBO}} = \mathbb{P}\left[\sum_{i \in \mathcal{L}_k} \mathcal{R}_{\mathrm{a}_i} > \mathcal{R}_{\mathrm{b}_k}\right], \tag{4.42}$$

where $\mathcal{R}_{\mathrm{a}_i}$ is a random variable that depends on the statistics of γ_u. There is no exact closed form solution in terms of ordinary functions for the probability in (4.42). Instead, a simple but tight analytical approximation is established in Theorem 2 with the aid of Lemma 3.

In fact, according to (3.18a), $\mathcal{R}_{\mathrm{a}_i} = \frac{1}{M_i} \sum_{u \in \mathcal{U}_i} \mathcal{R}_{\mathrm{a}}(\gamma_u)$ where $\mathcal{R}_{\mathrm{a}}(\gamma_u) = \xi_{\mathrm{a}} B_{\mathrm{a}} \log_2(1+\gamma_u)$ are M_i i.i.d. random variables. Note that $\mathcal{R}_{\mathrm{a}}(\gamma_u)$ is bounded such that $\mathcal{R}_{\min} \leq \mathcal{R}_{\mathrm{a}}(\gamma_u) \leq \mathcal{R}_{\max}$ where $\mathcal{R}_{\min} = \xi_{\mathrm{a}} B_{\mathrm{a}} \log_2(1 + \gamma_{\min})$ and $\mathcal{R}_{\max} = \xi_{\mathrm{a}} B_{\mathrm{a}} \log_2(1 + \gamma_{\max})$, and $\gamma_{\min}$ and $\gamma_{\max}$ are

available in closed form in (4.15). The mean of $\mathcal{R}_{\mathrm{a}}(\gamma_u)$ is readily given by $\mathbb{E}\left[\mathcal{R}_{\mathrm{a}}(\gamma_u)\right] = \bar{\mathcal{R}}_{\mathrm{a}}$ based on Lemma 1. The variance of $\mathcal{R}_{\mathrm{a}}(\gamma_u)$ is determined by Lemma 3.

Lemma 3. *The variance of $\mathcal{R}_{\mathrm{a}}(\gamma_u)$ is given by:*

$$\sigma^2_{\mathcal{R}_{\mathrm{a}}} = \mathbb{E}\big[\mathcal{R}^2_{\mathrm{a}}(\gamma_u)\big] - \mathbb{E}^2[\mathcal{R}_{\mathrm{a}}(\gamma_u)], \tag{4.43}$$

where:

$$\mathbb{E}\big[\mathcal{R}^2_{\mathrm{a}}(\gamma_u)\big] = \frac{\mathcal{R}^2_{\min} + \mathcal{R}^2_{\max}}{2} + \frac{1}{\pi}\left(\frac{2\xi_{\mathrm{a}} B_{\mathrm{a}}}{R_{\mathrm{e}} \ln 2}\right)^2 \int_{\gamma_{\min}}^{\gamma_{\max}} \int_{0}^{R_{\mathrm{e}}} \frac{\ln(1+\gamma)}{1+\gamma} \arcsin^{\dagger}\left(\mathcal{Z}(r,\gamma)\right) r dr d\gamma. \tag{4.44}$$

Proof. For a bounded random variable X given $x_{\min} \leq X \leq x_{\min}$, the second order moment of X is characterized by means of its CCDF using:

$$\mathbb{E}\big[X^2\big] = x^2_{\min} + \int_{x_{\min}}^{x_{\max}} 2x\mathbb{P}[X > x] dx.$$

Therefore:

$$\mathbb{E}\big[\mathcal{R}^2_{\mathrm{a}}(\gamma_u)\big] = \mathcal{R}^2_{\min} + \underbrace{\int_{\mathcal{R}_{\min}}^{\mathcal{R}_{\max}} 2x\mathbb{P}\left[\mathcal{R}_{\mathrm{a}}(\gamma_u) > x\right] dx}_{I_3}. \tag{4.45}$$

By applying the CDF of γ_u from (4.13), I_3 is derived with the following steps:

$$I_3 = 2\left(\frac{\xi_{\mathrm{a}} B_{\mathrm{a}}}{\ln 2}\right)^2 \int_{\gamma_{\min}}^{\gamma_{\min}} \frac{\ln(1+\gamma)}{1+\gamma} \mathbb{P}\left[\gamma_u > \gamma\right] d\gamma, \tag{4.46a}$$

$$= 2\left(\frac{\xi_{\mathrm{a}} B_{\mathrm{a}}}{\ln 2}\right)^2 \int_{\gamma_{\min}}^{\gamma_{\min}} \frac{\ln(1+\gamma)}{1+\gamma} \left(1 - \mathbb{P}\left[\gamma_u \leq \gamma\right]\right) d\gamma, \tag{4.46b}$$

$$= 2\left(\frac{\xi_{\mathrm{a}} B_{\mathrm{a}}}{\ln 2}\right)^2 \int_{\gamma_{\min}}^{\gamma_{\min}} \frac{\ln(1+\gamma)}{1+\gamma} \left[\frac{1}{2} + \frac{2}{\pi R^2_{\mathrm{e}}} \int_{0}^{R_{\mathrm{e}}} \arcsin^{\dagger}\left(\mathcal{Z}(r,\gamma)\right) r dr\right] d\gamma, \tag{4.46c}$$

$$= \frac{\mathcal{R}^2_{\max} - \mathcal{R}^2_{\min}}{2} + \frac{1}{\pi}\left(\frac{2\xi_{\mathrm{a}} B_{\mathrm{a}}}{R_{\mathrm{e}} \ln 2}\right)^2 \int_{\gamma_{\min}}^{\gamma_{\max}} \int_{0}^{R_{\mathrm{e}}} \frac{\ln(1+\gamma)}{1+\gamma} \arcsin^{\dagger}\left(\mathcal{Z}(r,\gamma)\right) r dr d\gamma, \tag{4.46d}$$

where the substitution $x = \xi_{\mathrm{a}} B_{\mathrm{a}} \log_2(1+\gamma)$ is used to arrive at (4.46a); and the last result in

(4.46d) is obtained through the use of:

$$\left(\frac{\xi_{\mathrm{a}}B_{\mathrm{a}}}{\ln 2}\right)^2 \int_{\gamma_{\min}}^{\gamma_{\min}} \frac{\ln(1+\gamma)}{1+\gamma} d\gamma = \left(\frac{\xi_{\mathrm{a}}B_{\mathrm{a}}}{\ln 2}\right)^2 \frac{\ln^2(1+\gamma_{\max}) - \ln^2(1+\gamma_{\min})}{2} = \frac{\mathcal{R}_{\max}^2 - \mathcal{R}_{\min}^2}{2}. \tag{4.47}$$

By substituting (4.46d) for I_3 in (4.45), the desired result of (4.44) is obtained. ■

The approximation of the BBO probability in (4.42) is given by Theorem 2.

Theorem 2. *For the kth backhaul branch with M UEs uniformly distributed over the total area covered by N_{BS} BSs, the BBO probability is tightly approximated by:*

$$\mathcal{P}_{\mathrm{BBO}} \approx \mathrm{Q}\left(\frac{\mathcal{R}_{\mathrm{b}_k} - N_{\mathrm{BS}}\bar{\mathcal{R}}_{\mathrm{a}}}{\frac{N_{\mathrm{BS}}}{\sqrt{M}}\sigma_{\mathcal{R}_{\mathrm{a}}}}\right), \tag{4.48}$$

where $\mathcal{R}_{\mathrm{b}_k}$ and $\bar{\mathcal{R}}_{\mathrm{a}}$ are given by (3.18b) *and Lemma 1, respectively; and $\sigma_{\mathcal{R}_{\mathrm{a}}}$ is the standard deviation of $\mathcal{R}_{\mathrm{a}}(\gamma_u)$ whose variance is identified in Lemma 3.*

Proof. Let the vector $\mathbf{M} = [M_i]_{N_{\mathrm{BS}}\times 1}$ be composed of the random numbers of UEs in individual attocells for the ith branch. Provided that the total number of UEs is fixed at $\sum_{i\in\mathcal{L}_k} M_i = M$, $\mathbf{M}$ follows a multinomial distribution with the probability mass function (PMF) [111]:

$$\mathbb{P}\left[\mathbf{M}=\mathbf{m}\right] = \frac{M!}{\prod_{i\in\mathcal{L}_k} m_i!} \prod_{i\in\mathcal{L}_k} p_i^{m_i} = \frac{M!\, N_{\mathrm{BS}}^{-M}}{\prod_{i\in\mathcal{L}_k} m_i!}, \tag{4.49}$$

where $\mathbf{m} = [m_i]_{N_{\mathrm{BS}}\times 1}$; and p_i is the probability of the event $\{M_i = m_i\}$. The second equality is because every UE has an equal chance to fall within any attocell, and hence $p_i = \frac{1}{N_{\mathrm{BS}}}$ $\forall i \in \mathcal{L}_k$. Based on the law of total probability, (4.42) is expanded as follows:

$$\mathcal{P}_{\mathrm{BBO}} = \mathbb{P}\left[\sum_{i\in\mathcal{L}_k} \frac{1}{M_i} \sum_{u\in\mathcal{U}_i} \mathcal{R}_{\mathrm{a}}(\gamma_u) > \mathcal{R}_{\mathrm{b}_k}\right], \tag{4.50a}$$

$$= \sum_{\mathbf{1}^T\mathbf{m}=M} \mathbb{P}\left[\mathbf{M}=\mathbf{m}\right] \mathbb{P}\left[\sum_{i\in\mathcal{L}_k} \frac{1}{M_i} \sum_{u\in\mathcal{U}_i} \mathcal{R}_{\mathrm{a}}(\gamma_u) > \mathcal{R}_{\mathrm{b}_k} \middle| \mathbf{M}=\mathbf{m}\right], \tag{4.50b}$$

where $\mathbf{1}^T\mathbf{m} = \sum_{i\in\mathcal{L}_k} m_i$. From the multinomial theorem, the number of summands in the RHS of (4.50b) is $\binom{M+N_{\mathrm{BS}}-1}{N_{\mathrm{BS}}-1}$ which can potentially be large depending on the values of M and N_{BS}. The argument of the conditional probability involves positive weights which encompass

the reciprocals of the numbers of UEs in each attocell. An appropriate approximation can be readily derived for this sum by means of minimizing the mean square error (MSE). This is presented in Lemma 4.

Lemma 4. *For a given distribution of UEs over individual attocells, i.e., for* $\mathbf{M} = \mathbf{m}$*, the summation under the conditional probability in* (4.50b) *is approximated based on the minimum mean square error (MMSE) criterion as follows:*

$$\sum_{i\in\mathcal{L}_k} \frac{1}{m_i} \sum_{u\in\mathcal{U}_i} \mathcal{R}_{\mathrm{a}}(\gamma_u) \approx \frac{N_{\mathrm{BS}}}{M} \sum_{i\in\mathcal{L}_k} \sum_{u\in\mathcal{U}_i} \mathcal{R}_{\mathrm{a}}(\gamma_u). \tag{4.51}$$

Proof. See Appendix F. ■

The expression $\sum_{i\in\mathcal{L}_k} \sum_{u\in\mathcal{U}_i} \mathcal{R}_{\mathrm{a}}(\gamma_u)$ appearing in (4.51) is independent of the random vector $\mathbf{M}$. In fact, this is a sum of M i.i.d. random variables $\mathcal{R}_{\mathrm{a}}(\gamma_u)$, the mean and variance of which are known according to Lemma 1 and Lemma 3, respectively. For a sufficiently large value of M, the distribution of this sum converges to Gaussian based on the central limit theorem (CLT). Therefore, for the RHS of (4.51), the following approximation is deduced:

$$\frac{N_{\mathrm{BS}}}{M} \sum_{i\in\mathcal{L}_k} \sum_{u\in\mathcal{U}_i} \mathcal{R}_{\mathrm{a}}(\gamma_u) \approx \mathcal{N}\left(N_{\mathrm{BS}}\bar{\mathcal{R}}_{\mathrm{a}}, \frac{N_{\mathrm{BS}}^2}{M}\sigma_{\mathcal{R}_{\mathrm{a}}}^2\right). \tag{4.52}$$

Combining (4.52) with (4.51), substituting the result into (4.50b) and evaluating the conditional probability gives rise to:

$$\mathcal{P}_{\mathrm{BBO}} \approx \sum_{\mathbf{1}^T\mathbf{m}=M} \mathbb{P}\left[\mathbf{M}=\mathbf{m}\right] \mathbb{P}\left[\frac{N_{\mathrm{BS}}}{M} \sum_{i\in\mathcal{L}_k} \sum_{u\in\mathcal{U}_i} \mathcal{R}_{\mathrm{a}}(\gamma_u) > \mathcal{R}_{\mathrm{b}_k}\right], \tag{4.53a}$$

$$\approx \mathbb{P}\left[\mathcal{N}\left(N_{\mathrm{BS}}\bar{\mathcal{R}}_{\mathrm{a}}, \frac{N_{\mathrm{BS}}^2}{M}\sigma_{\mathcal{R}_{\mathrm{a}}}^2\right) > \mathcal{R}_{\mathrm{b}_k}\right], \tag{4.53b}$$

$$= \mathrm{Q}\left(\frac{\mathcal{R}_{\mathrm{b}_k} - N_{\mathrm{BS}}\bar{\mathcal{R}}_{\mathrm{a}}}{\frac{N_{\mathrm{BS}}}{\sqrt{M}}\sigma_{\mathcal{R}_{\mathrm{a}}}}\right), \tag{4.53c}$$

where (4.53b) is deduced from (4.53a) since the probability under the summation is independent of the summation index, and the PMF sums to one. Hence, the proof is complete. ■

Configuration I	Configuration II
$\Phi_{\mathrm{a}} = 40^{\circ}$	$\Phi_{\mathrm{a}} = 60^{\circ}$
$R = 2.5$ m	$R = 3.1$ m

Table 4.1: *Attocell Configurations*

4.3.3 Illustrative Numerical Examples

This section presents a number of case studies to evaluate the performance of the proposed power control schemes. Monte-Carlo simulations are conducted using a large number of random realizations for distributing multiple UEs uniformly over the network. For numerical evaluations, the system parameters listed in Table 3.1 are used, unless otherwise stated. To gain more insight into the potential gains offered by different power control schemes, the ratio of the total backhaul power with power control to that without power control is considered as a metric in addition to the BBO probability. This metric is referred to as RTP which is defined as the normalized sum of the backhaul power for one branch of the super cell. For the kth branch of a super cell with N_{T} tiers, the RTP is mathematically defined as follows:

$$\mathrm{RTP} = \frac{\sum_{i \in \mathcal{L}_k} P_{\mathrm{b}_i}}{N_{\mathrm{BS}} P_{\mathrm{a}}} = \frac{1}{N_{\mathrm{BS}}} \sum_{i \in \mathcal{L}_k} K_i. \tag{4.54}$$

4.3.3.1 Power Control Coefficients

First, the range of variations of the power control coefficients is studied. To this end, two attocell configurations are considered based on the guidelines provided in [16]. The two configurations with different cell radius and downlink LED semi-angle are given in Table 4.1. Without loss of generality, the following results are presented with a focus on the first branch of the super cell.

Under the APC scheme, according to (4.25), $K_{1,\min}$ is a random variable that varies with the distribution of UEs. Fig. 4.2 shows the CDF of $K_{1,\min}$ as a function of the total number of tiers for both configurations and for different values of the bandwidth of the backhaul system. In this experiment, the total number of UEs is fixed at $M = 30$. First of all, it can be observed that in all four cases, an increase in the total number of tiers leads to a rise in the value of $K_{1,\min}$, as the CDF curves are shifted to the right. The reason for this is that adding more tiers increases the chance for UEs to be distributed in a larger number of attocells, and $K_{1,\min}$ is an increasing function of the number of active (i.e., non-empty) attocells. Furthermore, it can be seen that by

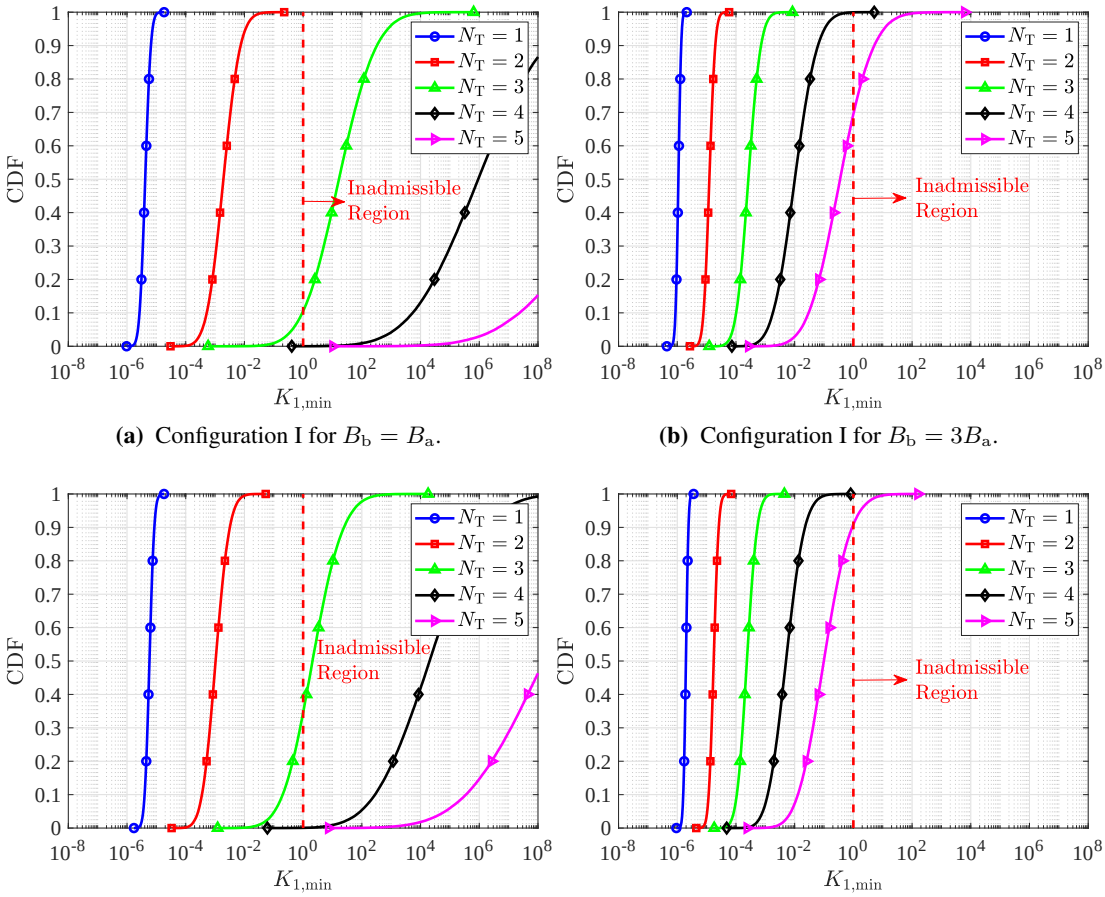

(a) Configuration I for $B_b = B_a$.

(b) Configuration I for $B_b = 3B_a$.

(c) Configuration II for $B_b = B_a$.

(d) Configuration II for $B_b = 3B_a$.

Figure 4.2: *The statistics of $K_{1,\min}$ under the APC scheme as a function of the total number of tiers for $M = 30$.*

increasing B_b from 1 to 3 in either configuration, the value of $K_{1,\min}$ is significantly reduced, which can be attributed to the presence of the backhaul SNR γ_b in the denominator of $K_{1,\min}$. For a three-tier super cell, the statistics of $K_{1,\min}$ under the APC scheme are plotted in Fig. 4.3 with different values of the total number of UEs. It is observed that increasing the number of UEs causes the slope of the CDF curves to increase, thus the variance of $K_{1,\min}$ is decreased.

In the case of FPC, the power control coefficients are given by Proposition 4 and Proposition 5 for FPC1 and FPC2, respectively. The range of values of $K_{1,\min}$ for the FPC1 and FPC2 cases are illustrated in Fig. 4.4. Similar to the APC case, by increasing the backhaul bandwidth, the overall level of $K_{1,\min}$ is lowered in both cases. This is derived from the power-bandwidth tradeoff, implying that for the same backhaul capacity, enlarging the bandwidth leads to less power requirement. Also, for a given value of N_T, the value of $K_{1,\min}$ corresponding to FPC1

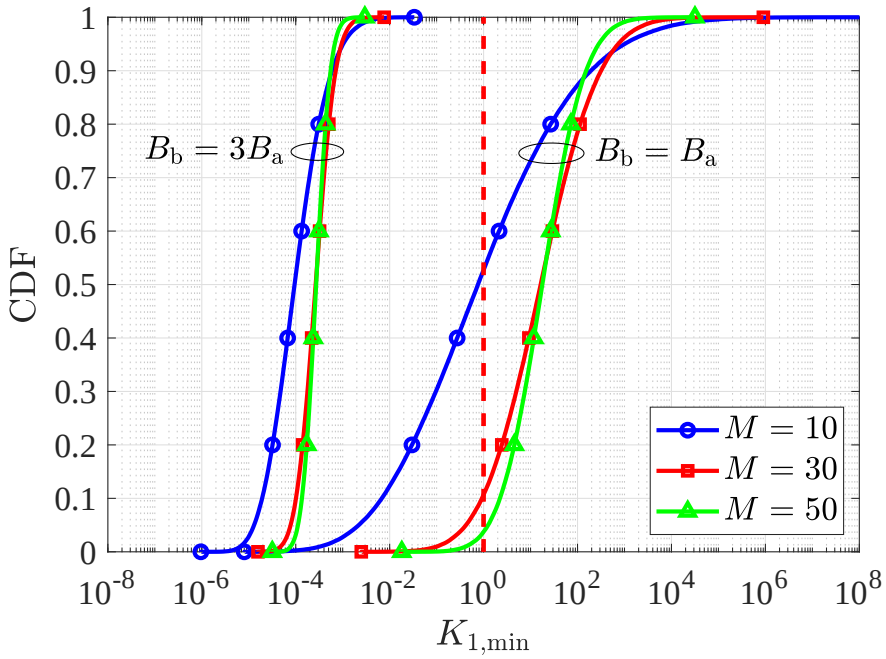

(a) Configuration I.

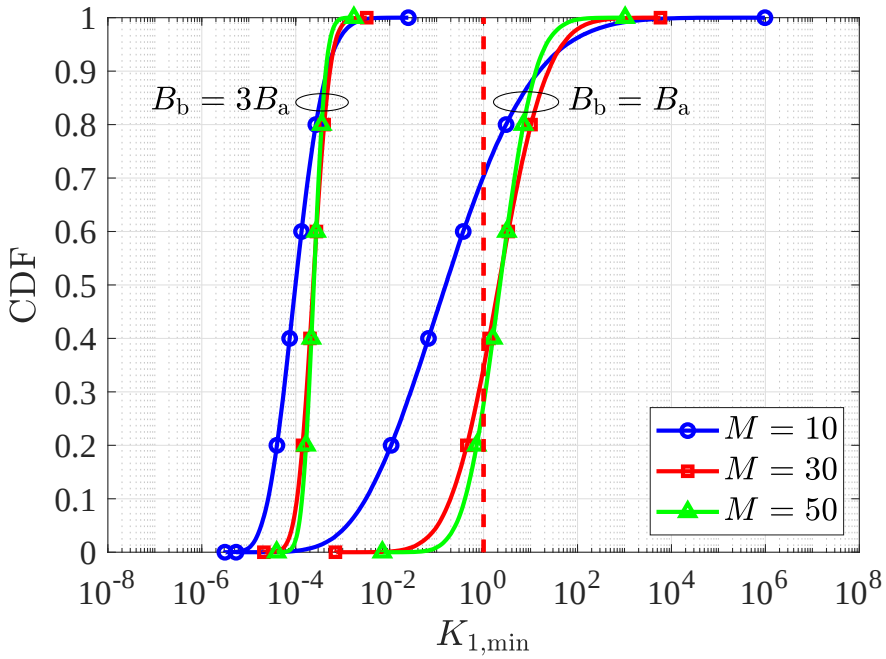

(b) Configuration II.

Figure 4.3: *The statistics of $K_{1,\min}$ under the APC scheme for a three-tier super cell with different values of the total number of UEs.*

is lower than that of FPC2, which indicates that FPC1 generally sets a lower backhaul power.

For both APC and FPC schemes, the power control coefficients rise continuously with increase

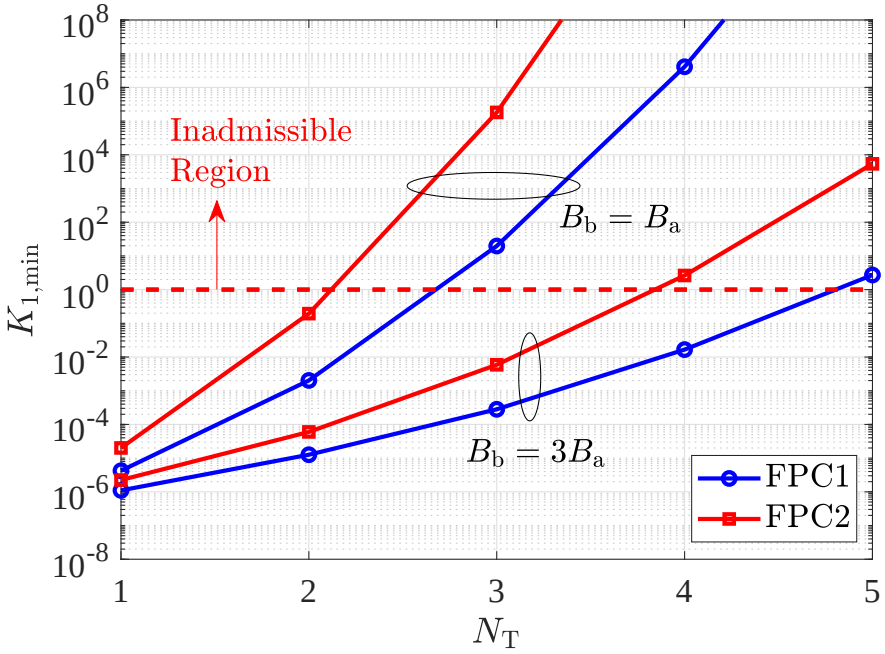

(a) Configuration I.

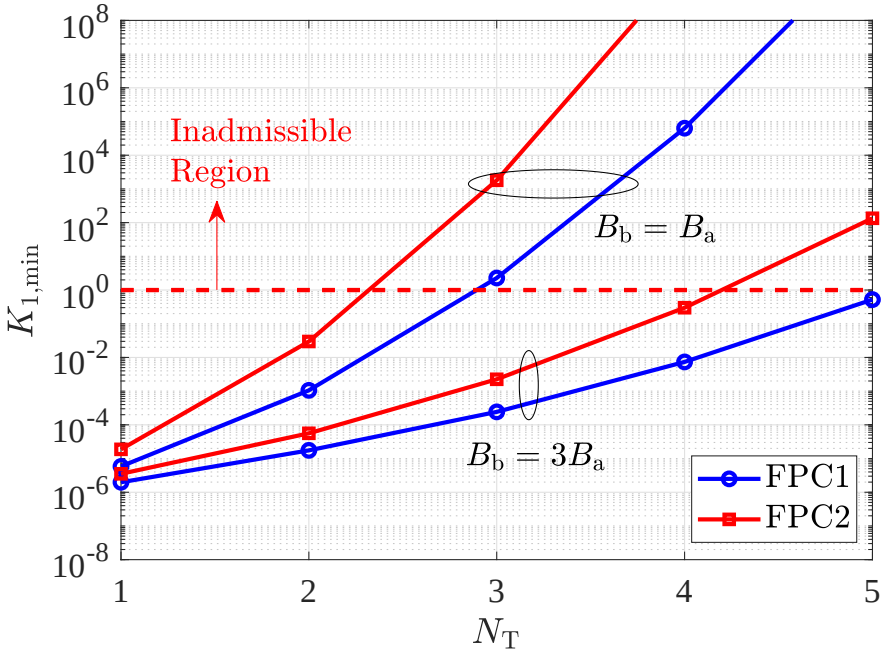

(b) Configuration II.

Figure 4.4: $K_{1,\min}$ *under FPC1 and FPC2 schemes as a function of the total number of tiers.*

in N_T, as observed from Figs. 4.2, 4.3 and 4.4. However, they are not allowed to be increased unboundedly due to practical limitations imposed by the maximum permissible optical power of backhaul LEDs. To set an upper limit for the transmission power of the backhaul system,

its counterpart from the access system, P_{a}, is used, as the access system operates with full power to comply with the illumination requirement. Note that the maximum allowable backhaul power could be an independent variable to model the practical specification of backhaul LEDs. Despite this possibility, setting a value equal to the power used in the access system simplifies the presentation of results, though it does not influence the generality of the power control analysis. That is the reason why a unit threshold is defined and represented using a dashed red line in Figs. 4.2, 4.3 and 4.4. This is the point where the backhaul transmission power computed by the power control schemes is not allowed to exceed that of the access system. It exerts a unit threshold constraint on $K_{1,\min}$, resulting in:

$$K^*_{1,\min} = \min[K_{1,\min}, 1]. \tag{4.55}$$

Such a threshold is not a physical limitation, but rather a chosen constraint. It is also adopted as a design consideration for two-tier full reuse visible light (FR-VL) and IR backhaul networks as discussed in Section 3.4.

The FPC coefficients are defined based on the analytical expressions of the average rate and the average SINR of the access system, which are separately derived in Lemma 1 and Lemma 1. For completeness, the average rate and the average SINR expressions are verified by simulations. To this end, the statistical mean of the access rate $\mathcal{R}_{\mathrm{a}} = \xi_{\mathrm{a}} B_{\mathrm{a}} \log_2(1+\gamma_u)$ is computed by Monte Carlo averaging over a large number of random realizations for distributing the UE coordinates in a single attocell. The resulting $\mathbb{E}\left[\mathcal{R}_{\mathrm{a}}\right]$ is compared to the analytical average as obtained by evaluating $\bar{\mathcal{R}}_{\mathrm{a}}$ in (4.26) to demonstrate the verification of $\mathbb{E}\left[\mathcal{R}_{\mathrm{a}}\right] = \bar{\mathcal{R}}_{\mathrm{a}}$. Similarly, the expectation of the UE SINR γ_u is directly computed in the Monte Carlo domain by taking the average of a large number of samples when the UE coordinates are distributed uniformly at random over an attocell. The resultant $\mathbb{E}[\gamma_u]$ is compared to the analytical assessment of the average access SINR $\bar{\gamma}_{\mathrm{a}}$ based on (4.36) to inspect $\mathbb{E}[\gamma_u] = \bar{\gamma}_{\mathrm{a}}$. The analytical and simulation results are presented in Fig. 4.5 as a function of the LED optical power for Configurations I and II. It can be seen that in both cases there is an excellent match between the analytical and simulation results. This verifies that the expressions of $K_{1,\min}$ can be safely used for backhaul power control based on FPC1 and FPC2. The reason that the analytical and simulation results almost perfectly match lies in the accurate approximation of the CCI term $\mathcal{I}(\theta_u | r_u = r)$ by (4.5) based on the flower model [110]. It is shown in [16] that this analytical expression exactly follows the simulated CCI over an angular period of $\theta_u \in [0, 2\pi]$.

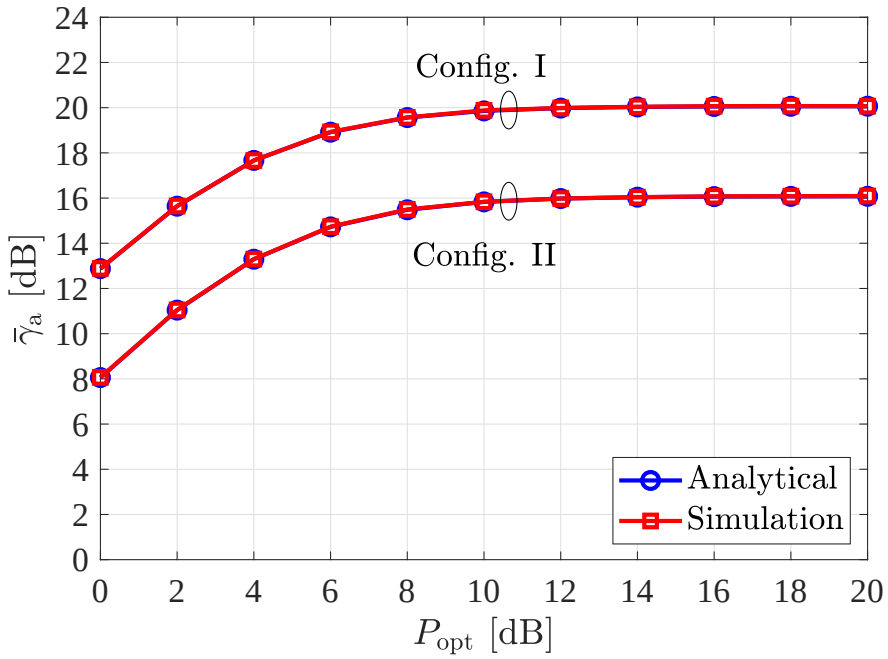

(a) Average access SINR.

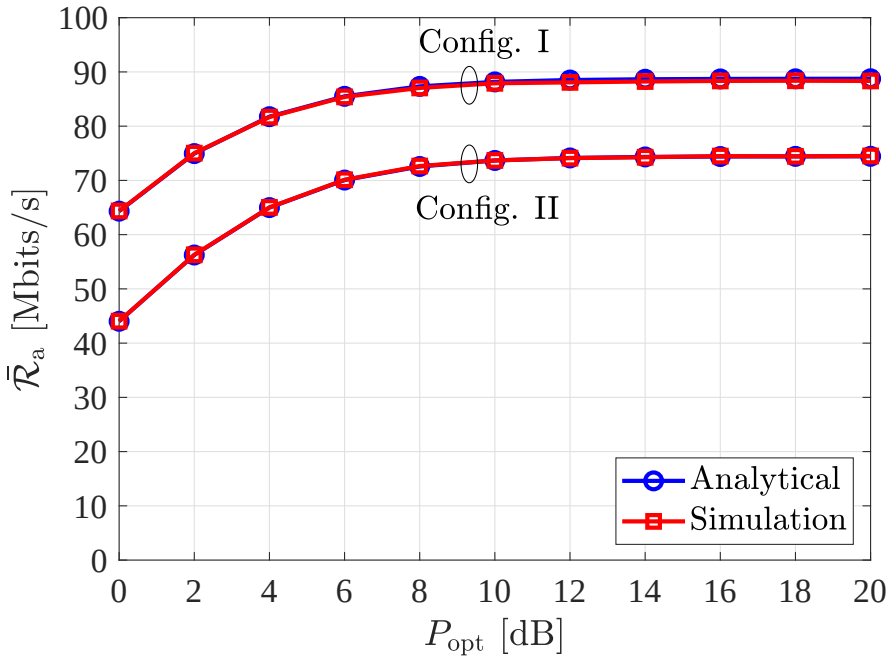

(b) Average access rate.

Figure 4.5: *Analytical and simulation results of the average SINR* $\bar{\gamma}_{\mathrm{a}}$ *and the average access rate* $\bar{\mathcal{R}}_{\mathrm{a}}$*. Analytical results are obtained based on the expressions* (4.26) *and* (4.36)*.*

Next, the RTP and BBO performance results are individually discussed. The following results are obtained with a focus on Configuration II.

4.3.3.2 Relative Total Power

Fig. 4.6 demonstrates the percentage of the RTP metric for APC, FPC1 and FPC2 schemes for 30 UEs in total. For both cases of $B_{\mathrm{b}} = B_{\mathrm{a}}$ and $B_{\mathrm{b}} = 3B_{\mathrm{a}}$, and for all three power control methods, the RTP exhibits an increasing trend with respect to the total number of tiers. This can be explained with the aid of Figs. 4.2 and 4.4, showing that the power control coefficients are increasing functions of the total number of the deployed tiers. In addition, more power needs to be allocated to the backhaul system when the bandwidth is decreased. This is consistent with the power-bandwidth tradeoff presented in Section 3.4.2. In the case of $B_{\mathrm{b}} = B_{\mathrm{a}}$, the RTP reaches almost a steady level for $N_{\mathrm{T}} \geq 3$. This is because the value of $K_{1,\min}$ is clipped at 1, which is the maximum allowable operating point for the backhaul power. Note that clipping predominately takes place at the bottleneck backhaul link, which is why the overall RTP performance saturates around a level of 10%. Moreover, since FPC2 operates according to the average SINR of the access system, it somewhat overestimates the required power of the backhaul system. Therefore, FPC2 leads to higher RTP levels compared to the other two schemes. When comparing FPC2 with APC, it can be observed that FPC2 slightly underestimates the required power for the backhaul system, as it assumes a constant rate equal to the statistical average of the access rate. Furthermore, the gap between the RTP level of FPC2 and those of APC and FPC1 is larger for less values of N_{T} and this is more pronounced for $B_{\mathrm{b}} = B_{\mathrm{a}}$ as shown in Fig. 4.6b.

To observe the RTP performance from another angle of view, Fig. 4.7 shows the behavior of RTP for different power control mechanisms. Note that FPC schemes are fixed schemes and do not vary with the number of UEs in the network. The only scheme that depends upon the load of the UEs is APC. However, it also does not display much variation over the considered range. In fact, this is an snapshot of the network realization for which $N_{\mathrm{T}} = 3$. In this case, the variations of $K_{1,\min}$ corresponding to APC conforms to Fig. 4.3b.

4.3.3.3 BBO Probability

To shed light on another aspect of the backhaul power control, the resulting BBO probability is shown with a percent scale in Figs. 4.8 and 4.9 as a function of the total number of UEs and the total number of tiers. These results well complement those of RTP in the sense that increasing the backhaul bandwidth leads to overall lower values of the BBO probability. The performance of the backhaul system with full power in which $P_{\mathrm{b}_i} = P_{\mathrm{a}}\ \forall i$ is included for comparison.

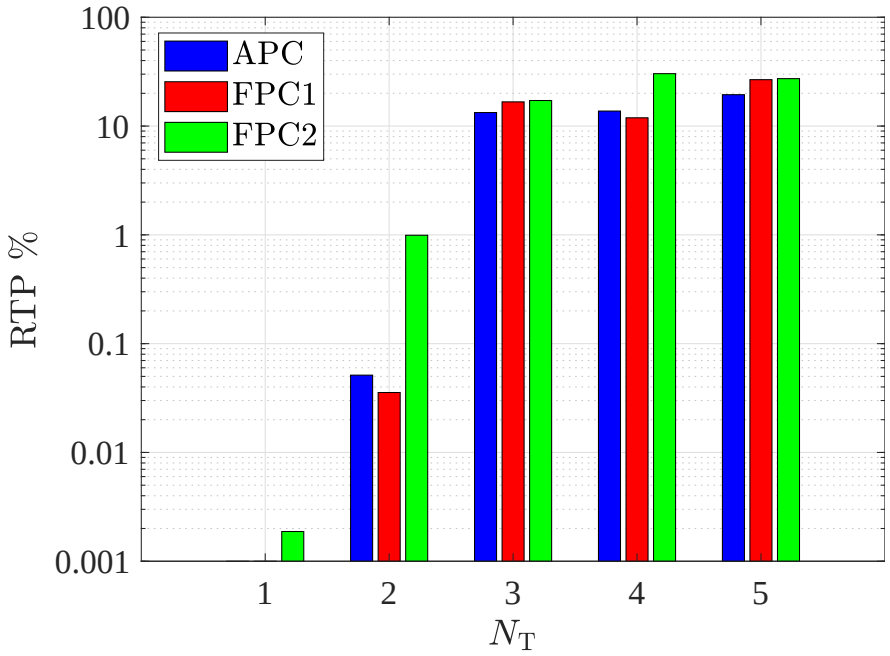

(a) $B_{\mathrm{b}} = B_{\mathrm{a}}$.

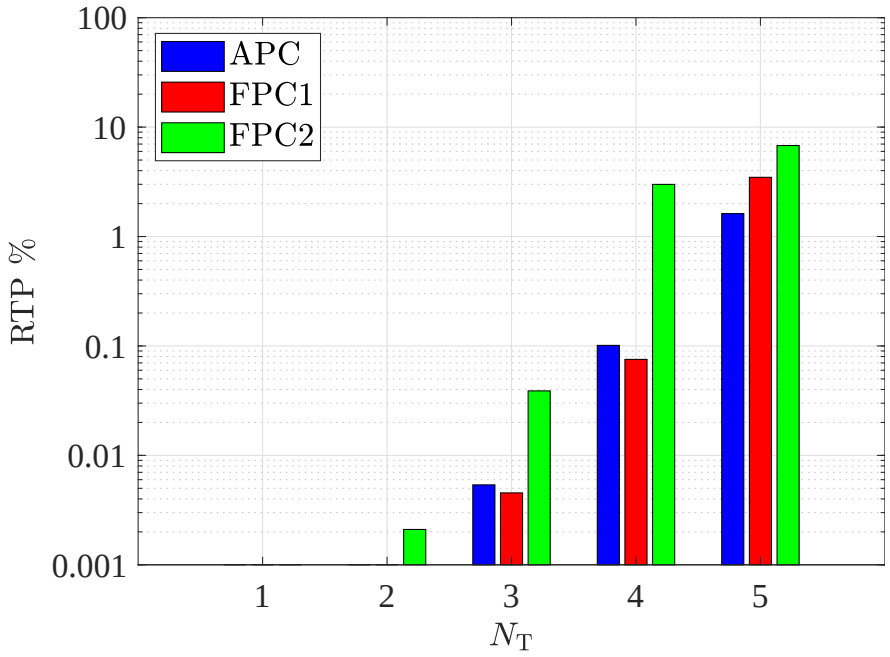

(b) $B_{\mathrm{b}} = 3B_{\mathrm{a}}$.

Figure 4.6: *The RTP performance of APC, FPC1 and FPC2 schemes versus the total number of tiers for* $M = 30$.

The full power backhaul system is labeled as no power control (NPC). It is observed that APC and FPC2 achieve almost equal BBO performance as NPC, while FPC1 performs worse than

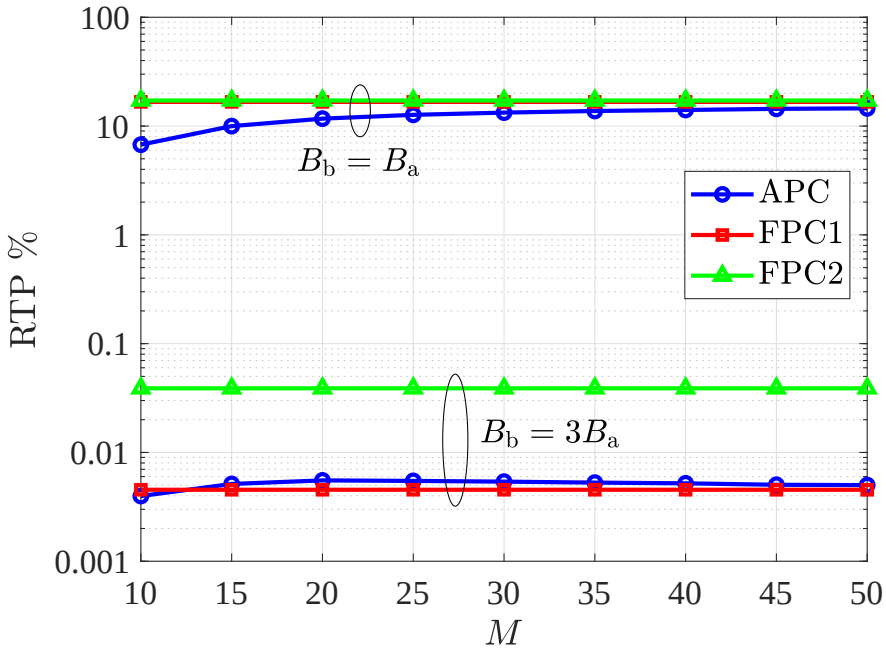

Figure 4.7: *The RTP performance for a three-tier super cell with APC, FPC1 and FPC2 schemes versus the total number of UEs.*

NPC. In the case of APC, until it does not cross the allowed power threshold, no bottleneck occurs and the BBO probability is almost equal to zero, which is evident for $N_{\rm T} = 1, 2$. By increasing $N_{\rm T}$ beyond $N_{\rm T} = 2$, the backhaul bottleneck happens and therefore the backhaul power is adjusted using a unit power ratio, and this makes the performance of APC the same as NPC. From the RTP perspective, FPC2 sets a higher performance relative to the APC and FPC1 schemes, but at the same time achieves a BBO performance similar to the baseline NPC scheme. This shows that there is an optimum threshold for designing FPC-based schemes that makes a tradeoff between the total power minimization and the bottleneck minimization. The use of FPC1, though offering significant power savings, can lead to 50% BBO probability even when it is used for single or double tier networks. This poor performance disqualifies the impressive gain that is offered by FPC1 in terms of the total backhaul power.

The BBO performance for each branch of the super cell can be analytically predicted by way of the approximate expression provided in Theorem 2. To verify the derivation of (4.48), the analytical and simulation results are plotted in Fig. 4.10 over a wide range of values of the power ratio K_1. The simulation results are directly obtained by computing the BBO probability in the Monte Carlo domain according to Definition 1. For comparison, different combinations of the total number of tiers, $N_{\rm T}$, and the total number of UEs, M, are considered. For both cases of

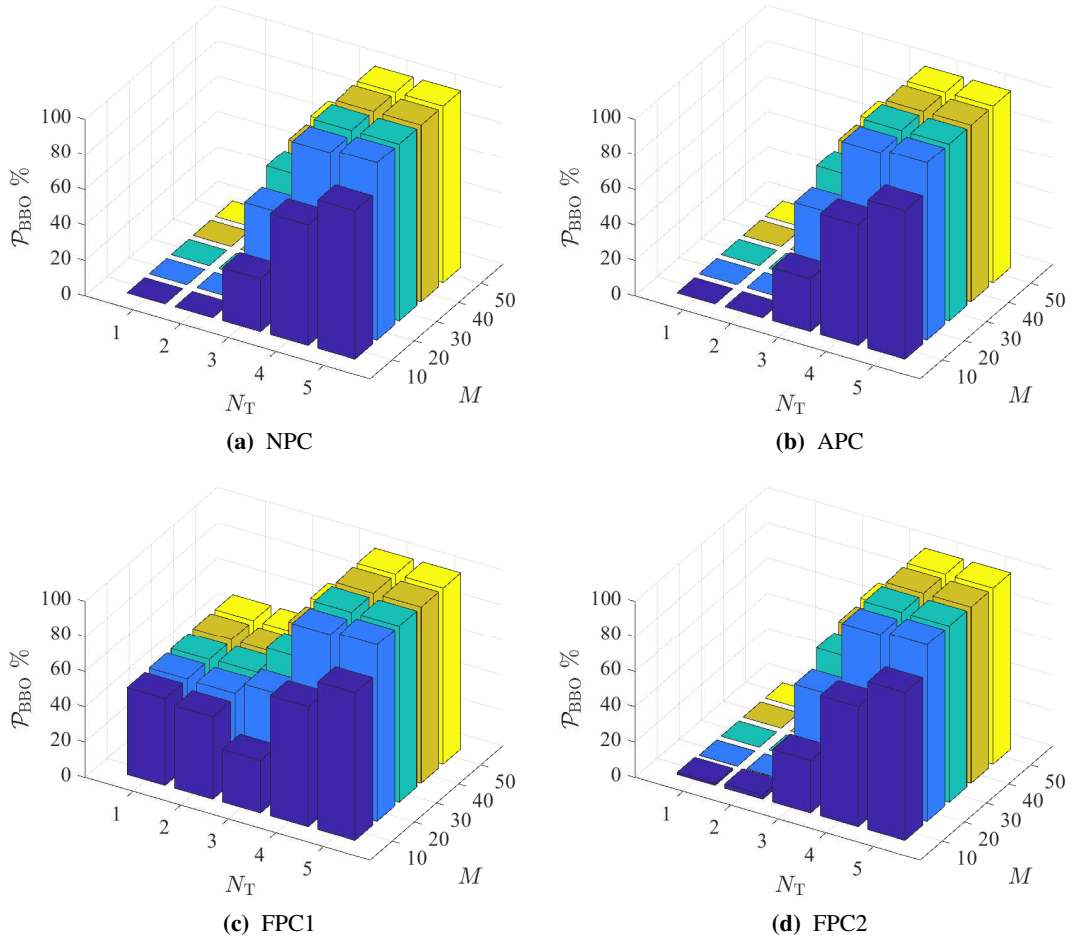

(a) NPC **(b)** APC

(c) FPC1 **(d)** FPC2

Figure 4.8: *The BBO probability for NPC, APC, FPC1 and FPC2 schemes versus the total number of tiers and the total number of UEs for* $B_{\mathrm{b}} = B_{\mathrm{a}}$.

$M = 30$ and $M = 50$, as shown in Figs. 4.10a and 4.10b, respectively, the analytical results are closely matching with those of simulations. By comparison, the approximation is tighter for the case of $M = 50$ than $M = 30$. This is the result of the Gaussian approximation whose accuracy improves for larger values of M. In addition, for a given number of UEs, there is a slight difference between the two sets of results when N_{T} increases, which is more apparent for $N_{\mathrm{T}} = 4$. However, the gap reduces by increasing M as observed from Fig. 4.10b. Note that the approximate expression is neither an upper bound nor a lower bound of the BBO probability, as it is derived on the basis of the MMSE criterion. These results confirm that the formula derived in (4.48), though its simple form, does estimate well the actual BBO performance of the network. It can be used for the system level design of multi-hop wireless optical backhauling in optical attocell networks in order to assess the interplay between the operating power and

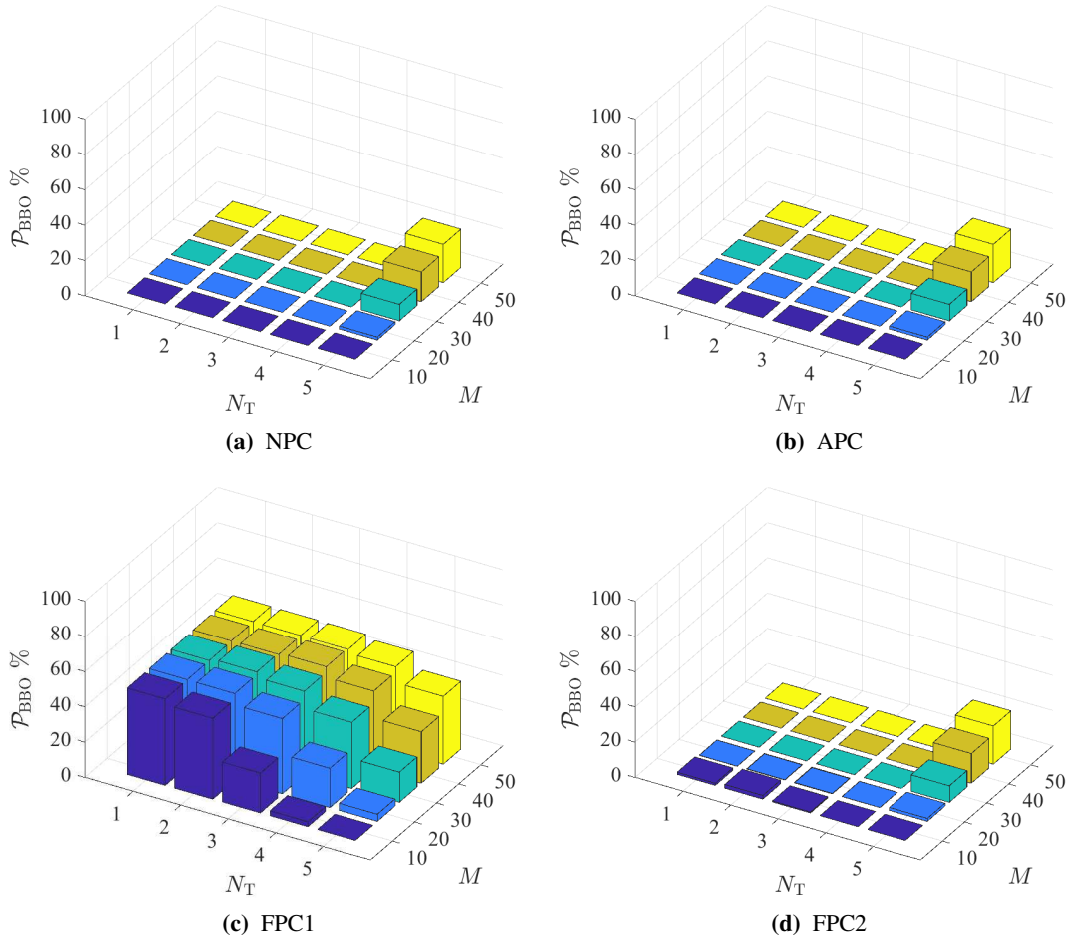

(a) NPC **(b)** APC

(c) FPC1 **(d)** FPC2

Figure 4.9: *The BBO probability for NPC, APC, FPC1 and FPC2 schemes versus the total number of tiers and the total number of UEs for* $B_{\mathrm{b}} = 3B_{\mathrm{a}}$.

the bottleneck performance of the backhaul system. Note that $\mathcal{P}_{\mathrm{BBO}}$ is a function of the power ratio K_1 through $\mathcal{R}_{\mathrm{b}_1} = \xi_{\mathrm{b}} B_{\mathrm{b}} \log_2(1 + K_1 \gamma_{\mathrm{b}})$. Therefore, the BBO probability of any FPC scheme including FPC1 and FPC2 can be evaluated by using the corresponding power control coefficient, i.e., for $K_1 = K_{1,\min}$.

4.3.3.4 Average Sum Rate Performance

To measure the sum rate performance, the backhaul bandwidth is equally divided between all the BSs within the considered backhaul branch with no distinction. This leads to a bandwidth allocation ratio of $\mu_i = \frac{1}{N_{\mathrm{BS}}}\ \forall i \in \mathcal{L}_k$ for an N_{T}-tier super cell.

Fig. 4.11 demonstrates the average sum rate performance for NPC, APC, FPC1 and FPC2

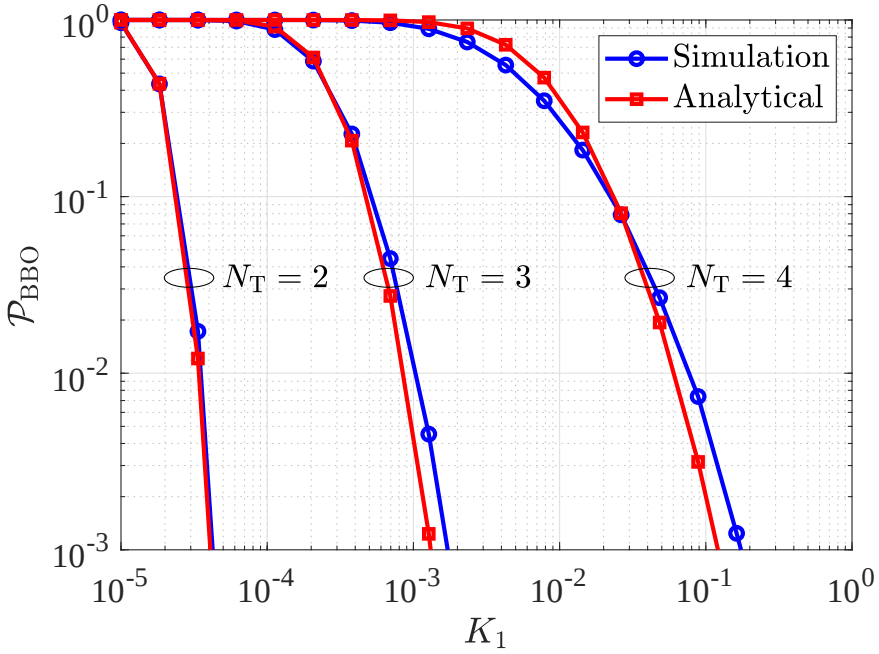

(a) $M = 30$.

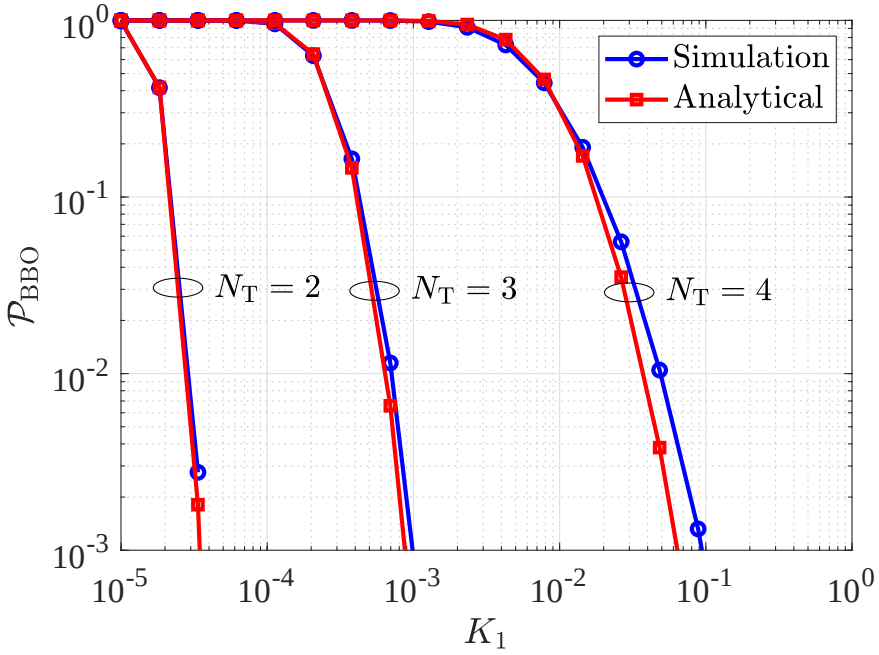

(b) $M = 50$.

Figure 4.10: *Analytical and simulation results of the BBO probability as a function of* K_1 *for different values of* N_{T} *and* M. *Analytical results are presented based on the approximate expression of the BBO probability in* (4.48).

schemes versus the total number of tiers and the total number of UEs for different values of

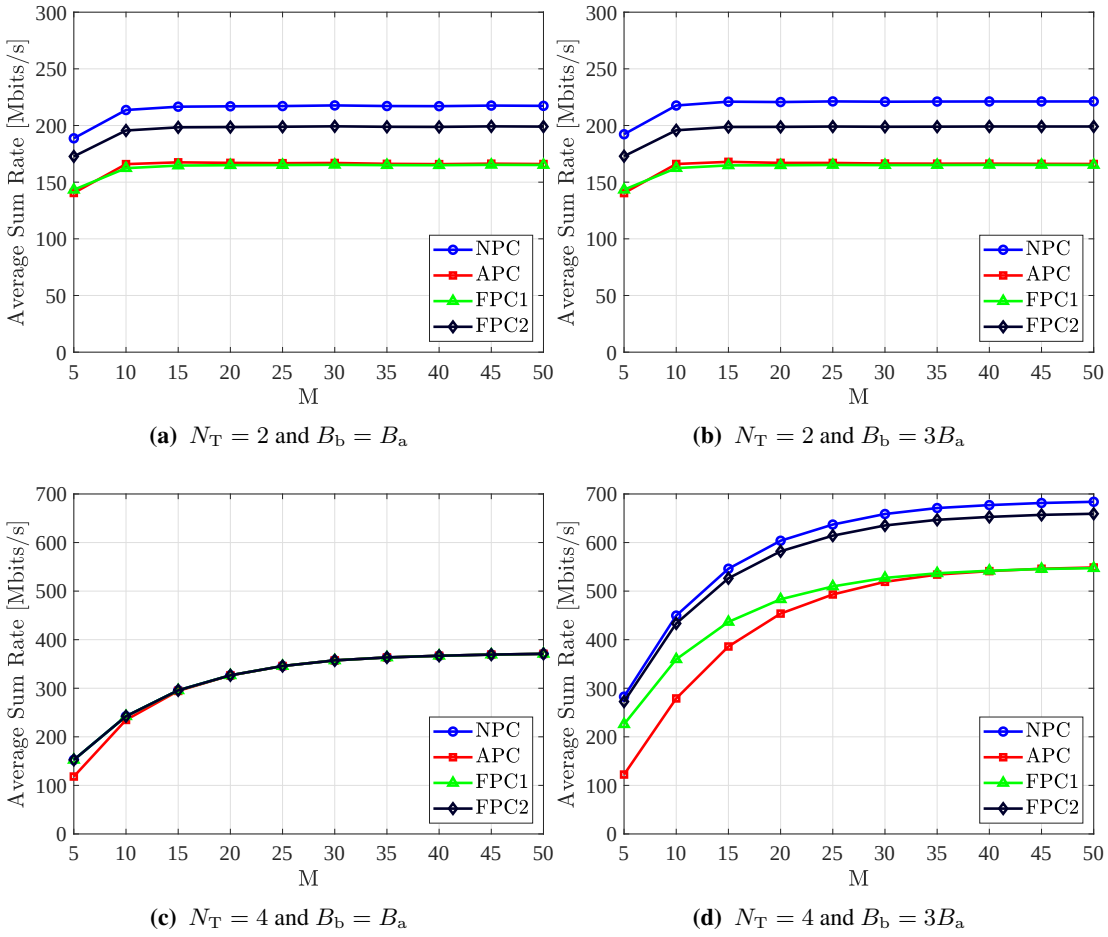

(a) $N_{\mathrm{T}} = 2$ and $B_{\mathrm{b}} = B_{\mathrm{a}}$ **(b)** $N_{\mathrm{T}} = 2$ and $B_{\mathrm{b}} = 3B_{\mathrm{a}}$

(c) $N_{\mathrm{T}} = 4$ and $B_{\mathrm{b}} = B_{\mathrm{a}}$ **(d)** $N_{\mathrm{T}} = 4$ and $B_{\mathrm{b}} = 3B_{\mathrm{a}}$

Figure 4.11: *The average sum rate performance for NPC, APC, FPC1 and FPC2 schemes versus the total number of tiers and the total number of UEs.*

the backhaul bandwidth. The end-to-end sum rate of the network is assessed by applying the analysis in Section 4.2.4. Configuration II from Table 4.1 is used for simulations. The performance of the NPC scheme is also included as a benchmark. First, it can be observed that the general trend of the results for all power control schemes is increasing with M. By contrast, for a given M, increasing N_{T} causes the overall sum rate to rise, e.g., Fig. 4.11a relative to Fig. 4.11c, or Fig. 4.11b compared with Fig. 4.11d. In fact, with an increase in the total number of tiers, a larger number of attocells host the same number of UEs, increasing the chance that more attocells are occupied by the UEs. Thus, the access sum rates of more BSs accumulate and, in effect, produce a greater sum rate.

In Figs. 4.11a and 4.11b, it can be seen that APC and FPC1 have the same performance, while the performance of FPC2 is near to that of NPC for $N_{\mathrm{T}} = 2$ and $B_{\mathrm{b}} = B_{\mathrm{a}}$. This can be

explained in terms of their RTP performance (resp. BBO performance), as FPC2 has higher RTP values (resp. lower BBO probabilities) and thus provides higher data rates than APC and FPC1, see Figs. 4.6, 4.8 and 4.9. For the particular case of $M = 30$, $N_{\mathrm{T}} = 4$ and $B_{\mathrm{b}} = 3B_{\mathrm{a}}$, by comparing the RTP shown in Fig. 4.6b with the sum rate in Fig. 4.11d, it can be observed that the sum rate of FPC2 is 100 Mbits/s higher than APC and FPC1 and its RTP is about 100 times that of APC and FPC1. However, the RTP value is 1%, which is still sufficiently low. Therefore, FPC2 reaches a compromise between the required power and the sum rate performance, and it achieves a comparable performance to that of the full power (i.e., NPC) backhaul system while operating with significantly less power. The same conclusion is drawn when comparing the sum rate performance of a two-tier case with $M = 30$ and $B_{\mathrm{b}} = B_{\mathrm{a}}$ to the RTP performance of the same case, i.e., Fig. 4.12b for $N_{\mathrm{T}} = 2$ versus Fig. 4.6b for $N_{\mathrm{T}} = 2$. This is in contrast to the case of FPC1 where the overall sum rate performance approaches that of APC as the total number of UEs increase, which is apparent in Fig. 4.11d. The tradeoff between the sum rate performance and the backhaul power computed by APC and FPC schemes is clear in Fig. 4.12b. Note that NPC globally attains the best performance as it always operates with the maximum allowed power, while APC and FPC reduce the amount of power to some value below the maximum allowed power according to their respective criteria. This way the backhaul PE is improved as highlighted by the outstanding RTP performance in Fig. 4.6b, but at the price of losing the average sum rate performance with respect to NPC. A scheme that sets relatively higher power achieves a better sum rate performance.

Furthermore, by comparing Figs. 4.11a and 4.11b with Figs. 4.11c and 4.11d, increasing the bandwidth from $B_{\mathrm{b}} = B_{\mathrm{a}}$ to $B_{\mathrm{b}} = 3B_{\mathrm{a}}$ has a significant effect on the sum rate performance for $N_{\mathrm{T}} = 4$, whereas the sum rate does not change for $N_{\mathrm{T}} = 2$ by this increase in bandwidth. This could be anticipated from the BBO performance in Figs. 4.8 and 4.9, which clearly show that the two-tier case is in no way under the backhaul bottleneck limitation (i.e., it has a zero BBO probability) for both choices of bandwidth. By contrast, the four-tier case has a very high value of BBO probability especially for $B_{\mathrm{b}} = B_{\mathrm{a}}$, which is why all the power control schemes including the baseline NPC scheme have an equally low level of the sum rate as shown in Fig. 4.11d. This is due to the fact that the access system is entirely limited by an inadequate capacity of the backhaul system. By tripling the bandwidth, the performance of NPC and FPC2 remarkably improve, while there is relatively less improvement in the performance of FPC1 and APC. Such a trend cannot be fully interpreted based on only BBO without considering the role of the equal bandwidth allocation in the bottleneck link. In fact, while BBO gives information

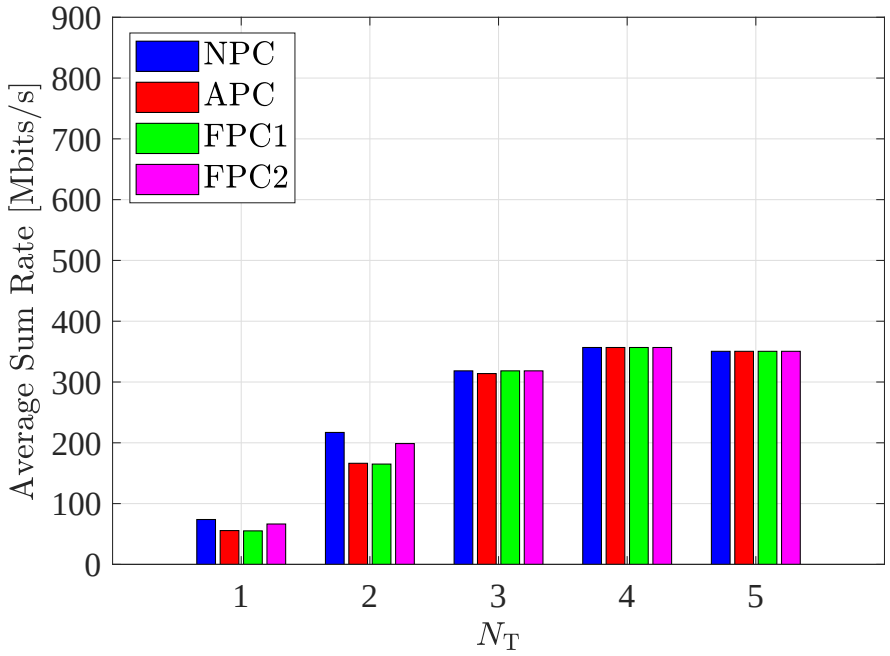

(a) $B_{\mathrm{b}} = B_{\mathrm{a}}$

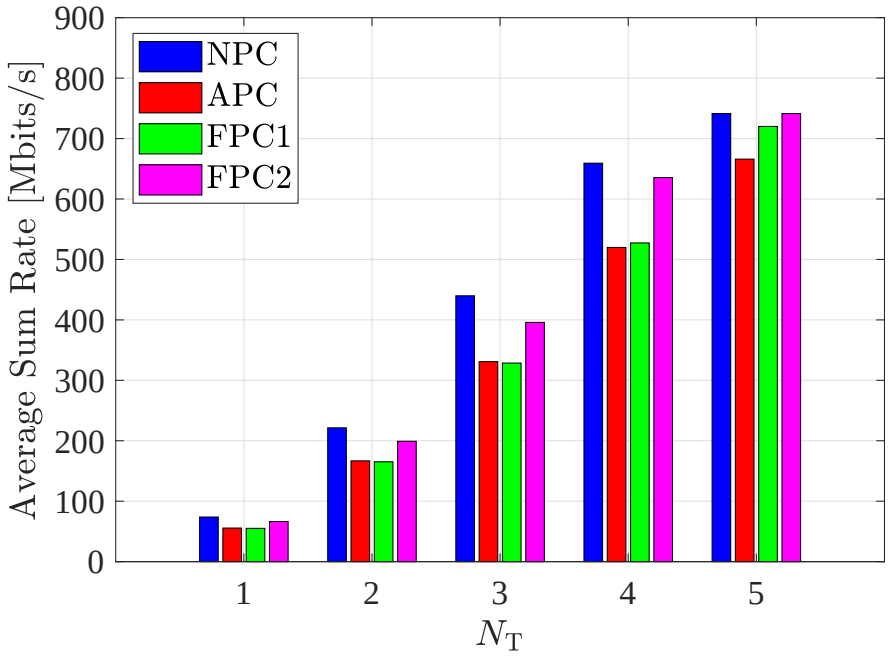

(b) $B_{\mathrm{b}} = 3B_{\mathrm{a}}$

Figure 4.12: *The average sum rate performance for NPC, APC, FPC1 and FPC2 schemes versus the total number of tiers for different values of the backhaul bandwidth. The total number of UEs is fixed at* $M = 30$.

on the overall bottleneck performance of the backhaul system, it does not provide information

on whether the allocated bandwidth bandwidth to individual BSs results in a backhaul bottleneck. In fact, the equal assignment of the backhaul bandwidth to different BSs in the desired backhaul branch is an important contributory factor to the overall sum rate performance. That is why the sum rate of APC is lower than that of NPC as shown in Fig. 4.11d, although APC has a zero BBO probability for $N_{\mathrm{T}} = 4$ according to Fig. 4.9b.

4.4 Optimal Bandwidth Scheduling

By using any FPC scheme including FPC1 and FPC2 as discussed in Section 4.3, there exists a backhaul bottleneck with a nonzero BBO probability. While the BBO performance provides information on the backhaul behavior in response to the overall sum rate of downlink flows, yet it does not explain how to apportion the limited capacity of the bottleneck link among individual flows. This section focuses on the problem of bandwidth scheduling for the bottleneck link, aiming to maximize the end-to-end performance. In particular, the design of bandwidth sharing coefficients is formulated as an optimization problem. To implement proportional fairness scheduling, a logarithmic utility-based objective function is employed. This enables the scheduler to maintain a balance between throughput and fairness for coincident flows [112]. In the following, two policies are proposed for optimal bandwidth scheduling per super cell. In any case, as discussed in Section 4.2.3, there are two constraints that apply to the kth branch of the super cell as follows:

$$\sum_{i \in \mathcal{L}_k} \mu_i = 1 \tag{4.56a}$$

$$0 \leq \mu_i \leq 1, \ \forall i \in \mathcal{L}_k \tag{4.56b}$$

4.4.1 User-based Bandwidth Scheduling

In UBS, the SINR information for entire UEs in the considered super cell are processed by a central controller at the gateway for global optimization of the bandwidth allocation. The underlying assumption of the downlink SINR of every UE being available to the central controller is justified as indoor wireless optical channels are often considered to be static for two reasons: 1) the short wavelength of the optical carrier along with the large photosensitive area of the photodiode (PD) eliminate rapid signal fluctuations due to multipath fading [54]; 2) in realistic indoor scenarios, the UEs are inclined to be either static or slowly moving. Consequently, each

BS collects the SINR information from an uplink channel and sends it as feedback to the central controller.

Recall from (4.19) the end-to-end rate for the uth UE served by BS$_i$ in the nth tier of the super cell. The aim of UBS is to maximize the sum of *per-user* utilities by solving an optimization problem of the global form:

$$\underset{\{\mu_i \in \mathbb{R}\}}{\text{maximize}} \quad \sum_{i \in \mathcal{L}_k} \sum_{u \in \mathcal{U}_i} \ln(\mathcal{R}_u) = \sum_{i \in \mathcal{L}_k} \sum_{u \in \mathcal{U}_i} \left[\ln\left(\frac{1}{M_i} \min[\mu_i, \rho_u] \right) + \ln(\xi_{\mathrm{b}} B_{\mathrm{b}} \log_2(1 + \gamma_{\mathrm{b}_k})) \right] \tag{4.57a}$$

$$\text{subject to} \ \text{(4.56a) \& (4.56b)} \tag{4.57b}$$

where the objective function is expanded by factorizing the term $\zeta \log_2(1 + \gamma_{\mathrm{b}_k})$ and defining a variable ρ_u to represent the normalized achievable rate for the uth UE in the kth branch:

$$\rho_u = \frac{\log_2(1 + \gamma_u)}{\zeta \log_2(1 + \gamma_{\mathrm{b}_k})}. \tag{4.58}$$

The second summand in (4.57a) is a constant term for the kth branch, independent of maximization variables. After removing the constant term from the objective function, the optimization problem is stated in a compact form of:

$$\underset{\{\mu_i \in \mathbb{R}\}}{\text{maximize}} \quad \sum_{i \in \mathcal{L}_k} \sum_{u \in \mathcal{U}_i} \ln\left(\frac{1}{M_i} \min[\mu_i, \rho_u] \right) \tag{4.59a}$$

$$\text{subject to} \quad \text{(4.56a) \& (4.56b)} \tag{4.59b}$$

The maximization objective in (4.59a) is a composite of concave operators, comprising summation, logarithm and minimization. Such a composition preserves concavity and the objective function is concave [113]. Therefore, this is a convex optimization problem with linear constraints stated in (4.56a) and (4.56b). For such a problem, Slater's condition holds and there is a global optimum [114]. However, standard methods such as Lagrange multipliers cannot be directly applied to find an analytical solution because the objective function is not differentiable in $\boldsymbol{\mu} = [\mu_i]_{N_{\mathrm{BS}} \times 1}$, where $\boldsymbol{\mu}$ is the vector of optimization variables.

For nonsmooth optimization, the subgradient method is a means to deal with nondifferentiable convex functions [115]. Particularly, the constrained optimization problem in (4.59) can be efficiently solved by using the *projected* subgradient method. Analogous to common subgradient

Algorithm 1 Iterative Projected Subgradient Algorithm for User-based Bandwidth Scheduling.

1: Initialize $\boldsymbol{\mu}^{(0)}$
2: **for** all $i \in \mathcal{L}_k$ **do**
3: Let $\check{\mathcal{U}}_i^{(l)} = \left\{ u \in \mathcal{U}_i \middle| \mu_i^{(l)} \leq \rho_u \right\}$
4: Compute $\check{M}_i^{(l)} = \left| \check{\mathcal{U}}_i^{(l)} \right|$
5: Compute $g_i^{(l)} = \dfrac{\check{M}_i^{(l)}}{\mu_i^{(l)}}$
6: **end for**
7: Update $\boldsymbol{\mu}^{(l)}$ through $\boldsymbol{\mu}^{(l+1)} = \boldsymbol{\mu}^{(l)} - \alpha \mathbf{P}\mathbf{g}^{(l)}$
8: $l \leftarrow l + 1$
9: **go to** 2
10: Return $\boldsymbol{\mu}$

methods, the vector $\boldsymbol{\mu}$ is sequentially updated using a subgradient of the objective function at $\boldsymbol{\mu}$. Compared with an ordinary subgradient method, there is an additional constraint $\mathbf{1}^T\boldsymbol{\mu} = 1$, which is required by (4.56a). To fulfil this constraint, at each iteration, the projected approach maps the components of $\boldsymbol{\mu}$ onto a unit space before proceeding with the next update, to bring them back to the feasible set. The convergence is attained upon setting a suitable step size for executing iterations [115]. To develop an efficient iterative algorithm, one requires an appropriate subgradient vector to provide a descent direction for a local maximizer to approach the global maximum when updating. Thus, the problem statement needs to be properly modified. To this end, the users in the attocell of BS_i are split into two disjoint groups: those for whom $\mu_i > \rho_u$ and those for whom $\mu_i \leq \rho_u$. The index sets for these two groups are denoted by $\hat{\mathcal{U}}_i$ and $\check{\mathcal{U}}_i$, respectively, implying $\hat{\mathcal{U}}_i \cup \check{\mathcal{U}}_i = \mathcal{U}_i$. The number of elements corresponding to $\hat{\mathcal{U}}_i$ and $\check{\mathcal{U}}_i$ is represented by $\hat{M}_i$ and $\check{M}_i$ so that $\hat{M}_i + \check{M}_i = M_i$. The optimization problem in (4.59) is then stated in the desired form:

$$\underset{\{\mu_i \in \mathbb{R}\}}{\text{maximize}} \quad \sum_{i \in \mathcal{L}_k} \left[\sum_{u \in \hat{\mathcal{U}}_i} \ln\left(\frac{\rho_u}{M_i}\right) + \check{M}_i \ln\left(\frac{\mu_i}{M_i}\right) \right] \tag{4.60a}$$

$$\text{subject to} \quad \text{(4.56a) \& (4.56b)} \tag{4.60b}$$

Note that the arrangements of $\check{\mathcal{U}}_i$ and $\hat{\mathcal{U}}_i$ depend on the value of μ_i. Based on (4.60a), the derivative of the objective function with respect to μ_i is estimated by $\frac{\check{M}_i}{\mu_i}$, resulting in the subgradient vector $\mathbf{g} = [g_i]_{N_{\text{BS}} \times 1}$ where $g_i = \frac{\check{M}_i}{\mu_i}$. The projected subgradient method for solving the primal problem is summarized in Algorithm 1. In step 7 of this algorithm, α is the step size for updating; and $\mathbf{P}$ is an $N_{\text{BS}} \times N_{\text{BS}}$ unitary space projection matrix [116].

4.4.2 Cell-based Bandwidth Scheduling

For CBS, the central controller gathers the overall access sum rate information sent individually by each BS via the feedback channel for further processing. This considerably reduces the amount of feedback with respect to UBS in which each BS conveys the SINR information for every single UE to the central controller. For this reason, CBS appeals to applications where a limited feedback is available [117]. Besides, the overall sum rate information is a quasi-static measure as it does not display much variation even though the SINR information changes dynamically. This is another feature of CBS that requires relatively less feedback rate. In effect, the overall overhead of feedback is significantly smaller in CBS.

Refer to (4.21) where the end-to-end sum rate for BS_i in the nth tier is given. The scheduler aims to maximize the aggregate *per-cell* utilities by computing an optimal solution to the following bandwidth allocation problem:

$$\underset{\{\mu_i \in \mathbb{R}\}}{\text{maximize}} \quad \sum_{i \in \mathcal{L}_k} \ln(\mathcal{R}_i^{\text{sum}}) = \sum_{i \in \mathcal{L}_k} \left[\ln \left(\frac{1}{M_i} \sum_{u \in \mathcal{U}_i} \min[\mu_i, \rho_u] \right) + \ln(\xi_{\mathrm{b}} B_{\mathrm{b}} \log_2(1 + \gamma_{\mathrm{b}_k})) \right] \tag{4.61a}$$

$$\text{subject to} \quad \text{(4.56a) \& (4.56b)} \tag{4.61b}$$

One can put aside the constant term appeared as $\ln(\xi_{\mathrm{b}} B_{\mathrm{b}} \log_2(1 + \gamma_{\mathrm{b}_k}))$ in (4.61a) without affecting the optimization problem. By switching the order of $\min$ with the inner summation, a compact representation is obtained for the problem statement in (4.61):

$$\underset{\{\mu_i \in \mathbb{R}\}}{\text{maximize}} \quad \sum_{i \in \mathcal{L}_k} \ln \left(\min \left[\mu_i, \frac{1}{M_i} \sum_{u \in \mathcal{U}_i} \rho_u \right] \right) \tag{4.62a}$$

$$\text{subject to} \quad \text{(4.56a) \& (4.56b)} \tag{4.62b}$$

Note that in (4.62a), the quantity $\frac{1}{M_i} \sum_{u \in \mathcal{U}_i} \rho_u$ is, in fact, equal to $\frac{\mathcal{R}_{\mathrm{a}_i}}{\mathcal{R}_{\mathrm{b}_k}}$ based on (4.58). This is consistent with the assumption of $\mathcal{R}_{\mathrm{a}_i}$ values being available to the scheduler. The projected subgradient method is used to solve the primal problem. With the current expression in (4.62a), the objective function is not differentiable in $\boldsymbol{\mu}$. To find the candidate subgradient vector, the BSs of the kth branch are classified into two categories: those that fulfil the condition $\mu_i > \frac{1}{M_i} \sum_{u \in \mathcal{U}_i} \rho_u$ and those that satisfy $\mu_i \leq \frac{1}{M_i} \sum_{u \in \mathcal{U}_i} \rho_u$. The former category is represented by

Algorithm 2 Iterative Projected Subgradient Algorithm for Cell-based Bandwidth Scheduling.

1: Initialize $\boldsymbol{\mu}^{(0)}$
2: Let $\check{\mathcal{L}}_k^{(l)} = \left\{ i \in \mathcal{L}_k \middle| \mu_i^{(l)} \leq \frac{1}{M_i} \sum_{u \in \mathcal{U}_i} \rho_u \right\}$
3: **for** all $i \in \mathcal{L}_k$ **do**
4: **if** $i \in \check{\mathcal{L}}_k$ **then**
5: Compute $g_i^{(l)} = \dfrac{1}{\mu_i^{(l)}}$
6: **else**
7: Set $g_i^{(l)} = 0$
8: **end if**
9: **end for**
10: Update $\boldsymbol{\mu}^{(l)}$ through $\boldsymbol{\mu}^{(l+1)} = \boldsymbol{\mu}^{(l)} - \alpha \mathbf{P}\mathbf{g}^{(l)}$
11: $l \leftarrow l + 1$
12: **go to** 2
13: Return $\boldsymbol{\mu}$

an index set of $\hat{\mathcal{L}}_k$ and the latter case by $\check{\mathcal{L}}_k$. The optimization problem in (4.62) turns into:

$$\underset{\{\mu_i \in \mathbb{R}\}}{\text{maximize}} \quad \sum_{i \in \hat{\mathcal{L}}_k} \ln \left(\frac{1}{M_i} \sum_{u \in \mathcal{U}_i} \rho_u \right) + \sum_{i \in \check{\mathcal{L}}_k} \ln(\mu_i) \tag{4.63a}$$

$$\text{subject to} \quad \text{(4.56a) \& (4.56b)} \tag{4.63b}$$

Therefore, the derivative of the objective function with respect to μ_i is readily evaluated by $\frac{1}{\mu_i}$, leading to the subgradient vector $\mathbf{g} = [g_i]_{N_{\mathrm{BS}} \times 1}$ where:

$$g_i = \begin{cases} \frac{1}{\mu_i}, & i \in \check{\mathcal{L}}_k \\ 0, & i \in \hat{\mathcal{L}}_k \end{cases} \tag{4.64}$$

The projected subgradient method used to solve the primal problem is outlined in Algorithm 2.

4.4.3 Numerical Results and Discussions

This section presents performance results for the proposed UBS and CBS policies based on Algorithm 1 and Algorithm 2, receptively. Monte-Carlo simulations are conducted over many random realizations to distribute multiple UEs uniformly over the network. The system parameters are taken from Table 3.1, and Configuration II from Table 4.1 is used. Also, a fixed power is used for the bottleneck backhaul link of the considered branch, and the backhaul bandwidth is fixed at $B_{\mathrm{b}} = B_{\mathrm{a}}$. For each random distribution of UEs, the end-to-end sum rate is measured

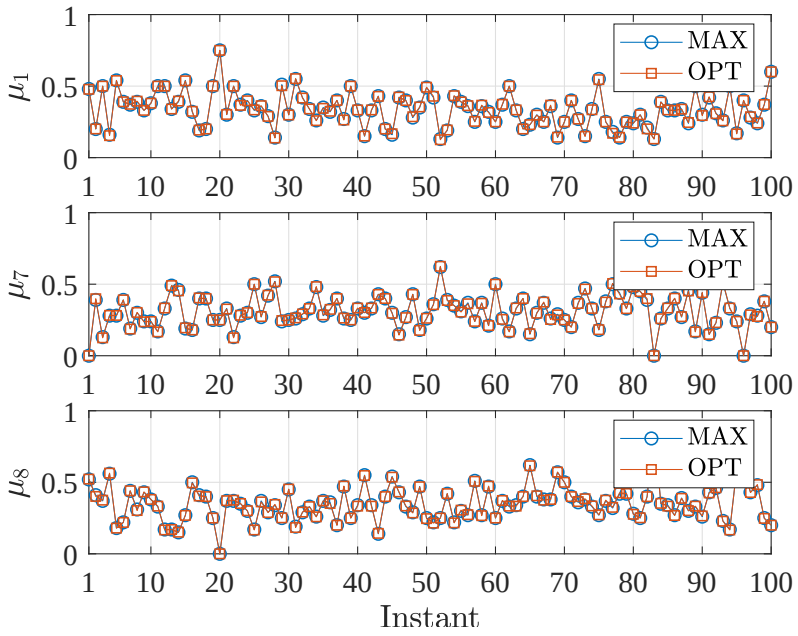

Figure 4.13: *An example of running Algorithm* 1 *(UBS) over* 100 *instant realizations for* $N_{\mathrm{T}} = 2$ *and* $M = 10$*. The labels 'MAX' and 'OPT' indicate the result of exhaustive search and the output of Algorithm* 1*, respectively.*

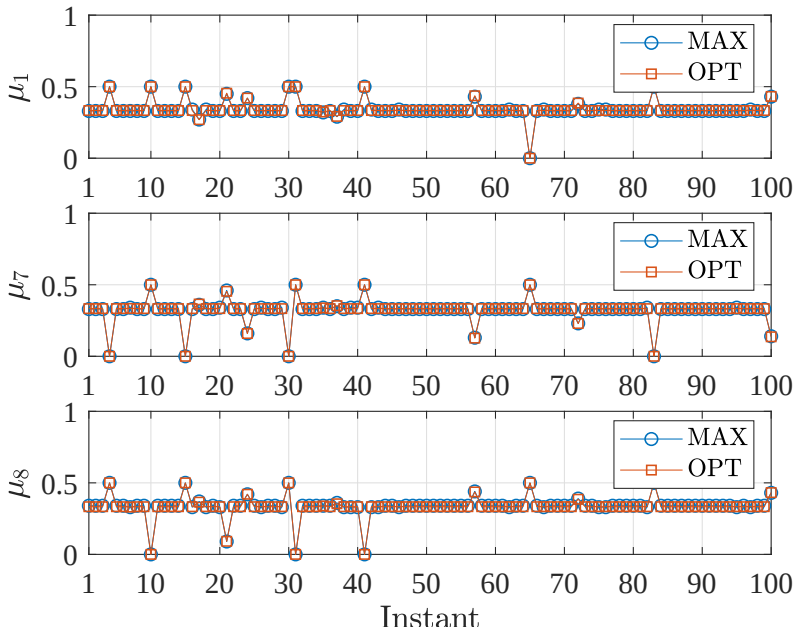

Figure 4.14: *An example of running Algorithm* 2 *(CBS) over* 100 *instant realizations for* $N_{\mathrm{T}} = 2$ *and* $M = 10$*. The labels 'MAX' and 'OPT' indicate the result of exhaustive search and the output of Algorithm* 2*, respectively.*

by computing the aggregate rate of every attocell. The total number of UEs is controlled by a fixed value of M, but the number of UEs associated with each attocell randomly varies for different realizations. By taking the average from a sufficiently large number of random samples for a given value of M, the resulting mean sum rate offers a clear picture of the average performance of the network as a whole.

Fig. 4.13 shows an example of running Algorithm 1, i.e., UBS, over 100 instant realizations for distributing $M = 10$ UEs for $N_{\mathrm{T}} = 2$. The labels 'MAX' and 'OPT' represent the result of exhaustive search and the output of Algorithm 1, respectively. It is observed that the algorithm dynamically follows the variations of the load distribution in the network. The optimal values of the three bandwidth scheduling ratios μ_1, μ_7 and μ_8 are perfectly matching with those obtained by the exhaustive search. Also, Fig. 4.14 demonstrates an example where Algorithm 2 processes 100 samples for the instant distribution of $M = 10$ UEs in the network. The assumptions are the same as those used for Fig. 4.13. According to Fig. 4.14, there is a perfect match between the results of the algorithm and those of the exhaustive search, which shows the optimal performance of the algorithm. Compared to Fog. 4.13, it can be observed that there is less variation in the optimal values of the bandwidth scheduling ratios, μ_i. The reason for this is that CBS scheduling takes the sum of the access rates, instead of taking the rate of individual UEs, and the sum of a number of i.i.d. random variables has a smaller variance than the variance of individual random variables.

Fig. 4.15 shows the average sum performance under both types of the proposed scheduling policies. The performance of an equal bandwidth scheduling (EBS) is also included for comparison. The EBS policy always allocates an equal amount of bandwidth to every BS in the backhaul branch. First of all, it can be observed that both UBS and CBS algorithms improve the performance with respect to the baseline EBS policy. This improvement is more pronounced when the total number of tiers increases from $N_{\mathrm{T}} = 2$ to $N_{\mathrm{T}} = 3$. In addition, both UBS and CBS achieve the same performance in terms of the average sum rate. However, CBS has much less complexity than UBS, as it requires only the sum of the access rates to compute the optimal bandwidth scheduling ratios. Finally, these algorithms are more effective for lower number of UEs, i.e., lower user densities. A possible explanation for this is that these algorithms adapt to the conditions in the access network. Therefore, they avoid wasting the bandwidth by assigning it to empty attocells. Such a condition is more likely when there is a less number of UEs.

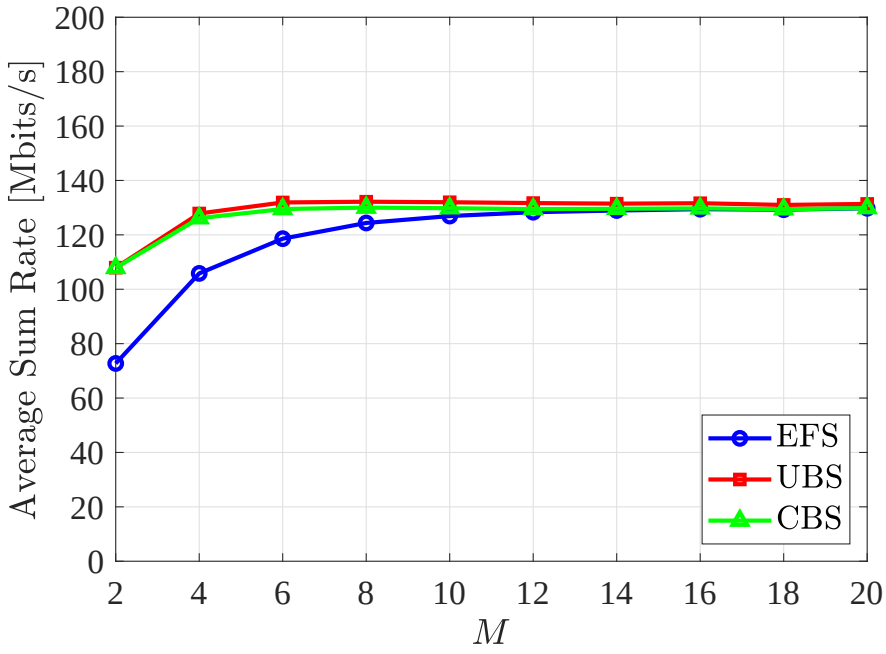

(a) $N_{\mathrm{T}} = 2$

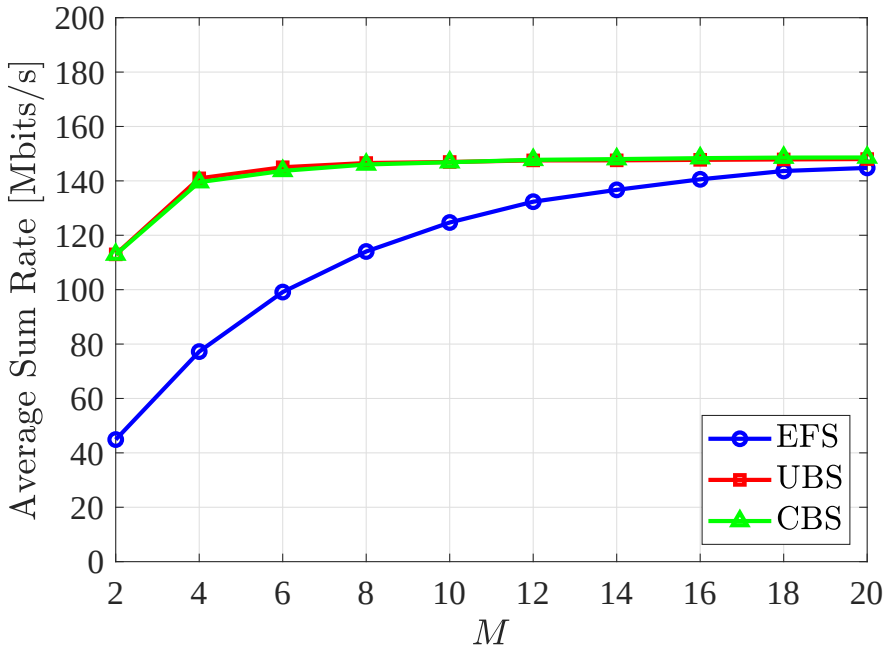

(b) $N_{\mathrm{T}} = 3$

Figure 4.15: *The average sum rate performance for UBS and CBS scheduling policies based on Algorithm* 1 *and Algorithm* 2*, respectively, for different values of* N_{T}.

4.5 Summary

In this chapter, multi-hop wireless optical backhauling is considered to extend the application of wireless optical backhauling to multi-tier networks. To this end, a novel concept of super cell is proposed in which there is a tree topology for each branch that covers all the BSs within the same backhaul branch. As multiple downlink paths pass through one shared bottleneck link, new design challenges arise for efficient use of the limited resources of the bottleneck link. The proposed APC and FPC schemes attempt to reduce the backhaul power. The APC scheme resorts to adapt the operating power of the backhaul system to the minimum required value such that the backhaul capacity is just sufficient to respond to the overall sum rate in the access system. However, it leaves no room for bandwidth sharing. By comparison, the FPC schemes set a fixed point for the backhaul power. The results suggest that an FPC scheme, called FPC2, which uses the average SINR of the access system to adjust the operating power performs better than the one, namely FPC1, which takes the average access rate to find the set point. The former scheme underestimates the required power and leads to significant losses in the terms of the BBO performance. From the perspective of the RTP performance, FPC2 consumes more power relative to APC and FPC1 schemes, but achieves a BBO performance similar to the baseline NPC scheme. This shows that there is an optimum threshold for designing FPC-based schemes that makes a tradeoff between the total power minimization and the bottleneck minimization. The use of FPC1, though offering significant power savings, can lead to 50% BBO probability even when it is used for single or double tier networks. While BBO gives information on the overall bottleneck performance of the backhaul system, it does not provide information on whether the allocated bandwidth bandwidth to individual BSs results in a backhaul bottleneck.

The assignment of the backhaul bandwidth to different BSs in the desired backhaul branch is also an important contributory factor to the overall sum rate performance. The allocation of bandwidth to different BSs involved in a backhaul branch is formulated as a convex optimization problem. Since the underlying objective function is not differentiable in the optimization variables, the solution is derived by applying the projected subgradient method using two criteria: user-based and cell-based scheduling. From a system design point of view, the CBS policy needs less information from the access system to operate than UBS. The results of implementing their algorithms confirm that both policies improve the sum rate performance especially when there is a small number of UEs in the network. These optimal scheduling policies avoid any waste of bandwidth due to unnecessarily giving some of this resource to empty attocells.

Chapter 5
Downlink Base Station Cooperation for Optical Attocell Networks

In this chapter, downlink base station (BS) cooperation using fractional frequency reuse (FFR) is proposed for optical attocell networks. This chapter has the following contributions: 1) Novel spectral efficient cooperative transmission techniques are put forward for optical attocell networks. Inspired by decode-and-forward (DF) relaying protocols from radio frequency (RF) wireless communications, combined with the FFR layout of the network, two cooperative FFR (CFFR) protocols are designed to improve upon the bandwidth management with FFR. A wireless visible light (VL) backhaul system is adopted from Chapter 3 to permit communication between the adjoining attocells. This introduces a new application for wireless optical backhauling proposed in Chapter 3; 2) The CFFR schemes are explicated and thoroughly analyzed. For each scheme, analytical derivations of the downlink signal-to-noise-plus-interference ratio (SINR) and the system spectral efficiency (SE) are presented; 3) The merit of the designed systems is evaluated by studying the statistics of their SE and comparing it with appropriate baseline systems. The optical attocell system model and assumptions are taken from Chapter 3.

The rest of this chapter is organized as follows: Section 5.1 provides system level preliminaries for the underlying FFR system, including the design of sub-bands. Section 5.2 presents the detailed description of the proposed CFFR protocols and gives the SINR and SE derivations. Section 5.3 includes performance results and discussions. Section 5.4 enumerates key points and gives concluding remarks.

5.1 Fractional Frequency Reuse

For orthogonal frequency division multiple access (OFDMA)-based wireless cellular networks, FFR is an effective interference management technique whereby the bandwidth of the cells is partitioned into a number of non-overlapping sub-bands with different frequency reuse factors (FRFs) [118, 119]. In this chapter, the symbol Δ is used to denote FRF. Fig. 5.1 depicts the

layout of a one-tier optical attocell network with FFR planning. The cell coverage splits into central and peripheral (i.e., cell-edge) areas, with two radii R_{c} and R_{e} specifying the interior and the exterior boundaries of the cell, respectively, as shown in Fig. 5.1. The bandwidth of the access system is divided up into four disjoint sub-bands. One common sub-band $\{f_1\}$ is globally assigned to the cell-central regions for all BSs in the network so that $\Delta = 1$, and three protected sub-bands $\{f_2, f_3, f_4\}$ are given to the cell edge regions according to $\Delta = 3$. These three protected sub-bands are distributed in the network in such a way that every three adjacent attocells obtain nonidentical sub-bands in theirs cell-edge regions. The number of subcarriers allocated to the common sub-band, N_{c}, and to each protected sub-band, N_{e}, are given by [118]:

$$N_{\mathrm{c}} = \left\lceil \tilde{N}_{\mathrm{a}} \left(\frac{R_{\mathrm{c}}}{R_{\mathrm{e}}} \right)^2 \right\rceil, \tag{5.1a}$$

$$N_{\mathrm{e}} = \left\lfloor \frac{\tilde{N}_{\mathrm{a}} - N_{\mathrm{c}}}{3} \right\rfloor, \tag{5.1b}$$

where $\tilde{N}_{\mathrm{a}} = \frac{N_{\mathrm{a}}}{2} - 1$ is the number of data-carrying subcarriers for DC-biased optical OFDM (DCO-OFDM) transmission in the access system. the proportion of the cell-interior radius to the cell-exterior radius, i.e., the ratio $\frac{R_{\mathrm{c}}}{R_{\mathrm{e}}}$, is a key parameter for the optimal design of FFR planning and it has a direct impact on the network coverage probability [119]. A low value of this ratio leads to an underutilization of the frequency resources. For optical attocell networks, a value satisfying $\frac{R_{\mathrm{c}}}{R_{\mathrm{e}}} \geq 0.7$ strikes a tradeoff between the coverage probability and the resource utilization [120].

For a given user equipment (UE), the choice of the downlink SINR depends on where the UE is located. The cell-central regions use full reuse (FR) planning, thus receiving inter-cell interference (ICI) from the neighboring BSs. Based on a polar coordinate system in which BS_0 is at the origin, the received SINR per subcarrier for a UE located at the point $z = (r, \theta)$ in the cell-central region is equal to (4.1):

$$\gamma_{\mathrm{FR}}(z) = \frac{\xi_{\mathrm{a}}^{-1}(r^2 + h^2)^{-m-3}}{\sum\limits_{j \in \mathcal{J}_0} (r_j^2(z) + h^2)^{-m-3} + \Omega}, \tag{5.2}$$

where Ω is given by (3.15). As a result of applying FFR planning, the cell-edge regions receive zero ICI from the neighboring BSs. Therefore, by removing the ICI effect from the denominator of the fraction on the right hand side (RHS) of (5.2), the received SINR per subcarrier for a UE

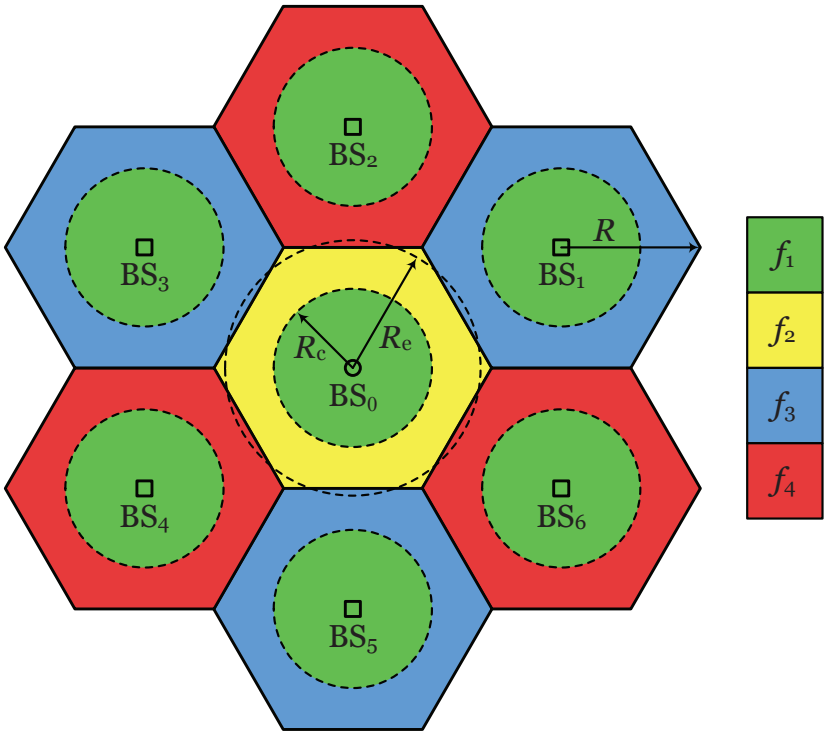

Figure 5.1: *A one-tier optical attocell network with FFR partitioning:* $\Delta = 1$ *for cell-central regions, and* $\Delta = 3$ *for cell-edge regions.*

located at the point z in the cell-edge region simplifies to:

$$\gamma_{\mathrm{FFR}}(z) = \Omega^{-1}\xi_{\mathrm{a}}^{-1}(r^2 + h^2)^{-m-3}. \tag{5.3}$$

5.2 Downlink Base Station Cooperation

The primary cooperation protocol used in this chapter is DF relaying. As an alternative option, amplify-and-forward (AF) relaying is also commonly adopted in cooperative wireless networks [102, 121]. A prominent feature of a DF system is that the signal is independently and fully decoded at every intermediate relay node before proceeding with retransmission to the next node. Hence, various modulation and forward error correction (FEC) techniques can adaptively be implemented for different hops depending on the local link quality. However, the individual implementation of DF relaying at the baseband processing unit of relays incurs additional costs and computational complexities. On the other hand, an AF system is quite simple to implement at relays, as it only requires to retransmit the scaled (i.e., amplified) version of the signal from each relay to its succeeding node. In this case, the signal is not decoded while traveling until

it arrives at the final destination. A major drawback of AF relaying lies in the propagation of noise and interference terms toward the destination node, which in turn limits the end-to-end performance. It is straightforward to extend the analysis framework presented in this chapter to the AF case. The difference is in the way the end-to-end SINR and the achievable end-to-end rate are derived. The design and analysis of cooperative AF relaying systems for the downlink of light fidelity (LiFi) attocell networks is available in [33, 34].

5.2.1 Cooperative Transmission Using FFR

The downlink cooperation necessitates exchanging data between the neighboring BSs, and this requires a backhaul network in place. The one-tier optical attocell network shown in Fig. 5.1 employs a star topology using inter-BS wireless optical backhaul links, with a focus on the case where they operate in the VL band, as described in Section 3.2.1. The cooperative transmission takes place only for the cell edge UEs based on DF relaying in conjunction with FFR planning. To this end, the relays are chosen from among the adjacent BSs to assist with transmitting the downlink data to the desired UE. The principal criterion for selecting the relay BSs is their signal strength at the UE receiver. To prevent generating unnecessary interference for the cell edge regions of the neighboring attocells, the backhaul links use the protected sub-band, which is f_2 for the attocell served by BS_0 as shown in Fig. 5.1. From a system design perspective, the relay downlink is subject to two conditions: 1) not interfere with the direct downlink; 2) allocate the same number of subcarriers to the cell-edge UE as on the direct downlink. According to the FFR layout, there is a free sub-band between BS_0 and every adjacent BS, satisfying both conditions. For instance, f_4 remains unallocated between BS_0 and the three BSs BS_1, BS_3 and BS_5, so it is used for downlink relaying when the relay BSs are among these BSs. The direct and the relay downlinks together constitute parallel channels because they use orthogonal sub-bands. Applying repetition coding to such channels leads to a waste of the system capacity [122], and it is shown to be inefficient [33]. Alternatively, the independent direct and relayed paths are utilized to send different parts of the UE data to enhance the SE.

Next, the proposed cooperative transmission schemes are elaborated, including non-orthogonal decode-and-forward (NODF) and joint transmission with decode-and-forward (JTDF). In order to maintain a reasonable balance between performance and complexity, no more than two relays are involved. In the following, the subscript q is used to indicate the index of the selected relay BS. Also, the operating time slot t is denoted by the superscript (t) where needed. Furthermore,

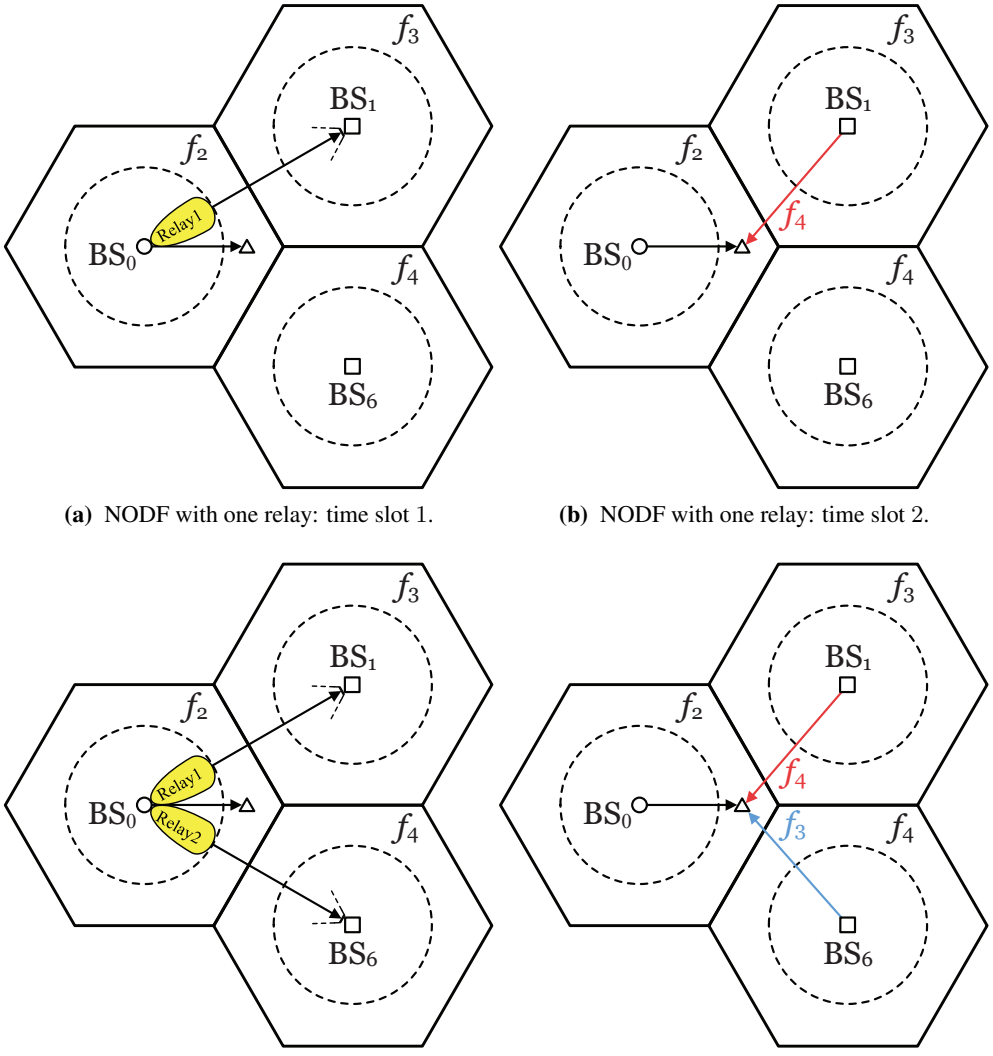

(a) NODF with one relay: time slot 1.

(b) NODF with one relay: time slot 2.

(c) NODF with two relays: time slot 1.

(d) NODF with two relays: time slot 2.

Figure 5.2: *An example of the cooperative downlink transmission in the cell edge region based on the NODF protocol.*

the SINR expressions are given per subcarrier and at the UE location, i.e., at the point $z = (r, \theta)$.

5.2.2 Non-Orthogonal Decode-and-Forward Relaying

The NODF protocol realizes non-orthogonal transmissions in the time domain using two time slots for the direct and the relay downlinks, similar to Protocol I in [121]. Fig. 5.2 illustrates the principle of operation of the NODF protocol through an example. The considered cases using one relay and two relays are separately discussed as follows.

5.2.2.1 NODF with One Relay

Only one relay is used for downlink relaying, which is chosen as the neighboring BS that has the highest DC gain to the desired UE. In particular, the nearest neighboring BS to the UE is selected, since the DC gain is a monotonically decreasing function of the horizontal distance of the UE from the neighboring BSs, see (3.3).

The downlink data intended for the UE is split into three chunks: C_0, C_1 and C_2. During the first time slot, BS_0 transmits C_0 directly to the UE and, at the same time, directs C_1 to BS_q over the corresponding backhaul link, i.e., b_q. During the second time slot, the relay decodes the noisy signal containing C_1 and retransmits the decoded data to the UE, while BS_0 transmits C_2 to the UE.

As shown in Fig. 5.2a, just one backhaul link is activated in time slot 1. Therefore, there is no inter-backhaul interference on the specific set of subcarriers allocated to the desired UE and the backhaul SINR is readily given by (3.7):

$$\gamma_{\mathrm{b}} = \frac{((\ell+1)A_{\mathrm{PD}}R_{\mathrm{PD}})^2 P_{\mathrm{a}}}{72\pi^2 R^4 N_0 B_{\mathrm{b}} \xi_{\mathrm{b}}^2}. \tag{5.4}$$

Considering that the backhaul transmission interferes with the direct downlink in time slot 1, by following the geometric modeling approach in Section 3.2.2 to calculate the backhaul-to-access interference, the received SINR of the UE is derived and expressed as:

$$\gamma_0^{(1)}(z) = \frac{\xi_{\mathrm{a}}^{-1}(r^2+h^2)^{-m-3}}{\left[\frac{(\ell+1)r^\ell}{(m+1)h^m}\right]^2 (r^2+h^2)^{-\ell-3}\cos^{2\ell}(\theta-\Theta_q)+\Omega}. \tag{5.5}$$

From Fig. 5.2b, in time slot 2, the received SINR of the UE on its sub-band with BS_0 is equal to that of the non-cooperative FFR system in (5.3):

$$\gamma_0^{(2)}(z) = \gamma_{\mathrm{FFR}}(z). \tag{5.6}$$

Assuming that BS_q successfully decodes the signal of the link b_q in time slot 1, the received SINR of the UE from its sub-band with BS_q can be derived as:

$$\gamma_q^{(2)}(z) = \frac{\xi_{\mathrm{a}}^{-1}(r_q^2(z)+h^2)^{-m-3}}{\sum\limits_{j\in\mathcal{J}_q}(r_j^2(z)+h^2)^{-m-3}+\Omega}, \tag{5.7}$$

where $\mathcal{J}_q$ is the index set of the interfering BSs with two possibilities depending on the choice of q: $\mathcal{J}_q = \{1, 3, 5\}$ if $q \in \{2, 4, 6\}$; and $\mathcal{J}_q = \{2, 4, 6\}$ if $q \in \{1, 3, 5\}$.

5.2.2.2 NODF with Two Relays

Two adjacent relays are used for downlink relaying. In addition to the first relay, the second relay is also determined by the highest DC gain criterion. In other words, the second nearest neighboring BS to the UE is selected as the second relay to contribute to the downlink cooperation. The UE data is divided up into four chunks: C_0, C_1, C_2 and C_3. During the first time slot, C_0 is directly transmitted to the UE, and concurrently two adjacent backhaul links carry C_1 and C_2 toward the corresponding relays. Subsequently, during the second time slot, BS_0 transmits C_3 directly to the UE and at the same time the relays retransmit C_1 and C_2 to the UE, after successful decoding.

On account of cross-coupling between the two adjacent backhaul links as shown Fig. 5.2c, the inter-backhaul interference arises in time slot 1. The backhaul SINR is calculated in terms of γ_b as follows:

$$\gamma_\mathrm{s} = \frac{\gamma_\mathrm{b}}{4^{-\ell}\gamma_\mathrm{b} + 1}. \tag{5.8}$$

By taking the backhaul interference on the downlink into consideration, the received SINR of the UE in time slot 1 is derived as:

$$\gamma_0^{(1)}(z) = \frac{\xi_\mathrm{a}^{-1}(r^2 + h^2)^{-m-3}}{\left[\frac{(\ell+1)r^\ell}{(m+1)h^m}\right]^2 (r^2+h^2)^{-\ell-3} \sum\limits_{q\in Q} \cos^{2\ell}(\theta - \Theta_q) + \Omega}, \tag{5.9}$$

where $Q = \{q_1, q_2\}$ is the index set of the first and the second relays. According to Fig. 5.2d, the backhaul links are inactive in time slot 2. Therefore, the UE SINR in the direct downlink is $\gamma_0^{(2)}(z) = \gamma_{\mathrm{FFR}}(z)$, similar the case of NODF with one relay. The received SINR of the UE in time slot 2 on its sub-band with BS_{q_1}, $\gamma_{q_1}^{(2)}(z)$, and on its sub-band with BS_{q_2}, $\gamma_{q_2}^{(2)}(z)$, are readily given by (5.7) for $q = q_1$ and $q = q_2$, respectively.

5.2.3 Joint Transmission with Decode-and-Forward Relaying

The JTDF protocol spends a single time slot to complete the data transmission with one or two relays. The principle of operation of this protocol is illustrated using an example in Fig. 5.3.

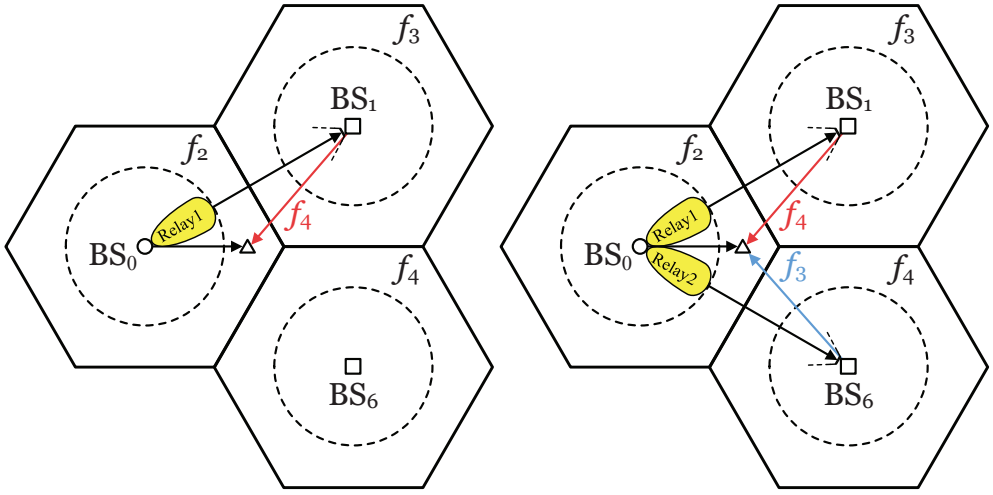

(a) JTDF with one relay. **(b)** JTDF with two relays.

Figure 5.3: *An example of the cooperative downlink transmission in the cell edge region based on the JTDF protocol.*

5.2.3.1 JTDF with One Relay

Only one relay is used, which is chosen in the same way as in NODF. The UE data is segmentized into two independent chunks of C_0 and C_1. Then, C_0 is transmitted over the direct downlink and C_1 through the relay downlink. This protocol opportunistically exploits the time and frequency resources by sending a continuous flow of data through the relay downlink on every time slot, unlike NODF where the relay downlink is active only in the second time slot. Under JTDF with one relay, the received SINR of the UE in the cell edge region on its subbands with BS$_0$ and BS$_q$, denoted by $\gamma_0(z)$ and by $\gamma_q(z)$, are exactly equal to that in (5.5) and that in (5.7), respectively.

5.2.3.2 JTDF with Two Relays

Two adjacent relays are used, similar to NODF with two relays. The UE data is divided into three independent chunks of C_0, C_1 and C_2, which are separately transmitted to the UE through three parallel channels comprising the direct downlink and the two relay downlinks. The received SINR of the UE for the direct downlink, $\gamma_0(z)$, is given by (5.9). The received SINR for the first and the second relay downlinks, denoted by $\gamma_{q_1}(z)$ and $\gamma_{q_2}(z)$, are given by using (5.7) for $q = q_1$ and $q = q_2$, respectively.

In the following, the proposed schemes are referred to as NODF1, NODF2, JTDF1 and JTDF2

for convenience, where the numbers 1 and 2 indicate the number of relays used.

5.2.4 End-to-End Spectral Efficiency

The SE is a proper metric to assess the performance of the proposed cooperative transmission schemes. For DCO-OFDM-based optical attocell networks, the SE at the UE location z can be calculated as a function of the received SINR $\gamma(z)$ with Δ as a parameter [44]:

$$\eta\left(\gamma(z);\Delta\right)=\frac{\xi}{\Delta}\log_2\left(1+\gamma(z)\right). \tag{5.10}$$

For the cell-central region wherein $\Delta=1$, by using (5.4), the SE is:

$$\eta_{\mathrm{FR}}=\eta\left(\gamma_{\mathrm{FR}}(z);1\right)=\xi\log_2\left(1+\gamma_{\mathrm{FR}}(z)\right). \tag{5.11}$$

In the case of non-cooperative FFR, the SE in the cell edge region is calculated by substituting (5.3) and $\Delta=3$ into (5.10) as follows:

$$\eta_{\mathrm{FFR}}=\eta\left(\gamma_{\mathrm{FFR}}(z);3\right)=\frac{\xi}{3}\log_2\left(1+\gamma_{\mathrm{FFR}}(z)\right). \tag{5.12}$$

For CFFR schemes, since different parts of the UE data are received from parallel communication channels, the overall data rate of the UE is simply equal to the sum of the data rates for every channel element. For NODF1, the end-to-end SE in the cell edge region can be calculated as:

$$\eta_{\mathrm{NODF1}}=\frac{\xi}{6}\left[\log_2\left(1+\gamma_0^{(1)}(z)\right)+\log_2\left(1+\gamma_0^{(2)}(z)\right)+\log_2\left(1+\min\left[\gamma_{\mathrm{b}},\gamma_q^{(2)}(z)\right]\right)\right], \tag{5.13}$$

where a factor $\frac{1}{2}$ arises from the use of two time slots; and $\min\left[\gamma_{\mathrm{b}},\gamma_q^{(2)}(z)\right]$ is the equivalent end-to-end SINR for the dual-hop DF relaying downlink through BS_q. For NODF2, the end-to-end SE can be expressed as:

$$\eta_{\mathrm{NODF2}}=\frac{\xi}{6}\times \left[\log_2\left(1+\gamma_0^{(1)}(z)\right)+\log_2\left(1+\gamma_0^{(2)}(z)\right)+\sum_{q\in Q}\log_2\left(1+\min\left[\gamma_{\mathrm{s}},\gamma_q^{(2)}(z)\right]\right)\right], \tag{5.14}$$

where $Q = \{q_1, q_2\}$. In a similar way, the end-to-end SE in the cell edge region for JTDF1 and JTDF2 are obtained as follows:

$$\eta_{\mathrm{JTDF1}} = \frac{\xi}{3}\left[\log_2\left(1+\gamma_0(z)\right) + \log_2\left(1+\min\left[\gamma_{\mathrm{b}}, \gamma_q^{(2)}(z)\right]\right)\right], \tag{5.15}$$

$$\eta_{\mathrm{JTDF2}} = \frac{\xi}{3}\left[\log_2\left(1+\gamma_0(z)\right) + \sum_{q\in Q}\log_2\left(1+\min\left[\gamma_{\mathrm{s}}, \gamma_q^{(2)}(z)\right]\right)\right]. \tag{5.16}$$

5.3 Numerical Results and Discussions

This section presents numerical results for the average SE performance of the proposed CFFR transmission schemes. To this end, a Monte Carlo simulation is set up in which the UE coordinates are randomly distributed in the cell coverage. The spectral efficiencies for different schemes are measured per random realization based on Section 5.2. The results are obtained by statistical averaging over a large number of samples. Two baseline scenarios are included for comparison: 1) a FR system whereby the downlink bandwidth is entirely reused across all attocells in the network without frequency reuse planning; 2) a non-cooperative FFR system as described in Section 5.1. The simulation parameters are the same as those listed in Table 3.1. Also, the ratio between the cell-interior and the cell-exterior radii is set to $\frac{R_{\mathrm{c}}}{R_{\mathrm{e}}} = 0.75$.

Fig. 5.4 plots the cumulative distribution function (CDF) of the SE for FR, FFR, CFFR-NODF and CFFR-JTDF systems. There are two cases for the emission semi-angle of the backhaul light emitting diodes (LEDs): $\Phi_{\mathrm{b}} = 10^\circ$ and $\Phi_{\mathrm{b}} = 20^\circ$ as shown in Fig. 5.4a and Fig. 5.4b, respectively. First of all, it is observed that the SE is distributed between two finite values, since the downlink SINR is a bounded random variable as discussed in Chapter 3. There is a threshold above which all the CDF curves overlap. Below that threshold, the difference in the SE statistics for different systems is evident. This difference is more pronounced in the case where $\Phi_{\mathrm{b}} = 10^\circ$. Such a breaking point in the CDF plots can be justified by considering unequal resource distributions in the cell-central and cell-edge regions. Furthermore, the lower bound performance belongs to the FR system and the upper bound of the SE is globally attained by a CFFR-JTDF scheme with two relays. Regardless of the number of relays used, CFFR-NODF performs significantly better than FFR, and CFFR-JTDF delivers a remarkably higher performance than CFFR-NODF. However, increasing the number of relays from 1 to 2 slightly improves the performance of the CFFR systems.

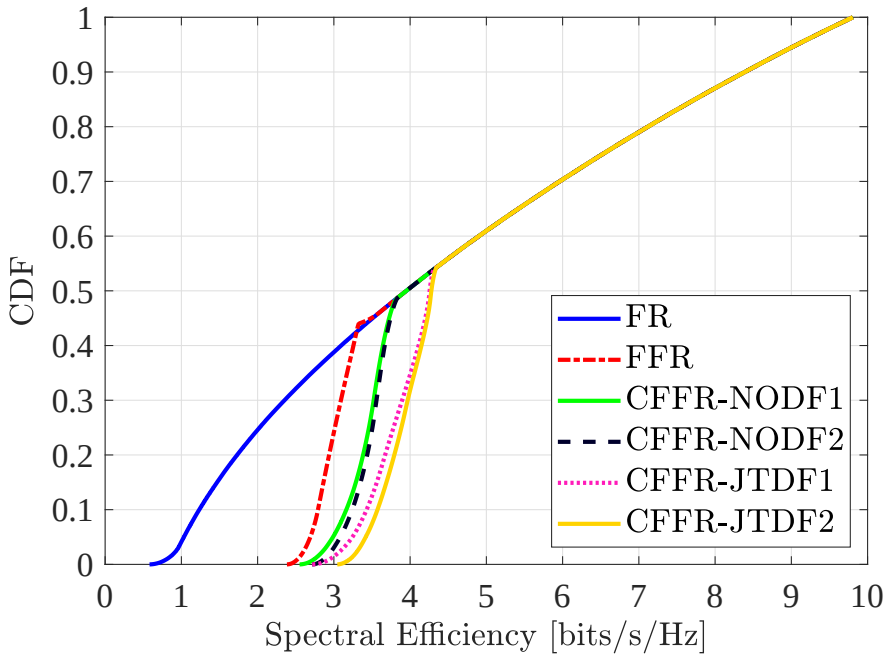

(a) $\Phi_{\mathrm{b}} = 10^{\circ}$.

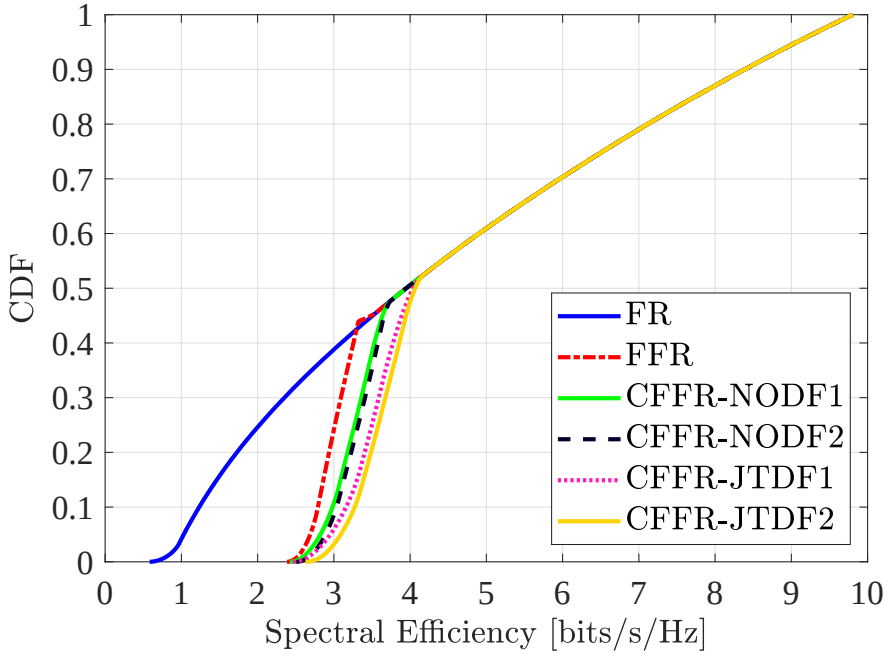

(b) $\Phi_{\mathrm{b}} = 20^{\circ}$.

Figure 5.4: *The statistics of the UE SE for FR, FFR, CFFR-NODF and CFFR-JTDF systems.*

To gain more into the performance of the proposed schemes, the cell coverage is divided into 10 rings with equal areas and the spatial distribution of the SE is studied with an emphasis on the outer rings corresponding to ring indexes $n = 6, 7, 8, 9, 10$. These ring indexes, in fact,

	Ring n	FFR	NODF1	NODF2	JTDF1	JTDF2
$\Phi_{\mathrm{b}} = 10^{\circ}$	6	0.018	0.154	0.177	0.291	0.336
	7	0.468	0.861	0.917	1.255	1.367
	8	0.991	1.423	1.475	1.855	1.958
	9	1.401	1.874	1.921	2.347	2.440
	10	1.576	1.975	2.038	2.374	2.500
$\Phi_{\mathrm{b}} = 20^{\circ}$	6	0.018	0.132	0.155	0.247	0.291
	7	0.467	0.759	0.814	1.052	1.162
	8	0.992	1.253	1.302	1.515	1.613
	9	1.399	1.625	1.668	1.850	1.936
	10	1.575	1.738	1.793	1.901	2.011

Table 5.1: *Average SE improvements for FFR, CFFR-NODF and CFFR-JTDF schemes relative to the FR system.*

represent the cell edge region. Fig. 5.5a shows the average SE over each ring around BS_0 for $\Phi_{\mathrm{b}} = 10^{\circ}$. It can be verified that the performance of the CFFR-NODF2 and CFFR-JTDF2 schemes are marginally higher than the CFFR-NODF1 and CFFR-JTDF1 schemes, respectively. Despite these little improvements, employing the second relay doubles the complexity of signal processing. Also, it can be observed that the use of JTDF relaying gives rise to considerable improvements compared with its NODF counterpart. The reason JTDF outperforms NODF is that JTDF takes advantage of transmitting data on all available channels in the time, space and frequency domains, thus maximizing the SE.

Fig. 5.5b demonstrates the average SE performance per ring around BS_0 for $\Phi_{\mathrm{b}} = 20^{\circ}$. Compared with Fig. 5.4a, it can be observed that the performance improvement for both NODF and JTDF schemes is decreased from $n = 6$ to 10. At $n = 10$ (i.e., the outermost ring in the cell edge region), the performance for all the FFR and CFFR systems become almost equal to one another. The increase of Φ_{b} intensifies the backhaul-to-access interference, which in turn compromises the performance gains achieved by the NODF and JTDF schemes especially in the outer rings.

Table 5.1 summarizes the results for the performance improvement of the FFR system and the CFFR system with NODF and JTDF schemes with respect to the FR system. For $\Phi_{\mathrm{b}} = 10^{\circ}$, when compared with the FFR case, JTDF1 and JTDF2 achieve relative improvements of 0.798 bits/s/Hz and 0.924 bits/s/Hz, respectively, in the average SE. For NDF1 and NDF2, this is 0.399 bits/s/Hz and 0.462 bits/s/Hz, respectively. The relative improvements of JTDF2 and NDF2 over JTDF1 and NDF1 are 0.126 bits/s/Hz and 0.063 bits/s/Hz, respectively.

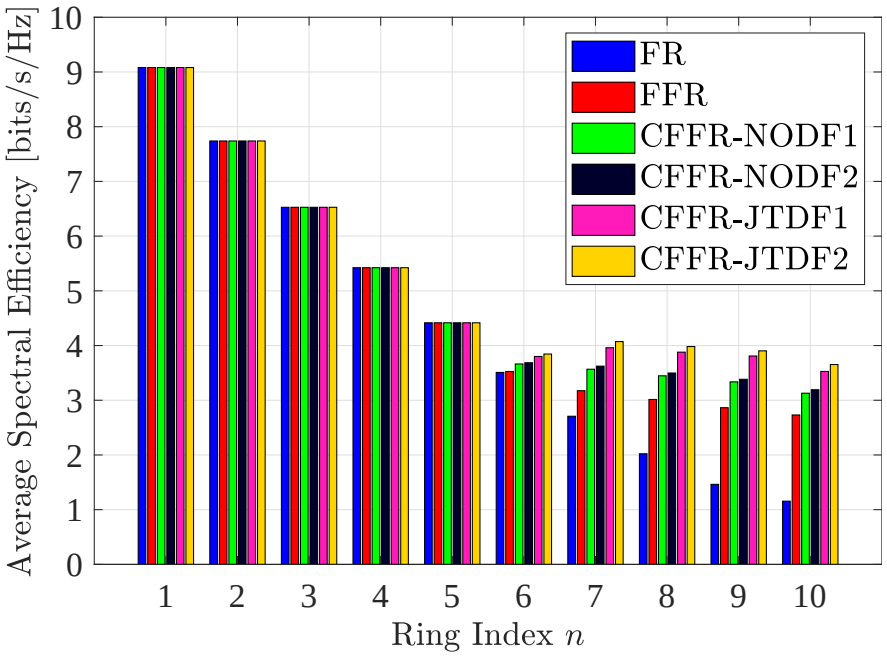

(a) $\Phi_{\mathrm{b}} = 10^{\circ}$.

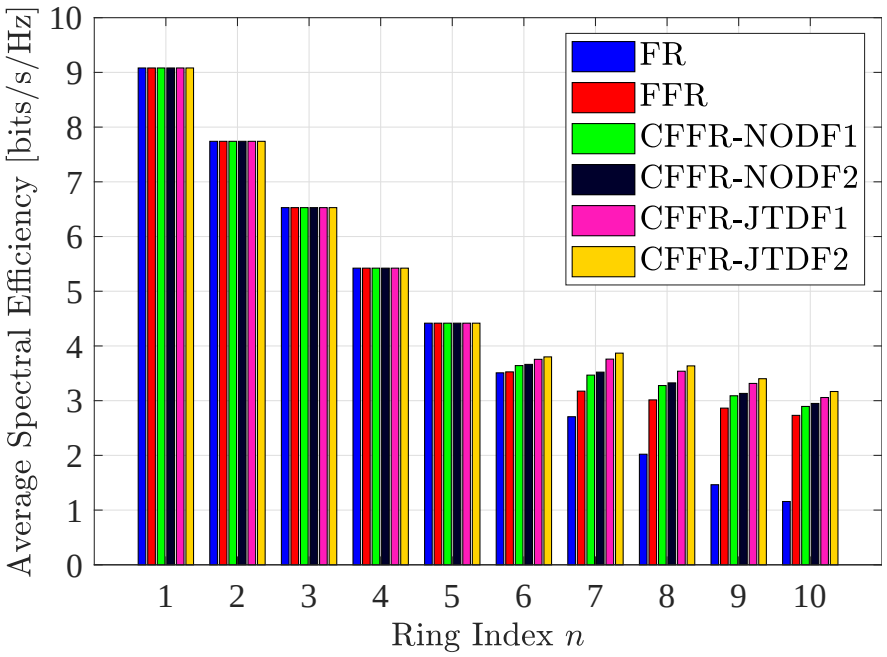

(b) $\Phi_{\mathrm{b}} = 20^{\circ}$.

Figure 5.5: *The average SE performance per ring around BS_0 for FR, FFR, CFFR-NODF and CFFR-JTDF systems.*

5.4 Summary

In this chapter, novel downlink cooperation techniques are proposed for indoor optical attocell networks, building on the wireless VL backhauling approach. By using FFR cell partitioning as the basis, two main cooperative FFR protocols are identified and elaborated: CFFR-NODF and CFFR-JTDF. Each protocol has an option to use one or two relay-assisted transmissions on the unused sub-bands from the underlying FFR planning. The downlink SINR and the SE at the UE receiver are analytically derived for each case. The average SE performance for both protocols is studied. The CFFR-JTDF protocol globally attains a superior performance in the cell-edge region, as it takes the opportunity of transmitting over every possible path in time, frequency and space dimensions. In addition, both CFFR-NODF and CFFR-JTDF outperform the baseline FR and FFR scenarios. Although the cooperative FFR protocols noticeably improve the performance relative the non-cooperative case, involving the second relay in downlink cooperation does not return a comparable improvement in the overall performance. To reach higher gains out of the proposed schemes, the backhaul-induced interference on the downlink needs to be properly managed, which is subject to a careful adjustment of the light emission pattern in the backhaul system. Notwithstanding the VL backhauling approach is employed to form cooperation channels between the BSs, the design and analysis principles presented in this chapter apply to any wireless optical communication technology for backhaul such as infrared (IR) communication.

Chapter 6
Conclusions and Future Works

6.1 Summary and Conclusions

In this thesis, the general objective was to devise and investigate wireless backhauling for indoor light fidelity (LiFi) attocell networks on the basis of wireless optical communications. A series of fundamental studies related to the functionality of and the system level performance of wireless optical backhauling were presented. To the best of the authors knowledge, this is the first comprehensive study in this context. The contribution of this thesis was threefold: First, a novel analytical framework was proposed for modeling, designing and optimization of wireless optical backhaul systems. The analysis includes the detailed derivation of the signal-to-noise-plus-interference ratio (SINR) and the end-to-end sum rate for the downlink of multi-user optical attocell networks in the presence of the backhaul interference. Also, full reuse visible light (FR-VL) and in-band visible light (IB-VL) techniques were proposed for visible light (VL) backhanding to allow the wireless VL access and backhaul systems to operate in the same indoor environment. In addition, the employment of the infrared (IR) band in wireless optical backhaul links was considered and analyzed. Moreover, a power optimization approach was proposed to optimally reduce the transmission power of backhaul. Second, by extending the problem scenario to multi-tier networks, a generalized analysis of the end-to-end performance was conducted. The conditions under which backhaul becomes the bottleneck for end-to-end networking were identified. To utilize the limited power and bandwidth resources of the backhaul system, novel power control schemes and bandwidth scheduling policies were proposed, including adaptive power control (APC), fixed power control (FPC), user-based bandwidth scheduling (UBS) and cell-based bandwidth scheduling (CBS). Finally, two cooperative transmission schemes were proposed and investigated for the downlink of optical attocell networks. The proposed schemes combine fractional frequency reuse (FFR) cell partitioning with decode-and-forward (DF) relaying to improve upon the inter-cell interference (ICI) suppression advantage of FFR for cell-edge regions.

In Chapter 2, the relevant background on the operation principles of optical attocell networks has been presented. Firstly, an overview of the basic definitions regarding optical attocells have

been given. Furthermore, the essential concepts and components of an optical attocell downlink system have been concisely discussed, which include the visible light communication (VLC) front-end elements, the indoor propagation channel, the frequency domain characteristics of the free space propagation channel, the bandwidth limitation due to the front-end elements, and optical orthogonal frequency division multiplexing (OFDM). Then, the focus has turned to the building blocks of a DC-biased optical OFDM (DCO-OFDM) communication system. In addition, the achievable rate of a DCO-OFDM link has been established. To this end, both the achievable spectral efficiency and the maximum signaling rate have been calculated. Finally, a brief review of prior studies related to the problem of backhauling for VLC system has been presented.

In Chapter 3, a novel wireless optical backhauling approach has been proposed for indoor optical attocell networks. By means of the proposed solution, the attocells reach the gateway through multi-hop wireless optical paths in the backhaul network. When using the VL band for backhauling based on FR-VL and IB-VL backhaul systems, the downlink performance depends to a large extent on the semi-angle of the light emitting diodes (LEDs) used in the backhaul links, i.e., Φ_{b}. By tuning the value of Φ_{b}, a better performance was achieved for a smaller value of Φ_{b}. Therefore, to attain a higher performance, the value of Φ_{b} needs to be minimized, though subject to practical limitations. For white LEDs, a narrow light emission can be produced by using proper optical lenses. In addition, to divide the VLC bandwidth between the access and backhaul systems based on the IB-VL backhaul system, the bandwidth allocation ratio was optimally adjusted for the entire network according to the rate distribution in the access system. This optimal value has been shown to be inversely proportional to the aggregate access sum rate corresponding to the backhaul branch with the maximum access sum rate over all branches of the backhaul network. In addition, it was concluded that, although IB-VL backhauling is a means to eliminate the backhaul interference effect, FR-VL backhanding leads to a significantly better performance when considering the network as a whole. Furthermore, the optimization conducted on the sum power of the backhaul system revealed a fundamental technical challenge as the backhaul power could not be reduced below the full power, even for small values of Φ_{b}. Therefore, the migration of wireless optical backhauling to alternative optical bands turned out to be an inevitable choice. By choosing the IR band as a possible option that provides a higher modulation bandwidth, the results were promising. The operating point for the power and bandwidth of the IR backhaul system were determined according to the power-bandwidth tradeoff characteristics. IR backhauling was shown to be

a viable solution to for networks with more than one tier. For the IR backhaul system, given a modulation bandwidth of only three times the bandwidth of the downlink VLC system, the backhaul transmission power was successfully reduced by factor of 100 times relative to the full power operation without influencing the network performance. Concerning misalignment in backhaul links, the impact of the orientation angle error varying in a given range has been found insignificant when Φ_{b} was properly set below a threshold value depending on the error magnitude. In other words, an appropriate choice for the semi-angle of the backhaul LEDs, which was not too small, has made the entire system robust against possible pointing errors.

In Chapter4, multi-hop wireless optical backhauling has been considered to extend the application of wireless optical backhauling to multi-tier networks. To this end, a novel concept of super cell has been introduced. New design challenges arose for efficient use of the limited resources of the bottleneck link. The proposed APC and FPC schemes have been designed to reduce the backhaul power. The APC scheme adapted the operating power of the backhaul system to the minimum required value such that the backhaul capacity was just sufficient to respond to the overall sum rate in the access system. However, it left no room for bandwidth sharing. By comparison, the FPC schemes set a fixed point for the backhaul power. The results suggested that FPC2, which used the average SINR of the access system to adjust the operating power performed better than the one, namely FPC1, which took the average access rate for finding the set point. The former scheme underestimated the required power and led to significant losses in the terms of the backhaul bottleneck occurrence (BBO) performance. From the perspective of the relative total power (RTP) performance, FPC2 consumed more power relative to APC and FPC1 schemes, but achieved a BBO performance similar to the baseline NPC scheme. This showed that there is an optimum threshold for designing FPC-based schemes that makes a tradeoff between the total power minimization and the bottleneck minimization. The use of FPC1, though offering significant power savings, led to 50% BBO probability even when it was used for single or double tier networks.

The assignment of the backhaul bandwidth to different base stations (BSs) in the desired backhaul branch was also an important contributory factor to the overall sum rate performance. The allocation of bandwidth to different BSs involved in a backhaul branch was formulated as a convex optimization problem. Since the underlying objective function was not differentiable in the optimization variables, the solution was derived by applying the projected subgradient method using two criteria: user-based and cell-based scheduling. From a system design point

of view, the CBS policy needed less information from the access system to operate than UBS. The results of implementing their algorithms confirmed that both policies improve the sum rate performance especially when there was a small number of user equipments (UEs) in the network. These optimal scheduling policies avoided any waste of bandwidth due to unnecessarily giving some of the bandwidth resource to empty attocells.

In Chapter 5, through the use of VL backhauling, novel downlink cooperation techniques have been proposed for indoor optical attocell networks. based on FFR planning, cooperative FFR (CFFR)-non-orthogonal decode-and-forward (NODF) and CFFR-joint transmission with decode-and-forward (JTDF) have been introduced and analyzed. Each protocol could use one or two relays to assist with the downlink transmissions. The operating band of the relay downlink has been chosen as the free sub-band between the two cooperating BSs. Analytical expressions of the downlink SINR and the UE spectral efficiency (SE) have derived for each case. Both CFFR-NODF and CFFR-JTDF outperformed the baseline full reuse (FR) and FFR scenarios. In addition, the CFFR-JTDF protocol globally attained a higher average SE performance in the cell-edge region. This was because CFFR-JTDF made use of every possible path in time, frequency and space dimensions for transmitting in the downlink. Although the cooperative FFR protocols noticeably improved the performance relative the non-cooperative case, involving the second relay in downlink cooperation did not return a comparable improvement in the overall performance. Although the VL backhauling approach has been employed to form cooperation channels between the BSs, the design and analysis principles presented in this chapter apply to any wireless optical backhaul technology including the IR case.

6.2 Limitations and Future Directions

In the analysis presented in this thesis, the most important factors that contribute into the downlink performance with wireless optical backhauling have been considered. However, a number of simplifying assumptions have been used to make the analysis more tractable because in some cases, no related analytical tool is available in the literature. Moreover, studies conducted in this thesis are purely based on mathematical analysis or computer simulations. Experimental research is thus needed to verify the presented results. In what follows, a number of research findings and limitations are identified to inspire potential future directions in the fast developing technology of LiFi.

Currently, most studies on indoor LiFi networks rely on either an experimental approach or an idealist model for the backhaul network. In this regard, experimental works are carried out for small networks with a few LED lamps to examine their backhaul connectivity. For example, to model and assess the Ethernet backhaul, only one access point (AP) is considered in [39]. Or, to model the power line communication (PLC) network, only four LED light fixtures are taken into consideration in [38]. Therefore, there is a lack of a comprehensive study on modeling and applying the existing wired backhaul solutions to indoor LiFi networks with a large number of APs. This might entail intricate physical layer (PHY) system and channel modeling which is challenging to consider in practice, but it is an important step toward establishing scalable topologies for optical attocell networks in the future.

For wireless optical backhauling proposed in this work, only the line-of-sight (LOS) propagation model is considered to render the analytical derivations tractable. Although it is true that by making the backhaul links highly directional, the interference of backhaul links can be taken under control, there are practical limitations that impede this to happen in reality. For instance, the semi-angle of white LEDs, whose output emission follows a Lambertian model, cannot be made very narrow unless appropriate optical equipment such as lenses are used. Alternatively, some commercial IR LEDs are equipped with integrated lenses so that their semi-angle can be as small as $10°$-$15°$. By means of laser diodes, the emission semi-angle can be in the order of a few degrees. Therefore, it is suggested to do experimental research studies on the feasibility of these methods for use in wireless optical backhauling of indoor networks. It would be useful to measure the backhaul interference and its relation to the semi-angle of backhaul LEDs in realistic scenarios, among other practical considerations.

An important functionality of any backhaul network is the ability to support bidirectional networking. In this work, the assumption that downstream and upstream directions can be realized with two non-interfering optical bands is used so that the two directions become independent of each other. From a PHY standpoint, it is possible to employ different wavelengths for downstream and upstream directions to realize bidirectional communications in the backhaul links. However, in the context of backhaul networks, bidirectional data communications is not related only to the air interface. In general, this is a cross-layer issue which, on the one hand, requires a solid understanding of the PHY characteristics of LiFi networks, and on the other hand, needs the medium access control (MAC) and network-layer modeling of data traffic flows in backhaul networks. Therefore, focusing only on PHY aspects does not provide a complete picture on the

functionality of the backhaul network. This is subject to careful research in the future.

One of the interesting problems in the scope of multi-hop wireless optical backhauling relates to latency. Unlike the case in outdoor radio frequency (RF) cellular networks with a multi-hop wireless backhaul infrastructure where latency is more attributed to the end-to-end link distance, this is not an issue for indoor scenarios because in the first place the dimensions of interior spaces are significantly smaller than those of outdoor sites. Despite shorter distances, indoor access networks are more likely to be under heavy data traffic loads on account of the fact that most of the data traffic originate from inside buildings. For this reason, the deployed backhaul network requires to properly respond to asymmetric data traffic patterns so as to avoid congestion. This is where load balancing techniques come into play. Target algorithms need to address the end-to-end throughput-latency tradeoff. In this context, latency becomes location dependent in light of congestion control and processing delays taking place at intermediate nodes. Such a problem is even more challenging when considering multi-cell multi-user LiFi networks, which opens a new avenue for future research.

Furthermore, the proposed super cells put a number of attocells together to connect all of them to the core network via the centrally located gateway. Therefore, if for some reason the central node is disconnected from the backbone network, the entire attocells within a super cell would experience access outage, without considering diversity routes to support multiple connected attocells under such failures. This issue points out resilience and implies the necessity of investigating the underlying network architecture. One possible direction is to consider the number of gateways required to achieve a certain degree of resilience. By increasing the deployment of gateways, more degrees of freedom are available to provide alternative connection paths in the event of failure. The optimal placement of gateways is another important design goal. Tackling these challenges need novel performance metrics and analytical methodologies to address the specifications of indoor LiFi networks with wireless optical backhauling.

Last but not least, although the proposed cooperative transmission techniques show potential benefits of adopting downlink cooperation for a single attocell by means of dual-hop wireless optical relaying and reuse partitioning, the scalability of such combined schemes need to be examined for multi-cell multi-user networks. More specifically, performing cooperative FFR transmission is subject to the availability of free sub-bands from the neighboring attocells, yet those resources might already be occupied by their own users, in which case downlink cooperation is not possible due to the lack of a cooperative transmission path. Therefore, there

is an inherent tradeoff for reserving some resources for cooperation, while otherwise they can be utilized to improve the performance of their original attocells. A careful understanding of this tradeoff and proper modeling of the associated optimization problem for multi-cell multi-user optical attocell networks entails an independent study in the future.

Appendix A
Proof of Proposition 1

For BS_0, always the entire visible light communication (VLC) bandwidth is used to serve the associated user equipments (UEs) for both full reuse visible light (FR-VL) and in-band visible light (IB-VL) cases. Under IB-VL backhauling in particular, the operating band of the downlink for BS_0 overlaps in part with that of the backhaul system and hence the backhaul interference affects the overlapping part. Concerning the number of UEs in the attocell of BS_0, two possible cases are considered: single-user case where $M_0 = 1$; and multi-user case where $M_0 > 1$. These cases are separately addressed in the following. In this appendix, for convenience of presentation, the UEs associated with BS_0 are labeled from 1 to M_0; that is $\mathcal{U}_0 = \{1, 2, \ldots, M_0\}$. The received signal-to-noise-plus-interference ratio (SINR) of the uth UE on subcarrier k can be mathematically expressed by using:

$$\gamma_{u,k} = \begin{cases} \gamma_u^{\text{IB-VL}}, & \text{if } k \in \mathcal{K}_\mathrm{a} \\ \gamma_u^{\text{FR-VL}}, & \text{if } k \in \mathcal{K}_\mathrm{b} \end{cases}, \ \forall u \in \mathcal{U}_0 \tag{A.1}$$

where $\gamma_u^{\text{IB-VL}}$ and $\gamma_u^{\text{FR-VL}}$ are explicitly given by (3.17) and (3.12), respectively. In addition, $\mathcal{K}_\mathrm{a} = \{1, 2, \ldots, \delta\tilde{N}\}$ and $\mathcal{K}_\mathrm{b} = \{\delta\tilde{N} + 1, \delta\tilde{N} + 2, \ldots, \tilde{N}\}$ represent two disjoint subcarrier index sets for access and backhaul systems, respectively, such that $\mathcal{K}_\mathrm{a} \cup \mathcal{K}_\mathrm{b} = \{1, 2, \ldots, \tilde{N}\}$. To support the following analysis, a conceptual diagram is provided in Fig. A.1, highlighting the effect of the bandwidth allocation to access and backhaul systems on the subcarrier assignment to the UEs served by BS_0.

1) Single User ($M_0 = 1$)

When there is only one UE in the attocell of BS_0, all the available subcarriers are exclusively owned by that UE as depicted in Fig. A.1a. According to the proportion δ to divide the total bandwidth of B, allocating the bandwidth fraction δB to the access system is equivalent to giving $\delta\tilde{N}$ data-carrying subcarriers. Note that $\delta\tilde{N}$ is not necessarily an integer but this is not a major concern as long as $\tilde{N} \gg 1$, since the difference between the real value of $\delta\tilde{N}$

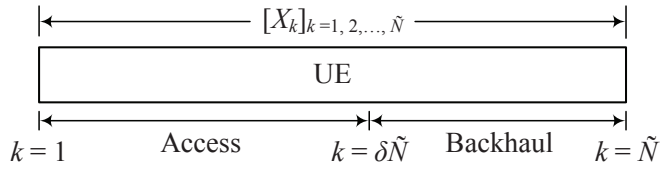

(a) Single User ($M_0 = 1$)

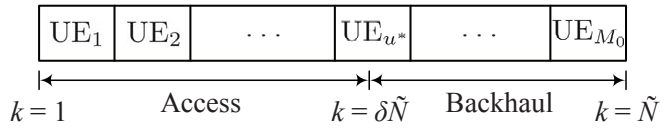

(b) Multi-User ($M_0 > 1$)

Figure A.1: *DCO-OFDM frame for the downlink of BS$_0$ under IB-VL backhauling.*

and its integer part is always less than unity. By means of IB-VL backhauling, the backhaul interference is perfectly canceled over all attocells except for BS$_0$ where the backhaul system still partly interferes with the downlink transmission. From (A.1), the overall downlink data rate for BS$_0$ is obtained as:

$$\mathcal{R}_0^{\text{IB-VL}} = \sum_{k=1}^{\tilde{N}} \frac{2B}{N} \log_2\left(1+\gamma_{u,k}\right), \tag{A.2a}$$

$$= \sum_{k=1}^{\delta\tilde{N}} \frac{2B}{N} \log_2\left(1+\gamma_u^{\text{IB-VL}}\right) + \sum_{k=\delta\tilde{N}+1}^{\tilde{N}} \frac{2B}{N} \log_2\left(1+\gamma_u^{\text{FR-VL}}\right), \tag{A.2b}$$

$$= \xi\delta B \log_2\left(1+\gamma_u^{\text{IB-VL}}\right) + \xi(1-\delta)B \log_2\left(1+\gamma_u^{\text{FR-VL}}\right). \tag{A.2c}$$

In (A.2b), the fact that $\gamma_u^{\text{IB-VL}}$ and $\gamma_u^{\text{FR-VL}}$ are independent of k are used to arrive at (A.2c).

2) Multi-User ($M_0 > 1$)

In the case where there are $M_0 > 1$ UEs in the attocell of BS$_0$, they are arbitrarily labeled from 1 to M_0 and each UE is preallocated an equal bandwidth of $\frac{B}{M_0}$ as illustrated in Fig. A.1b. Let $\mathcal{K}_u$ be the set that contains subcarrier indexes assigned to the uth UE by BS$_0$, satisfying $\cup_{u=1}^{M_0}\mathcal{K}_u = \{1,2,\ldots,\tilde{N}\}$. Fig. A.1b also underlines the event that the threshold $k = \delta\tilde{N}$ occurs in-between the subcarrier set of one of the UEs for $u = u^*$. For this specific UE, some of the subcarriers are in $\mathcal{K}_\text{a}$ while the rest of them are in $\mathcal{K}_\text{b}$. Note that $\mathcal{K}_{u^*}$ is neither a subset of $\mathcal{K}_\text{a}$ nor a subset of $\mathcal{K}_\text{b}$, whereas $\mathcal{K}_u \in \mathcal{K}_\text{a}$ for $u < u^*$; and $\mathcal{K}_u \in \mathcal{K}_\text{b}$ for $u > u^*$. Also, it is reasonable to assume that $\tilde{N} \gg M_0$. Therefore, $|\mathcal{K}_u| = \frac{\tilde{N}}{M_0}$ where $\frac{\tilde{N}}{M_0}$ is assumed to be an

integer using the same reasoning as stated for $\delta\tilde{N}$ in the single user case. To further elaborate, it can be deduced from Fig. A.1b that u^* satisfies the following inequalities:

$$\begin{cases} \delta\tilde{N} - (u^*-1)\frac{\tilde{N}}{M_0} > 0, \\ \delta\tilde{N} - u^*\frac{\tilde{N}}{M_0} \leq 0, \end{cases} \quad \Rightarrow \quad \boxed{\delta M_0 \leq u^* < \delta M_0 + 1} \tag{A.3}$$

With the aid of (A.1) and (A.3), the multi-user sum rate for BS_0 under IB-VL backhauling is derived according to the steps as explicated below:

$$\mathcal{R}_0^{\text{IB-VL}} = \sum_{u=1}^{M_0} \sum_{k\in\mathcal{K}_u} \frac{2B}{N} \log_2\left(1+\gamma_{u,k}\right), \tag{A.4a}$$

$$= \underbrace{\sum_{u=1}^{u^*-1} \sum_{k\in\mathcal{K}_u} \frac{2B}{N} \log_2\left(1+\gamma_{u,k}\right)}_{u<u^*,\ \mathcal{K}_u\subset\mathcal{K}_\mathrm{a}} + \underbrace{\sum_{k\in\mathcal{K}_{u^*}} \frac{2B}{N} \log_2\left(1+\gamma_{u^*,k}\right)}_{u=u^*} +$$

$$\underbrace{\sum_{u=u^*+1}^{M_0} \sum_{k\in\mathcal{K}_u} \frac{2B}{N} \log_2\left(1+\gamma_{u,k}\right)}_{u>u^*,\ \mathcal{K}_u\subset\mathcal{K}_\mathrm{b}}, \tag{A.4b}$$

$$= \sum_{u=1}^{u^*-1} \sum_{k\in\mathcal{K}_u} \frac{2B}{N} \log_2\left(1+\gamma_u^{\text{IB-VL}}\right) + \underbrace{\sum_{k=\frac{(u^*-1)\tilde{N}}{M_0}+1}^{\delta\tilde{N}} \frac{2B}{N} \log_2\left(1+\gamma_{u^*}^{\text{IB-VL}}\right)}_{u=u^*,\ k\in\mathcal{K}_\mathrm{a}} +$$

$$\underbrace{\sum_{k=\delta\tilde{N}+1}^{\frac{u^*\tilde{N}}{M_0}} \frac{2B}{N} \log_2\left(1+\gamma_{u^*}^{\text{FR-VL}}\right)}_{u=u^*,\ k\in\mathcal{K}_\mathrm{b}} + \sum_{u=u^*+1}^{M_0} \sum_{k\in\mathcal{K}_u} \frac{2B}{N} \log_2\left(1+\gamma_u^{\text{FR-VL}}\right), \tag{A.4c}$$

$$= \sum_{u=1}^{u^*-1} |\mathcal{K}_u| \frac{2B}{N} \log_2\left(1+\gamma_u^{\text{IB-VL}}\right) + \left(\delta\tilde{N} - \frac{(u^*-1)\tilde{N}}{M_0}\right) \frac{2B}{N} \log_2\left(1+\gamma_{u^*}^{\text{IB-VL}}\right)$$

$$+ \left(\frac{u^*\tilde{N}}{M_0} - \delta\tilde{N}\right) \frac{2B}{N} \log_2\left(1+\gamma_{u^*}^{\text{FR-VL}}\right) + \sum_{u=u^*+1}^{M_0} |\mathcal{K}_u| \frac{2B}{N} \log_2\left(1+\gamma_u^{\text{FR-VL}}\right), \tag{A.4d}$$

$$= \frac{\xi B}{M_0} \sum_{u=1}^{u^*-1} \log_2\left(1+\gamma_u^{\text{IB-VL}}\right) + (\delta M_0 - u^* + 1) \frac{\xi B}{M_0} \log_2\left(1+\gamma_{u^*}^{\text{IB-VL}}\right) +$$

$$(u^* - \delta M_0) \frac{\xi B}{M_0} \log_2\left(1+\gamma_{u^*}^{\text{FR-VL}}\right) + \frac{\xi B}{M_0} \sum_{u=u^*+1}^{M_0} \log_2\left(1+\gamma_u^{\text{FR-VL}}\right), \tag{A.4e}$$

where $|\mathcal{K}_u| = \frac{\tilde{N}}{M_0}$ is used in (A.4d) to arrive at (A.4e). Note that the exact value of u^* is tightly bounded by (A.3) and therefore it can be given by $u^* = \lfloor \delta M_0 + 1 \rfloor$. By substituting this into the last result in (A.4e), one obtains:

$$\mathcal{R}_0^{\text{IB-VL}} = \frac{\xi B}{M_0} \sum_{u=1}^{\lfloor \delta M_0 + 1 \rfloor - 1} \log_2 \left(1 + \gamma_u^{\text{IB-VL}}\right) + (\delta M_0 - \lfloor \delta M_0 + 1 \rfloor + 1) \frac{\xi B}{M_0} \log_2 \left(1 + \gamma_{\lfloor \delta M_0 + 1 \rfloor}^{\text{IB-VL}}\right) + (\lfloor \delta M_0 + 1 \rfloor - \delta M_0) \frac{\xi B}{M_0} \log_2 \left(1 + \gamma_{\lfloor \delta M_0 + 1 \rfloor}^{\text{FR-VL}}\right) + \frac{\xi B}{M_0} \sum_{u=\lfloor \delta M_0 + 1 \rfloor + 1}^{M_0} \log_2 \left(1 + \gamma_u^{\text{FR-VL}}\right). \tag{A.5}$$

For the special case of $M_0 = 1$, (A.5) reduces to the single user case in (A.2). To obtain a compact representation for the multi-user sum rate, by assuming that δM_0 is an integer, one can apply $\lfloor \delta M_0 + 1 \rfloor = \delta M_0 + 1$, simplifying (A.5) to:

$$\mathcal{R}_0^{\text{IB-VL}} = \frac{\xi B}{M_0} \sum_{u=1}^{\delta M_0} \log_2 \left(1 + \gamma_u^{\text{IB-VL}}\right) + \frac{\xi B}{M_0} \sum_{u=\delta M_0 + 1}^{M_0} \log_2 \left(1 + \gamma_u^{\text{FR-VL}}\right). \tag{A.6}$$

The representation in (A.6) is used as the appropriate form with the aim to avoid overcrowding the notation. However, in order to validate such a representation, the assumption of δM_0 being an integer needs to be mentioned, as δM_0 appears within the summation limits in (A.6). A more precise representation, though expanded, is provided by (A.5). Finally, by introducing two complementary subsets of $\{1, 2, \ldots, \delta M_0\} = \mathcal{U}_0^{(\delta)}$ and $\{\delta M_0 + 1, \delta M_0 + 2, \ldots, M_0\} = \mathcal{U}_0^{(1-\delta)}$, (A.6) matches (3.23). This concludes the proof.

Appendix B
Monotonicity of $g_1(K_1, K_7, K_8)$ in K_1

By taking the partial derivative of g_1 in (3.63) with respect to K_1, one can verify that:

$$\frac{\partial g_1}{\partial K_1} = \frac{\frac{\partial \gamma_{\mathrm{b}_1}}{\partial K_1}}{1+\gamma_{\mathrm{b}_1}} - \sum_{i=1,7,8} \frac{\frac{\partial \gamma_i^{\text{FR-VL}}}{\partial K_1}}{1+\gamma_i^{\text{FR-VL}}} > 0, \tag{B.1}$$

because:

$$\frac{\partial \gamma_{\mathrm{b}_1}}{\partial K_1} = \frac{\left(\frac{1}{4}\right)^{\ell+1} K_7 + \frac{1}{\gamma_{\mathrm{b}}}}{\left[2\left(\frac{1}{4}\right)^{\ell} K_1 + \left(\frac{1}{4}\right)^{\ell+1} K_7 + \frac{1}{\gamma_{\mathrm{b}}}\right]^2} > 0, \tag{B.2}$$

and the partial derivative of $\gamma_i^{\text{FR-VL}}$ with respect to K_1 is always negative as shown in the following:

$$\frac{\partial \gamma_i^{\text{FR-VL}}}{\partial K_1} = -\frac{\mathcal{F}_1(z_i;\mathcal{Q}_i)\mathcal{S}(z_i)}{\left[K_1\mathcal{F}_1(z_i;\mathcal{Q}_i) + K_7\mathcal{F}_2(z_i;\mathcal{O}_i) + K_8\mathcal{F}_2(z_i;\mathcal{E}_i) + \mathcal{F}_{\text{ICI}}(z_i) + \Omega\right]^2} < 0. \tag{B.3}$$

To derive (B.2) and (B.3), respectively, (3.34) and (3.12) are used.

Appendix C
A Remark on the Constraint in (3.64)

For sufficiently small values of Φ_{b}, according to Theorem 1, the backhaul interference effect tends to zero and $\mathcal{F}_{\mathrm{BI}}(z_i) \approx 0$, $\forall i$, taking into account the last constraint of P2, $0 < K_j \leq 1$ for $j = 1, 7, 8$. In such a case, $\gamma_i^{\text{FR-VL}}$ in (3.12) can be tightly approximated by $\gamma_i^{\text{FR-VL}} \approx \frac{\mathcal{S}(z_i)}{\mathcal{F}_{\mathrm{ICI}}(z_i)+\Omega}$, which is independent of K_1, K_7 and K_8. In addition, provided that the optical power is concentrated within the backhaul links, the cross-coupling interference among them is insignificant. Thus, γ_{b_1} in (3.34) reduces to $\gamma_{\mathrm{b}_1} \approx K_1\gamma_{\mathrm{b}}$ and, by using (3.63), (3.64) simplifies to:

$$K_1 \geq \frac{\prod\limits_{i=1,7,8}\left(1+\gamma_i^{\text{FR-VL}}\right)-1}{\gamma_{\mathrm{b}}} \geq \frac{\prod\limits_{i=1,7,8}\gamma_i^{\text{FR-VL}}}{\gamma_{\mathrm{b}}}. \tag{C.1}$$

The second inequality is due to $\gamma_i^{\text{FR-VL}} \gg 1$, which typically holds at the center of an attocell and the optimization is based on the downlink signal-to-noise-plus-interference ratio (SINR) at the center of attocells. The right hand side (RHS) of (C.1) is an asymptotic bound for $K_{1,\min}(K_7, K_8)$ in (3.64).

Appendix D
Minimum Element of the Feasible Set for P3

Let $K_7 = K_{7,\min}(K_8)$ and $K_8 = K_{8,\min}(K_7)$ be replaced by $x = g(y)$ and $y = f(x)$, respectively, and let (x_0, y_0) be their intersection point, to simplify notation. The feasible set can be expressed as:

$$\mathcal{D} = \left\{(x, y) \in \mathbb{R}^2_+ \middle| x \geq g(y), y \geq f(x)\right\}. \tag{D.1}$$

As a geometric description, to say that (x_0, y_0) is the minimum element of $\mathcal{D}$ means that all other points of $\mathcal{D}$ lie to the right and above the point (x_0, y_0). More precisely, the objective is to prove that $(x_0, y_0) \preceq (x, y)$, $\forall (x, y) \in \mathcal{D}$, where $\preceq$ is induced by the positive quadrant $\mathbb{R}^2_+$ [113]. To this end, since f and g in (D.1) are increasing with respect to their arguments, by jointly expanding the conditions $x \geq g(y)$ and $y \geq f(x)$, one arrives at:

$$\begin{cases} x \geq g(y) \geq g(y_0) = x_0, \\ y \geq f(x) \geq f(x_0) = y_0, \end{cases} \tag{D.2}$$

which is what was to be shown.

Appendix E
The Expressions of $\mathcal{I}_{0^\circ}(r)$ and $\mathcal{I}_{30^\circ}(r)$

The expressions of $\mathcal{I}_{0^\circ}(r)$ and $\mathcal{I}_{30^\circ}(r)$ are given in [16] and presented here for the completeness of presentation. Define the function w by:

$$w(x,y) = \left[(r+x)^2 + y\right]^{-m-3}. \tag{E.1}$$

Then:

$$\begin{aligned}\mathcal{I}_{0^\circ}(r) = &2w\left(-\tfrac{3}{2}R_\mathrm{e}, \tfrac{3}{4}R_\mathrm{e}^2 + h^2\right) + 2w\left(\tfrac{3}{2}R_\mathrm{e}, \tfrac{3}{4}R_\mathrm{e}^2 + h^2\right) + 2w\left(0, 3R_\mathrm{e}^2 + h^2\right) + \\ &2w\left(-3R_\mathrm{e}, 3R_\mathrm{e}^2 + h^2\right) + 2w\left(3R_\mathrm{e}, 3R_\mathrm{e}^2 + h^2\right) + 2w\left(0, 12R_\mathrm{e}^2 + h^2\right) + \\ &w\left(-3R_\mathrm{e}, h^2\right) + w\left(3R_\mathrm{e}, h^2\right) + 2w\left(-\tfrac{3}{2}R_\mathrm{e}, \tfrac{27}{4}R_\mathrm{e}^2 + h^2\right) + 2w\left(\tfrac{3}{2}R_\mathrm{e}, \tfrac{27}{4}R_\mathrm{e}^2 + h^2\right),\end{aligned} \tag{E.2}$$

and:

$$\begin{aligned}\mathcal{I}_{30^\circ}(r) = &w\left(-\sqrt{3}R_\mathrm{e}, h^2\right) + w\left(\sqrt{3}R_\mathrm{e}, h^2\right) + w\left(-2\sqrt{3}R_\mathrm{e}, h^2\right) + w\left(2\sqrt{3}R_\mathrm{e}, h^2\right) + \\ &2w\left(-\tfrac{\sqrt{3}}{2}R_\mathrm{e}, \tfrac{9}{4}R_\mathrm{e}^2 + h^2\right) + 2w\left(\tfrac{\sqrt{3}}{2}R_\mathrm{e}, \tfrac{9}{4}R_\mathrm{e}^2 + h^2\right) + 2w\left(-\sqrt{3}R_\mathrm{e}, 9R_\mathrm{e}^2 + h^2\right) + \\ &2w\left(\sqrt{3}R_\mathrm{e}, 9R_\mathrm{e}^2 + h^2\right) + 2w\left(-\tfrac{3\sqrt{3}}{2}R_\mathrm{e}, \tfrac{9}{4}R_\mathrm{e}^2 + h^2\right) + 2w\left(\tfrac{3\sqrt{3}}{2}R_\mathrm{e}, \tfrac{9}{4}R_\mathrm{e}^2 + h^2\right) + \\ &2w\left(0, 9R_\mathrm{e}^2 + h^2\right).\end{aligned} \tag{E.3}$$

Appendix F
Proof of Lemma (4)

To simplify notation, let $X_u = \mathcal{R}_{\mathrm{a}}(\gamma_u)$. The expression $\sum_{i\in\mathcal{L}_k} \frac{1}{m_i} \sum_{u\in\mathcal{U}_i} X_u$ is approximated using the minimum mean square error (MMSE) criterion. To this end, a parameter β is used to perform the following estimation:

$$\underbrace{\sum_{i\in\mathcal{L}_k} \frac{1}{m_i} \sum_{u\in\mathcal{U}_i} X_u}_{A} \approx \beta \underbrace{\sum_{i\in\mathcal{L}_k} \sum_{u\in\mathcal{U}_i} X_u}_{S}. \tag{F.1}$$

The aim is to determine the optimal estimator $\beta = \beta^*$ so that the mean square error (MSE) between the two sides of (F.1) is minimized. This can mathematically be expressed by:

$$\underset{\beta\,\in\,\mathbb{R}}{\text{minimize}} \quad \mathrm{MSE} = \mathbb{E}\left[(A-\beta S)^2\right] \tag{F.2a}$$

$$\text{subject to} \quad \beta > 0 \tag{F.2b}$$

The objective MSE is expanded as follows:

$$\mathrm{MSE} = \mathbb{E}\left[A^2\right] + \beta^2 \mathbb{E}\left[S^2\right] - 2\beta \mathbb{E}\left[AS\right]. \tag{F.3}$$

Taking the derivative of the MSE with respect to β and equating it to zero results in the optimal estimator:

$$\frac{d\mathrm{MSE}}{\beta} = 2\beta \mathbb{E}\left[S^2\right] - 2\mathbb{E}\left[AS\right] = 0 \;\Rightarrow\; \beta^* = \frac{\mathbb{E}\left[AS\right]}{\mathbb{E}\left[S^2\right]}. \tag{F.4}$$

In the right hand side (RHS) of (F.1), S can alternatively be represented as $S = \sum_{u\in\mathcal{U}} X_u$, where $\mathcal{U}$ accounts for indexes of all user equipments (UEs) in the kth branch of the network, i.e., $\mathcal{U} = \bigcup_{i\in\mathcal{L}_k} \mathcal{U}_i$. Thus, the expectation $\mathbb{E}\left[AS\right]$ in (F.4) is expanded as follows:

$$\mathbb{E}\left[AS\right] = \mathbb{E}\left[\left(\sum_{i\in\mathcal{L}_k} \frac{1}{m_i} \sum_{u\in\mathcal{U}_i} X_u\right)\left(\sum_{v\in\mathcal{U}} X_v\right)\right], \tag{F.5a}$$

$$= \sum_{i\in\mathcal{L}_k} \frac{1}{m_i} \sum_{u\in\mathcal{U}_i} \sum_{v\in\mathcal{U}} \mathbb{E}\left[X_u X_v\right], \tag{F.5b}$$

where:

$$\mathbb{E}\left[X_u X_v\right] = \begin{cases} \mathbb{E}^2\left[X_u\right] = \bar{\mathcal{R}}_{\mathrm{a}}^2, & u \neq v \\ \mathbb{E}\left[X_u^2\right] = \sigma_{\mathcal{R}_{\mathrm{a}}}^2 + \bar{\mathcal{R}}_{\mathrm{a}}^2, & u = v \end{cases} \tag{F.6}$$

in which $\bar{\mathcal{R}}_{\mathrm{a}}$ and $\sigma_{\mathcal{R}_{\mathrm{a}}}^2$ are given by (4.26) and (4.43), respectively. Therefore:

$$\sum_{u \in \mathcal{U}_i} \sum_{v \in \mathcal{U}} \mathbb{E}\left[X_u X_v\right] = \sum_{\substack{u \in \mathcal{U}_i, v \in \mathcal{U} \\ u \neq v}} \mathbb{E}\left[X_u X_v\right] + \sum_{\substack{u \in \mathcal{U}_i, v \in \mathcal{U} \\ u = v}} \mathbb{E}\left[X_u X_v\right], \tag{F.7a}$$

$$= m_i(M-1)\bar{\mathcal{R}}_{\mathrm{a}}^2 + m_i\left(\sigma_{\mathcal{R}_{\mathrm{a}}}^2 + \bar{\mathcal{R}}_{\mathrm{a}}^2\right), \tag{F.7b}$$

$$= m_i\left(M\bar{\mathcal{R}}_{\mathrm{a}}^2 + \sigma_{\mathcal{R}_{\mathrm{a}}}^2\right). \tag{F.7c}$$

By substituting (F.7c) into (F.5b), and using $|\mathcal{L}_k| = N_{\mathrm{BS}}$, $\mathbb{E}\left[AS\right]$ is derived as follows:

$$\mathbb{E}\left[AS\right] = N_{\mathrm{BS}}\left(M\bar{\mathcal{R}}_{\mathrm{a}}^2 + \sigma_{\mathcal{R}_{\mathrm{a}}}^2\right). \tag{F.8}$$

In addition, by using (F.6), the expectation $\mathbb{E}\left[S^2\right]$ in (F.4) is derived as follows:

$$\mathbb{E}\left[S^2\right] = \mathbb{E}\left[\left(\sum_{u \in \mathcal{U}} X_u\right)\left(\sum_{v \in \mathcal{U}} X_v\right)\right], \tag{F.9a}$$

$$= \sum_{\substack{u,v \in \mathcal{U} \\ u \neq v}} \mathbb{E}\left[X_u X_v\right] + \sum_{\substack{u,v \in \mathcal{U} \\ u = v}} \mathbb{E}\left[X_u X_v\right], \tag{F.9b}$$

$$= M\left(M\bar{\mathcal{R}}_{\mathrm{a}}^2 + \sigma_{\mathcal{R}_{\mathrm{a}}}^2\right). \tag{F.9c}$$

Finally, by substituting (F.8) and (F.9c) in (F.4), the optimal estimator reduces to:

$$\beta^* = \frac{N_{\mathrm{BS}}}{M}. \tag{F.10}$$

This completes the proof.

Appendix G
Publications

G.1 Conference Papers

H. Kazemi and H. Haas, "Downlink Cooperation with Fractional Frequency Reuse in DCO-OFDMA Optical Attocell Networks," in *Proc. IEEE Int. Conf. Commun.*, (Kuala Lumpur, Malaysia), pp. 16, May 2016.

H. Kazemi, M. Safari, and H. Haas, "Spectral Efficient Cooperative Downlink Transmission Schemes for DCO-OFDM-Based Optical Attocell Networks," in *Proc. IEEE 84th Veh. Technol. Conf.*, (Montreal, Canada), pp. 16, Sep. 2016.

H. Kazemi, M. Safari, and H. Haas, "A Wireless Backhaul Solution Using Visible Light Communication for Indoor Li-Fi Attocell Networks," in *Proc. IEEE Int. Conf. Commun.*, (Paris, France), pp. 17, May 2017.

H. Kazemi, M. Safari, and H. Haas, "Bandwidth Scheduling and Power Control for Wireless Backhauling in Optical Attocell Networks," in *Proc. IEEE Global Commun. Conf.*, (Abu Dhabi, UAE), pp. 16, Dec. 2018.

G.2 Journal Papers

H. Kazemi, M. Safari, and H. Haas, "A Wireless Optical Backhaul Solution for Optical Attocell Networks," *IEEE Trans. Wireless Commun.*, vol. 18, no. 2, Feb. 2019.

H. Kazemi, M. Safari, and H. Haas, "Multi-Hop Wireless Optical Backhauling in Optical Attocell Networks: Bandwidth Scheduling and Power Control," *Ready for submission to IEEE Trans. Wireless Commun.*.

IEEE ICC 2016 - Optical Networks and Systems

Downlink Cooperation with Fractional Frequency Reuse in DCO-OFDMA Optical Attocell Networks

Hossein Kazemi and Harald Haas
Li-Fi Research and Development Center, The University of Edinburgh, Edinburgh, EH9 3JL, United Kingdom.
Email: {h.kazemi, h.haas}@ed.ac.uk

***Abstract*—In this paper, downlink cooperation is proposed for indoor visible light communication (VLC) cellular networks, also termed as optical attocell networks, with the aim of improving the spectral efficiency performance. An orthogonal frequency division multiple access (OFDMA) system based on direct current optical orthogonal frequency division multiplexing (DCO-OFDM) with fractional frequency reuse (FFR) planning is considered, and a system level analysis is carried out. A line-of-sight (LOS) light propagation model is used for the indoor VLC channel. The downlink cooperation is realized by means of a relay-assisted transmission with the aid of neighboring base stations (BSs) using a non-orthogonal amplify-and-forward (NAF) protocol. The links between the source BS and the relay BSs are provided by perfectly aligned VLC connections. Four relaying schemes with a different number of relays are considered, and for each scheme analytical signal-to-interference-plus-noise ratio (SINR) and spectral efficiency expressions for a user equipment (UE) with random coordinates in an optical attocell are derived. Also, average spectral efficiency performance of the system is studied using Monte-Carlo simulations.**

***Index Terms*—Visible light communication (VLC), optical attocell networks, direct current optical orthogonal frequency division multiplexing (DCO-OFDM), fractional frequency reuse (FFR), non-orthogonal amplify-and-forward (NAF).**

I. Introduction

Ever increasing data traffic in wireless communication networks poses a severe challenge to meet the end-user bandwidth requirement primarily due to the limited radio frequency (RF) spectrum. An alternative solution can be realized by visible light communication (VLC) using off-the-shelf light emitting diodes (LEDs) [1]. The existing white LED-based lighting infrastructure of indoor environments is utilized to develop extremely small scale cellular networks, termed optical attocell networks [1]. A VLC system performs intensity modulation (IM) of the LED light as the signal transmitter and direct detection (DD) with a solid-state photodiode (PD) as the receiver. VLC systems offer a number of advantages over RF systems [2]: i) hundreds of THz unregulated bandwidth from the visible light spectrum; ii) easy deployment with low cost LEDs and PDs; iii) robust security against interception; iv) no co-channel interference (CCI) to adjacent rooms; v) no interference with RF devices; vi) higher signal-to-noise ratio (SNR); and vii) no multi-path fading.

In VLC systems, optical orthogonal frequency division multiplexing (O-OFDM) is widely used as a practical and spectrally efficient modulation format [3]. A simple variant of it is direct current (DC) biased O-OFDM (DCO-OFDM), in which the DC bias is optimized for illumination purposes [4]. The downlink performance of a DCO-OFDM-based optical attocell network has been studied in terms of average spectral efficiency in [5]. From the results in [5], inter-cell interference (ICI) is the principal factor that restricts the performance. To mitigate the ICI effect, downlink transmission techniques have been proposed, such as fractional frequency reuse (FFR) [6].

For cooperative VLC systems, the achievable rate region of a two-user VLC system with two interfering transmitters employing O-OFDM and joint power control has been studied in [7]. Relay-assisted transmission based on DCO-OFDM for a point-to-point VLC system has been introduced in [8], where the end-to-end performance of a dual-hop link with amplify-and-forward (AF) relaying has been studied in terms of bit error rate (BER). However, these studies do not cover optical attocell networks. In this paper, base stations (BSs) downlink cooperation is proposed to improve the spectral efficiency of optical attocell networks. A DCO-OFDM-based system with a hexagonal cellular layout and FFR planning is considered, and a system level analysis of the proposed approach is carried out. The downlink cooperation is realized by means of a relay-assisted transmission with the aid of neighboring BSs by using non-orthogonal AF (NAF) protocol, which is the best AF protocol in terms of achievable rate [9].

The remainder of the paper is organized as follows. In Section II, the model for the underlying optical attocell system is described. In Section III, the methodology and modeling for the proposed downlink cooperation of BSs with four relaying schemes based on the NAF protocol are described, and signal-to-interference-plus-noise ratio (SINR) derivations are presented. In Section IV, spectral efficiency calculations are expressed. In Section V, simulation results are presented, and finally, conclusions are given in Section VI.

II. Optical Attocell System Model

Fig. 1 illustrates the geometric configuration of the downlink in an indoor optical attocell network. The system consists of a BS transmitter with a white LED installed on the ceiling of an indoor environment and a PD receiver on user equipment (UE). The LEDs are assumed as point sources with Lambertian emission patterns and as operating in the linear region. Also, the LEDs are assumed to be facing downward and the PD receiver of each UE is facing straight up. The area on the receiver plane within which the intended UE being served by a BS is termed an optical attocell.

978-1-4799-6664-6/16/$31.00 ©2016 IEEE

Fig. 2 illustrates the hexagonal cellular layout of an optical attocell network with seven attocells considered here. For each UE in a given attocell, the receiver field of view (FOV) is assumed to be sufficiently wide to allow simultaneous detection of optical signals from the source BS and the six neighboring BSs. The downlink performance of a UE in the zeroth attocell (for BS_0) is studied when the UE location is random with a uniform distribution. The coverage area of each attocell is divided into two parts: a cell central region with a circular radius R_c, and a cell edge region with an equivalent circular radius R_e. The approximated circular cell has the same coverage area as the original hexagonal cell with a radius R, yielding $R_\mathrm{e} \approx 0.9R$.

A. Indoor Visible Light Propagation Model

In this study, only the line-of-sight (LOS) is considered for indoor visible light propagation and reflection paths are not considered, as shown in Fig. 1. It was shown in [6] that the reflection paths have insignificant effect on the attocells that are sufficiently away from the network boundaries. The VLC channel is assumed to have a nearly flat frequency response dominated by the LOS path, which can be characterized by its DC gain. Assuming a unity gain for both the concentrator and optical filter, the DC gain of the VLC channel from BS_i to UE, for $i = 0, 1, \ldots, 6$, is given as [10, Eq. (10)]:

$$G_i = \frac{(m+1)A_\mathrm{PD}}{2\pi d_i^2}\cos^m(\varphi_i)\cos(\psi_i)\mathrm{rect}\left(\frac{\psi_i}{\Psi_\mathrm{a}}\right), \quad (1)$$

where $m = -\ln 2/\ln(\cos\Phi_\mathrm{a})$ is the Lambertian order and Φ_a is the semi-angle at half-power of the LED emission pattern; A_PD is the effective PD area; d_i is the Euclidean distance from UE to BS_i; φ_i is the light radiance angle with respect to the maximum power direction for BS_i; ψ_i is the light incidence angle with respect to the direction perpendicular to the PD plane; and Ψ_a is the FOV of the UE receiver. The last factor in (1) is for the rectangular function defined as $\mathrm{rect}(x) = 1$ if $|x| \leq 1$, and 0 otherwise.

B. Orthogonal Frequency Division Multiple Access

In order to support multiple access, an orthogonal frequency division multiple access (OFDMA) system based on DCO-OFDM is considered. The quadrature amplitude modulation (QAM) data symbols of different UEs, X_k, are arranged on N subcarriers of the OFDMA frame in the frequency domain to get $\mathbf{X} = [X_0, X_1, \ldots, X_{N-1}]$, before the application of the inverse discrete fourier transform (IDFT). Average power of every symbol is normalized to unity such that $\mathbb{E}[|X_k|^2] = 1$, for $k = 0, 1, \ldots, N-1$, where $\mathbb{E}[\cdot]$ denotes the expectation operator. For optical IM systems, the modulating signal must be both real and positive [11]. This requires that $X_k = X_{N-k}^*$, for $k \neq 0$, where $[\cdot]^*$ denotes the complex conjugate operator, and $X_0 = X_{N/2} = 0$. Hence, only $\tilde{N} = N/2 - 1$ symbols bear information. The DCO-OFDMA signal can be expressed as $x(n) = x_\mathrm{DC} + \tilde{x}(n)$ where x_DC is the DC bias, and:

$$\tilde{x}(n) = \sum_{k=0}^{N-1}\tilde{x}_k(n) = \frac{1}{\sqrt{N}}\sum_{k=0}^{N-1}X_k\exp\left(j\frac{2\pi kn}{N}\right), \quad (2)$$

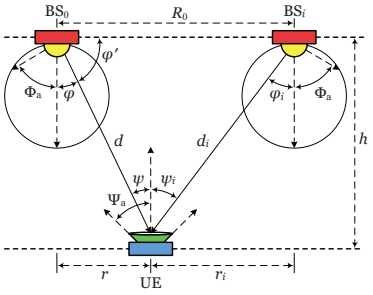

Figure 1. Downlink geometry in an indoor optical attocell network.

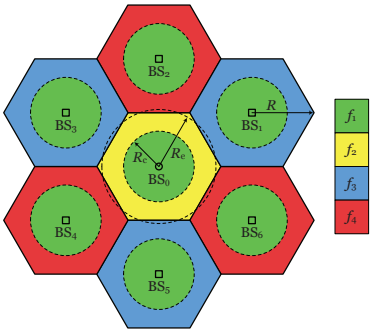

Figure 2. Hexagonal cellular layout of seven attocells with an FFR plan: $\Delta = 1$ for cell central regions, and $\Delta = 3$ for cell edge regions.

in which n is the sample number for $n = 0, 1, \ldots, N-1$; $\tilde{x}_k(n)$ is the alternating current (AC) signal component modulated on subcarrier k at time sample n; and $j = \sqrt{-1}$. Here, $x_\mathrm{DC} = \alpha\sqrt{P_\mathrm{elec,AC}}$ where α is a scaling factor and $P_\mathrm{elec,AC} = \sum_{k=0}^{N-1}\mathbb{E}[\tilde{x}_k^2(n)]$ is the total electrical power for transmission [11]. The average optical power is defined as $P_\mathrm{opt} = \mathbb{E}[x(n)] = x_\mathrm{DC}$, and thus $P_\mathrm{elec,AC} = P_\mathrm{opt}^2/\alpha^2$.

C. Frequency Reuse Planning

Two frequency reuse plans are examined: full frequency reuse (FR) and fractional frequency reuse (FFR).

In the FR plan, the frequency reuse factor (FRF), denoted as Δ, is equal to 1 for every attocell in the network. The FR plan is taken as a baseline for performance evaluations. After removing the DC bias followed by perfect sampling and synchronization, the received photocurrent of a given UE on subcarrier k at time sample n is given by:

$$y_k(n) = R_\mathrm{PD}\sum_{i=0}^{6}G_i\sqrt{P_{\mathrm{elec},i,k}}\tilde{x}_{i,k}(n) + v_k(n), \quad (3)$$

where R_PD denotes the PD responsivity; $P_{\mathrm{elec},i,k}$ denotes the electrical signal power transmitted by BS_i on subcarrier k; and $\tilde{x}_{i,k}(n)$ is the transmitted signal from BS_i on subcarrier k at time sample n. Note that for $i = 0$, $\tilde{x}_{0,k}(n)$ is the only desired

signal transmitted from BS_0 for the UE. In (3), $v_k(n)$ is white Gaussian noise modeling shot noise and thermal noise in the UE receiver with zero mean and variance of $\sigma_k^2 = N_0 B/N$, where N_0 denotes the noise power spectral density (PSD); and B is the modulation bandwidth. All BSs emit the same average optical power, and the total electrical transmission power is equally allocated among $N-2$ available subcarriers so that $P_{\mathrm{elec},i,k} = P_{\mathrm{opt}}^2/(N-2)\alpha^2$, $\forall i,k$.

The FFR plan divides the system bandwidth up into four disjoint sub-bands: one individual common sub-band (f_1) for cell central regions with $\Delta = 1$, and three protected sub-bands (f_2, f_3, f_4) for cell edge regions with $\Delta = 3$, as shown in Fig. 2. The number of subcarriers allocated to the common sub-band, N_c, and to the protected sub-band, N_e, are determined as $N_c = \lceil \tilde{N}\delta^2 \rceil$ and $N_e = \lfloor (\tilde{N} - N_c)/3 \rfloor$, respectively, where $\delta = R_c/R_e$ [6]. The received signal model for a given UE located in the cell central region is identical to that of the FR system and is given by (3). When a UE is located in the cell edge region, the corresponding received photocurrent on subcarrier k at time sample n is expressed as:

$$y_k(n) = R_{\mathrm{PD}} G_0 \sqrt{P_{\mathrm{elec},0,k}}\, \tilde{x}_{0,k}(n) + v_k(n). \tag{4}$$

D. Signal-to-Interference-plus-Noise Ratio

In wireless communication systems, SINR is defined as the ratio of the desired electrical signal power to the total noise and interference power. For the FR system, using (1) and (3), the received SINR of a UE on subcarrier k at location $z = (r, \theta)$ in a polar coordinate system with BS_0 at the origin can be derived as [5]:

$$\gamma_{\mathrm{FR}}(z) = \frac{(r^2 + h^2)^{-m-3}}{\sum_{i=1}^{6} (r_i^2(z) + h^2)^{-m-3} + \Omega}, \tag{5}$$

where $r_i(z) = \sqrt{r^2 - 2R_0 r \cos(\theta - \Theta_i) + R_0^2}$ represents the Euclidean distance between BS_i and UE for $i = 1, 2, \ldots, 6$, and $r_0(z) = r$. Here, (R_0, Θ_i) are the polar coordinates of BS_i in which $R_0 = \sqrt{3}R$ and $\Theta_i = i\pi/3 - \pi/6$. Also,

$$\Omega = \frac{4\pi^2 \alpha^2 N_0 B (N-2)}{((m+1)h^{m+1} A_{\mathrm{PD}} R_{\mathrm{PD}} P_{\mathrm{opt}})^2 N}. \tag{6}$$

For the FFR system, using (1) and (4), the received SINR of a UE for each allocated subcarrier at location z in the cell edge region is derived as:

$$\gamma_{\mathrm{FFR}}(z) = \Omega^{-1} \left(r^2 + h^2\right)^{-m-3}. \tag{7}$$

III. Base Stations Downlink Cooperation

A. Proposed Approach

The downlink cooperation is performed only for those UEs located in the cell edge region in conjunction with FFR planning. A cooperative downlink transmission with the NAF protocol is completed in two time slots, and one or more neighboring BSs may participate in it. The UE data is split into two parts. During the first time slot, BS_0 transmits the first part directly to UE and, at the same time, to the chosen relay BSs.

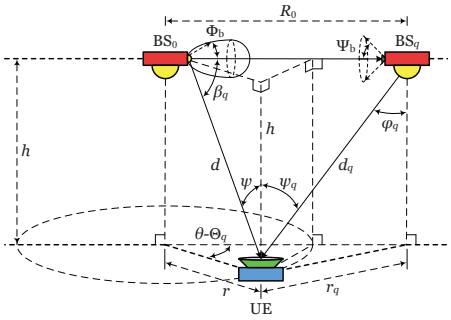

Figure 3. Downlink cooperation geometry.

During the second time slot, the relay BSs amplify the noisy signal and then retransmit it to the UE, while BS_0 transmits the second part to the UE. To realize the connections between BS_0 and its neighboring BSs, suppose six auxiliary LEDs are mounted around BS_0 allowing each one to point at the corresponding relay BS, and there are six PD receivers on the relay BSs side perfectly aligned to the LED transmitters of BS_0. Since AP-to-AP links operate in the visible light spectrum, they need to access the shared bandwidth of the downlink system. To avoid generating unnecessary interference, AP-to-AP links use the protected sub-band, which is f_2 for the attocell associated with BS_0, see Fig. 2. The relay downlink has to fulfil two conditions: i) not interfere with the direct downlink, and ii) allocate the same number of subcarriers to UE as on the direct downlink. According to the FFR plan, there is a free sub-band between BS_0 and every neighboring BS satisfying both conditions, as shown in Fig. 2. For example, f_4 remains unallocated between BS_0 and three BSs $\{1, 3$ and $5\}$, hence it is used for downlink relaying when the relay BSs are among these BSs. Similarly, f_3 is a free sub-band and it is used for downlink relaying if the relay BSs are selected from three BSs $\{2, 4$ or $6\}$. The effect of ceiling reflections from AP-to-AP links is not considered in this study, and will be the subject of future studies.

B. Cooperative Relaying Schemes

In the following, the notation q is used for the index of the selected relay BS, and k is used for the index of the subcarrier allocated to UE on either the source BS or the relay BS. Let $\mathbf{x}_{i,k} = [\tilde{x}_{i,k,1}\ \tilde{x}_{i,k,2}]^{\mathrm{T}}$ be the vector of signals transmitted by BS_i and $\mathbf{y}_k = [y_{k,1}\ y_{k,2}]^{\mathrm{T}}$ be the vector of signals received by UE on subcarrier k over two time slots, where $[\cdot]^{\mathrm{T}}$ denotes the transpose operator. Four relaying schemes with a different number of relay BSs are considered as follows.

Scheme (a): Only one relay is used for downlink relaying. The chosen relay is the neighboring BS that maximizes the DC gain to the UE. This means that the closest neighboring BS to the UE is selected for downlink relaying, since G_i is monotonically decreasing with respect to $r_i(z)$ [5]. It is assumed that the UE signal from BS_0 is directed only to BS_q

on the corresponding AP-to-AP link. The signal received by BS_q on subcarrier k in time slot 1 can be expressed as:

$$w_{k,1}(n) = R_{\mathrm{PD}} G_{\mathrm{s}} \sqrt{P_{\mathrm{elec},0,k}} \tilde{x}_{0,k,1}(n) + v_{k,1}(n), \quad (8)$$

where $v_{k,1}(n)$ is the associated noise, identically distributed as the downlink noise discussed in Section II; and G_{s} is the DC gain of the VLC channel for an AP-to-AP link, which can be found using (1) for $d_i = R_0$ and $\varphi_i = \psi_i = 0$ as $G_{\mathrm{s}} = (\ell+1)A_{\mathrm{PD}}/2\pi R_0^2$, where $\ell = -\ln 2/\ln(\cos\Phi_{\mathrm{b}})$ is the Lambertian order and Φ_{b} is the semi-angle at half-power of the emission pattern for auxiliary LEDs on BS_0. Based on (8), the SNR of the AP-to-AP link between BS_0 and BS_q for each allocated subcarrier, denoted as γ_0, can be calculated as $\gamma_0 = R_{\mathrm{PD}}^2 G_{\mathrm{s}}^2 P_{\mathrm{opt}}^2 N/\alpha^2 N_0 B(N-2)$.

The downlink cooperation geometry given in Fig. 3 is used for the calculation of the signal leakage from an AP-to-AP link to the UE receiver. Assuming that the auxiliary LEDs on BS_0 are labeled according to the indexes of the neighboring BSs, the signal received by a UE in the cell edge region on subcarrier k in time slot 1 can be written as:

$$y_{k,1}(n) = R_{\mathrm{PD}}(G_0 + G'_q)\sqrt{P_{\mathrm{elec},0,k}}\tilde{x}_{0,k,1}(n) + v_{k,1}(n), \quad (9)$$

where G'_q represents the DC gain from auxiliary LED q to UE, which is given by:

$$G'_q = \frac{(\ell+1)A_{\mathrm{PD}}}{2\pi d^2}\cos^{\ell}(\beta_q)\cos(\psi)\mathrm{rect}\left(\frac{\psi}{\Psi_{\mathrm{b}}}\right), \quad (10)$$

where β_q is the light radiance angle with respect to the maximum power direction of auxiliary LED q; and Ψ_{b} is the FOV of the AP-to-AP link receiver. Comparing Fig. 3 with Fig. 1, it is observed that the angle β_q is obtained by a cylindrical rotation of the planar angle φ' as much as $\theta - \Theta_q$, and thereby the transformation $\cos(\beta_q) = \cos(\varphi')\cos(\theta - \Theta_q)$ can be used in (10). Combining (10) with (9), and using (7), the received SINR of a UE at location z in the cell edge region on each allocated subcarrier in time slot 1 for scheme (a) can be derived and expressed as:

$$\gamma_1(z) = \gamma_{\mathrm{FFR}}(z)\left[1 + \frac{(\ell+1)r^{\ell}\cos^{\ell}(\theta-\Theta_q)}{(m+1)h^m}\left(r^2+h^2\right)^{-\frac{\ell-m}{2}}\right]^2. \quad (11)$$

The received signal of UE on subcarrier k from its sub-band with BS_0 in time slot 2 is similar to that of the non-cooperative FFR in (4), and the corresponding SINR, denoted as $\gamma_{2,0}(z)$, is equal to $\gamma_{\mathrm{FFR}}(z)$ given in (7), which is identical for all of the considered schemes. Also, the received signal of a UE on subcarrier k from its sub-band with BS_q in time slot 2 can be written using (8) as:

$$y_{k,2}(n) = R_{\mathrm{PD}} G_q G_{\mathrm{AF}} w_{k,1}(n) + R_{\mathrm{PD}} \sum_{i\in\mathcal{I}} G_i \sqrt{P_{\mathrm{elec},i,k}}\tilde{x}_{i,k,2}(n) + v_{k,2}(n), \quad (12)$$

where $\mathcal{I}$ is the index set of interfering BSs with two possibilities, either $\mathcal{I} = \{1,3,5\}$ or $\mathcal{I} = \{2,4,6\}$, depending on the UE location, and G_{AF} is the AF gain given by:

$$G_{\mathrm{AF}} = \sqrt{\frac{P_{\mathrm{elec},q,k}}{\mathbb{E}\left[|w_{k,1}(n)|^2\right]}} = \sqrt{\frac{P_{\mathrm{elec},q,k}}{R_{\mathrm{PD}}^2 G_{\mathrm{s}}^2 P_{\mathrm{elec},0,k} + \sigma_k^2}}. \quad (13)$$

By combining (13) with (12), and defining $\mu = (\gamma_0+1)^{-1}$, the received SINR of UE in time slot 2 for each allocated subcarrier on its sub-band with BS_q is derived as:

$$\gamma_{2,\mathrm{q}}(z) = \frac{(1-\mu)(r_q^2(z)+h^2)^{-m-3}}{\sum_{i\in\mathcal{I}}(r_i^2(z)+h^2)^{-m-3} + \mu(r_q^2(z)+h^2)^{-m-3} + \Omega}. \quad (14)$$

Scheme (b): Three relays are used for downlink relaying. The first relay is determined by the DC gain criterion similar to scheme (a). Subsequently, the other two neighboring BSs that operate on the same protected sub-band with the first relay are also selected to contribute to the downlink cooperation. Therefore, three AP-to-AP links convey the UE data from the source BS to the corresponding relay BSs during the first time slot. There are two possible realizations for the set of these links: one including the AP-to-AP links pointing at the neighboring BSs with blue cell edge areas; and one for the neighboring BSs with red cell edge areas, as observed from Fig. 2. This means that there is no cross-coupling between the AP-to-AP links simultaneously carrying the UE signal, as the angle between any two of such AP-to-AP links is $120^\circ > 90^\circ$. Also, since $\Psi_{\mathrm{a}} \leq 90^\circ$, the UE receives the signal leakage from only one auxiliary LED on BS_0. As a result, the received SINR of UE for scheme (b) in time slot 1 on the sub-band with BS_0, $\gamma_1(z)$, is exactly the same as scheme (a) given in (11). The received SINR of UE in time slot 2 for each allocated subcarrier on its sub-band with three relay BSs is obtained as:

$$\gamma_{2,\mathrm{q}}(z) = \frac{(1-\mu)\sum_{q\in\mathcal{I}'}(r_q^2(z)+h^2)^{-m-3}}{\sum_{i\in\mathcal{I}}(r_i^2(z)+h^2)^{-m-3} + \mu\sum_{q\in\mathcal{I}'}(r_q^2(z)+h^2)^{-m-3} + \Omega}, \quad (15)$$

where $\mathcal{I}'$ is the complement set of $\mathcal{I}$ defined in scheme (a).

Scheme (c): Two adjacent relays are used for downlink relaying. In addition to the first relay, the second relay is also determined by the DC gain criterion. Specifically, the second closest neighboring BS to the UE next to the first relay BS is selected as the second relay to contribute to the downlink cooperation, and two adjacent AP-to-AP links carry the UE signal towards the relay BSs during the first time slot. Using (1), the effective DC gain of the AP-to-AP link considering the cross-coupling with the adjacent AP-to-AP link can be calculated as $G_{\mathrm{s}} = (\ell+1)(1+2^{-\ell})A_{\mathrm{PD}}/2\pi R_0^2$. The received SINR of UE in time slot 1 is derived as:

$$\gamma_1(z) = \gamma_{\mathrm{FFR}}(z)\left[1 + \frac{(\ell+1)r^{\ell}\left(r^2+h^2\right)^{-\frac{\ell-m}{2}}}{(m+1)h^m}\sum_{q\in Q}\cos^{\ell}(\theta-\Theta_q)\right]^2, \quad (16)$$

where $Q = \{q_1, q_2\}$ is the index set of the first and second relays. The received SINR of UE in time slot 2 on its sub-band with BS_{q_1}, denoted as $\gamma_{2,q_1}(z)$, is given by (14), and in time slot 2 on its sub-band with BS_{q_2}, denoted as $\gamma_{2,q_2}(z)$, is given by (14) when replacing $r_q(z)$ by $r_{q_2}(z)$, and the index set of interfering BSs $\mathcal{I}$ by its complement $\mathcal{I}'$.

Scheme (d): Only one relay is used for downlink relaying, which is selected with the DC gain maximization criterion

similar to scheme (a), but the UE signal is transmitted by BS_0 in all six directions over AP-to-AP links with the neighboring BSs during the first time slot. Considering angular separation of 60° between adjacent AP-to-AP links and Lambertian emission patterns, an AP-to-AP link is cross-coupled with two adjacent ones only. The effective DC gain of the AP-to-AP link is obtained as $G_{\rm s} = (\ell+1)(1+2^{-\ell+1})A_{\rm PD}/2\pi R_0^2$. The received SINR of UE in time slot 1, $\gamma_1(z)$, is similar to that of scheme (c) given in (16), and the only difference is for the index set of the relays, which is given as $Q = \{q-1, q, q+1\}$ for $q = 1, 2, \ldots, 6$, such that if $q = 1$ then $q-1 = 6$, or if $q = 6$ then $q+1 = 1$. Also, the received SINR of UE in time slot 2 on its sub-band with BS_q, $\gamma_{2,{\rm q}}(z)$, is given by (14).

IV. Spectral Efficiency Assessment

The quality of an optical attocell downlink is measured by its throughput. The Shannon-Hartley theorem gives a simple upper bound for wireless transmission capacity, and is used to estimate the downlink throughput of the system. Define $\xi = \tilde{N}/N = (N-2)/2N$ as the bandwith utilization factor for a DCO-OFDMA system, the spectral efficiency of a UE at location z can be calculated as a function of $\gamma(z)$ with Δ as a parameter [6]:

$$\rho\left(\gamma(z);\Delta\right) = \frac{\xi}{\Delta}\log_2\left(1+\gamma(z)\right). \tag{17}$$

For the FR system, inserting (5) and $\Delta = 1$ in (17), the spectral efficiency of the UE can be calculated as:

$$\rho_{\rm FR} = \rho\left(\gamma_{\rm FR}(z);1\right) = \xi\log_2\left(1+\gamma_{\rm FR}(z)\right). \tag{18}$$

In the case of non-cooperative FFR, if the UE location is in the cell central region, the spectral efficiency of the UE is given by (18), and if the UE location is in the cell edge region, the spectral efficiency of the UE can be calculated by substituting (7) and $\Delta = 3$ into (17) as:

$$\rho_{\rm FFR} = \rho\left(\gamma_{\rm FFR}(z);3\right) = \frac{\xi}{3}\log_2\left(1+\gamma_{\rm FFR}(z)\right). \tag{19}$$

To present the spectral efficiency for cooperative FFR (CFFR) schemes, let $\tilde{\mathbf{v}}_k = [\tilde{v}_{k,1}\ \tilde{v}_{k,2}]^{\rm T}$ be the normalized noise vector such that $\mathbb{E}\left[\tilde{\mathbf{v}}_k\tilde{\mathbf{v}}_k^{\rm T}\right] = \mathbf{I}$, and let $\tilde{\mathbf{y}}_k = [\tilde{y}_{k,1}\ \tilde{y}_{k,2}]^{\rm T}$ be the vector of the corresponding received signals for a UE on subcarrier k in two time slots. An alternative vector representation can be obtained as $\tilde{\mathbf{y}}_k = \mathbf{H}\tilde{\mathbf{x}}_{0,k} + \tilde{\mathbf{v}}_k$, where $\tilde{\mathbf{x}}_{0,k} = [\tilde{x}_{0,k,1}\ \tilde{x}_{0,k,2}]^{\rm T}$ is the vector of the desired signals transmitted by BS_0; and $\mathbf{H}$ is the input-output transfer matrix given as:

$$\mathbf{H} = \begin{bmatrix} \sqrt{\gamma_1(z)+\gamma_{2,{\rm q}}(z)} & 0 \\ 0 & \sqrt{\gamma_{2,0}(z)} \end{bmatrix}, \tag{20}$$

whose entries include SINRs explicitly defined for all CFFR schemes in Section III. In the first row of $\mathbf{H}$, the fact that $y_{k,1}$ in (9) and $y_{k,2}$ in (12) both contain $\tilde{x}_{0,k,1}$ is used to acquire $\tilde{y}_{k,1}$ by means of maximal ratio combining (MRC), assuming that the full channel state information (CSI) is available at the UE receiver. Note that here the MRC rule is optimum in the sense that it maximizes the output SINR, since interferences from different sub-bands are uncorrelated [12]. For scheme (c), $\gamma_{2,{\rm q}}(z) = \gamma_{2,q_1}(z) + \gamma_{2,q_2}(z)$. By using (20) and Theorem 1 in [13], the spectral efficiency of the UE in the cell edge region for CFFR schemes can be calculated as:

$$\begin{aligned}\rho_{\rm CFFR} &= \frac{1}{2}\times\frac{\xi}{3}\log_2\left[\det\left(\mathbf{I}+\mathbf{H}\mathbf{H}^{\rm T}\right)\right], \\ &= \frac{\xi}{6}\log_2\left[\left(1+\gamma_1(z)+\gamma_{2,{\rm q}}(z)\right)\left(1+\gamma_{2,0}(z)\right)\right],\end{aligned} \tag{21}$$

where a factor $\frac{1}{2}$ in the first line arises from the use of two time slots; and $\det(\cdot)$ denotes the determinant operator.

TABLE I
System Parameters.

Parameter	Symbol	Value	Unit
LED optical power	$P_{\rm opt}$	10	W
Vertical separation	h	2.15	m
Noise PSD	N_0	1×10^{-21}	$\rm A^2/Hz$
Effective PD area	$A_{\rm PD}$	1×10^{-4}	$\rm m^2$
PD responsivity	$R_{\rm PD}$	0.6	A/W
Modulation bandwidth	B	20	MHz
DFT/IDFT length	N	512	–
DC bias scale factor	α	3	–
Cell partitioning ratio	δ	0.8	–

V. Performance Results

This section presents performance results for the average spectral efficiency of the non-cooperative system described in Section II, and the cooperative system with four schemes described in Section III, based on Monte-Carlo averaging of (18), (19) and (21) from Section IV. Table I lists the values of the system parameters used for simulations. In addition, there are two configurations considered for the attocell setup as [5]: A) $R = 2.5$ m, $\Phi_{\rm a} = 40^\circ$; and B) $R = 3.2$ m, $\Phi_{\rm a} = 60^\circ$. In order to observe and study the effect of the UEs location on the system performance, the attocell of BS_0 is divided into 10 rings with equal areas.

Fig. 4 gives the average spectral efficiency of UEs within each ring around BS_0 for configuration A and $\Phi_{\rm b} = 40^\circ$. In the following, the focus is on the cell edge region (i.e., for ring indexes $n = 7, 8, 9, 10$). Fig. 4 shows that the system performance is improved with all CFFR schemes in respect to both the FR and non-cooperative FFR systems. The average spectral efficiency of CFFR schemes (a) and (c) are almost equal to that of schemes (b) and (d), respectively. This means that there is no advantage in employing three relays for scheme (b) compared with only one relay for scheme (a). The reason is that the additional UE signal provided by the other two relays on the same sub-band in scheme (b) is negligible in comparison with the first relay. Furthermore, schemes (c) and (d) outperform schemes (a) and (b). Therefore, employing the second relay in scheme (c) is more effective than using three maximally distant relays in scheme (b). In contrast, the signal processing complexity for scheme (c) is more than that for scheme (b), due to the implementation of another MRC. Interestingly, scheme (d) achieves almost the same performance as scheme (c), without using the second relay.

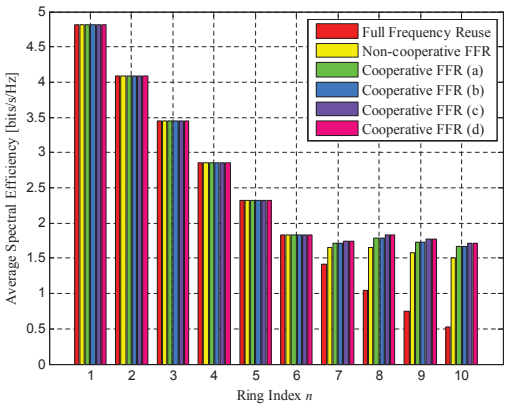

Figure 4. Average spectral efficiency of UEs per ring around BS_0 with four CFFR schemes for configuration A and $\Phi_b = 40°$.

Table II summarizes the performance results for the average spectral efficiency improvement of the non-cooperative FFR and CFFR schemes relative to the FR system in the cell edge region for both configurations A and B, and $\Phi_b = 40°$. Also, Table III presents the performance improvement results for both of the configurations, and $\Phi_b = 20°$. From Tables II and III, comparing configurations A and B, the performance improvement is overall lessened by enlarging the attocell size. By comparing Table II and Table III, it can be seen that the average spectral efficiency improvements of the CFFR schemes with respect to the non-cooperative FFR are directly proportional to the value of Φ_b. As the semi-angle of the auxiliary LEDs on BS_0 is halved from $\Phi_b = 40°$ to $20°$, the average spectral efficiency improvement for different CFFR schemes become nearly equal to one another, and slightly higher than the non-cooperative FFR. This in turn indicates that the performance improvement offered by CFFR schemes is decreased when the semi-angle at half-power of auxiliary LEDs on BS_0 is smaller.

VI. Conclusions

In this paper, BSs downlink cooperation was proposed to improve the average spectral efficiency performance of a UE randomly located in a DCO-OFDMA indoor optical attocell network with an FFR plan. Four relaying schemes were considered based on the NAF protocol. It was found that the performance of the scheme with one relay and an omnidirectional transmission on the AP-to-AP links is nearly equal to that with two relays and a directional transmission on the AP-to-AP links, and it outperforms the other schemes with one and three relays using a directional transmission on the AP-to-AP links. It was also found that the spectral efficiency improvements offered by the CFFR schemes over the non-cooperative FFR are directly proportional to the semi-angle at half-power of auxiliary LEDs used for the AP-to-AP links.

TABLE II
Average Spectral Efficiency Improvement of FFR and CFFR Schemes Relative to FR System for $\Phi_b = 40°$.

	Ring	FFR	CFFR (a)	CFFR (b)	CFFR (c)	CFFR (d)
A	7	0.236	0.305	0.305	0.328	0.331
	8	0.611	0.738	0.738	0.781	0.785
	9	0.830	0.975	0.975	1.021	1.026
	10	0.984	1.145	1.145	1.194	1.199
B	7	0.165	0.272	0.272	0.303	0.306
	8	0.448	0.637	0.637	0.692	0.697
	9	0.619	0.822	0.822	0.879	0.885
	10	0.741	0.956	0.956	1.015	1.021

TABLE III
Average Spectral Efficiency Improvement of FFR and CFFR Schemes Relative to FR System for $\Phi_b = 20°$.

	Ring	FFR	CFFR (a)	CFFR (b)	CFFR (c)	CFFR (d)
A	7	0.234	0.240	0.240	0.240	0.240
	8	0.611	0.626	0.626	0.627	0.627
	9	0.830	0.851	0.851	0.853	0.853
	10	0.985	1.016	1.016	1.018	1.018
B	7	0.165	0.193	0.193	0.195	0.195
	8	0.448	0.508	0.508	0.512	0.512
	9	0.619	0.697	0.697	0.703	0.703
	10	0.741	0.839	0.839	0.846	0.846

Acknowledgment

Professor Harald Haas acknowledges support by the UK Engineering and Physical Research Council (EPSRC) under Grant EP/K008757/1.

References

[1] H. Haas, "High-speed wireless networking using visible light," *SPIE Newsroom*, 19 Apr. 2013.
[2] X. Bao, G. Yu, J. Dai, and X. Zhu, "Li-Fi: Light fidelity-a survey," *J. Wireless Netw.*, vol. 21, no. 6, pp. 1879–1889, Aug. 2015.
[3] S. Dimitrov and H. Haas, *Principles of LED Light Communication Towards Networked Li-Fi*, 1st ed. Cambridge University Press, Mar. 2015.
[4] H. Elgala, R. Mesleh, and H. Haas, "Practical Considerations for Indoor Wireless Optical System Implementation using OFDM," in *Proc. 10th Int. Conf. Telecommun. (ConTEL)*, Jun. 2009, pp. 25–29.
[5] C. Chen, M. Ijaz, D. Tsonev, and H. Haas, "Analysis of Downlink Transmission in DCO-OFDM-based Optical Attocell Networks," in *Proc. IEEE Global Commun. Conf.*, Dec. 2014, pp. 2072–2077.
[6] C. Chen, S. Videv, D. Tsonev, and H. Haas, "Fractional Frequency Reuse in DCO-OFDM-Based Optical Attocell Networks," *IEEE/OSA J. Lightw. Technol.*, vol. 33, no. 19, pp. 3986–4000, Oct. 2015.
[7] M. Kashef, M. Abdallah, K. Qaraqe, H. Haas, and M. Uysal, "On the Benefits of Cooperation via Power Control in OFDM-Based Visible Light Communication Systems," in *Proc. Pers. IEEE 25th Int. Symp. Indoor Mobile Radio Commun.*, Sept. 2014, pp. 856–860.
[8] R. C. Kizilirmak and M. Uysal, "Relay-Assisted OFDM Transmission for Indoor Visible Light Communication," in *Proc. IEEE Int. Black Sea Conf. Commun. Netw.*, May 2014, pp. 11–15.
[9] R. U. Nabar, H. Bolcskei, and F. W. Kneubuhler, "Fading Relay Channels: Performance Limits and Space-Time Signal Design," *IEEE J. Sel. Areas Commun.*, vol. 22, no. 6, pp. 1099–1109, Aug. 2004.
[10] J. M. Kahn and J. R. Barry, "Wireless Infrared Communications," *Proceedings of the IEEE*, vol. 85, no. 2, pp. 265–298, Feb. 1997.
[11] J. Armstrong and B. Schmidt, "Comparison of Asymmetrically Clipped Optical OFDM and DC-Biased Optical OFDM in AWGN," *IEEE Commun. Lett.*, vol. 12, no. 5, pp. 343–345, May 2008.
[12] Z. Chen, D. Tsonev, and H. Haas, "Improving SINR in Indoor Cellular Visible Light Communication Networks," in *Proc. IEEE Int. Conf. Commun.*, Jun. 2014, pp. 3383–3388.
[13] E. Telatar, "Capacity of Multi-antenna Gaussian Channels," *European Trans. Telecommun.*, vol. 10, no. 6, pp. 585–595, Nov./Dec. 1999.

Spectral Efficient Cooperative Downlink Transmission Schemes for DCO-OFDM-Based Optical Attocell Networks

Hossein Kazemi, Majid Safari and Harald Haas
Li-Fi Research and Development Center, The University of Edinburgh, Edinburgh, EH9 3JL, United Kingdom.
Email: {h.kazemi, majid.safari, h.haas}@ed.ac.uk

***Abstract*—In this paper, novel spectral efficient cooperative transmission schemes are proposed for downlink in indoor light-fidelity (Li-Fi) cellular networks, also termed as optical attocell networks. Downlink cooperation builds upon dual-hop decode-and-forward (DF) relaying with the aid of one or two neighboring base stations (BSs). The connections between the source BS and the relay BSs are provided by perfectly aligned visible light communication (VLC) links. Two cooperation protocols are introduced and evaluated, namely, non-orthogonal DF (NDF) and joint transmission with DF (JDF). A multiple access system based on direct current optical orthogonal frequency division multiplexing (DCO-OFDM) with fractional frequency reuse (FFR) is considered. Also, a line-of-sight (LOS) Lambertian propagation model is used for the indoor VLC channel. For each scheme, the signal-to-interference-plus-noise ratio (SINR) and spectral efficiency for user equipment (UE) with random coordinates in an attocell are derived. The average spectral efficiency within an optical attocell is studied using Monte Carlo simulations.**

***Index Terms*—Light-fidelity (Li-Fi), optical attocell networks, visible light communication (VLC), direct current optical orthogonal frequency division multiplexing (DCO-OFDM), fractional frequency reuse (FFR), decode-and-forward (DF) relaying.**

I. Introduction

Exponential increase in the number of smart phones during the last decade has produced a burden on the wireless data networks, and it is greatly challenging to fulfil the bandwidth requirements primarily due to the limited radio frequency (RF) spectrum. Visible light communication (VLC) using off-the-shelf light emitting diodes (LEDs) provides a complementary solution. The white LED-based lighting infrastructure existing in indoor environments is used to develop light-fidelity (Li-Fi) cellular networks composed of many tiny cells, termed optical attocell networks [1], [2]. Li-Fi offers important advantages over RF [3]: i) hundreds of terahertz unlicensed bandwidth available from the visible light spectrum; ii) easy integration into the existing LED luminaires; iii) much higher signal-to-noise ratio (SNR); iv) no co-channel interference (CCI) to adjacent rooms separated with opaque walls; and v) no fading.

A VLC system uses intensity modulation (IM) at the LED transmitter and direct detection (DD) at the receiver using a solid-state photodiode (PD). Optical orthogonal frequency division multiplexing (O-OFDM) is a viable modulation format for VLC [3]. There are several variants and direct current (DC) biased O-OFDM (DCO-OFDM) has the highest spectral efficiency and is simple to implement, thus attracting most research attention [4]. The downlink performance of DCO-OFDM-based optical attocell networks has been studied in [5]. To mitigate the effect of inter-cell interference (ICI), fractional frequency reuse (FFR) has been further studied in [6].

For cooperative VLC systems, relay-assisted transmission based on DCO-OFDM for a point-to-point VLC system is studied in [7], and the system performance is assessed in terms of bit error ratio (BER). Also, the feasible rate regions of a system with two interfering DCO-OFDM transmitters and two receivers is investigated in [8], using an interference coordination method based on orthogonal transmission and joint power control. However, the approaches in these studies are not directly applicable to optical attocell networks that essentially include multiple Li-Fi base stations (BSs) and user equipments (UEs). In this paper, novel spectral efficient cooperative transmission schemes are proposed for downlink in optical attocell networks. The cooperation is based on dual-hop decode-and-forward (DF) relaying through neighboring BSs by two protocols: non-orthogonal DF (NDF) [9] and joint transmission with DF (JDF). A multiple access DCO-OFDM system with FFR planning is considered, and the downlink spectral efficiency is studied using Monte Carlo simulations.

The remainder of the paper is organized as follows. In Section II, the optical attocell system model is described. In Section III, the methodology and modeling for the proposed cooperative downlink transmission schemes are described, and signal-to-interference-plus-noise ratio (SINR) derivations are presented. In Section IV, spectral efficiency calculations are introduced. In Section V, simulation results are presented, and finally, concluding remarks are given in Section VI.

II. System Model

Fig. 1 illustrates the geometric configuration of the downlink in an indoor optical attocell network. The system consists of a BS transmitter with a white LED installed on the ceiling of an indoor environment and a PD receiver embedded in the UE. Throughout this paper, the term access point (AP) may be used interchangably for BS. The LEDs are assumed to be point sources with Lambertian emission patterns, and also to operate within the linear dynamic range of the current-to-power characteristic curve so as to avoid nonlinear distortion effects. In addition, the LEDs are assumed to be oriented vertically downwards and the PD receiver of each UE is

oriented vertically upwards. An optical attocell is defined as the area on the receiver plane within which the intended UE is served by any BS.

Fig. 2 illustrates the hexagonal cellular layout of an optical attocell network with seven attocells considered here. For each UE in a given attocell, the receiver field of view (FOV) is assumed to be sufficiently wide to allow simultaneous detection of optical signals from the source BS and the six neighboring BSs. The downlink performance of a UE in the zeroth attocell (for BS_0) is studied. The position of the UE is random and uniform in space. The coverage area of each attocell is divided into two parts: a cell central region with a circular radius R_c, and a cell edge region with an equivalent circular radius R_e. The approximated circular cell has the same coverage area as the original hexagonal cell with a radius R, yielding $R_\mathrm{e} \approx 0.91R$.

A. Light Propagation Model

In this paper, only line-of-sight (LOS) is considered for indoor visible light propagation and reflection paths are not considered, as shown in Fig. 1. It was shown in [6] that the reflection paths have insignificant effect on the attocells that are sufficiently away from the network boundaries. The VLC channel is assumed to have a low-pass flat frequency response dominated by the LOS path, which can be characterized by its DC gain. Assuming a unity gain for both the concentrator and optical filter, the DC gain of the VLC channel from BS_i to UE, for $i = 0, 1, \ldots, 6$, is given as [10, Eq. (10)]:

$$G_i = \frac{(m+1)A_\mathrm{PD}}{2\pi d_i^2}\cos^m(\varphi_i)\cos(\psi_i)\mathrm{rect}\left(\frac{\psi_i}{\Psi_\mathrm{a}}\right), \quad (1)$$

where $m = -\ln 2/\ln(\cos\Phi_\mathrm{a})$ is the Lambertian order and Φ_a is the semi-angle at half-power of the LED emission pattern; A_PD is the effective PD area; d_i is the Euclidean distance from UE to BS_i; φ_i is the light radiance angle with respect to the maximum power direction for BS_i; ψ_i is the light incidence angle with respect to the direction perpendicular to the PD plane; and Ψ_a is the FOV of the UE receiver. The last factor in (1) is for the rectangular function defined as $\mathrm{rect}(x) = 1$ if $|x| \leq 1$, and 0 otherwise.

B. Multiple Access and Frequency Reuse Planning

To provide multiple access for UEs, an orthogonal frequency division multiple access (OFDMA) system based on DCO-OFDM is considered. The quadrature amplitude modulation (QAM) data symbols of different UEs, X_k, are arranged on N subcarriers of the OFDMA frame in the frequency domain to get $\mathbf{X} = [X_0, X_1, \ldots, X_{N-1}]$, before the application of the inverse discrete fourier transform (IDFT). Average power of every symbol is normalized to unity such that $\mathbb{E}[|X_k|^2] = 1$, for $k = 0, 1, \ldots, N-1$, where $\mathbb{E}[\cdot]$ denotes the expectation operator. For optical IM systems, the modulating signal must be both real and positive [4]. This requires that $X_k = X_{N-k}^*$, for $k \neq 0$, where $[\cdot]^*$ denotes the complex conjugate operator, and $X_0 = X_{N/2} = 0$. Hence, only $\tilde{N} = N/2 - 1$ symbols

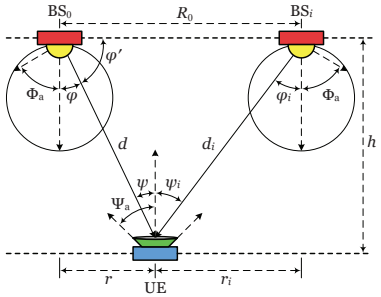

Fig. 1. Downlink geometry in an indoor optical attocell network.

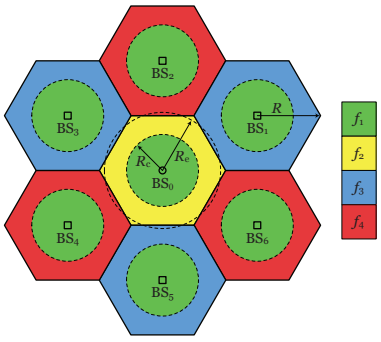

Fig. 2. Hexagonal cellular layout of seven attocells with an FFR plan: $\Delta = 1$ for cell central regions, and $\Delta = 3$ for cell edge regions.

carry information. The DCO-OFDMA signal can be expressed as $x(n) = x_\mathrm{DC} + \tilde{x}(n)$ where x_DC is the DC bias, and:

$$\tilde{x}(n) = \sum_{k=0}^{N-1}\tilde{x}_k(n) = \frac{1}{\sqrt{N}}\sum_{k=0}^{N-1}X_k\exp\left(j\frac{2\pi kn}{N}\right), \quad (2)$$

in which n is the sample number for $n = 0, 1, \ldots, N-1$; $\tilde{x}_k(n)$ is the alternating current (AC) signal component modulated on subcarrier k at time sample n; and $j = \sqrt{-1}$. Here, $x_\mathrm{DC} = \alpha\sqrt{P_\mathrm{elec,AC}}$ where α is a scaling factor and $P_\mathrm{elec,AC} = \sum_{k=0}^{N-1}\mathbb{E}[\tilde{x}_k^2(n)]$ is the total electrical power for transmission [4]. The average optical power is defined as $P_\mathrm{opt} = \mathbb{E}[x(n)] = x_\mathrm{DC}$, and thus $P_\mathrm{elec,AC} = P_\mathrm{opt}^2/\alpha^2$. The DC bias is chosen to meet the illumination requirement.

Two frequency reuse plans are examined, including full frequency reuse (FR) and FFR. In FR, the frequency reuse factor (FRF), denoted as Δ, is equal to 1 for every attocell in the network. The FR system is taken as a baseline for performance evaluations. After removing the DC bias followed by perfect sampling and synchronization, the received photocurrent of a given UE on subcarrier k at time sample n is given by:

$$y_k(n) = R_\mathrm{PD}\sum_{i=0}^{6}G_i\sqrt{P_{\mathrm{elec},i,k}}\tilde{x}_{i,k}(n) + v_k(n), \quad (3)$$

where $R_{\rm PD}$ denotes the PD responsivity; $P_{{\rm elec},i,k}$ denotes the electrical signal power transmitted by BS$_i$ on subcarrier k; and $\tilde{x}_{i,k}(n)$ is the transmitted signal from BS$_i$ on subcarrier k at time sample n. Note that for $i=0$, $\tilde{x}_{0,k}(n)$ is the only desired signal transmitted from BS$_0$ for UE. In (3), $v_k(n)$ is white Gaussian noise modeling shot noise and thermal noise in the UE receiver with zero mean and variance of $\sigma_k^2 = N_0 B/N$, where N_0 denotes the noise power spectral density (PSD); and B is the modulation bandwidth. All BSs emit the same average optical power, and the total electrical transmission power is equally allocated among $N-2$ signal-carrying subcarriers so that $P_{{\rm elec},i,k} = P_{\rm opt}^2/(N-2)\alpha^2$, $\forall i,k$.

FFR divides the system bandwidth up into four disjoint sub-bands: one individual common sub-band (f_1) for cell central regions with $\Delta=1$; and three protected sub-bands (f_2,f_3,f_4) for cell edge regions with $\Delta=3$, as shown in Fig. 2. The number of subcarriers allocated to the common sub-band, $N_{\rm c}$, and to the protected sub-band, $N_{\rm e}$, are given as $N_{\rm c} = \lceil \tilde{N}\delta^2 \rceil$ and $N_{\rm e} = \lfloor (\tilde{N}-N_{\rm c})/3 \rfloor$, where $\delta = R_{\rm c}/R_{\rm e}$ [6]. The received signal model for a given UE located in the cell central region is identical to that of the FR system and is given by (3). When a UE is located in the cell edge region, the interference terms existing in (3) are eliminated and, therefore, the corresponding received photocurrent on subcarrier k is obtained as:

$$y_k(n) = R_{\rm PD} G_0 \sqrt{P_{{\rm elec},0,k}}\,\tilde{x}_{0,k}(n) + v_k(n). \tag{4}$$

C. Signal-to-Interference-plus-Noise Ratio

The ratio of the desired electrical signal power to the total noise and interference power is defined as SINR. Fig. 3 shows the network geometry in a polar coordinate system with BS$_0$ at the origin used for SINR calculations. The variables d_i, φ_i and ψ_i for G_i in (1) can be expressed in terms of the polar coordinates of the UE shown in Fig. 3 as $z=(r,\theta)$, using a change of variables: $d_i(z) = \sqrt{r_i^2(z)+h^2}$ and $\cos(\varphi_i) = \cos(\psi_i) = h/d_i(z)$ where $r_i(z) = \sqrt{r^2 - 2R_0 r\cos(\theta-\Theta_i) + R_0^2}$ is the Euclidean distance between BS$_i$ and UE for $i=1,2,\ldots,6$, and $r_0(z)=r$. Here, (R_0,Θ_i) are the polar coordinates of BS$_i$ in which $R_0=\sqrt{3}R$ and $\Theta_i = i\pi/3 - \pi/6$. For the FR system, using (1) and (3), the received SINR of a UE on subcarrier k at location z can be derived as:

$$\gamma_{\rm FR}(z) = \frac{(r^2+h^2)^{-m-3}}{\sum_{i=1}^{6}(r_i^2(z)+h^2)^{-m-3} + \Omega}, \tag{5}$$

where the parameter Ω is obtained as:

$$\Omega = \frac{4\pi^2\alpha^2 N_0 B(N-2)}{((m+1)h^{m+1}A_{\rm PD}R_{\rm PD}P_{\rm opt})^2 N}. \tag{6}$$

For the FFR system, if the UE location is in the cell central region, the received SINR is given by (5). In the cell edge region, using (1) and (4), the received SINR of a UE for each allocated subcarrier at location z is derived as:

$$\gamma_{\rm FFR}(z) = \Omega^{-1}\left(r^2+h^2\right)^{-m-3}. \tag{7}$$

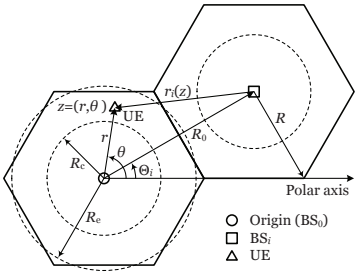

Fig. 3. Optical attocell network geometry in a polar coordinate system.

III. Spectral Efficient Downlink Cooperation

A. Base Stations Cooperative Transmission

Downlink cooperation is performed only for the cell edge UEs by using DF relaying in conjunction with FFR planning. The relays are chosen from the neighboring BSs, and the required connections between BS$_0$ and relays are realized by AP-to-AP VLC links. To this end, the number of LEDs on BS$_0$ is augmented by the addition of six auxiliary LEDs allowing each one to point at the corresponding relay BS and, accordingly, six PD receivers are considered on the relay BSs side, perfectly aligned to the LED transmitters of BS$_0$. With this setup, AP-to-AP links also operate in the visible light spectrum, and thus they need to access the shared bandwidth of the downlink system. To prevent unwanted interference for the cell edge regions of the neighboring attocells, AP-to-AP links use the protected sub-band, which is f_2 for the attocell served by BS$_0$ as shown in Fig. 2. The relay downlink has to comply with two conditions i) that it does not interfere with the direct downlink; and ii) that it allocates the same number of subcarriers to the UE as on the direct downlink. According to the FFR plan, there is a free sub-band between BS$_0$ and every neighboring BS satisfying both conditions, as shown in Fig. 2. For instance, f_4 remains unallocated between BS$_0$ and three BSs 1, 3 and 5, hence this free sub-band is used for downlink relaying when the relay BSs are among these BSs. From an information theoretical perspective, the direct downlink along with the relay downlink create parallel communication channels, because they use two non-overlapping frequency sub-bands. Therefore, they can be utilized for sending different parts of the UE data to maximize the achievable rate. The effect of ceiling reflections from AP-to-AP links is not considered in this paper, and will be the subject of future works.

B. Non-orthogonal Decode-and-Forward Relaying

The NDF protocol realizes non-orthogonal transmissions in the time domain for the direct and relay downlinks using two time slots, similar to Protocol I in [9]. To maintain a good balance between performance and complexity, at most two relays may be involved [11]. In the following, the notation q is used for the index of the selected relay BS, and k is used for

the index of the subcarrier allocated to UE on either the source or relay BSs regardless of the operating sub-bands. Let $\tilde{x}_{i,k,t}$ be the signal transmitted by BS_i and $y_{k,t}$ be the signal received by UE on subcarrier k and time slot t, for $t = 1, 2$. Also, the notation $\tilde{x}^{(c)}_{i,k,t}$ is used to distinguish between different parts of the UE data, for $c = 1, 2, 3, 4$.

NDF1: Only one relay is used for downlink relaying, which is chosen as the neighboring BS that has the highest DC gain to the desired UE. Specifically, the nearest neighboring BS to the UE is selected as the relay. The UE data is split into three parts. During the first time slot, BS_0 transmits the first part directly to UE and, at the same time, directs the second part to the relay over the corresponding AP-to-AP link. During the second time slot, the relay decodes the signal and then retransmits it to UE, while BS_0 transmits the third part to UE. The signal received by BS_q on subcarrier k in time slot 1 can be expressed as:

$$w_{k,1}(n) = R_{\text{PD}} G_{\text{s}} \sqrt{P_{\text{elec},0,k}}\, \tilde{x}^{(2)}_{0,k,1}(n) + v_{k,1}(n), \quad (8)$$

where $v_{k,1}(n)$ is the associated noise, independent identically distributed as the downlink noise in Section II; and G_{s} is the DC gain of the VLC channel for an AP-to-AP link. According to (1) for $d_i = R_0$ and $\varphi_i = \psi_i = 0$, $G_{\text{s}} = (\ell+1)A_{\text{PD}}/2\pi R_0^2$ where $\ell = -\ln 2/\ln(\cos\Phi_{\text{b}})$ is the Lambertian order and Φ_{b} is the semi-angle at half-power of the emission pattern for auxiliary LEDs on BS_0. Based on (8), the SNR of the AP-to-AP link between BS_0 and BS_q can be calculated as:

$$\gamma_0 = \frac{R_{\text{PD}}^2 G_{\text{s}}^2 P_{\text{elec},0,k}}{\sigma_k^2} = \frac{\left((\ell+1)A_{\text{PD}} R_{\text{PD}} P_{\text{opt}}\right)^2 N}{4\pi^2 \alpha^2 R_0^4 N_0 B(N-2)}. \quad (9)$$

Given that the auxiliary LEDs on BS_0 are labeled according to the indexes of the neighboring BSs, the signal received by a UE in the cell edge region on subcarrier k in time slot 1 can be written as:

$$\begin{aligned} y_{k,1}(n) =& R_{\text{PD}} G_0 \sqrt{P_{\text{elec},0,k}}\, \tilde{x}^{(1)}_{0,k,1}(n) + \\ & R_{\text{PD}} G'_q \sqrt{P_{\text{elec},0,k}}\, \tilde{x}^{(2)}_{0,k,1}(n) + v_{k,1}(n), \end{aligned} \quad (10)$$

where G'_q denotes the DC gain from auxiliary LED q to UE. Note that the second term in (10) is the interference received from the AP-to-AP link. Considering Lambertian emission patterns for auxiliary LEDs and following the methodology in [11] to model G'_q, the received SINR of a UE at location z in time slot 1 for NDF1 can be derived and expressed as:

$$\gamma_1(z) = \frac{(r^2+h^2)^{-m-3}}{\left[\frac{(\ell+1)r^\ell}{(m+1)h^m}\right]^2 (r^2+h^2)^{-\ell-3}\cos^{2\ell}(\theta-\Theta_q) + \Omega}. \quad (11)$$

The received signal of UE on subcarrier k from its sub-band with BS_0 in time slot 2, containing $\tilde{x}^{(3)}_{0,k,2}$, is similar to that of the FFR system in (4), and the corresponding SINR, denoted as $\gamma_{2,0}(z)$, is equal to $\gamma_{\text{FFR}}(z)$ given in (7). Assuming that BS_q successfully decodes the signal in (8), the received signal of a UE in time slot 2 on subcarrier k from its sub-band with BS_q can be written as:

$$\begin{aligned} y_{k,2}(n) =& R_{\text{PD}} G_0 \sqrt{P_{\text{elec},0,k}}\, \tilde{x}^{(2)}_{0,k,1}(n) + \\ & R_{\text{PD}} \sum_{i\in\mathcal{I}} G_i \sqrt{P_{\text{elec},i,k}}\, \tilde{x}_{i,k,2}(n) + v_{k,2}(n), \end{aligned} \quad (12)$$

where $\mathcal{I}$ is the index set of interfering BSs with two possibilities, either $\mathcal{I} = \{1, 3, 5\}$ or $\mathcal{I} = \{2, 4, 6\}$, depending on the UE location. The received SINR of UE in time slot 2 on its sub-band with BS_q is derived as:

$$\gamma_{2,\text{q}}(z) = \frac{\left(r_q^2(z)+h^2\right)^{-m-3}}{\sum\limits_{i\in\mathcal{I}} \left(r_i^2(z)+h^2\right)^{-m-3} + \Omega}. \quad (13)$$

NDF2: Two adjacent relays are used for downlink relaying. In addition to the first relay, the second relay is also determined by the highest DC gain criterion. In other words, the second nearest neighboring BS to UE is selected as the second relay to contribute to the downlink cooperation. The UE data is split into four parts. During the first time slot, $\tilde{x}^{(1)}_{0,k,1}$ is directly transmitted to UE, and concurrently two adjacent AP-to-AP links carry $\tilde{x}^{(2)}_{0,k,1}$ and $\tilde{x}^{(3)}_{0,k,1}$ towards the relays. Subsequently, during the second time slot, BS_0 transmits $\tilde{x}^{(4)}_{0,k,2}$ directly to UE and the relays retransmit $\tilde{x}^{(2)}_{0,k,1}$ and $\tilde{x}^{(3)}_{0,k,1}$ to UE, after successful decoding. Using (1) and (9), and considering the cross-coupling between the two adjacent AP-to-AP links, the SINR of the AP-to-AP link can be calculated as:

$$\gamma_{\text{b}} = \frac{\gamma_0}{2^{-2\ell}\gamma_0 + 1}. \quad (14)$$

The received SINR of UE in time slot 1 is derived as:

$$\gamma_1(z) = \frac{(r^2+h^2)^{-m-3}}{\left[\frac{(\ell+1)r^\ell}{(m+1)h^m}\right]^2 (r^2+h^2)^{-\ell-3} \sum\limits_{q\in Q} \cos^{2\ell}(\theta-\Theta_q) + \Omega}, \quad (15)$$

where $Q = \{q_1, q_2\}$ is the index set of the first and second relays. The received SINR of UE in time slot 2 on its sub-band with BS_{q_1}, denoted as $\gamma_{2,q_1}(z)$, is given by (13), and in time slot 2 on its sub-band with BS_{q_2}, denoted as $\gamma_{2,q_2}(z)$, is given by (13) when replacing $r_q(z)$ by $r_{q_2}(z)$, and the index set of interfering BSs $\mathcal{I}$ by its complement $\mathcal{I}'$.

C. Joint Transmission with Decode-and-Forward Relaying

The JDF protocol takes a single time slot for complete data transmission using one or two relays as follows.

JDF1: Only one relay is used, which is chosen in the same way as NDF1. The UE data is divided into two independent parts, and one part is transmitted over the direct downlink and another part through the relay downlink using DF relaying. This protocol exploits the time and frequency resources by sending a continuous flow of data through the relay downlink on every time slot, unlike NDF1 where the relay downlink is active only in the second time slot. Under JDF1, the received signals of a UE in the cell edge region on its sub-bands with BS_0 and BS_q are identical to that in (10) and that in (12),

respectively. The corresponding SINR for the direct and relay downlinks, denoted as $\gamma_1(z)$ and $\gamma_{\rm q}(z)$, are exactly equal to that in (11) and $\gamma_{2,{\rm q}}(z)$ in (13).

JDF2: Two adjacent relays are used, similar to NDF2. The UE data is divided into three independent parts, which are separately transmitted to UE through three parallel channels comprising the direct downlink and the two relay downlinks. The SINR of UE for the direct downlink, $\gamma_1(z)$, is given by (11), and the SINR for the first and second relay downlinks, denoted as $\gamma_{q1}(z)$ and $\gamma_{q2}(z)$, are exactly equal to $\gamma_{2,q_1}(z)$ and $\gamma_{2,q_2}(z)$ as in NDF2, respectively.

IV. Assessment of Spectral Efficiency

In this paper, the Shannon-Hartley upper bound is used to estimate the throughput of the optical attocell downlink. Define $\xi = \tilde{N}/N = (N-2)/2N$ as the bandwith utilization ratio for a DCO-OFDMA system, then the spectral efficiency of a UE at location z can be calculated as a function of $\gamma(z)$ with Δ as a parameter [6]:

$$\rho\left(\gamma(z);\Delta\right) = \frac{\xi}{\Delta}\log_2\left(1+\gamma(z)\right). \tag{16}$$

For the FR system, inserting (5) and $\Delta = 1$ in (16), the spectral efficiency of the UE can be calculated as:

$$\rho_{\rm FR} = \rho\left(\gamma_{\rm FR}(z);1\right) = \xi\log_2\left(1+\gamma_{\rm FR}(z)\right). \tag{17}$$

In the case of FFR, if the UE location is in the cell central region, the spectral efficiency of the UE is given by (17), and if the UE location is in the cell edge region, the spectral efficiency of the UE can be calculated by substituting (7) and $\Delta = 3$ into (16) as:

$$\rho_{\rm FFR} = \rho\left(\gamma_{\rm FFR}(z);3\right) = \frac{\xi}{3}\log_2\left(1+\gamma_{\rm FFR}(z)\right). \tag{18}$$

For cooperative FFR (CFFR) schemes, since different parts of the UE data are received from independent parallel channels as discribed in Section III, the aggregate data rate of the UE is simply equal to the summation of the data rates for every channel element. Note that the successful decoding of the signal at the relay imposes a fundamental constraint on the achievable end-to-end rate of the relay downlink with a dual-hop DF relaying. For NDF1, the spectral efficiency of the UE in the cell edge region can be calculated as:

$$\rho_{\rm NDF1} = \frac{1}{2}\times\frac{\xi}{3}\big[\log_2(1+\gamma_1(z)) + \log_2(1+\gamma_{2,0}(z)) + \log_2(1+\min\{\gamma_{2,{\rm q}}(z),\gamma_0\})\big], \tag{19}$$

where a factor $\frac{1}{2}$ arises from the use of two time slots; and $\min\{\gamma_{2,{\rm q}}(z),\gamma_0\}$ is the equivalent end-to-end SINR for the dual-hop DF relaying downlink through BS$_q$. Also, for NDF2, the spectral efficiency of the UE can be expressed as:

$$\rho_{\rm NDF2} = \frac{\xi}{6}\Bigg[\log_2(1+\gamma_1(z)) + \log_2(1+\gamma_{2,0}(z)) + \sum_{q\in Q}\log_2(1+\min\left\{\gamma_{2,q}(z),\gamma_{\rm b}\right\})\Bigg], \tag{20}$$

TABLE I
System Parameters.

Parameter	Symbol	Value	Unit
LED optical power	$P_{\rm opt}$	10	W
Downlink LED semi-angle	$\Phi_{\rm a}$	40	$^\circ$
Vertical separation	h	2.15	m
Hexagonal cell radius	R	2.5	m
Cell partitioning ratio	δ	0.72	–
Modulation bandwidth	B	20	MHz
DFT/IDFT length	N	512	–
Noise PSD	N_0	1×10^{-21}	A^2/Hz
Effective PD area	$A_{\rm PD}$	1×10^{-4}	m^2
PD responsivity	$R_{\rm PD}$	0.6	A/W
DC bias scaling factor	α	3	–

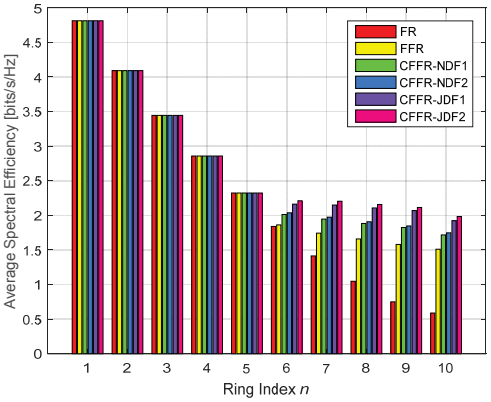

Fig. 4. Average spectral efficiency performance of UEs per ring around BS$_0$ with FR, FFR, CFFR-NDF and CFFR-JDF schemes for $\Phi_{\rm b} = 10^\circ$.

where $Q = \{q_1, q_2\}$. Similarly, the spectral efficiency of the UE in the cell edge region for JDF1 and JDF2 are given as:

$$\rho_{\rm JDF1} = \frac{\xi}{3}\big[\log_2(1+\gamma_1(z)) + \log_2(1+\min\{\gamma_{\rm q}(z),\gamma_0\})\big], \tag{21}$$

$$\rho_{\rm JDF2} = \frac{\xi}{3}\Bigg[\log_2(1+\gamma_1(z)) + \sum_{q\in Q}\log_2(1+\min\{\gamma_q(z),\gamma_{\rm b}\})\Bigg]. \tag{22}$$

V. Results and Discussions

This section presents performance results for the average spectral efficiency of the FR and FFR systems described in Section II, and the CFFR system with NDF and JDF schemes described in Section III, based on Monte Carlo averaging of (17)–(22) from Section IV. Table I lists the system parameters used for simulations. In order to study the effect of the UE location on the system performance, the attocell of BS$_0$ is divided into 10 rings with equal areas, and the focus is on the cell edge region (i.e., for ring indexes $n = 6, 7, 8, 9, 10$).

Fig. 4 gives the average spectral efficiency of UEs within each ring around BS$_0$ for $\Phi_{\rm b} = 10^\circ$. This figure clearly shows that the system performance is improved for both NDF and JDF schemes compared with the FR and FFR systems. It

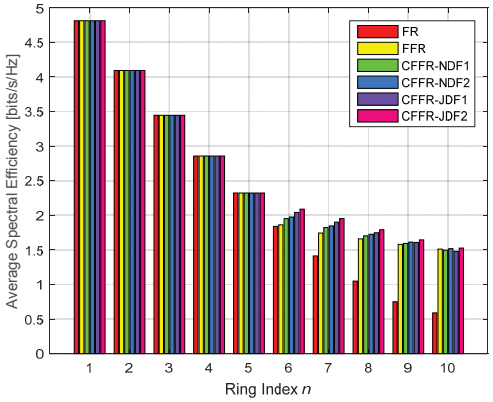

Fig. 5. Average spectral efficiency performance of UEs per ring around BS_0 with FR, FFR, CFFR-NDF and CFFR-JDF schemes for $\Phi_b = 20°$.

is observed that the average spectral efficiency performance of the NDF2 and JDF2 schemes are slightly higher than the NDF1 and JDF1 schemes, respectively. However, the signal processing complexity required for employing the second relay may not be worthwhile when compared with the low improvements achieved, particularly for the NDF scheme. Also, it is observed that the JDF scheme globally achieves higher improvements compared with NDF. The reason is that JDF exploits the opportunity for transmission on all parallel channels available in the time, space and frequency domains provided by dual-hop relaying together with FFR planning to maximize the UE data rate, as explained in Section III.A.

Fig. 5 presents the average spectral efficiency performance of UEs in each ring around BS_0 for $\Phi_b = 20°$. Comparing this figure with Fig. 4, it can be seen that the overall performance is decreased by doubling the semi-angle of auxiliary LEDs on BS_0 from $\Phi_b = 10°$ to $20°$. It is observed from Fig. 5 that the performance improvement for the NDF and JDF schemes is decreased from $n = 6$ to 10, and eventually for $n = 10$ (i.e., the outermost ring in the cell edge region) the performance for the FFR and all of CFFR schemes become almost equal to one another. In fact, by increasing Φ_b, the extent of interference from the AP-to-AP links at the UE is increased, and this compromises the performance gains for the NDF and JDF schemes, especially for the outer rings. Therefore, in order to achieve the desirable spectral efficiency gains with the NDF and JDF schemes, a careful adjustment of Φ_b is required so as to make it adequately small. This can be accomplished using proper optics (e.g., optical lenses) for auxiliary LEDs on BS_0.

Table II summarizes the results for the performance improvement of the FFR system and the CFFR system with NDF and JDF schemes relative to the FR system in the cell edge region for $\Phi_b = 10°$ and $\Phi_b = 20°$. Also, compared with FFR, it is observed from Table II that for JDF1 and JDF2, improvements of 0.410 and 0.472 bits/s/Hz, respectively, are achieved for the average spectral efficiency. For NDF1 and NDF2, this is 0.205 and 0.235 bits/s/Hz, respectively.

TABLE II
AVERAGE SPECTRAL EFFICIENCY IMPROVEMENT OF FFR, CFFR-NDF AND CFFR-JDF SCHEMES RELATIVE TO FR SYSTEM.

Φ_b	Ring n	FFR	NDF1	NDF2	JDF1	JDF2
10°	6	0.022	0.172	0.197	0.322	0.371
	7	0.329	0.532	0.560	0.735	0.790
	8	0.611	0.835	0.860	1.059	1.108
	9	0.830	1.074	1.097	1.319	1.364
	10	0.922	1.127	1.158	1.332	1.394
20°	6	0.022	0.111	0.135	0.201	0.248
	7	0.329	0.408	0.434	0.487	0.538
	8	0.611	0.655	0.677	0.699	0.743
	9	0.829	0.843	0.862	0.857	0.895
	10	0.922	0.907	0.930	0.891	0.937

VI. CONCLUDING REMARKS

Novel spectrally efficient cooperative transmission schemes are proposed for downlink in optical attocell networks based on two protocols, namely, CFFR-NDF and CFFR-JDF. Each protocol may have either one or two relay-assisted transmissions on the sub-bands exploited from an underlying FFR planning. The best performance in terms of the average spectral efficiency is attained by a JDF scheme using two relays among all schemes. It is also found that the spectral efficiency gains offered by the NDF and JDF schemes are inversely related to the emission semi-angle of the auxiliary LEDs used for the AP-to-AP links.

ACKNOWLEDGMENT

Professor Harald Haas acknowledges support by the UK Engineering and Physical Research Council (EPSRC) under Grant EP/K008757/1.

REFERENCES

[1] H. Haas, "High-speed wireless networking using visible light," *SPIE Newsroom*, 19 Apr. 2013.
[2] H. Haas, L. Yin, Y. Wang, and C. Chen, "What is LiFi?" *IEEE/OSA J. Lightw. Technol.*, vol. 34, no. 6, pp. 1533–1544, Mar. 2016.
[3] S. Dimitrov and H. Haas, *Principles of LED Light Communication Towards Networked Li-Fi*. Cambridge University Press, Mar. 2015.
[4] J. Armstrong and B. Schmidt, "Comparison of Asymmetrically Clipped Optical OFDM and DC-Biased Optical OFDM in AWGN," *IEEE Commun. Lett.*, vol. 12, no. 5, pp. 343–345, May 2008.
[5] C. Chen, D. A. Basnayaka, and H. Haas, "Downlink Performance of Optical Attocell Networks," *IEEE/OSA J. Lightw. Technol.*, vol. 34, no. 1, pp. 137–156, Jan. 2016.
[6] C. Chen, S. Videv, D. Tsonev, and H. Haas, "Fractional Frequency Reuse in DCO-OFDM-Based Optical Attocell Networks," *IEEE/OSA J. Lightw. Technol.*, vol. 33, no. 19, pp. 3986–4000, Oct. 2015.
[7] R. Kizilirmak, O. Narmanlioglu, and M. Uysal, "Relay-Assisted OFDM-Based Visible Light Communications," *IEEE Trans. Commun.*, vol. 63, no. 10, pp. 3765–3778, Oct. 2015.
[8] M. Kashef, M. Abdallah, K. Qaraqe, H. Haas, and M. Uysal, "Coordinated Interference Management for Visible Light Communication Systems," *IEEE/OSA J. Opt. Commun. Netw.*, vol. 7, no. 11, pp. 1098–1108, Nov. 2015.
[9] R. U. Nabar, H. Bolcskei, and F. W. Kneubuhler, "Fading Relay Channels: Performance Limits and Space-Time Signal Design," *IEEE J. Sel. Areas Commun.*, vol. 22, no. 6, pp. 1099–1109, Aug. 2004.
[10] J. M. Kahn and J. R. Barry, "Wireless Infrared Communications," *Proceedings of the IEEE*, vol. 85, no. 2, pp. 265–298, Feb. 1997.
[11] H. Kazemi and H. Haas, "Downlink Cooperation with Fractional Frequency Reuse in DCO-OFDMA Optical Attocell Networks," in *Proc. IEEE Int. Conf. Commun.*, May 2016 (to appear).

IEEE ICC 2017 Optical Networks and Systems Symposium

A Wireless Backhaul Solution Using Visible Light Communication for Indoor Li-Fi Attocell Networks

Hossein Kazemi, Majid Safari and Harald Haas
Li-Fi R&D Centre, Institute for Digital Communications, University of Edinburgh, Edinburgh, EH9 3JL, UK.
Email: {h.kazemi, majid.safari, h.haas}@ed.ac.uk

***Abstract*—Light-fidelity (Li-Fi) is an emerging technology for wireless optical networking using the principle of visible light communication (VLC). Li-Fi attocells are smaller in size than the radio frequency (RF) femtocells, suitable for deploying ultra-dense cellular networks. In this paper, a novel wireless backhaul solution is proposed for indoor Li-Fi attocell networks using VLC, which is already embedded in the Li-Fi base station (BS) units. Since the backhaul links operate in the visible light spectrum, two methods are proposed for bandwidth allocation between the access and backhaul links, namely, full frequency reuse (FR) and in-band (IB). In order to realize dual-hop transmission over the backhaul and access links, both amplify-and-forward (AF) and decode-and-forward (DF) relaying protocols are analyzed. Considering a direct current optical orthogonal frequency division multiplexing (DCO-OFDM)-based multiple access system, novel signal-to-interference-plus-noise ratio (SINR) and spectral efficiency expressions are then derived for user equipment (UE) randomly distributed in each attocell. Downlink performance of the optical attocell network is assessed in terms of the average spectral efficiency using Monte Carlo simulations. Guidelines are given for the design of the proposed wireless backhaul system.**

***Index Terms*—Light-fidelity (Li-Fi), optical attocell network, visible light communication (VLC), direct current optical orthogonal frequency division multiplexing (DCO-OFDM), wireless backhaul, amplify-and-forward (AF), decode-and-forward (DF).**

I. Introduction

Overwhelming demand for access to wireless data networks during the recent years has created huge data traffic due to the abundance of portable digital multimedia devices such as smart phones and laptops. Thus, network operators have encountered a fundamental challenge to meet the bandwidth requirements due to the limited radio frequency (RF) spectrum. Visible light communication (VLC) using off-the-shelf light emitting diodes (LEDs) is a complementary solution [1]. Based upon VLC, light-fidelity (Li-Fi) has been proposed to achieve very dense cellular networks, termed optical attocell networks, by reusing the existing white LED luminaires in indoor environments [2].

In Li-Fi wireless communications, data is modulated by intensity variations of the LED light at the base station (BS) transmitter. The received optical signal is then directly detected by a solid-state photodiode (PD) at the user equipment (UE) receiver. Optical orthogonal frequency division multiplexing (OFDM) is a spectrally efficient and widely used modulation format for Li-Fi [3]. Among several variants, direct current (DC) biased optical OFDM (DCO-OFDM) has yielded the highest spectral efficiency and is simple to implement [4]. In [5], a detailed system-level study is provided for the downlink performance of DCO-OFDM-based optical attocell networks. In [6], fractional frequency reuse (FFR) cell partitioning is further considered to mitigate the effect of inter-cell interference (ICI) on the downlink. The underlying assumption in these papers is that there are unlimited capacity backhaul links for the Li-Fi BSs to connect to the backbone network.

A number of wired backhaul approaches for Li-Fi exist in published research [7]–[10]. In [7], the use of in-building electrical power wiring as the backhaul links is proposed in order to integrate power line communication (PLC) with VLC. Also, in [8], the application of a PLC backhaul for indoor broadband broadcasting is practically demonstrated. In [9], a cascaded system of Fast Ethernet and Power-over-Ethernet (PoE) with VLC is designed and implemented. In [10], an indoor Li-Fi local area network (LAN) architecture is proposed where standard single mode fiber (SMF) cables are used as the backhaul links. In these proposals, however, high complexity and implementation cost of cabling for the wired backhaul links are inevitable. The aim of this paper is to propose a novel wireless backhaul solution using VLC for indoor optical attocell networks. VLC is a natural choice for the wireless backhaul links, since it is already embedded in the Li-Fi BS units. Two methods are proposed for bandwidth allocation between the access and backhaul links including full frequency reuse (FR) and in-band (IB). Also, in order to realize dual-hop transmission through the backhaul and access links, both amplify-and-forward (AF) and decode-and-forward (DF) protocols are evaluated. A multiple access system based on DCO-OFDM is considered. System-level modeling and analysis are performed in this work. Downlink performance of the optical attocell network is studied in terms of the average spectral efficiency using Monte Carlo simulations.

The rest of the paper is structured as follows. In Section II, the optical attocell system model is described. In Section III, methodology and modeling for the proposed wireless backhaul system are described, and signal-to-interference-plus-noise ratio (SINR) derivations are presented. In Section IV, spectral efficiency derivations are presented. In Section V, simulation results are discussed, and conclusions are given in Section VI.

II. Optical Attocell System Model

Fig. 1 illustrates the geometric configuration of the downlink in an indoor optical attocell network. The system consists of a BS transmitter with a white LED installed on the ceiling of an indoor environment and a PD receiver mounted on the UE. The LEDs are assumed to be point sources with Lambertian

978-1-4673-8999-0/17/$31.00 ©2017 IEEE

emission patterns and also to operate within the linear dynamic range of the LED current-to-power characteristic curve so as to avoid nonlinear distortion effects. It is further assumed that the LEDs are oriented vertically downward and that the PD receiver of each UE is oriented vertically upward. An optical attocell is defined as the area on the receiver plane in which the intended UE is served by a BS. Throughout this paper, the term access point (AP) may be used interchangably for BS.

A. Light Propagation Model

In this paper, only line-of-sight (LOS) is considered for indoor visible light propagation and reflection paths are not considered, as shown in Fig. 1. According to [6], the effect of reflection paths is not significant for the attocells that are sufficiently distant from the network boundaries. The VLC channel is assumed to have a low-pass flat frequency response dominated by the LOS path, which can be characterized by its DC gain. Assuming a unity gain for both the concentrator and optical filter, the DC gain of the VLC channel from BS_i to UE, for $i = 0, 1, \ldots, 6$, is given as [11, Eq. (10)]:

$$G_i = \frac{(m+1)A_{\mathrm{PD}}}{2\pi d_i^2}\cos^m(\varphi_i)\cos(\psi_i)\mathrm{rect}\left(\frac{\psi_i}{\Psi_{\mathrm{a}}}\right), \quad (1)$$

where $m = -\ln 2/\ln(\cos\Phi_{\mathrm{a}})$ is the Lambertian order and Φ_{a} is the semi-angle at half-power of the LED emission pattern; A_{PD} is the effective PD area; d_i is the Euclidean distance from BS_i to UE; φ_i is the light radiance angle with respect to the maximum power direction for BS_i; ψ_i is the light incidence angle with respect to the direction perpendicular to the PD plane; and Ψ_{a} is the field of view (FOV) of the UE receiver. The last factor in (1) is the rectangular function defined as $\mathrm{rect}(x) = 1$ if $|x| \leq 1$, and 0 otherwise.

B. Optical Orthogonal Frequency Division Multiple Access

An optical orthogonal frequency division multiple access (OFDMA) system based on DCO-OFDM is used. To this end, quadrature amplitude modulation (QAM) data symbols of associated UEs, X_k, are arranged on N subcarriers in the frequency domain before the application of the inverse discrete fourier transform (IDFT). The resulting OFDMA frame has the form $\mathbf{X} = [X_0, X_1, \ldots, X_{N-1}]$. The average power of every symbol is normalized to unity such that $\mathbb{E}[|X_k|^2] = 1$, for $k = 0, 1, \ldots, N-1$, where $\mathbb{E}[\cdot]$ denotes the expectation operator. For optical intensity modulation and direct detection (IM/DD) systems, the modulating signal must be both real and positive [4]. This requires that $X_{N-k} = X_k^*$, for $k \neq 0$, and $X_0 = X_{N/2} = 0$, where $[\cdot]^*$ denotes the complex conjugate operator. Hence, a DCO-OFDM-based OFDMA frame carries $\tilde{N} = N/2 - 1$ data symbols. The time domain signal at the output of the IDFT can be expressed as $x(n) = x_{\mathrm{DC}} + \tilde{x}(n)$ where x_{DC} is the DC bias, and:

$$\tilde{x}(n) = \sum_{k=0}^{N-1}\tilde{x}_k(n) = \frac{1}{\sqrt{N}}\sum_{k=0}^{N-1}X_k\exp\left(j\frac{2\pi kn}{N}\right), \quad (2)$$

where $n = 0, 1, \ldots, N-1$; $\tilde{x}_k(n)$ is the signal component modulated on subcarrier k at time sample n; $j = \sqrt{-1}$; and

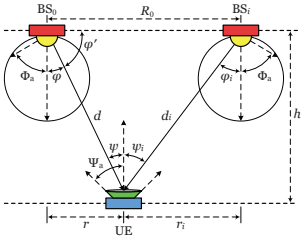

Fig. 1. Downlink geometry in an indoor optical attocell network.

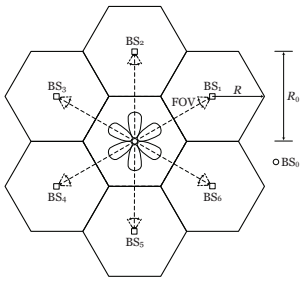

Fig. 2. Hexagonal cellular layout of seven attocells, and a plan view of wireless backhaul links provided by AP-to-AP VLC connections.

$x_{\mathrm{DC}} = \alpha\sqrt{P_{\mathrm{elec}}}$ where α is a scaling factor. Here, the total electrical transmission power is $P_{\mathrm{elec}} = \sum_{k=0}^{N-1}\mathbb{E}[\tilde{x}_k^2(n)]$ [4]. Also, the average optical power is $P_{\mathrm{opt}} = \mathbb{E}[x(n)] = x_{\mathrm{DC}}$, and thus $P_{\mathrm{elec}} = P_{\mathrm{opt}}^2/\alpha^2$. The output illumination level for LEDs is directly proportional to the DC bias.

III. Wireless VLC Backhaul System Design

Fig. 2 illustrates the hexagonal cellular layout of an optical attocell network with seven attocells. Other deployments for optical attocell networks include square and Poisson point process (PPP) [6]. Overall, the hexagonal cellular deployment gives an upper bound for the performance of practical optical attocell networks [6]. The UEs are associated with attocells according to the strongest received signal intensity (RSI) from the BSs, similar to the DC gain maximization criterion in [12], [13], which means that the UEs are associated with the nearest BS. The receiver FOV is assumed to be sufficiently wide to allow simultaneous detection of optical signals from all BSs. The downlink performance of UEs in each attocell is studied when their location is random with a uniform distribution.

A. Proposed Wireless Backhaul Configuration

The proposed wireless backhaul configuration using a star topology is depicted in Fig. 2. With this setup, BS_0 is directly connected to the backbone network by a high speed SMF cable and it is the gateway for its neighboring BSs. Consequently, BS_i, for $i = 1, 2, \ldots, 6$, are routed to the backbone network via the wireless backhaul links with BS_0 provided by perfectly aligned AP-to-AP VLC links. These links can be established

$$y_{0,k}(n) = R_{\rm PD} G_0 \sqrt{P_{{\rm elec},0,k}}\, \tilde{x}^{\rm a}_{0,k}(n) + R_{\rm PD} \sum_{i\in\mathcal{Q}} G'_i \sqrt{P_{{\rm elec},0,k}}\, \tilde{x}^{\rm b}_{i,k}(n) + R_{\rm PD} \sum_{i\in\mathcal{I}_0} G_i \sqrt{P_{{\rm elec},i,k}}\, \tilde{x}^{\rm a}_{i,k}(n) + v^{\rm a}_{0,k}(n). \quad (3)$$

$$\gamma_0(z) = \frac{(r^2+h^2)^{-m-3}}{\left[\frac{(\ell+1)r^\ell}{(m+1)h^m}\right]^2 (r^2+h^2)^{-\ell-3} \sum\limits_{i\in\mathcal{Q}} \cos^{2\ell}(\theta-\Theta_i) + \sum\limits_{i\in\mathcal{I}_0} \left(r_i^2(z)+h^2\right)^{-m-3} + \Omega}. \quad (4)$$

by the addition of six auxiliary LEDs on BS_0 allowing each one to point at a neighboring BS and six PD receivers on the neighboring BSs side, as shown in Fig. 2. Accordingly, the UEs in the attocell of BS_i receive data with a dual-hop transmission through the backhaul and access links, using either amplify-and-forward (AF) or decode-and-forward (DF) protocols [14]. Since the wireless backhaul links operate in the visible light spectrum, they need to use the shared bandwidth of the access links for data communication. Two methods are proposed for bandwidth allocation between the access and backhaul links including FR and IB. In the FR method, the entire bandwidth is fully reused accross all the access and backhaul links, while the IB method allocates the bandwidth depending on the spectral efficiency supported individually by the access and backhaul links. Two orthogonal IB sub-bands are allocated to the access and backhaul links, and each sub-band may be fully reused by either links. Further details will be provided in Section IV.B. The relaying downlink transmission in either AF or DF modes takes two time slots, one for the backhaul link, from the gateway to BS_i, and one for the access link, from BS_i to UE. For BS_0, no relaying is performed, and the entire bandwidth is always fully reused for downlink. The gateway sends a continuous flow of data toward BS_i without interruption. As a result, the backhaul links may interfere with the access links, particularly for the FR method by which both links operate on the same frequency band.

Note that the primary focus of this work is on the downlink. The uplink in optical attocell networks can be realized using the infrared (IR) band [1], [3], [11]. Using IR for the uplink, the links between the UEs and the BSs as well as the wireless backhaul links can be made bidirectional. Nevertheless, since the IR band does not interfere with the visible light band, the uplink is an independent problem and is not considered here. In addition, another option for the wireless backhaul is to use laser-based free space optical (FSO) links, but the use of laser in indoor environments is highly restricted due to eye safety [11], and this is not considered here. Moreover, in some indoor environments there is a suspended ceiling under the actual ceiling creating an enclosed space that can be used to separate the backhaul links from the access links. However, this is not available everywhere, and the purpose of this work is to avoid introducing any change to the existing infrastructure by cosidering a more general scenario with no suspended ceiling.

B. SINR Analysis for Full Frequency Reuse VLC Backhaul

Let $\tilde{x}^{\rm a}_{i,k}$ and $\tilde{x}^{\rm b}_{i,k}$ denote the signals transmitted in the access and backhaul links on subcarrier k for BS_i, $i = 1, 2, \ldots, 6$.

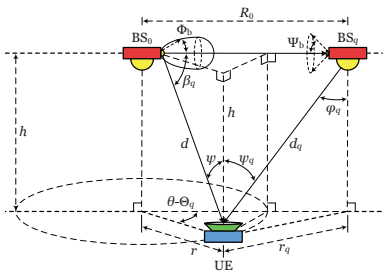

Fig. 3. Interferences caused by access and backhaul links on UE receiver in downlink with BS_0 from a neighboring BS and an AP-to-AP VLC link.

Fig. 3 illustrates interference sources at the UE receiver in the downlink with BS_0 from the access and backhaul links. After removing the DC bias followed by perfect sampling and synchronization, the received photocurrent of a UE in the attocell of BS_0 on subcarrier k at time sample n can be written as in (3) at the top of the page, where $R_{\rm PD}$ denotes the PD responsivity; and $P_{{\rm elec},i,k}$ denotes the electrical power transmitted by BS_i on subcarrier k. All BSs emit the same average optical power, and the total transmission power is equally allocated among $N-2$ signal-carrying subcarriers so that $P_{{\rm elec},i,k} = P^2_{\rm opt}/(N-2)\alpha^2$, $\forall i,k$. In (3), $v^{\rm a}_{0,k}(n)$ is white Gaussian noise modeling shot noise and thermal noise in the UE receiver with zero mean and variance of $\sigma_k^2 = N_0 B/N$, where N_0 denotes the noise power spectral density (PSD); and B is the modulation bandwidth. Note that $\tilde{x}^{\rm a}_{0,k}(n)$ in (3) is the only desired signal for UE. Also, in (3), $\mathcal{I}_0 = \{1,2,3,4,5,6\}$ is the index set of interfering BSs; and $\mathcal{Q} = \{q-1, q, q+1\} \subset \mathcal{I}_0$, where $q \in \mathcal{I}_0$, is the index set of interefering backhaul links with a cyclic shift for $q = 1, 6$, provided that the auxiliary LEDs on BS_0 are labeled according to the indexes of the neighboring BSs. For a given UE, q is equal to the index of the nearest neighboring BS [12], [13]. The corresponding DC gain for the VLC channel between an interfering backhaul link and UE is denoted as G'_i in (3).

The ratio of the desired signal power to the total noise and interference power in the electrical domain is defined as SINR. Fig. 4 shows the optical attocell network geometry in a polar coordinate system with BS_0 at the origin, which is used for SINR calculations. The geometric variables d_i, φ_i and ψ_i for G_i in (1) can be expressed in terms of the polar coordinates of UE shown in Fig. 4 as $z = (r, \theta)$ using a change of variables: $d_i(z) = \sqrt{r_i^2(z) + h^2}$ and $\cos(\varphi_i) = \cos(\psi_i) = h/d_i(z)$ where $r_i(z) = \sqrt{r^2 - 2R_0 r\cos(\theta - \Theta_i) + R_0^2}$ represents the

$$y_{1,k}^{\mathrm{AF}}(n) = R_{\mathrm{PD}} \sum_{i\in\mathcal{Q}_1} G_i G_{\mathrm{AF},i} w_{i,k}(n) + R_{\mathrm{PD}} \sum_{i\in\mathcal{Q}_1} G_i' \sqrt{P_{\mathrm{elec},0,k}}\tilde{x}_{i,k}^{\mathrm{b}}(n) + R_{\mathrm{PD}} \sum_{i\in\mathcal{I}_1} G_i \sqrt{P_{\mathrm{elec},i,k}}\tilde{x}_{i,k}^{\mathrm{a}}(n) + v_{1,k}^{\mathrm{a}}(n). \quad (8)$$

$$\mathcal{F}_{\mathrm{AFI}}(z_1) = \beta \sum_{i=2,6} \left[\left(2^{-\ell} \left(r_1^2 + h^2\right)^{-\frac{m+3}{2}} + \left(r_i^2(z_1) + h^2\right)^{-\frac{m+3}{2}} \right)^2 + 2^{-2\ell} \left(r_i^2(z_1) + h^2\right)^{-m-3} \right] + \mu \sum_{i\in\mathcal{Q}_1} \left(r_i^2(z_1) + h^2\right)^{-m-3}. \quad (14)$$

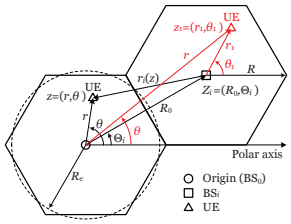

Fig. 4. Optical attocell network geometry in a polar coordinate system.

Euclidean distance between UE and BS_i for $i = 1, 2, \ldots, 6$, and $r_0(z) = r$. Here, (R_0, Θ_i) are the polar coordinates of BS_i where $R_0 = \sqrt{3}R$ and $\Theta_i = i\pi/3 - \pi/6$. For the FR backhaul system, considering Lambertian emission patterns for auxiliary LEDs and following the methodology from [12] to model G_i' in (3), the received SINR per subcarrier of a UE at location z in the attocell of BS_0 is derived and presented in (4). The parameter Ω in (4) is equal to:

$$\Omega = \frac{4\pi^2\alpha^2 N_0 B(N-2)}{\left((m+1)h^{m+1}A_{\mathrm{PD}}R_{\mathrm{PD}}P_{\mathrm{opt}}\right)^2 N}. \quad (5)$$

For BS_i, $i = 1, 2, \ldots, 6$, it is observed from Fig. 2 that the network topology is symmetric around BS_0. Thus, without loss of generality, hereinafter the focus is on BS_1. In either AF or DF modes, the signal received by BS_1 from the corresponding backhaul link during the first time slot on subcarrier k can be expressed as:

$$\begin{aligned} w_{1,k}(n) =& R_{\mathrm{PD}} G_{\mathrm{s}} \sqrt{P_{\mathrm{elec},0,k}}\tilde{x}_{1,k}^{\mathrm{b}}(n) + v_{1,k}^{\mathrm{b}}(n) + \\ & R_{\mathrm{PD}} \left(2^{-\ell} G_{\mathrm{s}}\right) \sqrt{P_{\mathrm{elec},0,k}} \left[\tilde{x}_{2,k}^{\mathrm{b}}(n) + \tilde{x}_{6,k}^{\mathrm{b}}(n)\right], \end{aligned} \quad (6)$$

where $v_{k,1}^{\mathrm{b}}(n)$ is the associated noise, independent identically distributed (i.i.d.) as the downlink noise; and G_{s} is the DC gain of the VLC channel for the backhaul link. According to (1) for $d_i = R_0$ and $\varphi_i = \psi_i = 0$, $G_{\mathrm{s}} = (\ell+1)A_{\mathrm{PD}}/2\pi R_0^2$ where $\ell = -\ln 2/\ln(\cos\Phi_{\mathrm{b}})$ is the Lambertian order and Φ_{b} is the semi-angle at half-power of the emission pattern for auxiliary LEDs on BS_0. The last term in (6) is the interference caused by cross-coupling with two adjacent backhaul links, see Fig. 2. It is evident that the signals received by the two adjacent BSs (i.e., BS_2 and BS_6) through the backhaul links during the first time slot on subcarrier k, denoted as $w_{i,k}$ for $i = 2, 6$, are correlated with $w_{1,k}$, since they both contain $\tilde{x}_{1,k}^{\mathrm{b}}$. Using (6), the SINR of the backhaul link can be calculated as:

$$\gamma_{\mathrm{b}} = \frac{R_{\mathrm{PD}}^2 G_{\mathrm{s}}^2 P_{\mathrm{elec},0,k}}{2^{-2\ell+1} R_{\mathrm{PD}}^2 G_{\mathrm{s}}^2 P_{\mathrm{elec},0,k} + \sigma_k^2}, \quad (7)$$

and this is identical for all backhaul links. In AF mode, during the second time slot, BS_1 amplifies the impure signal in (6) and then retransmits it to UE. The signal received by a UE in the attocell of BS_1 on subcarrier k at time sample n can be written as in (8) at the top of the page, where $\mathcal{I}_1 = \{0, 3, 4, 5\}$ is the index set of interfering BSs; and $\mathcal{Q}_1 = \{1, 2, 6\}$. In (8), $w_{1,k}$ contains $\tilde{x}_{1,k}^{\mathrm{b}}$ based on (6), which is the only desired signal for UE; and $G_{\mathrm{AF},i} = \sqrt{P_{\mathrm{elec},i,k}/\mathbb{E}[|w_{i,k}(n)|^2]}$ is defined as the AF gain for BS_i, $i = 1, 2, \ldots, 6$, which is obtained as:

$$G_{\mathrm{AF},i} = \sqrt{\frac{P_{\mathrm{elec},i,k}}{(1 + 2^{-2\ell+1})R_{\mathrm{PD}}^2 G_{\mathrm{s}}^2 P_{\mathrm{elec},0,k} + \sigma_k^2}}. \quad (9)$$

Substituting (6) and (9) into (8) then expanding, and defining $\beta = \gamma_{\mathrm{b}}/(\gamma_{\mathrm{b}} + 1)$ and $\mu = \sigma_k^2/\mathbb{E}[|w_{i,k}(n)|^2]$, the end-to-end SINR of a UE at location $z_1 = (r_1, \theta_1)$ in the attocell of BS_1 as shown with a red color in Fig. 4, can be derived as:

$$\gamma_{1,\mathrm{FR}}^{\mathrm{AF}}(z_1) = \frac{\mathcal{S}_{\mathrm{AF}}(z_1)}{\mathcal{F}_{\mathrm{BI}}(z_1) + \mathcal{F}_{\mathrm{AFI}}(z_1) + \mathcal{F}_{\mathrm{ICI}}(z_1) + \Omega}, \quad (10)$$

where $\mathcal{S}_{\mathrm{AF}}(z_1)$ is the AF signal effect at location z_1; $\mathcal{F}_{\mathrm{BI}}(z_1)$ is the backhaul interference effect; and $\mathcal{F}_{\mathrm{ICI}}(z_1)$ is the ICI effect. These are given by:

$$\mathcal{S}_{\mathrm{AF}}(z_1) = \beta \left[\left(r_1^2 + h^2\right)^{-\frac{m+3}{2}} + 2^{-\ell} \sum_{i=2,6} \left(r_i^2(z_1) + h^2\right)^{-\frac{m+3}{2}} \right]^2, \quad (11)$$

$$\mathcal{F}_{\mathrm{BI}}(z_1) = \frac{(\ell+1)^2 r^{2\ell} (r^2 + h^2)^{-\ell-3}}{(m+1)^2 h^{2m}} \sum_{i\in\mathcal{Q}_1} \cos^{2\ell}(\theta - \Theta_i), \quad (12)$$

$$\mathcal{F}_{\mathrm{ICI}}(z_1) = \sum_{i\in\mathcal{I}_1} \left(r_i^2(z_1) + h^2\right)^{-m-3}, \quad (13)$$

where $r_i(z_1)$, for $i \neq 1$, is the Euclidean distance between UE and BS_i. In (12), (r, θ) are the relative coordinates of the point z_1 with respect to the origin of the polar coordinate system, see Fig. 4. Also, in (10), $\mathcal{F}_{\mathrm{AFI}}(z)$ is the total AF interference effect due to the amplification of the backhaul interference and noise at the relays, which is given in (14). In DF mode, assuming that BS_1 can successfully decode the signal in (6) during the first time slot, the signal received by a UE in the attocell of BS_1 during the second time slot on subcarrier k can be written as:

$$\begin{aligned} y_{1,k}^{\mathrm{DF}}(n) =& R_{\mathrm{PD}} \sum_{i=0}^{6} G_i \sqrt{P_{\mathrm{elec},i,k}}\tilde{x}_{i,k}^{\mathrm{a}}(n) + \\ & R_{\mathrm{PD}} \sum_{i\in\mathcal{Q}_1} G_i' \sqrt{P_{\mathrm{elec},0,k}}\tilde{x}_{i,k}^{\mathrm{b}}(n) + v_{1,k}^{\mathrm{a}}(n). \end{aligned} \quad (15)$$

Based on (15), and using (12), the received SINR of UE at location z_1 is derived as:

$$\gamma_{1,\mathrm{FR}}^{\mathrm{DF}}(z_1)=\frac{(r_1^2+h^2)^{-m-3}}{\mathcal{F}_{\mathrm{BI}}(z_1)+\sum\limits_{i=0,i\neq 1}^{6}(r_i^2(z_1)+h^2)^{-m-3}+\Omega}. \quad (16)$$

C. SINR Analysis for In-Band VLC Backhaul

With the IB method, in principle, the backhaul interference for downlink is eliminated due to the fact that the access and backhaul links operate on two non-overlapping frequency sub-bands as discussed in Section III.A. The received signal model and SINR derivation procedure for the IB system are similar to the FR system except for excluding the backhaul interference, and are omitted here to avoid duplication. Using (11), (13) and (14), the received SINR of UE at location z_1 for BS_1 in AF mode is obtained as:

$$\gamma_{1,\mathrm{IB}}^{\mathrm{AF}}(z_1)=\frac{\mathcal{S}_{\mathrm{AF}}(z_1)}{\mathcal{F}_{\mathrm{AFI}}(z_1)+\mathcal{F}_{\mathrm{ICI}}(z_1)+\Omega}. \quad (17)$$

Similar to (16), the received SINR of UE at location z_1 for BS_1 in DF mode is obtained as:

$$\gamma_{1,\mathrm{IB}}^{\mathrm{DF}}(z_1)=\frac{(r_1^2+h^2)^{-m-3}}{\sum\limits_{i=0,i\neq 1}^{6}(r_i^2(z_1)+h^2)^{-m-3}+\Omega}. \quad (18)$$

IV. Assessment of Spectral Efficiency

In this paper, the Shannon-Hartley upper bound is used to estimate the data rate of the optical attocell downlink. Define $\xi=\tilde{N}/N=(N-2)/2N$ as the bandwith utilization ratio for a DCO-OFDM system, then the spectral efficiency in bits/s/Hz for a UE at location z in an attocell can be calculated as a function of $\gamma(z)$ using [6]:

$$\rho\left(\gamma(z)\right)=\xi\log_2\left(1+\gamma(z)\right). \quad (19)$$

For the attocell of BS_0, substituting (4) into (19), the spectral efficiency of the UE at location z can be calculated as:

$$\rho_0=\xi\log_2\left(1+\gamma_0(z)\right). \quad (20)$$

A. FR VLC Backhaul

For the FR VLC backhaul system, in AF mode, the spectral efficiency of the UE at location z_1 in the attocell of BS_1 can be calculated by inserting (10) in (19) as:

$$\rho_{\mathrm{FR-AF}}=\xi\log_2\left(1+\gamma_{1,\mathrm{FR}}^{\mathrm{AF}}(z_1)\right). \quad (21)$$

In DF mode, note that the successful decoding of the signal at the relay imposes a fundamental constraint on the achievable end-to-end rate of the downlink with a dual-hop DF relaying. Using (7) and (16), the spectral efficiency of the UE at location z_1 can be expressed as:

$$\rho_{\mathrm{FR-DF}}=\xi\log_2\left(1+\min\left[\gamma_{\mathrm{b}},\gamma_{1,\mathrm{FR}}^{\mathrm{DF}}(z_1)\right]\right), \quad (22)$$

where $\min\left[\gamma_{\mathrm{b}},\gamma_{1,\mathrm{FR}}^{\mathrm{DF}}(z_1)\right]$ is the equivalent end-to-end SINR for the dual-hop DF relaying downlink through BS_1.

B. IB VLC Backhaul

For the IB VLC backhaul system, let $\mathcal{R}_{\mathrm{a}}$ and $\mathcal{R}_{\mathrm{b}}$ denote the achievable data rates in bits/s for the access and backhaul links with the SINR of γ_{a} and γ_{b}, respectively. The corresponding allocated sub-bands are denoted as B_{a} and B_{b}. For a backhaul link to be able to support the data rate demanded by the access link, in general, the essential inequality $\mathcal{R}_{\mathrm{a}}\leq\mathcal{R}_{\mathrm{b}}$ must hold. Inserting $\mathcal{R}_{\mathrm{a}}=\xi B_{\mathrm{a}}\log_2(1+\gamma_{\mathrm{a}})$ and $\mathcal{R}_{\mathrm{b}}=\xi B_{\mathrm{b}}\log_2(1+\gamma_{\mathrm{b}})$ in this inequality, and rearranging, gives:

$$\frac{B_{\mathrm{a}}}{B_{\mathrm{b}}}\leq\frac{\log_2(1+\gamma_{\mathrm{b}})}{\log_2(1+\gamma_{\mathrm{a}})}, \quad (23)$$

which shows that to make the IB method feasible, the ratio of the sub-bands allocated to the access and backhaul links has to be inversely proportional to the ratio of the spectral efficiencies individually supported by each of the links. The inequality in (23) is subject to the condition such that $B_{\mathrm{a}}+B_{\mathrm{b}}=B$. Therefore, the design criteria for bandwidth allocations to the access and backhaul links in terms of the system bandwidth of B can be derived as:

$$B_{\mathrm{a}}\leq\frac{\log_2(1+\gamma_{\mathrm{b}})}{\log_2(1+\gamma_{\mathrm{a}})+\log_2(1+\gamma_{\mathrm{b}})}B, \quad (24)$$

$$B_{\mathrm{b}}\geq\frac{\log_2(1+\gamma_{\mathrm{a}})}{\log_2(1+\gamma_{\mathrm{a}})+\log_2(1+\gamma_{\mathrm{b}})}B. \quad (25)$$

The maximum (minimum) allowed bandwidth for allocating to the access (backhaul) link is obtained with equality in (24) (in (25)). This leads to the maximum reliable data rate for the end-to-end dual-hop transmission. The achievable common rate, denoted as $\mathcal{R}_{\mathrm{c}}$, can then be calculated as:

$$\mathcal{R}_{\mathrm{c}}=\mathcal{R}_{\mathrm{a}}=\mathcal{R}_{\mathrm{b}}=\xi B\frac{\log_2(1+\gamma_{\mathrm{a}})\log_2(1+\gamma_{\mathrm{b}})}{\log_2(1+\gamma_{\mathrm{a}})+\log_2(1+\gamma_{\mathrm{b}})}. \quad (26)$$

Finally, the effective spectral efficiency for the IB method can be expressed by using (26) as:

$$\rho_{\mathrm{IB}}=\frac{\mathcal{R}_{\mathrm{c}}}{B}=\xi\left[\frac{1}{\log_2(1+\gamma_{\mathrm{a}})}+\frac{1}{\log_2(1+\gamma_{\mathrm{b}})}\right]^{-1}. \quad (27)$$

Note that ρ_{IB} is equal to the harmonic mean of the spectral efficiencies $\rho_{\mathrm{a}}=\xi\log_2(1+\gamma_{\mathrm{a}})$ and $\rho_{\mathrm{b}}=\xi\log_2(1+\gamma_{\mathrm{b}})$. The derivation presented here for the effective spectral efficiency expression in (27) is independent of the relaying mode, and is valid for both AF and DF modes. For AF mode, substituting (17) for γ_{a} and (7) for γ_{b} into (27), the spectral efficiency of the UE at location z_1 in the attocell of BS_1 is calculated as:

$$\rho_{\mathrm{IB-AF}}=\xi\left[\frac{1}{\log_2(1+\gamma_{1,\mathrm{IB}}^{\mathrm{AF}}(z_1))}+\frac{1}{\log_2(1+\gamma_{\mathrm{b}})}\right]^{-1}. \quad (28)$$

In the case of DF, inserting (18) for γ_{a} and (7) for γ_{b} in (27), the spectral efficiency of the UE at location z_1 in the attocell of BS_1 is obtained as:

$$\rho_{\mathrm{IB-DF}}=\xi\left[\frac{1}{\log_2(1+\gamma_{1,\mathrm{IB}}^{\mathrm{DF}}(z_1))}+\frac{1}{\log_2(1+\gamma_{\mathrm{b}})}\right]^{-1}. \quad (29)$$

TABLE I
SYSTEM PARAMETERS.

Parameter	Symbol	Value	Unit
LED Optical Power	P_{opt}	10	W
Downlink LED Semi-Angle	Φ_{a}	40	$^\circ$
Vertical Separation	h	2.15	m
Hexagonal Cell Radius	R	2.5	m
Modulation Bandwidth	B	20	MHz
DFT/IDFT Length	N	512	–
Noise PSD	N_0	1×10^{-21}	A^2/Hz
Effective PD Area	A_{PD}	1×10^{-4}	m^2
PD Responsivity	R_{PD}	0.6	A/W
DC Bias Scaling Factor	α	3	–

V. RESULTS AND DISCUSSIONS

This section presents simulation results for average spectral efficiency performance of the optical attocell system using FR and IB VLC backhaul methods described in Section III, based on Monte Carlo averaging of (20)–(22), (28) and (29) from Section IV. Table I lists the system parameters used for simulations. In order to observe the effect of the UE location on the system performance, the area of each attocell is divided into 10 rings with equal areas. In addition, the coverage area of each attocell is approximated by a circle with the same area as the original hexagonal cell with radius R, as shown in Fig. 4. The radius of the approximated circular cell obeys $R_{\text{e}} \approx 0.91R$. Performance results are mainly presented in terms of the emission semi-angle, Φ_{b}, of the auxiliary LEDs.

Fig. 5 gives the average spectral efficiency of UEs within each ring in the attocells of BS_0 and BS_1 for $\Phi_{\text{b}} = 15^\circ$. It is observed that the performance is overall decreased in both attocells from $n = 1$ for the cell center up to $n = 10$ for the cell edge. This is because the interference level becomes stronger and the desired signal level becomes weaker along the radial distance from the cell center to the cell edge. Also, it is observed that the average spectral efficiency in the attocell of BS_0 is higher than or equal to that in the attocell of BS_1 for the first three rings using the FR backhaul, and for the first five rings using the IB backhaul. In other words, the performance in the attocell of BS_1 becomes higher than or equal to that in the attocell of BS_0 for the last five rings including the cell edge region. The reason is that the attocell of BS_0 is at the center of the network and thus receives the highest level of ICI especially in the cell edge region from the six adjacent attocells (i.e., the first tier). Note that for the attocell of BS_i, $i = 1, 2, \ldots, 6$, there are only three adjacent attocells. For example, the adjacent BSs for BS_1 include BS_0, BS_2 and BS_6, while BS_3, BS_4 and BS_5 are regarded as the second tier with respect to BS_1, as shown in Fig. 2. Comparing the performance of the FR and IB backhaul methods for BS_1 in Fig. 5, it can be observed that the FR method performs better for the first six rings around the cell center and, in contrast, the IB method performs better for the last four rings, in the cell edge region. Also, the AF and DF protocols provide an equal performance for both FR and IB backhaul methods, as observed from Fig. 5.

Fig. 6 shows the average spectral efficiency performance of

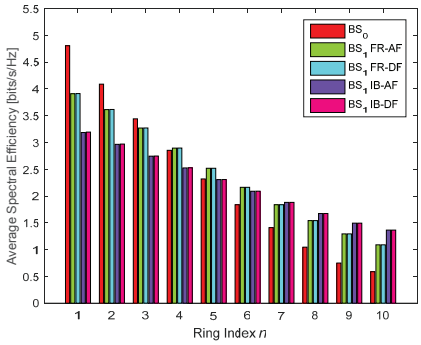

Fig. 5. Average spectral efficiency of UEs per ring in the attocells of BS_0 and BS_1 using FR and IB VLC backhaul methods for $\Phi_{\text{b}} = 15^\circ$.

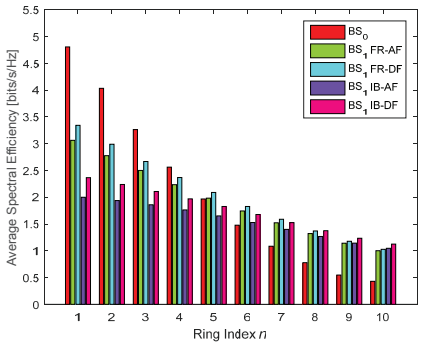

Fig. 6. Average spectral efficiency of UEs per ring in the attocells of BS_0 and BS_1 using FR and IB VLC backhaul methods for $\Phi_{\text{b}} = 30^\circ$.

UEs per ring in the attocells of BS_0 and BS_1 for $\Phi_{\text{b}} = 30^\circ$. In comparison with Fig. 5, it can be seen that the performance is overall decreased by doubling the emission semi-angle of auxiliary LEDs on BS_0 from $\Phi_{\text{b}} = 15^\circ$ to 30°. This may be justified by intuition, as the wider the light beam on the AP-to-AP links, the more interference the backhaul links generate for downlink. Comparing the effect of increasing Φ_{b} on the attocells of BS_0 and BS_1, it is observed from Fig. 6 in respect to Fig. 5 that this has a negligible effect on the performance for BS_0 with emphasis on the outer rings ($n = 3, 4, \ldots, 10$), whereas the impact on the results for BS_1 is distinguishable for all rings. In fact, the location of the attocell of BS_0 as the gateway is such that it receives less interference from the backhaul links, compared with the attocells of BS_i, for $i = 1, 2, \ldots, 6$, which equally receive greater interference due to the smaller angle of incidence for the LOS coupling with the backhaul links, as shown in Fig. 3. Also, Fig. 6 shows that the DF relaying outperforms the AF one for both FR and IB backhaul methods. This is due to the propagated interference in AF mode, $\mathcal{F}_{\text{AFI}}$, given by (14), which significantly impairs the downlink SINR for large values of Φ_{b}.

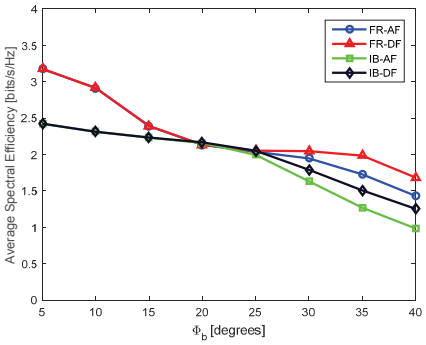

Fig. 7. Overall average spectral efficiency of the optical attocell network using FR and IB VLC backhauls in AF and DF modes as a function of Φ_b.

Fig. 7 demonstrates the overall average performance for the spectral efficiency of the optical attocell network including all seven attocells, denoted by $\bar{\rho}$, as a function of Φ_b in an interval of $[5°, 40°]$. It is observed that in general, the trends for both FR and IB backhaul methods in AF and DF relaying modes are monotonically decreasing with respect to Φ_b. The results in Fig. 7 can be categorized into three groups based on the subintervals of $I_1 = [5°, 20°]$, $I_2 = [20°, 25°]$ and $I_3 = [25°, 40°]$. For I_1, the FR method performs better than the IB method, and for each of these methods the AF and DF modes have the same performance. In particular, at the beginning of I_1 for $\Phi_b = 5°$, the FR method gives an average spectral efficiency of $\bar{\rho} = 3.20$ bits/s/Hz, while the IB method provides $\bar{\rho} = 2.40$ bits/s/Hz. To realize such performance, a careful adjustment for Φ_b is required in order to make it as small as $5°$. This can be achieved by using appropriate optics such as optical lenses to collimate the light beam in the AP-to-AP links. As the value of Φ_b increases within I_1, the difference between the performance for the FR and IB methods decreases, and finally coincide at $\Phi_b = 20°$ and $\bar{\rho} = 2.20$ bits/s/Hz. For I_2, the FR and IB methods give almost the same performance, slightly decreasing from $\bar{\rho} = 2.20$ bits/s/Hz for $\Phi_b = 20°$ to $\bar{\rho} = 2.00$ bits/s/Hz for $\Phi_b = 25°$. After $\Phi_b = 25°$, and within I_3, it can be seen that the curves start to deviate from one another. However, FR still has higher performance compared with IB in terms of the average spectral efficiency performance. Also, DF has higher performance compared with AF, and the performance difference increases by increasing Φ_b. In AF mode, the interference between the backhaul links is amplified and propagated to the downlink, and by widening the light beam in the backhaul links, the interference is further increased and substantially degrades the performance. The FR-DF backhaul system maintains the overall performance on more than $\bar{\rho} = 2.00$ bits/s/Hz until $\Phi_b = 35°$, and from there decreases to $\bar{\rho} = 1.70$ bits/s/Hz for $\Phi_b = 40°$. The FR-AF backhaul system is the second best, with an average spectral efficiency of $\bar{\rho} = 1.45$ bits/s/Hz for $\Phi_b = 40°$. For the IB-DF and IB-AF backhaul systems, this is $\bar{\rho} = 1.25$ bits/s/Hz and $\bar{\rho} = 1.00$ bits/s/Hz, respectively.

VI. Conclusions

A novel wireless VLC backhaul solution is proposed for indoor optical attocell networks. The FR and IB bandwidth allocation methods are introduced to apportion the system bandwidth to the access and backhaul links for both AF and DF relaying protocols. By studying the average downlink spectral efficiency performance of the network, it is identified that the performance depends especially on the emission semi-angle, Φ_b, of the auxiliary LEDs used for the AP-to-AP links. It is found that the FR backhaul outperforms the IB backhaul over a broad range of values for Φ_b. This highlights the benefit of the FR method due to the exploitation of the entire system bandwidth for the access and backhaul links, despite the higher interference compared with the IB method. It is also found that for either FR or IB methods, DF relaying outperforms AF relaying for $\Phi_b \geq 25°$. Future research will consider an extended analysis for the performance of optical attocell networks with wireless backhaul and will study the effects of downlink LED semi-angle, vertical seperation and cell radius.

Acknowledgment

Professor Harald Haas acknowledges support by the UK Engineering and Physical Research Council (EPSRC) under Grant EP/K008757/1.

References

[1] H. Burchardt, N. Serafimovski, D. Tsonev, S. Videv, and H. Haas, "VLC: Beyond Point-to-Point Communication," *IEEE Commun. Mag.*, vol. 52, no. 7, pp. 98–105, Jul. 2014.

[2] H. Haas, L. Yin, Y. Wang, and C. Chen, "What is LiFi?" *IEEE/OSA J. Lightw. Technol.*, vol. 34, no. 6, pp. 1533–1544, Mar. 2016.

[3] S. Dimitrov and H. Haas, *Principles of LED Light Communication Towards Networked Li-Fi*. Cambridge University Press, Mar. 2015.

[4] J. Armstrong and B. Schmidt, "Comparison of Asymmetrically Clipped Optical OFDM and DC-Biased Optical OFDM in AWGN," *IEEE Commun. Lett.*, vol. 12, no. 5, pp. 343–345, May 2008.

[5] C. Chen, D. A. Basnayaka, and H. Haas, "Downlink Performance of Optical Attocell Networks," *IEEE/OSA J. Lightw. Technol.*, vol. 34, no. 1, pp. 137–156, Jan. 2016.

[6] C. Chen, S. Videv, D. Tsonev, and H. Haas, "Fractional Frequency Reuse in DCO-OFDM-Based Optical Attocell Networks," *IEEE/OSA J. Lightw. Technol.*, vol. 33, no. 19, pp. 3986–4000, Oct. 2015.

[7] T. Komine and M. Nakagawa, "Integrated System of White LED Visible-Light Communication and Power-Line Communication," *IEEE Trans. Consum. Electron.*, vol. 49, no. 1, pp. 71–79, Feb. 2003.

[8] J. Song, W. Ding, F. Yang, H. Yang, B. Yu, and H. Zhang, "An Indoor Broadband Broadcasting System Based on PLC and VLC," *IEEE Trans. Broadcast.*, vol. 61, no. 2, pp. 299–308, Jun. 2015.

[9] P. Mark, "Ethernet over Light," Master's thesis, University of British Columbia, Dec. 2014.

[10] Y. Wang, N. Chi, Y. Wang, L. Tao, and J. Shi, "Network Architecture of a High-Speed Visible Light Communication Local Area Network," *IEEE Photon. Technol. Lett.*, vol. 27, no. 2, pp. 197–200, Jan. 2015.

[11] J. M. Kahn and J. R. Barry, "Wireless Infrared Communications," *Proc. IEEE*, vol. 85, no. 2, pp. 265–298, Feb. 1997.

[12] H. Kazemi and H. Haas, "Downlink Cooperation with Fractional Frequency Reuse in DCO-OFDMA Optical Attocell Networks," in *Proc. IEEE Int. Conf. Commun. (ICC)*, May 2016.

[13] H. Kazemi, M. Safari, and H. Haas, "Spectral Efficient Cooperative Downlink Transmission Schemes for DCO-OFDM-Based Optical Attocell Networks," in *Proc. IEEE 84th Veh. Technol. Conf. (VTC Fall)*, Sep. 2016.

[14] R. U. Nabar, H. Bolcskei, and F. W. Kneubuhler, "Fading Relay Channels: Performance Limits and Space-Time Signal Design," *IEEE J. Sel. Areas Commun.*, vol. 22, no. 6, pp. 1099–1109, Aug. 2004.

Bandwidth Scheduling and Power Control for Wireless Backhauling in Optical Attocell Networks

Hossein Kazemi, Majid Safari and Harald Haas
LiFi R&D Centre, Institute for Digital Communications, School of Engineering, University of Edinburgh, EH9 3FD, UK.
Email: {h.kazemi, majid.safari, h.haas}@ed.ac.uk

***Abstract*—The backhaul of tens and hundreds of light fidelity (LiFi)-enabled light bulbs constitutes a major challenge. In this paper, a multi-hop wireless backhaul configuration is investigated for optical attocell networks. The backhaul system proposed in this work uses visible light communication (VLC) to realize wireless connections between adjacent LiFi base stations (BSs). By using a tree topology for the backhaul system, the central BS is collocated with the gateway, and the other BSs are connected to the core network via multi-hop wireless backhaul links with the gateway based on decode-and-forward (DF) relaying. The system-level modeling and analysis is presented for the end-to-end sum rate of multiple user equipment (UE) devices with random coordinates in the network. The closest backhaul link to the gateway needs to support multiple independent data flows at the same time. To this end, novel bandwidth scheduling policies are proposed and evaluated. In addition, in order to opportunistically reduce the transmission power of the backhaul system, novel power control schemes are derived. Performance gains of the proposed schemes and their impact on the average sum rate of the downlink optical attocell network are studied using Monte Carlo simulations.**

***Index Terms*—Optical attocell network, wireless backhaul, multi-hop relaying, bandwidth scheduling, power control.**

I. Introduction

Light-emitting diodes (LEDs) are commonly adopted for indoor illumination purposes because of their high energy efficiency, long operational lifetime and low cost. At the same time, the emergence of smart environments necessitates a diversification of advanced services for light fixtures in addition to illumination [1]. A key enabler for this service diversification is visible light communication (VLC) [1]. Light fidelity (LiFi) is the high speed wireless networking variant of VLC [2]. By utilizing the existing lighting infrastructure, LiFi enables LED luminaires to provide broadband wireless connectivity, leading to ultra-dense cellular networks, termed optical attocell networks [2].

The problem of backhauling for optical attocell networks has been approached by a number of wired solutions [3]–[6]. In [3], a backhaul solution based on power line communication (PLC) through the electricity wiring infrastructure in buildings is proposed. In [5], a cascaded system of Power-over-Ethernet and VLC is implemented. In [6], standard single mode optical fiber cables are used to provide backhaul connections for an indoor VLC-based local area network. As an alternative to the existing wired backhaul solutions, the idea of using VLC for wireless backhauling in optical attocell networks was first put forward in [7], where a one tier network with a star topology is considered for dual-hop VLC transmission and the spectral efficiency performance of the network is studied for both amplify-and-forward (AF) and decode-and-forward (DF) relaying protocols. Under the assumption that the access and backhaul systems share the indoor propagation medium, the emission semi-angle of the backhaul LEDs is the determining factor for the network performance [7]. In particular, it is shown in [7] that by choosing a sufficiently small semi-angle for the backhaul LEDs, the adverse effect of the backhaul interference on the downlink performance is eliminated.

In this paper, by employing a focused VLC transmission in the backhaul system, the application of wireless backhauling based on VLC is extended to a two-tier network by which a multi-hop wireless backhaul system is thoroughly designed for multi-user optical attocell networks. Consequently, new challenges arise for backhaul bandwidth scheduling and power control which are not addressed in [7]. This paper primarily attempts to shed light on such new aspects. To this end, a tree topology is used for backhaul configuration and DF relaying is employed to realize multi-hop transmissions based on the use of direct current optical orthogonal frequency division multiplexing (DCO-OFDM). For every branch of the backhaul tree, there is a bottleneck backhaul link that is shared among multiple data flows. In order to fairly apportion the bandwidth of the bottleneck backhaul link, three scheduling policies are proposed, namely adaptively weighted fair (AWF), proportionally weighted fair (PWF) and equally weighted fair (EWF). Furthermore, in order to enhance the power efficiency of the backhaul system, two main power control schemes are proposed including adaptive power control (APC) and fixed power control (FPC). Assuming that a number of user equipment (UE) devices are randomly distributed over the network, the performance of the bandwidth scheduling policies and power control schemes and the average sum rate of the network are assessed using Monte Carlo simulations.

The rest of the paper is structured as follows. The model of the underlying optical attocell system is briefly described in Section II. The design and modeling of the multi-hop wireless backhaul system is presented in Section III. The analysis of the proposed bandwidth scheduling policies and power control schemes is presented in Section IV. Simulation results are discussed in Section V. Conclusions are drawn in Section VI.

II. System-Level Preliminaries

The underlying system model and assumptions are similar to those used in [7]. They are briefly described in this section for the completeness of presentation.

978-1-5386-4727-1/18/$31.00 ©2018 IEEE

A. Optical Attocell Network

An optical attocell system uses a LiFi-enabled LED luminaire as an optical BS to provide wireless access for multiple UE devices. The UE devices are equipped with a photodiode (PD) sensor to detect the incident modulated light. Every BS covers a certain area on the receiver plane which is called an optical attocell. Fig. 1 illustrates the layout of a two-tier optical attocell network using a hexagonal tessellation. A hexagonal cell deployment model gives an upper bound performance for practical optical attocell networks compared to other alternatives such as square network and random Poisson point process (PPP) network models [8]. There are M UEs in total in the network which are globally numbered from 1 to M. They are distributed over the entire coverage of the network uniformly at random and each one is connected to the BS with the maximum downlink SINR [9]. It is further assumed that the UE devices are oriented vertically upward and that the receiver field of view (FOV) is sufficiently wide, leading to the simultaneous detection of optical signals from all BSs. The term access point (AP) is used interchangeably with BS throughout the paper.

B. Light Propagation

In this study, only line-of-sight (LOS) is considered for light propagation and a Lambertian emission pattern is assumed for LEDs. A study in [8] shows that the received power from the LOS path solely, constitutes more than 90% of the overall power contribution. The same study also shows that the effect of non-line-of-sight (NLOS) multi-paths appears mostly around network boundaries. The multi-path effect is, however, negligible for the attocells that are situated at a distance from the boundaries. The VLC channel is assumed to have a low-pass flat frequency response dominated by the LOS path.

C. Optical OFDMA

Orthogonal frequency division multiple access (OFDMA) is widely used in cellular communications to eliminate intra-cell interference. For multi-user LiFi systems, optical OFDMA is efficiently realized by using DCO-OFDM [8]. To this end, the baseband bandwidth of a LiFi system, B, is divided into N orthogonal subchannels, with each subchannel acquiring a share of $\frac{B}{N}$. An input binary information stream containing data for intended UEs is buffered into blocks of b bits to be loaded onto $\frac{N}{2}-1$ data-carrying subcarriers. The bits assigned to the kth subcarrier are mapped to the kth complex subsymbol, X_k, using quadrature amplitude modulation (QAM). The total number of subsymbols is extended to N by enforcing Hermitian symmetry. The elements of the DCO-OFDM frame satisfy $X_{N-k} = X_k^*$ for $k \neq 0$, where $[\cdot]^*$ denotes the complex conjugate operator, and $X_0 = X_{\frac{N}{2}} = 0$. By applying an N-point inverse fast Fourier transform (IFFT), the N subsymbols are then transformed into N real samples in the time domain.

After adding a DC bias, denoted by x_{DC}, to the IFFT output, the resulting positive signal drives the forward current of the LED. The total transmission power, denoted by P_{elec}, is equally allocated to the modulated subcarriers. The DC bias satisfies $x_{\mathrm{DC}} = \alpha\sqrt{P_{\mathrm{elec}}}$ with α as a scaling factor. To make use of the input dynamic range of the LED while avoiding nonlinear clipping effects, the scaling factor is often set to $\alpha = 3$. It guarantees that 99.7% of the signal envelope remains undistorted [10]. The average optical power is determined by the DC bias such that $P_{\mathrm{opt}} = x_{\mathrm{DC}}$. Hence, the output illumination for LEDs is directly proportional to the DC bias.

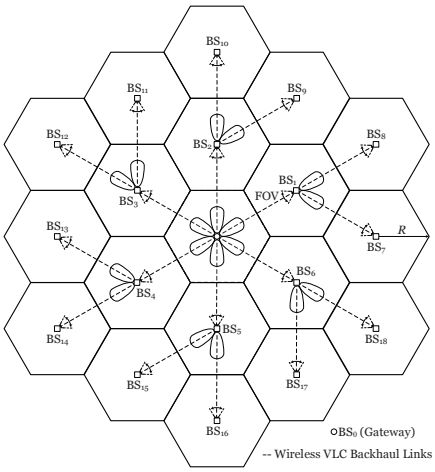

Fig. 1. The layout of a two tier optical attocell network with a plan view of multi-hop wireless backhaul configuration based on AP-to-AP VLC links.

III. Wireless Backhaul System Design and Sum Rate Analysis

A. Multi-Hop Wireless Backhaul Configuration

The proposed multi-hop wireless backhaul configuration employing a tree topology is depicted in Fig. 1. The central BS is directly connected to the core network through a high capacity wired link. Consequently, BS_0 is the gateway to the core network, and BS_i, for $i = 1, 2, \ldots, 18$, is routed to BS_0 via multi-hop wireless backhaul links with BS_0 by using DF relaying [11]. The aim of this work is to focus on the *end-to-end* performance from the gateway to the UEs assuming that the wired link between the gateway and the core network has an adequate capacity to support the aggregate data flowing in the backhaul links. Inter-BS wireless backhauling is provided by perfectly aligned AP-to-AP VLC links as shown in Fig. 1. These links are established by adding auxiliary LEDs and PDs to the corresponding BSs in the first and second tiers.

Each relay BS performs full-duplex relaying so that it can concurrently transmit and receive signals on the same operating frequency. Full-duplex relaying is possible because: firstly there is no direct LOS path for self-interference from the backhaul transmitter to the backhaul receiver of the same relay as they are mounted on two opposite sides of the BS unit; secondly the interference caused by NLOS propagation from the backhaul transmitter to the backhaul receiver at the same relay is not significant [12]. This allows the gateway to send a

continuous flow of data toward BS_i without interruption. The access and backhaul systems operate over the same frequency band in the visible light spectrum. To avoid reducing the spectral efficiency, the available bandwidth is fully reused by both systems [7]. When the backhaul links operate in a shared propagation medium, each one turns into a source of interference affecting all other VLC links in the network. The interference can be prevented by using a focused light beam in the backhaul links. For typical network dimensions, choosing a half-power semi-angle of 5° for the auxiliary LEDs gives rise to almost zero interference by the backhaul links [7].

Note that the uplink in LiFi networks is realized by means of infrared (IR) or radio frequency (RF) bands [13]–[15]. Particularly, an IR wavelength that does not interfere with the downstream can be used for the upstream to make both access and backhaul systems bidirectional. Nevertheless, this needs a separate study which is a potential future direction.

B. Backhaul Link Signal-to-Noise Ratio

Similar to the access system, the backhaul system employs a DCO-OFDM modulation with the same number of subcarriers. In this study, shot noise and thermal noise are the only limiting phenomena for the backhaul system. The total noise is Gaussian distributed with zero mean and variance of $\sigma^2 = \frac{N_0 B}{N}$ where N_0 is the noise power spectral density (PSD). Denote the incoming backhaul link of BS_i by b_i. By considering a Lambertian emission profile for the auxiliary LEDs, and using Fig. 1 to calculate the LOS channel gain based on [14, Eq. (10)], the electrical signal-to-noise ratio (SNR) per subcarrier for b_i is readily obtained as follows:

$$\gamma_{\mathrm{b}_i} = \frac{((\ell+1)A_{\mathrm{PD}}R_{\mathrm{PD}})^2 N P_{\mathrm{b}_i}}{36\pi^2 R^4 N_0 B}, \tag{1}$$

where $\ell = -1/\log_2(\cos\Phi_{\mathrm{b}})$ is the Lambertian order and Φ_{b} is the emission semi-angle of the auxiliary LEDs; A_{PD} is the photosensitive area of the PD; R_{PD} is the PD responsivity; P_{b_i} is the transmission power for b_i; and R is the radius of the hexagonal cells as shown in Fig. 1.

C. Downlink Signal-to-Interference-plus-Noise Ratio

With the assumption of the whole bandwidth being fully reused across all attocells, the downlink quality in each attocell is influenced by co-channel channel interference (CCI) from neighboring BSs. Also, a zero mean white Gaussian noise with variance σ^2, due to shot noise and thermal noise, perturbs the received signal of downlink. With the help of [14, Eq. (10)], based on the attocell geometry presented in [7], and by using a polar coordinate system with BS_0 at the origin, the electrical signal-to-interference-plus-noise ratio (SINR) per subcarrier for the uth UE located at the point z_u with polar coordinates (r_u, θ_u) inside the attocell of BS_i can be derived as:

$$\gamma_u = \frac{(r_i^2(z_u)+h^2)^{-m-3}}{\sum_{j\in\mathcal{J}_i}(r_j^2(z_u)+h^2)^{-m-3}+\Omega}, \tag{2}$$

where h is the vertical separation between the BS plane and the receiver plane; $m = -1/\log_2(\cos\Phi_{\mathrm{a}})$ is the Lambertian order and Φ_{a} is the half-power semi-angle of the downlink LEDs; $r_i(z_u) = \sqrt{r_u^2 + R_i^2 - 2R_i r_u \cos(\theta_u - \Theta_i)}$ indicates the horizontal distance of z_u from BS_i with (R_i, Θ_i) denoting the coordinates of BS_i; and $\mathcal{J}_i$ denotes the index set of the neighboring BSs that cause CCI on the downlink of BS_i. The parameter Ω in (2) is given by:

$$\Omega = \frac{4\pi^2 N_0 B(N-2)}{((m+1)h^{m+1}A_{\mathrm{PD}}R_{\mathrm{PD}})^2 N P_{\mathrm{a}}}, \tag{3}$$

where P_{a} is the downlink transmission power.

D. Sum Rate Analysis

To facilitate the analysis, the capacity of a DCO-OFDM link is required in closed form. For a dynamic range limited VLC system based on DCO-OFDM, the Shannon-Hartley capacity theorem can be applied individually to each subcarrier in the frequency domain; in-between the two points before the IFFT operation at the transmitter and after the FFT operation at the receiver. In principle, through a large number of subcarriers, the FFT operation effectively converts any independent and identically distributed perturbation term added to the received signal, including CCI and clipping noise, into a Gaussian noise according to the central limit theorem (CLT) [10]. Therefore, the achievable rate per subcarrier *in the electrical domain* can be evaluated by $\mathcal{R} = \frac{B}{N}\log_2(1+\gamma)$ where γ is the link SINR.

Let $\mathcal{U}_i$ be the index set of the UEs associated with BS_i such that $|\mathcal{U}_i| = M_i$ and $\sum_{i=0}^{18} M_i = M$, where $|\cdot|$ denotes the cardinality of a set. Each UE served by BS_i is equally given a bandwidth $\frac{B}{M_i}$. The aim is to arrive at the sum of the achievable *end-to-end* rates of the UEs which is referred to as the end-to-end sum rate. The UEs in a given attocell may receive signal from the gateway with a two-hop or a three-hop transmission depending on whether the attocell is in the first or in the second tier. The bandwidth of the bottleneck backhaul link between the gateway and the first tier is decomposed into three orthogonal portions to be allocated to three BSs in each backhaul branch. Consider, for example, the backhaul branch that involves BS_1, BS_7 and BS_8, see Fig. 1. A dedicated fraction, denoted by μ_i, of the bandwidth of b_1 is assigned to BS_i for $i = 1, 7, 8$, such that $\sum_{i=1,7,8}\mu_i = 1$. More details on the design of μ_i are available in Section IV. Based on DF relaying, BS_1 first fully decodes the downlink data intended for BS_1, BS_7 and BS_8. Upon successful decoding, BS_1 then retransmits each signal toward the desired destination.

For the central attocell, the UEs receive data directly from the gateway with no relaying involved. The sum rate for BS_0 is readily calculated by:

$$\mathcal{R}_0 = \frac{\xi B}{M_0}\sum_{u\in\mathcal{U}_0}\log_2(1+\gamma_u), \tag{4}$$

where $\xi = \frac{N-2}{2N}$ accounts for the bandwidth utilization of DCO-OFDM; and γ_u is given by (2) for $i = 0$. For the first and second tiers, the end-to-end rate of the UEs cannot be better than the allocated capacity of each intermediate hop based on the maximum flow–minimum cut theorem [16]. For

$$\mathcal{R}_i = \frac{\xi B}{M_i} \sum_{u \in \mathcal{U}_i} \min \left[\mu_i \log_2 \left(1 + \gamma_{\mathrm{b}_s}\right), \log_2 \left(1 + \gamma_{\mathrm{b}_i}\right), \log_2(1 + \gamma_u) \right], \ \forall i \in \mathcal{T}_2 = \{7, 8, \ldots, 18\}. \tag{6}$$

BS_i in the first tier, $\forall i \in \mathcal{T}_1 = \{1, 2, \ldots, 6\}$, the end-to-end sum rate is derived as:

$$\mathcal{R}_i = \frac{\xi B}{M_i} \sum_{u \in \mathcal{U}_i} \min \left[\mu_i \log_2 \left(1 + \gamma_{\mathrm{b}_i}\right), \log_2 \left(1 + \gamma_u\right) \right]. \tag{5}$$

For BSs of the second tier, the end-to-end sum rate expression is derived and presented in (6) at the top of the page, where $s = \lfloor \frac{i-5}{2} \rfloor$ and $\lfloor x \rfloor$ is the largest integer that is $\leq x$.

IV. Bandwidth Scheduling and Power Control for Wireless Backhaul System

To elaborate, let $\mathcal{R}_{\mathrm{a}_i}$ be the sum rate of the access system for BS_i and let $\mathcal{R}_{\mathrm{b}_i}$ be the overall achievable rate for b_i. From (1) and (2), it follows that $\mathcal{R}_{\mathrm{a}_i} = \frac{\xi B}{M_i} \sum_{u \in \mathcal{U}_i} \log_2 \left(1 + \gamma_u\right)$ and $\mathcal{R}_{\mathrm{b}_i} = \xi B \log_2 \left(1 + \gamma_{\mathrm{b}_i}\right)$. Since the network topology is symmetric around the gateway as shown in Fig. 1, without loss of generality, one of the six backhaul branches is sufficient for the purpose of analysis. Hence, the analysis is mainly presented for BS_1, BS_7 and BS_8 in the sequel.

A. Bandwidth Scheduling

For bandwidth scheduling, the focus is on the variable μ_i in (5) and (6) which depends upon the policy used for bandwidth allocation in the bottleneck backhaul link. Assume that the backhaul system does not limit the end-to-end performance of the network. In that case, for b_1, b_7 and b_8, the following conditions hold:

$$\mathcal{R}_{\mathrm{b}_1} \geq \mathcal{R}_{\mathrm{a}_1} + \mathcal{R}_{\mathrm{a}_7} + \mathcal{R}_{\mathrm{a}_8}, \tag{7a}$$

$$\mathcal{R}_{\mathrm{b}_7} \geq \mathcal{R}_{\mathrm{a}_7}, \tag{7b}$$

$$\mathcal{R}_{\mathrm{b}_8} \geq \mathcal{R}_{\mathrm{a}_8}. \tag{7c}$$

According to (7a), the capacity of b_1 has to fulfil the aggregate sum rate in the downlinks of BS_1, BS_7 and BS_8. However, in realistic scenarios, this is not always possible and the limited capacity of b_1 may turn into a backhaul bottleneck. Satisfying (7b) and (7c) is not challenging in contrast to (7a), as b_7 and b_8 each one just need to respond to the sum rate of a single downlink. By means of μ_i, (7a) is expanded as:

$$\mu_1 \mathcal{R}_{\mathrm{b}_1} \geq \mathcal{R}_{\mathrm{a}_1}, \tag{8a}$$

$$\mu_7 \mathcal{R}_{\mathrm{b}_1} \geq \mathcal{R}_{\mathrm{a}_7}, \tag{8b}$$

$$\mu_8 \mathcal{R}_{\mathrm{b}_1} \geq \mathcal{R}_{\mathrm{a}_8}, \tag{8c}$$

$$\mu_1 + \mu_7 + \mu_8 = 1. \tag{8d}$$

For fair allocation of the bandwidth of b_1, three scheduling policies are proposed. The first policy is referred to as AWF scheduling. The AWF scheduler assigns an adaptive weight to each BS according to the achievable sum rate of the access system. By replacing inequalities with equalities in (8a)–(8c), the solution to μ_i is obtained for $i = 1, 7, 8$, through which a unified expression for μ_i, $\forall i \in \mathcal{T}_1 \cup \mathcal{T}_2$, can be derived:

$$\mu_i = \frac{\frac{1}{M_i} \sum_{u \in \mathcal{U}_i} \log_2(1 + \gamma_u)}{\sum_{j \in \mathcal{L}_i} \frac{1}{M_j} \sum_{u \in \mathcal{U}_j} \log_2(1 + \gamma_u)}, \tag{9}$$

where $\mathcal{L}_i = \{s, 2s + 5, 2s + 6\}$ such that $s = i$ if $i \in \mathcal{T}_1$, and $s = \lfloor \frac{i-5}{2} \rfloor$ if $i \in \mathcal{T}_2$. Note that the real-time values of M_i and γ_u are required to specify μ_i for AWF, and these are obtained through a feedback channel under quasi-static conditions [17]. The second policy is referred to as PWF scheduling. The PWF scheduler allocates a weight to each BS proportionally to the number of the associated UEs. The corresponding μ_i is:

$$\mu_i = \frac{M_i}{\sum_{j \in \mathcal{L}_i} M_j}. \tag{10}$$

The third scheduling policy is called EWF. It gives an equal share from the bandwidth to each BS with no distinction, yielding $\mu_i = \frac{1}{3}$ $\forall i \in \mathcal{T}_1 \cup \mathcal{T}_2$. This policy is considered as a benchmark for comparison purposes.

B. Power Control

The auxiliary LEDs used in the backhaul links do not need to provide illumination for the environment, and their optical power can therefore be reduced to enhance the power efficiency of the backhaul system. Reducing the optical power translates into a reduction in the transmission power which is constrained by the available optical power. This has an inevitable impact on the capacity of the backhaul links which in turn may compromise the network performance. In order to reach a balance for the power efficiency of the backhaul system while maintaining the desired sum rate performance, two main power control schemes are proposed in the following. To this end, as P_{a} is already fixed to meet the illumination requirement, the power ratio $K_i = \frac{P_{\mathrm{b}_i}}{P_{\mathrm{a}}}$ is considered. Also, a constant SNR $\gamma_{\mathrm{b}} = \gamma_{\mathrm{b}_i} \frac{P_{\mathrm{a}}}{P_{\mathrm{b}_i}}$ is introduced so that $\gamma_{\mathrm{b}_i} = K_i \gamma_{\mathrm{b}}$.

1) Adaptive Power Control (APC): The transmission power for the backhaul system is adaptively adjusted according to the sum rates in the access system. The conditions in (7a)–(7c) can be expressed in terms of K_i, for $i = 1, 7, 8$, as:

$$K_1 \geq \frac{\exp\left(\frac{\ln 2}{\xi B} \sum_{i=1,7,8} \mathcal{R}_{\mathrm{a}_i}\right) - 1}{\gamma_{\mathrm{b}}}, \tag{11a}$$

$$K_7 \geq \frac{\exp\left(\frac{\ln 2}{\xi B} \mathcal{R}_{\mathrm{a}_7}\right) - 1}{\gamma_{\mathrm{b}}}, \tag{11b}$$

$$K_8 \geq \frac{\exp\left(\frac{\ln 2}{\xi B} \mathcal{R}_{\mathrm{a}_8}\right) - 1}{\gamma_{\mathrm{b}}}. \tag{11c}$$

Based on the boundary of the feasible set as defined by (11a)–(11c), the minimum values of K_i, denoted by $K_{i,\min}$, for the first tier and for the second tier, respectively, are derived as:

$$K_{i,\min} = \frac{\exp\left(\sum_{j\in\mathcal{L}_i}\frac{1}{M_j}\sum_{u\in\mathcal{U}_j}\ln\left(1+\gamma_u\right)\right)-1}{\gamma_{\rm b}}, \quad (12a)$$

$$K_{i,\min} = \frac{\exp\left(\frac{1}{M_i}\sum_{u\in\mathcal{U}_i}\ln\left(1+\gamma_u\right)\right)-1}{\gamma_{\rm b}}. \quad (12b)$$

2) Fixed Power Control (FPC): The transmission power for the backhaul system once designed is fixed for the entire network. Two criteria are identified for this purpose. The first criterion is to allocate power so as to satisfy the statistical average of the achievable rate for the access system over the area covered by each attocell. The second criterion is by taking into account the achievable rate corresponding to the statistical average of the downlink SINR over the area covered by each attocell. The resulting power control schemes are referred to as FPC1 and FPC2, respectively, and the corresponding power control coefficients are given in the following propositions.

Proposition 1. *The minimum power control coefficient for b_i based on FPC1 is given by:*

$$K_{i,\min} = \frac{\exp\left(3\bar{R}_{\rm a}\ln 2\right)-1}{\gamma_{\rm b}},\ \forall i\in\mathcal{T}_1 \quad (13a)$$

$$K_{i,\min} = \frac{\exp\left(\bar{R}_{\rm a}\ln 2\right)-1}{\gamma_{\rm b}},\ \forall i\in\mathcal{T}_2 \quad (13b)$$

where $\bar{R}_{\rm a}$ is the average achievable rate over an attocell, and it is calculated by:

$$\bar{R}_{\rm a} = \frac{\xi B}{2\ln 2}\ln\left(\frac{1+\gamma_{\max}}{1+\gamma_{\min}}\right) + \frac{2\xi B}{\pi R_{\rm e}^2\ln 2}\int_{\gamma_{\min}}^{\gamma_{\max}}\int_{0}^{R_{\rm e}}\frac{\arcsin^{\dagger}\left(\mathcal{Z}(r,\gamma)\right)r}{1+\gamma}drd\gamma,$$

$$\mathcal{Z}(r,\gamma) = \frac{2\gamma^{-1}(r^2+h^2)^{-m-3}-2\Omega}{|\mathcal{I}_{0^\circ}(r)-\mathcal{I}_{30^\circ}(r)|} - \frac{\mathcal{I}_{0^\circ}(r)+\mathcal{I}_{30^\circ}(r)}{|\mathcal{I}_{0^\circ}(r)-\mathcal{I}_{30^\circ}(r)|},$$

$$\arcsin^{\dagger}(x) = \begin{cases} 1, & x>1 \\ \arcsin(x), & |x|\le 1 \\ -1, & x<-1 \end{cases},$$

and, $\gamma_{\min}$ and $\gamma_{\max}$ are the minimum and maximum downlink SINR, respectively, in an attocell, and $R_{\rm e}$ represents the radius of an equivalent circular cell that preserves the area of the hexagonal cell with radius R. Also, the functions $\mathcal{I}_{0^\circ}(r)$ and $\mathcal{I}_{30^\circ}(r)$ are available in closed form in [8].

Proposition 2. *The minimum power control coefficient for b_i based on FPC2 is given by:*

$$K_{i,\min} = \frac{\left(1+\bar{\gamma}_{\rm a}\right)^3-1}{\gamma_{\rm b}},\ \forall i\in\mathcal{T}_1 \quad (14a)$$

$$K_{i,\min} = \frac{\bar{\gamma}_{\rm a}}{\gamma_{\rm b}},\ \forall i\in\mathcal{T}_2 \quad (14b)$$

TABLE I
SYSTEM PARAMETERS.

Parameter	Symbol	Value
Downlink LED Optical Power	$P_{\rm opt}$	10 W
Downlink LED Semi-Angle	$\Phi_{\rm a}$	60°
Auxiliary LED Semi-Angle	$\Phi_{\rm b}$	5°
Vertical Separation	h	2.25 m
Hexagonal Cell Radius	R	3.1 m
Modulation Bandwidth	B	20 MHz
FFT/IFFT Length	N	1024
Noise PSD	N_0	10^{-21} A^2/Hz
Effective PD Area	$A_{\rm PD}$	10^{-4} m^2
PD Responsivity	$R_{\rm PD}$	0.6 A/W
DC Bias Scaling Factor	α	3

where $\bar{\gamma}_{\rm a}$ is the average downlink SINR which is given by:

$$\bar{\gamma}_{\rm a} = \frac{\gamma_{\max}-\gamma_{\min}}{2} + \frac{2}{\pi R_{\rm e}^2}\int_{\gamma_{\min}}^{\gamma_{\max}}\int_{0}^{R_{\rm e}}\arcsin^{\dagger}\left(\mathcal{Z}(r,\gamma)\right)rdrd\gamma.$$

Note that (13a)–(13b) and (14a)–(14b) follow from definitions of FPC1 and FPC2 in conjunction with use of (7a)–(7c). The derivations for $\bar{R}_{\rm a}$ and $\bar{\gamma}_{\rm a}$ are based on the cumulative distribution function (CDF) of the downlink SINR presented in [8]. The details are, however, excluded due to space limitation. The integrations are efficiently computed with numerical methods.

V. NUMERICAL RESULTS

This section presents Monte Carlo simulation results using a large number of random realizations for distributing multiple UEs uniformly over the total area of the network. For each realization, only the CCI from non-empty neighboring attocells is taken into account, and empty attocells are considered to be *inactive*. The proposed bandwidth scheduling policies and power control schemes are evaluated by using (9), (10) and (12)–(14) in Section IV. The average end-to-end sum rate is assessed by the statistical averaging of (4)–(6) from Section II. Performance results are presented mainly in terms of the total number of UEs in the network. Table I lists the system parameters used for simulations.

A. Backhaul Bandwidth Scheduling

At first, the focus is on bandwidth scheduling with the assumption that $P_{{\rm b}_i} = P_{\rm a}\ \forall i$. Fig. 2 presents the overall average sum rate of the network based on AWF, PWF and EWF scheduling policies for the backhaul system. The performance of an unlimited backhaul (UB) network is included as the baseline scenario in which every single BS is individually equipped with a high capacity wired connection to the core network. The sum rate in all cases is monotonically increasing with the total number of UEs. The UB network sets the upper limit performance, and it achieves an average sum rate of 821.5 Mbits/s for $M = 50$. Among the three scheduling policies, AWF globally attains the best performance and it closely follows the upper limit sum rate. For a low to moderate number of UEs, PWF performs better than EWF, while for a moderate to high number of UEs, EWF takes the lead relative to PWF. Note that when the number of UEs is low, they are

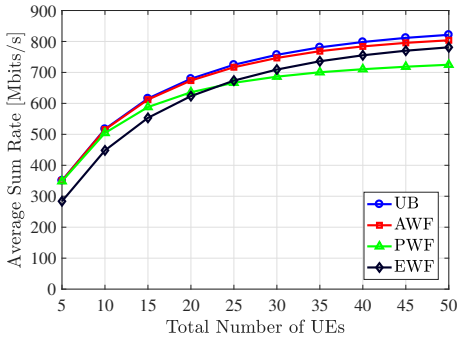

Fig. 2. Average sum rate against the total number of UEs using AWF, PWF and EWF scheduling policies for the backhaul system.

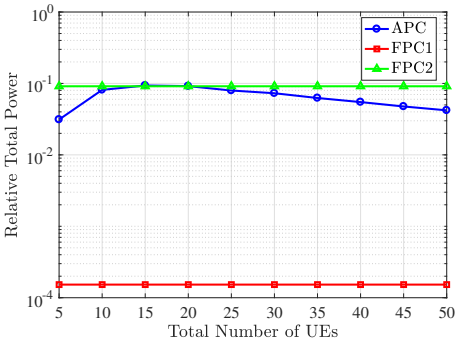

Fig. 3. Relative total power versus the total number of UEs for the backhaul system under APC, FPC1 and FPC2 schemes.

likely to be sparsely scattered in the network. That is the reason for the poor performance of EWF as it always allocates an equal proportion of the backhaul bandwidth to every BS regardless of whatever load they have. Such an attribute turns into an advantage for EWF when it comes to a high number of UEs, which is why its performance approaches that of AWF. Intuitively, the probability of imbalanced loads at the BSs of adjacent attocells decreases by adding more UEs to the network. Hence, the PWF policy loses the opportunity to introduce further gains for the average sum rate as it performs best under imbalanced loads.

B. Backhaul Power Control

The ratio of the total backhaul power with power control to that without power control is considered as a metric to study the potential gains offered by different power control schemes. The metric is referred to as relative total power (RTP) which is defined as follows:

$$\mathrm{RTP} = \frac{\sum_{i=1}^{18} P_{\mathrm{b}_i}}{18 P_{\mathrm{a}}} = \frac{1}{18} \sum_{i=1}^{18} K_i.$$

Fig. 3 demonstrates the RTP metric for APC, FPC1 and FPC2 schemes. It can be observed that the performance is bounded between that of FPC1 and that of FPC2. The RTP value of slightly more than 10^{-4} is achieved by FPC1 which uses the average achievable rate of the access system to set the power control coefficient. By comparison, the RTP value is around 10^{-1} for FPC2 where the average downlink SINR is adopted to determine the power control coefficient. In the case of APC by which the backhaul power control is adapted to the load in the network, the RTP remains between 3×10^{-2} and 10^{-1}.

To gain more insight into the performance of the power control schemes, another metric called backhaul bottleneck occurrence (BBO) is defined. It measures the probability that the aggregate sum rate of the access system in a backhaul branch exceeds the capacity of the bottleneck backhaul link. Equivalently, the BBO metric evaluates the probability that the condition in (7a) is violated. The percentage of the BBO

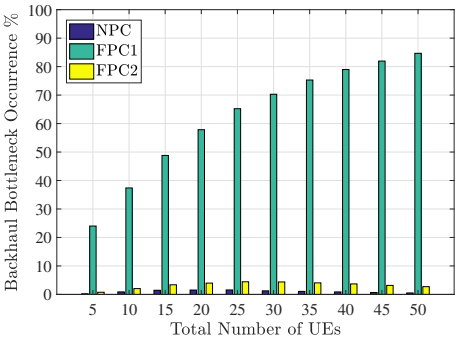

Fig. 4. Backhaul bottleneck occurrence versus the total number of UEs for the backhaul system under FPC1 and FPC2 schemes. NPC stands for no power control and corresponds to the full power backhaul system.

probability for FPC1 and FPC2 schemes is shown Fig. 4. The performance of the backhaul system with full power in which $P_{\mathrm{b}_i} = P_{\mathrm{a}}\ \forall i$ is included for the purpose of comparison. The full power backhaul system is labeled as no power control (NPC). Note that APC has always zero BBO probability, since it is designed in such a way that the backhaul bottleneck event never occurs. Fig. 4 reveals that, with respect to NPC and FPC2, FPC1 returns by far a higher BBO probability which reaches 85% for $M = 50$. A possible explanation for this poor performance is that FPC1 underestimates the sum rate of the access system, which in fact disqualifies the impressive gain that is offered by FPC1 in terms of the total backhaul power. In contrast to FPC1, FPC2 achieves a much better performance with a BBO probability marginally higher than that of NPC. FPC2 retains the BBO of less than 4% for all values of M.

The impact of using backhaul power control on the average sum rate performance is presented in Fig. 5 and Fig. 6. By comparing these figures to Fig. 2, it can be observed that the general trend of the results for all scheduling policies is always preserved. By contrast, applying either power control scheme

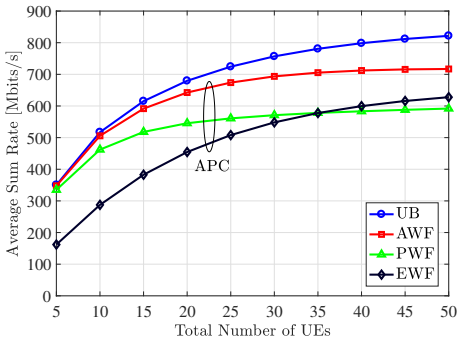

Fig. 5. Average sum rate against the total number of UEs using APC in combination with different scheduling policies for the backhaul system.

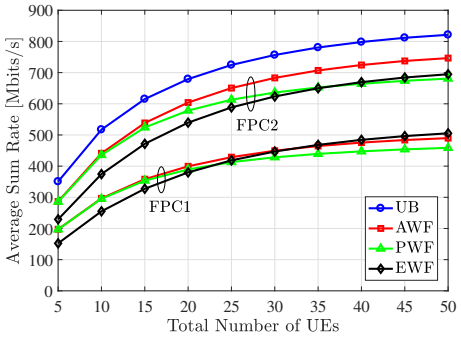

Fig. 6. Average sum rate against the total number of UEs using FPC in combination with different scheduling policies for the backhaul system.

gives rise to a degradation in the overall network performance. When comparing APC, FPC1 and FPC2, it can be seen that the average sum rate for APC is moderately affected and the worst-case sum rate for $M = 50$ stays just below 600 Mbits/s. This threshold is about 720 Mbits/s for the full power backhaul system as shown in Fig. 2, while it is 460 Mbits/s for FPC1 and 680 Mbits/s for FPC2 according to Fig. 6. Clearly, the sum rate performance under FPC1 is substantially degraded. This could be anticipated from the BBO performance, see Fig. 4. In comparison with APC and FPC1, the average sum rate for FPC2 is much less influenced. In fact, FPC2 reaches a tradeoff between the required power and the sum rate performance, and it achieves a comparable performance to that of the full power backhaul system while operating with 90% less power.

VI. Conclusions

The design of a multi-hop wireless VLC backhaul system with a tree topology is proposed for indoor optical attocell networks. The end-to-end downlink sum rate of the network using DF relaying is analyzed. Also, a number of bandwidth scheduling policies and power control schemes are proposed for the backhaul system. The results suggest that AWF scheduling performs better that both PWF and EWF policies. The performance of PWF can be better or worse than EWF depending on how many UEs in total exist in the network. In addition, the power control performance of FPC2 is significantly better with respect to the other two candidates including APC and FPC1, and it can attain competitive performances in terms of the average sum rate of the network while saving 90% of the transmission power for the backhaul system. Future research involves theoretical analysis and optimization of the proposed scheduling policies and power control schemes.

Acknowledgment

Professor Harald Haas gratefully acknowledges the support by the Engineering and Physical Research Council (EPSRC) under Grant EP/R007101/1. He also acknowledges the financial support by the Wolfson Foundation and the Royal Society.

References

[1] M. Figueiredo, L. N. Alves, and C. Ribeiro, "Lighting the Wireless World: The Promise and Challenges of Visible Light Communication," *IEEE Consum. Electron. Mag.*, vol. 6, no. 4, pp. 28–37, Oct. 2017.

[2] H. Haas, L. Yin, Y. Wang, and C. Chen, "What is LiFi?" *IEEE/OSA J. Lightw. Technol.*, vol. 34, no. 6, pp. 1533–1544, Mar. 2016.

[3] T. Komine and M. Nakagawa, "Integrated System of White LED Visible-Light Communication and Power-Line Communication," *IEEE Trans. Consum. Electron.*, vol. 49, no. 1, pp. 71–79, Feb. 2003.

[4] J. Song, W. Ding, F. Yang, H. Yang, B. Yu, and H. Zhang, "An Indoor Broadband Broadcasting System Based on PLC and VLC," *IEEE Trans. Broadcast.*, vol. 61, no. 2, pp. 299–308, Jun. 2015.

[5] P. Mark, "Ethernet over Light," Master's thesis, University of British Columbia, Dec. 2014.

[6] Y. Wang, N. Chi, Y. Wang, L. Tao, and J. Shi, "Network Architecture of a High-Speed Visible Light Communication Local Area Network," *IEEE Photon. Technol. Lett.*, vol. 27, no. 2, pp. 197–200, Jan. 2015.

[7] H. Kazemi, M. Safari, and H. Haas, "A Wireless Backhaul Solution Using Visible Light Communication for Indoor Li-Fi Attocell Networks," in *Proc. IEEE Int. Conf. Commun. (ICC)*, May 2017, pp. 1–7.

[8] C. Chen, D. A. Basnayaka, and H. Haas, "Downlink Performance of Optical Attocell Networks," *IEEE/OSA J. Lightw. Technol.*, vol. 34, no. 1, pp. 137–156, Jan. 2016.

[9] H. Kazemi and H. Haas, "Downlink Cooperation with Fractional Frequency Reuse in DCO-OFDMA Optical Attocell Networks," in *Proc. IEEE Int. Conf. Commun. (ICC)*, May 2016.

[10] S. Dimitrov, S. Sinanovic, and H. Haas, "Clipping Noise in OFDM-Based Optical Wireless Communication Systems," *IEEE Trans. Commun.*, vol. 60, no. 4, pp. 1072–1081, Apr. 2012.

[11] R. U. Nabar, H. Bolcskei, and F. W. Kneubuhler, "Fading Relay Channels: Performance Limits and Space-Time Signal Design," *IEEE J. Sel. Areas Commun.*, vol. 22, no. 6, pp. 1099–1109, Aug. 2004.

[12] O. Narmanlioglu, R. C. Kizilirmak, F. Miramirkhani, and M. Uysal, "Cooperative Visible Light Communications With Full-Duplex Relaying," *IEEE Photon. J.*, vol. 9, no. 3, pp. 1–11, Jun. 2017.

[13] H. Burchardt, N. Serafimovski, D. Tsonev, S. Videv, and H. Haas, "VLC: Beyond Point-to-Point Communication," *IEEE Commun. Mag.*, vol. 52, no. 7, pp. 98–105, Jul. 2014.

[14] J. M. Kahn and J. R. Barry, "Wireless Infrared Communications," *Proc. IEEE*, vol. 85, no. 2, pp. 265–298, Feb. 1997.

[15] S. Shao, A. Khreishah, M. Ayyash, M. B. Rahaim, H. Elgala, V. Jungnickel, D. Schulz, T. D. C. Little, J. Hilt, and R. Freund, "Design and Analysis of a Visible-Light-Communication Enhanced WiFi System," *IEEE/OSA J. Opt. Commun. Netw.*, vol. 7, no. 10, pp. 960–973, Oct. 2015.

[16] T. Cover and A. E. Gamal, "Capacity Theorems for the Relay Channel," *IEEE Trans. Inf. Theory*, vol. 25, no. 5, pp. 572–584, Sep. 1979.

[17] M. D. Soltani, X. Wu, M. Safari, and H. Haas, "Bidirectional User Throughput Maximization Based on Feedback Reduction in LiFi Networks," *IEEE Trans. Commun.*, vol. 66, no. 7, pp. 3172–3186, Jul. 2018.

IEEE TRANSACTIONS ON WIRELESS COMMUNICATIONS, VOL. 18, NO. 2, FEBRUARY 2019 807

A Wireless Optical Backhaul Solution for Optical Attocell Networks

Hossein Kazemi, *Student Member, IEEE*, Majid Safari, *Member, IEEE*, and Harald Haas, *Fellow, IEEE*

***Abstract*— The problem of backhauling for optical attocell networks has been approached by a number of wired solutions such as in-building power line communication (PLC), Ethernet, and optical fiber. In this paper, an alternative solution is proposed based on the wireless optical communication in visible light and infrared (IR) bands. A thorough analysis of signal-to-noise-plus-interference ratio (SINR) is elaborated for a multi-user optical attocell network based on the direct current biased optical orthogonal frequency division multiplexing (DCO-OFDM) and decode-and-forward (DF) relaying, taking into account the effects of inter-backhaul and backhaul-to-access interferences. Inspired by concepts developed for radio frequency (RF) cellular networks, full-reuse visible light (FR-VL) and in-band visible light (IB-VL) bandwidth allocation policies are proposed to realize backhauling in the visible light band. The transmission power is opportunistically minimized to enhance the backhaul power efficiency. For a two-tier FR-VL network, there is a technological challenge due to the limited capacity of the bottleneck backhaul link. The IR band is employed to add an extra degree of freedom for the backhaul capacity. For the IR backhaul system, a power-bandwidth trade-off formulation is presented. Closed form analytical expressions are derived for the corresponding power control coefficients. Finally, the network sum rate performance is studied using extensive Monte Carlo simulations.**

***Index Terms*— Light-fidelity (LiFi), optical attocell network, visible light communication (VLC), infrared (IR) communication, wireless backhaul, power control, multi-hop relaying, decode-and-forward (DF), direct current biased optical orthogonal frequency division multiplexing (DCO-OFDM).**

I. Introduction

NOWADAYS light emitting diodes (LEDs) are commonly adopted for indoor illumination purposes due to their high energy efficiency, long operational lifetime and low cost. The emergence of smart environments necessitates a diversification of advanced services for light fixtures in addition to illumination [1]. A key enabler for this service diversification is visible light communication (VLC), allowing wireless communication by intensity variations of the LED light at a rate that the human eye cannot detect [1].

The growing popularity of mobile-connected devices in conjunction with ubiquitous internet access has led to an exponential increase in global mobile data traffic [2]. Fulfilling bandwidth requirements constitutes a fundamental challenge due to the scarcity of the radio frequency (RF) spectrum. The coincidence of this trend in parallel with the above trend for LEDs has created a unique opportunity for research and development professionals to consider the visible light spectrum as a promising solution. The visible light spectrum offers a vast and unregulated bandwidth (i.e., 1000 times greater than the entire RF spectrum), which can be unlocked by means of VLC.

The application of VLC is not limited only to point-to-point communication [3]. The high speed wireless networking variant of VLC is recognized as light fidelity (LiFi) [4]. By utilizing the existing lighting infrastructure, LiFi enables LED luminaires to provide broadband wireless connectivity [4]. Due to its distinguished features such as cost effective deployment and security, LiFi will be used as a key technology in fifth generation (5G) heterogeneous wireless networks and beyond [4], [5]. The fact that more than 70% of the wireless data traffic originates inside buildings [6], makes LiFi especially advantageous for indoor applications in order to alleviate the RF spectrum crunch. Indoor networks that incorporate ultra-dense LiFi base stations (BSs) are referred to as optical attocell networks [4]. Optical attocells are tiny cells deployed with an extremely dense spatial reuse. Such cells have an equivalent circular radius between 1 m and 3 m [7]. This is analogous to long term evolution (LTE) femtocells, yet offering a much higher area spectral efficiency performance [8].

In optical intensity modulation and direct detection (IM/DD) systems, the transmitter directly modulates the intensity of the LED light. Therefore, the modulating signal is constrained to be both unipolar (i.e., non-negative) and real-valued [7]. In addition to conforming to these requirements, in order to attain high data rates with the limited communication bandwidth in VLC systems, a multi-carrier modulation scheme is preferred. The available variants of orthogonal frequency division multiplexing (OFDM) such as direct current biased optical OFDM (DCO-OFDM), asymmetrically clipped optical OFDM (ACO-OFDM) and enhanced unipolar optical OFDM (eU-OFDM) are tailored to reach a compromise for spectral efficiency and energy efficiency [7], [9], [10]. Among them,

Manuscript received December 30, 2017; revised June 18, 2018 and September 14, 2018; accepted November 10, 2018. Date of publication December 4, 2018; date of current version February 11, 2019. This work was supported in part by the Engineering and Physical Research Council (EPSRC) under Grant EP/R007101/1, and in part by the Wolfson Foundation and the Royal Society. This paper was presented in part at the IEEE International Conference on Communications, May 2017. The associate editor coordinating the review of this paper and approving it for publication was M. S. Alouini. *(Corresponding author: Hossein Kazemi.)*

The authors are with the LiFi Research and Development Center, Institute for Digital Communications, School of Engineering, The University of Edinburgh, Edinburgh EH9 3FD, U.K. (e-mail: h.kazemi@ed.ac.uk; majid.safari@ed.ac.uk; h.haas@ed.ac.uk).

Color versions of one or more of the figures in this paper are available online at http://ieeexplore.ieee.org.

Digital Object Identifier 10.1109/TWC.2018.2883465

DCO-OFDM has the highest spectral efficiency and entails a relatively low implementation complexity, and this appeals to optical attocell networks [7], [11].

Backhaul is an integral part of wireless cellular networks, providing communication links to connect BSs to the core network. The backhaul quality has an unavoidable significance and impact on the overall network performance, and designing a cost effective backhaul is a major challenge for cellular networks [12]. For indoor wireless networks, there are in-building wireless backhauling technologies based on RF communications [13]. For indoor optical attocell networks, most studies focus only on the access part, making the implicit assumption that every BS is separately equipped with an infinite capacity backhaul link to connect to the gateway, e.g., [7], [11], [14], while others use the assumption that the backhaul links are ideal (i.e., lossless and noiseless), albeit they imply a wired backhauling approach, e.g., [15], [16].

Komine and Nakagawa [17] initially proposed the idea of exploiting the existing electricity wiring within buildings for the purpose of backhauling, leading to an integrated power line communication (PLC) and VLC system. Later, in [18], the application of a hybrid PLC-VLC system for indoor broadband broadcasting was experimentally demonstrated. Moreover, Ma *et al.* [19] considered further optimization of the system performance using amplify-and-forward (AF) and decode-and-forward (DF) relaying for signal transmission in PLC and VLC hops. Another option for wired backhauling is Ethernet. In particular, based on the power-over-ethernet (PoE) standard, both data and electricity can be delivered to light fixtures by a single cable. Mark [20] designed and implemented a cascaded system of PoE and VLC using a dual-hop AF relaying transmission over Ethernet and VLC hops. In addition, Delgado *et al.* [21] designed an Ethernet-VLC interface to realize indoor broadcasting from an Ethernet-based local area network (LAN) using VLC. As an alternative to Ethernet, backhauling is also possible with optical fiber. Wang *et al.* [22] proposed an indoor VLC-based LAN architecture where optical BSs are connected to the core network via single mode fiber links. Furthermore, to enable multi-Gbits/s connectivity based on optical fiber, the integration of a passive optical network (PON) architecture with VLC was proposed [23].

The above-mentioned backhauling approaches are all wired. A major drawback of wired solutions is that they highly depend on the wiring infrastructure where any failure directly translates into a loss on the overall network performance. Also, to enable the Ethernet solution, it is necessary to redesign the wiring infrastructure in order to distribute PoE cables to every single luminaire, incurring extra costs that scale proportionately with the network size. In addition, the optical fiber solution, though offering the highest performance, is hardly justifiable in terms of installation costs when it comes to large networks with densely deployed BSs. Moreover, the PLC installation needs additional equipment to interface between the PLC and VLC channels which introduce further complexity.

To the best of the authors' knowledge, wireless backhauling has never been considered as an option for optical attocell networks. The wireless optical backhaul solution proposed in this work makes the backhaul network independent of the wiring infrastructure. The required transceivers to establish inter-BS links are built by adding a number of low-cost LEDs and photodiodes (PDs) to LiFi BS units. In a prior study [24], for the first time, the authors have proposed and devised a wireless backhaul solution whereby the LiFi BSs are interconnected with the gateway using VLC links. In that study, a one-tier optical attocell network with a hexagonal cellular deployment was considered where each BS serves one user equipment (UE). This paper intends to take the work [24] further. By contrast, the distinct contributions of this work are summarized as follows:

- The analysis is extended for a two-tier hexagonal network model using a tree topology to evaluate the scalability of the proposed backhaul solution.
- Novel analytical signal-to-noise-plus-interference ratio (SINR) expressions are derived for multi-hop DF relaying from the gateway to a UE, taking the effects of inter-backhaul and backhaul-to-access interferences into consideration.
- A multi-user scenario is considered where a given number of UEs are randomly distributed in the network.
- A power control mechanism is proposed, aiming for the optimization of the transmission power in the backhaul system. For one-tier and two-tier cases, the corresponding power allocation coefficients are derived in closed form in terms of the system parameters.
- The application of wireless infrared (IR) communication is proposed for backhauling, to enhance the performance of the backhaul system. With a power-bandwidth tradeoff analysis for a two-tier network, it is shown that a properly designed IR backhaul system can deliver the performance of an unlimited backhaul (UB) network.

TABLE I
MATHEMATICAL NOTATIONS

Notation	Description
B_{b}	Bandwidth of the backhaul system
$x^{\mathrm{b}}_{i,k}$	Transmitted signal in the backhaul link of BS_i on subcarrier k
$y^{\mathrm{b}}_{i,k}$	Received signal for the backhaul link of BS_i on subcarrier k
$v^{\mathrm{b}}_{i,k}$	Received noise for the backhaul link of BS_i on subcarrier k
γ_{b_i}	Received SINR per subcarrier for the backhaul link of BS_i
$\mathcal{R}_{\mathrm{b}_i}$	Overall achievable rate for the backhaul link of BS_i
B_{a}	Bandwidth of the access system
$x^{\mathrm{a}}_{i,k}$	Transmitted signal in the access link of BS_i on subcarrier k
$y_{u,k}$	Received signal for the uth UE on subcarrier k
$v^{\mathrm{a}}_{u,k}$	Received noise for the uth UE on subcarrier k
γ_u	Received SINR per subcarrier for the uth UE
$\mathcal{R}_{\mathrm{a}_i}$	Overall achievable rate for the access link of BS_i
$\mathcal{R}_i$	Multi-user sum rate for the end-to-end downlink of BS_i

A. Notations

The main mathematical notations used in this paper are listed in Table I. In addition, throughout the paper, $|\ |$ denotes the cardinality of a set; * is the complex conjugate operator; $\mathbb{E}$ represents the statistical expectation; $\lfloor\ \rfloor$ is the floor function

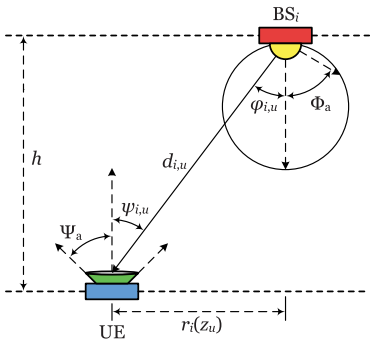

Fig. 1. Downlink geometry in an indoor optical attocell network using these parameters: Φ_a is the semi-angle at half-power of the Lambertian pattern; $d_{i,u}$ is the Euclidean distance between the UE and BS$_i$; $\varphi_{i,u}$ is the light radiance angle with respect to the normal vector of the ceiling; $\psi_{i,u}$ is the light incidence angle with respect to the normal vector of the receiver plane; Ψ_a is the FOV of the UE receiver; $r_i(z_u)$ is the horizontal distance between the UE and BS$_i$; h is the vertical distance separating the UE from the ceiling.

returning the largest integer that is less than or equal to its input argument; and $\preceq$ denotes the componentwise inequality.

II. System Preliminaries

Fig. 1 illustrates the geometric configuration of the downlink system in an indoor optical attocell network. The transmitter consists of a white LED installed on the ceiling and there is a solid-state PD mounted on the UE receiver. It is assumed that the LEDs are oriented vertically downward and the UE devices have a vertically upward orientation.

A. Optical Attocell Network

An optical attocell network with a hexagonal cellular deployment is considered. Other potential deployments include a square network, and a random network based on the Poisson point process (PPP) [7]. The hexagonal model gives the upper bound performance for practical optical attocell networks in terms of the SINR and cell data rate [7]. Fig. 2 depicts the layouts for a one-tier and a two-tier network, encompassing 7 and 19 attocells, respectively. There are M UEs in total in the network which are globally numbered from 1 to M. The UEs are uniformly scattered over the exact coverage of the network and they are associated with their nearest BSs according to the maximum received signal strength criterion [25], [26]. Let $\mathcal{U}_i$ be the index set of the UEs associated with BS$_i$ such that $|\mathcal{U}_i| = M_i$ and $\sum_{i=1}^{N_{\rm BS}} M_i = M$, where $N_{\rm BS}$ is the total number of BSs. Each UE served by BS$_i$ is equally given a bandwidth of $\frac{B_a}{M_i}$, assuming a low-pass and flat frequency response for the VLC channel. The receiver field of view (FOV) is assumed to be sufficiently wide to allow simultaneous detection of optical signals from all BSs.

In this paper, a line-of-sight (LOS) light propagation model is used, as shown in Fig. 1. Note that multipath reflections due to non-line-of-sight (NLOS) paths have an insignificant effect on the attocells that are sufficiently away from the network boundaries [11]. Except in small regions near the walls,

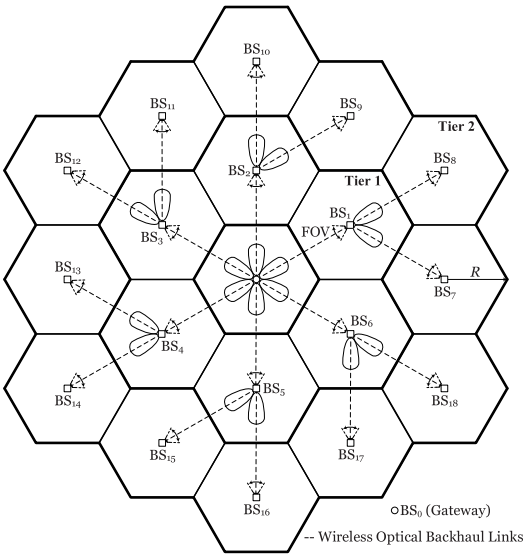

Fig. 2. Hexagonal cellular layouts for a one-tier and a two-tier optical attocell network, and a plan view of multi-hop wireless optical backhaul links.

the LOS component constitutes most of the received power, i.e., more than 90% of the overall power contribution [11]. By using a Lambertian emission pattern for LEDs, the DC gain of the VLC channel from BS$_i$ to the uth UE is given as follows [27, eq. (10)]:

$$H_{i,u} = \frac{(m+1)A_{\rm PD}}{2\pi d_{i,u}^2}\cos^m(\varphi_{i,u})\cos(\psi_{i,u})\mathbb{1}_{\rm FOV}(\psi_{i,u}), \quad (1)$$

where $m = -\frac{\ln 2}{\ln(\cos\Phi_a)}$ is the Lambertian order and Φ_a is the semi-angle at half-power of the LED emission pattern; $A_{\rm PD}$ is the effective PD area; $d_{i,u}$ is the Euclidean distance between the UE and BS$_i$; $\varphi_{i,u}$ is the light radiance angle with respect to the maximum power direction for BS$_i$; $\psi_{i,u}$ is the light incidence angle with respect to the normal vector of the PD plane; and Ψ_a is the FOV for the UE receiver. These are depicted in Fig. 1. The last factor in (1) is an indicator function defined as $\mathbb{1}_{\rm FOV}(\psi_{i,u}) = 1$ if $0 \le \psi_{i,u} \le \Psi_a$, and 0 otherwise. To elaborate, a polar coordinate system with BS$_0$ at the origin is considered, as shown in Fig. 3. For geometric variables related to BS$_0$, the BS subscript 0 is dropped to simplify notation. More specifically, $z_u = (r_u, \theta_u)$ represents polar coordinates of the UE with respect to BS$_0$. One can express the variables $d_{i,u}$, $\cos(\varphi_{i,u})$ and $\cos(\psi_{i,u})$ in terms of $z_u = (r_u, \theta_u)$ by using the relations $d_{i,u} = \sqrt{r_i^2(z_u) + h^2}$ and $\cos(\varphi_{i,u}) = \cos(\psi_{i,u}) = \frac{h}{d_{i,u}}$, where $r_i(z_u)$ is the horizontal distance between the UE and BS$_i$. The polar coordinates of BS$_i$ are denoted by (R_i, Θ_i). Assuming $0 \le \psi_{i,u} \le \Psi_a$, an alternative representation is obtained for (1):

$$H_{i,u} = \frac{(m+1)h^{m+1}A_{\rm PD}}{2\pi}\left(r_i^2(z_u) + h^2\right)^{-\frac{m+3}{2}}, \quad (2)$$

where $r_i(z_u) = \sqrt{r_u^2 + R_i^2 - 2R_i r_u\cos(\theta_u - \Theta_i)}$.

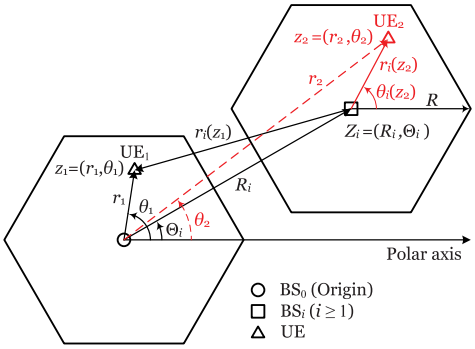

Fig. 3. Optical attocell network geometry in a polar coordinate system. An example with two UEs shows relative radial distances and polar angles.

The focus of this paper is primarily on the downlink. In optical attocell networks, the uplink can be realized by using IR or RF bands [3], [27], [28]. Particularly, by means of IR, and using a wavelength for the upstream direction that does not interfere with the downstream direction, both access and backhaul links can be made bidirectional. Nonetheless, the uplink is an independent problem and it is left for future works.

B. Multiple Access

In this paper, DCO-OFDM is used to realize multiple access. For each attocell, quadrature amplitude modulation (QAM) modulated symbols of the associated UEs are arranged on N subcarriers in the frequency domain. The resulting frame is of the form $\mathbf{X} = [X_0, X_1, \ldots, X_{N-1}]$, such that $X_{N-k} = X_k^*$, for $k \neq 0$. Before the application of the inverse fast Fourier transform (IFFT), the condition $X_0 = X_{\frac{N}{2}} = 0$ has to be fulfilled in order to make the output purely real-valued. The factor $\xi = \frac{N-2}{N}$ is defined as the bandwidth utilization ratio. A cyclic prefix insertion is not considered to simplify the system model. In VLC systems, a typically short-length cyclic prefix and a single-tap equalization in the frequency domain together compensate the multipath dispersion in the channel impulse response [29]. The IFFT output signal is given by:

$$x(n) = \frac{1}{\sqrt{N}} \sum_{k=0}^{N-1} X_k \exp\left(\hat{j}\frac{2\pi kn}{N}\right), \tag{3}$$

for $n = 0, 1, \ldots, N-1$; and $\hat{j} = \sqrt{-1}$. The required DC bias is added in the time domain and the resulting positive signal, $\tilde{x}(n) = x(n) + x_{\mathrm{DC}}$, drives the forward current of the LED. The DC component is given by $x_{\mathrm{DC}} = \alpha\sqrt{P_{\mathrm{elec}}}$, where α is a scaling factor; and P_{elec} is the total electrical power available for transmission. The DC bias controls the average optical power according to $P_{\mathrm{opt}} = \mathbb{E}[x(n)] = x_{\mathrm{DC}}$. Therefore, $P_{\mathrm{elec}} = \frac{P_{\mathrm{opt}}^2}{\alpha^2}$. Note that P_{opt} is fixed for all BSs to comply with the uniform illumination [30]. As a result, P_{elec} is constrained by the illumination requirement. In addition, P_{elec} is equally divided among data-carrying subcarriers so that each subcarrier acquires the same power of $P_{\mathrm{a}} = \frac{P_{\mathrm{opt}}^2}{(N-2)\alpha^2}$.

III. Wireless Backhaul System Design

Two configurations are investigated including a one-tier and a two-tier hexagonal network, as shown in Fig. 2. In the following, first, the modeling and analysis for a one-tier network is presented. Subsequently, the presented methodology is extended for a two-tier network.

A. Wireless Optical Backhauling

The proposed system employs point-to-point wireless optical communication so as to build a wireless backhaul network. To this end, either visible light or IR bands in the optical spectrum can be utilized, both of which are considered in this paper. There are cost-effective LED and PD devices for both bands that can be used to integrate backhaul transceivers with the BS units.

The wireless backhaul configuration using a star topology for a one-tier network is depicted in Fig. 2. As shown, only the central BS is directly connected to the core network. The remaining BSs in the first or the second tier are routed to the core network via multi-hop wireless backhaul links with the central BS using DF relaying [31]. Therefore, BS_0 is the gateway for BS_i, $\forall i \geq 1$. Relay BSs are permitted to operate in a full duplex mode because of two reasons: 1) there is no direct LOS path from the backhaul transmitter to the backhaul receiver at the same relay as they are mounted on two opposite sides of the BS unit; 2) the self-interference caused by the multipath propagation from the transmitter to the receiver on the same relay is not significant for typical indoor environments according to a study in [32]. The aim of this work is to focus on the *end-to-end* performance from the gateway to the UEs, assuming that there is a wired link between the gateway and the core network with an adequate capacity to support the aggregate data flowing in the whole backhaul network plus the downlink data for BS_0. The wireless backhaul links are provided by perfectly aligned VLC or wireless IR links. Such links can be established by adding six auxiliary LEDs on BS_0 allowing each one to point at a BS in the first tier. For each auxiliary LED, a PD is then added to the corresponding BS on the other side of the backhaul link.

The gateway continuously sends a flow of data toward BS_i without interruption. When backhaul links operate in the visible light spectrum, the access and backhaul links inevitably share the same frequency band and as a consequence, mutually interfere, assuming they are spatially transparent to each other. Note that there may be a suspended ceiling under the actual ceiling, creating an enclosed space which can physically separate the VLC channels of the access and backhaul parts. However, such a facility is not available everywhere and the purpose of this work is to avoid introducing any change to the existing indoor infrastructure. In order to manage the backhaul-to-access interference, two bandwidth allocation methods are proposed, including full reuse visible light (FR-VL) and in-band visible light (IB-VL). In the FR-VL method, the entire bandwidth is fully reused across all the access and

$$y^{\mathrm{b}}_{1,k}(n) = R_{\mathrm{PD}} G_{\mathrm{b}} \sqrt{P_{\mathrm{b}_1}} x^{\mathrm{b}}_{1,k}(n) + R_{\mathrm{PD}} (1/2)^{\ell} G_{\mathrm{b}} \sqrt{P_{\mathrm{b}_1}} \left[x^{\mathrm{b}}_{2,k}(n) + x^{\mathrm{b}}_{6,k}(n) \right] + v^{\mathrm{b}}_{1,k}(n). \tag{4}$$

$$y^{\text{FR-VL}}_{u,k}(n) = R_{\mathrm{PD}} H_{i,u} \sqrt{P_{\mathrm{a}}} x^{\mathrm{a}}_{i,k}(n) + R_{\mathrm{PD}} \sum_{j \in \mathcal{Q}_i} G_{j,u} \sqrt{P_{\mathrm{b}_j}} x^{\mathrm{b}}_{j,k}(n) + R_{\mathrm{PD}} \sum_{j \in \mathcal{I}_i} H_{j,u} \sqrt{P_{\mathrm{a}}} x^{\mathrm{a}}_{j,k}(n) + v^{\mathrm{a}}_{u,k}(n). \tag{7}$$

backhaul links. In the IB-VL method, two orthogonal sub-bands are allocated to the access and backhaul links and each sub-band may be fully reused by either one. More details are available in Section IV. For BS_i in the first tier, i.e., $i \in \mathcal{T}_1 = \{1, 2, \ldots, 6\}$, a dual-hop relaying transmission is performed over one backhaul hop and one hop for the access link. For BS_0, the entire bandwidth is fully used for downlink access even in the IB method, since BS_0 is directly connected to the gateway. Note that the access links do not affect the backhaul links based on the LOS propagation.

As an alternative to the visible light band, the IR band is considered for wireless optical backhaul design. IR LEDs typically have a much wider modulation bandwidth than white LEDs, with cutoff frequencies in the order of 440 MHz and up to 1.7 GHz [33]. Such high bandwidths are usually produced by reducing the radiative lifetime of the minority carries [34], however at the expense of decreasing the output optical power, since the internal power-bandwidth product is fixed [34]. Most commercial and low-cost IR LEDs emit wavelengths in the range between 780 nm and 950 nm [27]. The principal drawback of radiation in this range relates to eye safety, which is globally governed by international electromechanical commission (IEC) standards. In particular, the IEC Class 1 determines an allowable exposure limit for IR transmitters depending on their wavelength, diameter and emission semi-angle [27]. Also, it is desirable to limit the transmission power for IR backhauling in consideration of the power consumption.

B. Signal-to-Noise-Plus-Interference Ratio

The backhaul link of BS_i, b_i, and the LED on its transmit end are both labeled with the index of the BS on its receive end. In the following, the time domain signal models are always given on subcarrier k and at time sample n, by assuming perfect sampling and synchronization. Also, it is assumed that the uth UE is associated with BS_i $\forall i \in \{0\} \cup \mathcal{T}_1$. These are not mentioned again in the sequel for the sake of brevity. Moreover, one can see in Fig. 2 that the backhaul network topology is symmetric around BS_0. Without loss of generality, the received signal model for the backhaul system is presented in terms of BS_1 and b_1.

1) Backhaul Link: For any of the proposed wireless optical backhaul systems, the signal intended for the downlink of BS_1 has to be decoded at BS_1 first. After removing the DC bias, the received signal at BS_1 from b_1 is calculated as in (4), shown at the top of the page, where R_{PD} is the PD responsivity; $G_{\mathrm{b}} = \frac{(\ell+1)A_{\mathrm{PD}}}{6\pi R^2}$ is the DC gain of the wireless optical channel for a backhaul link and $\ell = -\frac{\ln 2}{\ln(\cos \Phi_{\mathrm{b}})}$ is the Lambertian order and Φ_{b} is the emission semi-angle of the auxiliary LEDs, by assuming a Lambertian emission for the auxiliary LEDs and using (1); and $v^{\mathrm{b}}_{1,k}(n)$ is a zero mean white Gaussian noise that captures the aggregate effect of signal-independent shot noise induced by the ambient light, and thermal noise of the receiver. The variance of $v^{\mathrm{b}}_{1,k}(n)$ is given by $\sigma^2_{\mathrm{b}} = \frac{N_0 B_{\mathrm{b}}}{N}$, where N_0 denotes the noise power spectral density (PSD). On the right hand side (RHS) of (4), $x^{\mathrm{b}}_{2,k}(n)$ and $x^{\mathrm{b}}_{6,k}(n)$ are interference terms caused by cross-coupling with b_2 and b_6; see Fig. 2. In (4), $P_{\mathrm{b}_j} = K_j P_{\mathrm{a}}$ is the power allocated to the backhaul links of the first tier, where K_j is introduced as the power control coefficient for b_j. With an equal power allocation such that $P_{\mathrm{b}_j} = K_1 P_{\mathrm{a}}$ $\forall j \in \mathcal{T}_1$, all the backhaul links have the same SINR. The SINR of b_j can be derived as:

$$\gamma_{\mathrm{b}_j} = K_1 \left[2 \left(\frac{1}{4} \right)^{\ell} K_1 + \frac{1}{\gamma_{\mathrm{b}}} \right]^{-1}, \quad \forall j \in \mathcal{T}_1 \tag{5}$$

where:

$$\gamma_{\mathrm{b}} = \frac{((\ell+1)A_{\mathrm{PD}} R_{\mathrm{PD}})^2 N P_{\mathrm{a}}}{36\pi^2 R^4 N_0 B_{\mathrm{b}}}. \tag{6}$$

For each backhaul system, the analysis of the downlink SINR is separately presented as follows.

2) Full Reuse Visible Light Backhaul: The received photocurrent of the uth UE situated in the attocell of BS_i, $\forall u \in \mathcal{U}_i$ and $\forall i \in \{0\} \cup \mathcal{T}_1$, can be written as in (7), shown at the top of the page, where $\mathcal{I}_i$ is the index set of interfering BSs for BS_i; $\mathcal{Q}_i$ is the index set of interfering backhaul links for BS_i; and $G_{j,u}$ represents the DC gain of the wireless optical channel between b_j and the UE. There are two types of interference on the RHS of (7). The second term is the backhaul interference and the third term is the inter-cell interference (ICI). The backhaul interference arises from the links connecting BS_0 to the first tier. Fig. 4 illustrates the backhaul interference of b_j affecting the downlink of BS_i, $\forall j \in \mathcal{T}_1$ and $\forall i \in \{0\} \cup \mathcal{T}_1$. Based on (1), one obtains $G_{j,u} = \frac{(\ell+1)A_{\mathrm{PD}}}{2\pi d^2_u} \cos^{\ell}(\beta_{j,u}) \cos(\psi_u)$, where $\beta_{j,u}$ is the light radiance angle of the auxiliary LED for b_j relative to the UE receiver. From Fig. 4, it can be observed that $\beta_{j,u}$ is related to the complementary angle $\varphi'_u = 90^\circ - \varphi_u$ by a cylindrical rotation of $\theta_u - \Theta_j$, and therefore $\cos(\beta_{j,u}) = \cos(\varphi'_u)\cos(\theta_u - \Theta_j)$, where $\cos(\varphi'_u) = \frac{r_u}{d_u}$. Consequently, $G_{j,u}$ can be expressed as:

$$G_{j,u} = \frac{(\ell+1)hA_{\mathrm{PD}}}{2\pi} r^{\ell}_u \cos^{\ell}(\theta_u - \Theta_j)(r^2_u + h^2)^{-\frac{\ell+3}{2}}. \tag{8}$$

In (7), the variance of the noise term, $v^{\mathrm{a}}_{u,k}(n)$, is $\sigma^2_{\mathrm{a}} = \frac{N_0 B_{\mathrm{a}}}{N}$. By using (7), a unified expression is derived for the received SINR at the UE location:

$$\gamma^{\text{FR-VL}}_u = \frac{\mathcal{S}(z_u)}{\mathcal{F}_{\mathrm{BI}}(z_u) + \mathcal{F}_{\mathrm{ICI}}(z_u) + \Omega}, \tag{9}$$

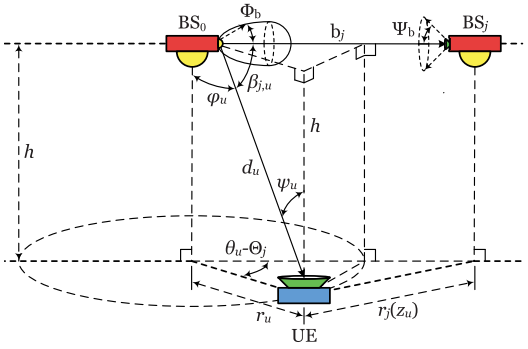

Fig. 4. Backhaul interference caused by b_j, $j \in \mathcal{T}_1$, on the downlink of the UE associated with BS_i, $i \in \{0\} \cup \mathcal{T}_1$.

where $\mathcal{S}(z_u)$, $\mathcal{F}_{\mathrm{ICI}}(z_u)$ and $\mathcal{F}_{\mathrm{BI}}(z_u)$ are defined as the desired signal effect, the ICI effect and the backhaul interference effect, respectively. The first two effects are given by:

$$\mathcal{S}(z_u) = \left(r_i^2(z_u) + h^2\right)^{-m-3}, \tag{10}$$

$$\mathcal{F}_{\mathrm{ICI}}(z_u) = \sum_{j \in \mathcal{I}_i} \left(r_j^2(z_u) + h^2\right)^{-m-3}. \tag{11}$$

The parameter Ω in (9) is given by:

$$\Omega = \frac{4\pi^2 \alpha^2 N_0 B_{\mathrm{a}} (N-2)}{\left((m+1)h^{m+1} A_{\mathrm{PD}} R_{\mathrm{PD}} P_{\mathrm{opt}}\right)^2 N}, \tag{12}$$

Using (8), the backhaul interference effect can be derived as $\mathcal{F}_{\mathrm{BI}}(z_u) = K_1 \mathcal{F}_1(z_u; \mathcal{Q}_i)$ where $\mathcal{Q}_i \subset \mathcal{T}_1$, and:

$$\mathcal{F}_1(z_u; \mathcal{Q}_i) = \frac{(\ell+1)^2}{(m+1)^2 h^{2m}} \sum_{j \in \mathcal{Q}_i} \frac{r_u^{2\ell} \cos^{2\ell}\left(\theta_u - \Theta_j\right)}{\left(r_u^2 + h^2\right)^{\ell+3}}. \tag{13}$$

3) In-Band Visible Light Backhaul: By means of the IB-VL backhaul system, the backhaul interference effect is eliminated. From (9), the received SINR of the uth UE is readily given by:

$$\gamma_u^{\text{IB-VL}} = \frac{\left(r_i^2(z_u) + h^2\right)^{-m-3}}{\sum\limits_{j \in \mathcal{I}_i} \left(r_j^2(z_u) + h^2\right)^{-m-3} + \Omega}. \tag{14}$$

4) Infrared Backhaul: By employing a single IR wavelength that is fully reused across all the backhaul links, the backhaul SINR is identical to that in (5). Also, since the backhaul interference effect is perfectly canceled, the downlink SINR denoted by γ_u^{IR} is equal to $\gamma_u^{\text{IB-VL}}$ given by (14).

C. Sum Rate Analysis

To facilitate the sum rate analysis, the achievable rate of a DCO-OFDM link is required in closed form. To this end, note that for a dynamic range limited wireless optical system based on DCO-OFDM, the Shannon-Hartley capacity theorem can be applied individually to each subcarrier in between two points: the input of the IFFT at the transmitter and the output of the FFT at the receiver. In principle, through a large number of subcarriers, the FFT operation effectively converts any independent and identically distributed (*i.i.d.*) perturbation term added to the received signal, including clipping noise and interference, into a Gaussian noise according to the central limit theorem [35]. In addition, there is an average power constraint to achieve the desired peak-to-average power ratio performance. Therefore, for the aforementioned input-output points *in the electrical domain*, the Shannon-Hartley capacity formula can be used. The achievable rate for a DCO-OFDM link over a flat wireless optical channel with bandwidth B is readily obtained as:

$$\mathcal{R} = \xi B \log_2(1+\gamma), \tag{15}$$

where γ is the received electrical SINR.

1) FR-VL Backhaul: From the definition of FR-VL backhauling, it follows that $B_{\mathrm{a}} = B_{\mathrm{b}} = B$. For BS_0, the sum rate of UEs can be calculated as:

$$\mathcal{R}_0^{\text{FR-VL}} = \frac{\xi B}{M_0} \sum_{u \in \mathcal{U}_0} \log_2\left(1 + \gamma_u^{\text{FR-VL}}\right). \tag{16}$$

Using (5) and (9), the sum rate of UEs for BS_i, $\forall i \in \mathcal{T}_1$, can be expressed as:

$$\mathcal{R}_i^{\text{FR-VL}} = \frac{\xi B}{M_i} \sum_{u \in \mathcal{U}_i} \log_2\left(1 + \min\left[\gamma_{\mathrm{b}_i}, \gamma_u^{\text{FR-VL}}\right]\right). \tag{17}$$

The derivation of (17) is based on [31, Eq. (15)] through setting the direct source-to-destination channel gain to zero. The factor $\frac{1}{2}$ in [31, eq. (15)] is omitted because the relay BSs operate in full-duplex mode. In (17), $\min\left[\gamma_{\mathrm{b}_i}, \gamma_u^{\text{FR-VL}}\right]$ represents the equivalent SINR of a dual-hop DF relaying transmission for the uth UE associated with BS_i.

2) IB-VL Backhaul: In this case, B_{a} and B_{b} correspond to two orthogonal sub-bands allocated to the access and backhaul parts. Let δ be the ratio of the bandwidth fraction allocated to the access part relative to the total VLC bandwidth. It follows that $B_{\mathrm{a}} = \delta B$ and $B_{\mathrm{b}} = (1-\delta)B$ for $0 < \delta < 1$. Considering that BS_0 is directly connected to the gateway, the sum rate of UEs for BS_0 can be equivalently represented by:

$$\mathcal{R}_0^{\text{IB-VL}} = \frac{\xi B}{M_0} \sum_{u \in \mathcal{U}_0^{(\delta)}} \log_2\left(1 + \gamma_u^{\text{IB-VL}}\right) + \frac{\xi B}{M_0} \sum_{u \in \mathcal{U}_0^{(1-\delta)}} \log_2\left(1 + \gamma_u^{\text{FR-VL}}\right), \tag{18}$$

where $\mathcal{U}_0^{(\delta)}$ and $\mathcal{U}_0^{(1-\delta)}$ are two complementary subsets of $\mathcal{U}_0$ such that $\left|\mathcal{U}_0^{(\delta)}\right| = \delta M_0$ and $\left|\mathcal{U}_0^{(1-\delta)}\right| = (1-\delta)M_0$, assuming δM_0 is an integer. The detailed design of δ is discussed next.

For a one-tier network, the bandwidth allocation criterion is derived as:

$$\delta \leq \frac{\log_2(1+\gamma_{\mathrm{b}_i})}{\frac{1}{M_i} \sum\limits_{u \in \mathcal{U}_i} \log_2\left(1 + \gamma_u^{\text{IB-VL}}\right) + \log_2(1+\gamma_{\mathrm{b}_i})}, \quad \forall i \in \mathcal{T}_1 \tag{19}$$

where the equality leads to the maximum reliable rate for the dual-hop DF transmission. As the condition in (19) holds $\forall i \in \mathcal{T}_1$, among the six backhaul branches, the one with the maximum sum rate is considered to specify the value of δ.

$$y^{\mathrm{b}}_{1,k}(n) = R_{\mathrm{PD}}G_{\mathrm{b}}\sqrt{P_{\mathrm{b}_1}}x^{\mathrm{b}}_{1,k}(n) + R_{\mathrm{PD}}(1/2)^{\ell}G_{\mathrm{b}}\sqrt{P_{\mathrm{b}_1}}\left[x^{\mathrm{b}}_{2,k}(n) + x^{\mathrm{b}}_{6,k}(n)\right] + R_{\mathrm{PD}}(1/2)^{\ell+1}G_{\mathrm{b}}\sqrt{P_{\mathrm{b}_9}}x^{\mathrm{b}}_{9,k}(n) + v^{\mathrm{b}}_{1,k}(n). \quad (22)$$

$$y^{\mathrm{b}}_{7,k}(n) = R_{\mathrm{PD}}G_{\mathrm{b}}\sqrt{P_{\mathrm{b}_7}}x^{\mathrm{b}}_{7,k}(n) + R_{\mathrm{PD}}(1/3)\big(\sqrt{3}/2\big)^{\ell+1}G_{\mathrm{b}}\sqrt{P_{\mathrm{b}_1}}\left[x^{\mathrm{b}}_{1,k}(n) + x^{\mathrm{b}}_{6,k}(n)\right] + R_{\mathrm{PD}}(1/2)^{\ell}G_{\mathrm{b}}\sqrt{P_{\mathrm{b}_8}}x^{\mathrm{b}}_{8,k}(n) + R_{\mathrm{PD}}(1/2)^{\ell+1}G_{\mathrm{b}}\sqrt{P_{\mathrm{b}_8}}x^{\mathrm{b}}_{18,k}(n) + v^{\mathrm{b}}_{7,k}(n). \quad (23)$$

$$y^{\mathrm{b}}_{8,k}(n) = R_{\mathrm{PD}}G_{\mathrm{b}}\sqrt{P_{\mathrm{b}_8}}x^{\mathrm{b}}_{8,k}(n) + R_{\mathrm{PD}}(1/2)^{\ell}G_{\mathrm{b}}\sqrt{P_{\mathrm{b}_7}}x^{\mathrm{b}}_{7,k}(n) + R_{\mathrm{PD}}(1/3)\big(\sqrt{3}/2\big)^{\ell+1}G_{\mathrm{b}}\sqrt{P_{\mathrm{b}_7}}x^{\mathrm{b}}_{9,k}(n) + R_{\mathrm{PD}}(5/7)\big(1/2\sqrt{7}\big)^{\ell+1}G_{\mathrm{b}}\sqrt{P_{\mathrm{b}_7}}x^{\mathrm{b}}_{11,k}(n) + v^{\mathrm{b}}_{8,k}(n). \quad (24)$$

Note that once the value of δ is determined, it is fixed for the entire network. Therefore:

$$\delta = \frac{\log_2(1+\gamma_{\mathrm{b}_1})}{\max\limits_i \left[\frac{1}{M_i}\sum\limits_{u\in\mathcal{U}_i}\log_2\left(1+\gamma_u^{\text{IB-VL}}\right)\right] + \log_2(1+\gamma_{\mathrm{b}_1})}. \quad (20)$$

Based on (14) and (20), the sum rate of UEs for BS_i, $\forall i \in \mathcal{T}_1$, is obtained as:

$$\mathcal{R}_i^{\text{IB-VL}} = \frac{\xi\delta B}{M_i}\sum_{u\in\mathcal{U}_i}\log_2\left(1+\gamma_u^{\text{IB-VL}}\right). \quad (21)$$

Note that the methodology used here to acquire the bandwidth allocation ratio δ is consistent with that for multi-hop wireless networks using orthogonal resources for intermediate hops [36]. For example, the result presented in Lemma 1 in [36] can be derived by substituting the RHS of (19) into (21) which gives the capacity of the dual-hop system as the harmonic mean of the capacities of the two hops.

3) IR Backhaul: The IR case is similar to the FR-VL case in terms of the sum rate analysis, and the corresponding expressions for the sum rate, denoted by $\mathcal{R}_i^{\text{IR}}$, can be given by (16) and (17) provided that $\gamma_u^{\text{FR-VL}}$ is replaced by γ_u^{IR}.

IV. Extension to Two-Tier Network

The application of wireless optical backhauling is extended for a two-tier hexagonal network. Consequently, a tree topology is used for the backhaul network as shown in Fig. 2. To this end, two extra auxiliary LEDs are added to each BS in the first tier to point at two BSs in the second tier. For BS_i in the second tier, $\forall i \in \mathcal{T}_2 = \{7, 8, \ldots, 18\}$, a triple-hop relaying transmission is performed over two intermediate backhaul hops and another hop for the access link.

Due to the symmetric topology of the network around BS_0, according to Fig. 2, any one of the six backhaul branches in the tree topology is an indicator for the performance of the remaining branches. This observation especially simplifies the presentation of the received signal model for the backhaul system by focusing on BS_1, BS_7 and BS_8. First, the SINR of the backhaul links is established. Afterward, the SINR and sum rate of the downlink under different backhaul systems are individually discussed.

A. Backhaul Links

The three signals sent for the downlinks of BS_1, BS_7 and BS_8 are fully decoded at BS_1. The signal received by BS_1 through b_1 is calculated in (22), shown at the top of the page. The signals received by BS_7 and BS_8 from b_7 and b_8 are presented in (23) and (24), shown at the top of the page, respectively. In (22)–(24), $P_{\mathrm{b}_j} = K_j P_{\mathrm{a}}$ is the power allocated to b_j, with K_j as the corresponding power control coefficient. An equal power is assigned to the backhaul links of the first tier. The backhaul links of the second tier are divided into two groups of odd and even-numbered, with a different power allocated to each group. This is primarily because of the asymmetric spatial distribution of the received SINR on the attocells of odd and even-numbered BSs in the second tier. The SINR of b_j can be derived and expressed as:

$$\gamma_{\mathrm{b}_j} = K_1\left[2\left(\frac{1}{4}\right)^{\ell}K_1 + \left(\frac{1}{4}\right)^{\ell+1}K_7 + \frac{1}{\gamma_{\mathrm{b}}}\right]^{-1}, \quad \forall j \in \mathcal{T}_1 \quad (25)$$

$$\gamma_{\mathrm{b}_j} = K_7\left[\frac{2}{9}\left(\frac{3}{4}\right)^{\ell+1}K_1 + 5\left(\frac{1}{4}\right)^{\ell+1}K_8 + \frac{1}{\gamma_{\mathrm{b}}}\right]^{-1}, \quad \forall j \in \mathcal{T}_2^{\mathrm{o}} \quad (26)$$

$$\gamma_{\mathrm{b}_j} = \frac{K_8}{K_7}\left[\left(\frac{1}{4}\right)^{\ell} + \frac{1}{9}\left(\frac{3}{4}\right)^{\ell+1} + \frac{25}{49}\left(\frac{1}{28}\right)^{\ell+1} + \frac{1}{K_7\gamma_{\mathrm{b}}}\right]^{-1}, \quad \forall j \in \mathcal{T}_2^{\mathrm{e}} \quad (27)$$

where $\mathcal{T}_2^{\mathrm{o}} = \{7, 9, \ldots, 17\}$ and $\mathcal{T}_2^{\mathrm{e}} = \{8, 10, \ldots, 18\}$ are the index sets of odd and even-numbered BSs in the second tier, respectively.

B. FR-VL Backhaul

In a two-tier network, the downlink experiences the backhaul interference caused by both the links connecting BS_0 to the first tier and those lying in between the first and the second tiers. For the first tier, the DC gain of the interference channel, $G_{j,u}$, corresponding to b_j, $\forall j \in \mathcal{T}_1$, is given by (8). For the second tier, the calculation of $G_{j,u}$ for the downlink interference channel for b_j, $\forall j \in \mathcal{T}_2$, is similar in principle to that of (8). By contrast, the only difference comes from the need to shift the origin of the coordinate system to the coordinates of the BS in the first tier to which the transmit end of b_j is connected. Nevertheless, this is omitted here to avoid duplication. Consequently, the downlink SINR is readily

$$\mathcal{R}_i^{\text{FR-VL}} = \frac{\xi B}{M_i} \sum_{u \in \mathcal{U}_i} \min\left[\mu_i \log_2\left(1+\gamma_{\mathrm{b}_i}\right), \log_2\left(1+\gamma_u^{\text{FR-VL}}\right)\right], \quad \forall i \in \mathcal{T}_1 \tag{29}$$

$$\mathcal{R}_i^{\text{FR-VL}} = \frac{\xi B}{M_i} \sum_{u \in \mathcal{U}_i} \min\left[\mu_i \log_2\left(1+\gamma_{\mathrm{b}_s}\right), \log_2\left(1+\gamma_{\mathrm{b}_i}\right), \log_2\left(1+\gamma_u^{\text{FR-VL}}\right)\right], \quad \forall i \in \mathcal{T}_2 \tag{30}$$

available in (9) with a total backhaul interference of the form $\mathcal{F}_{\text{BI}}(z_u) = K_1\mathcal{F}_1(z_u;\mathcal{Q}_i) + K_7\mathcal{F}_2(z_u;\mathcal{O}_i) + K_8\mathcal{F}_2(z_u;\mathcal{E}_i)$, where $\mathcal{F}_1(z_u;\mathcal{Q}_i)$ is given by (13); $\mathcal{O}_i \subset \mathcal{T}_2^{\text{o}}$ and $\mathcal{E}_i \subset \mathcal{T}_2^{\text{e}}$ are the index sets of interfering odd and even-numbered backhaul links of the second tier, respectively; and:

$$\mathcal{F}_2(z_u;\mathcal{A}_i) = \frac{(\ell+1)^2}{(m+1)^2 h^{2m}} \sum_{j \in \mathcal{A}_i} \frac{r_s^{2\ell}(z_u)\cos^{2\ell}\left(\theta_s - \Theta_{\mathrm{b}_j}\right)}{\left(r_s^2(z_i)+h^2\right)^{\ell+3}}, \tag{28}$$

for $\mathcal{A}_i = \mathcal{O}_i, \mathcal{E}_i$. In (28), (r_s, θ_s) are the relative coordinates of z_u, and Θ_{b_j} is the relative angle of b_j, with respect to the polar axis of BS_s for $s = \lfloor \frac{j-5}{2} \rfloor$.

In [24], the backhaul LED semi-angle Φ_{b} is identified as a key determinant of the performance for a visible light backhaul system. A special case of interest for the downlink SINR is to evaluate an asymptotic behavior of the backhaul interference effect when the wireless backhaul links are extremely directive. Such a case is used in the following as a theoretical bound for the system performance. This is established in Theorem 1.

Theorem 1: For the FR-VL backhaul system, in the limit as Φ_{b} tends to zero, the backhaul interference effect on the downlink approaches zero at any location in the network, for either a one-tier or a two-tier network.

Proof: See Appendix A. ∎

For a two-tier network, the six backhaul links branched from the gateway carry most of the data traffic in the network, and each one has to accommodate three downstream data flows. In order to fairly apportion the backhaul capacity, an equally weighted fair scheduling method is employed [37], by which every data flow in a shared backhaul link is allocated an equal proportion of the available capacity. The allocated resources are orthogonal so that b_1 is effectively decomposed into three independent parallel channels, each one having an achievable rate of $\mu_j \mathcal{R}_{\mathrm{b}_1}$, where $\mu_j = \frac{1}{3}$ is the weight assigned to the jth data flow. The capacity of b_1 can be decomposed in the frequency domain. According to μ_j, the DCO-OFDM frame is divided into three parts and each one is independently loaded with an information block from the jth data flow. At BS_1, different sub-bands are separated in the frequency domain based on the FFT of the received signal. Once the symbols encapsulated in the three sub-bands are individually decoded, each group is modulated with a distinct OFDM frame which is retransmitted in the corresponding direction. Furthermore, for the first and the second tiers, the end-to-end rate of UEs cannot be higher than the allocated capacity of each intermediate hop based on the maximum flow–minimum cut theorem [38]. By using (25)–(27) and (9), the sum rate of UEs for BS_i, is derived as in (29), for $i \in \mathcal{T}_1$, and in (30), for $i \in \mathcal{T}_2$, shown at the top of the page, where $s = \lfloor \frac{i-5}{2} \rfloor$.

C. IB-VL Backhaul

For a two-tier network, the bandwidth allocation ratio δ is upper bounded as follows:

$$\delta \leq \frac{\log_2(1+\gamma_{\mathrm{b}_i})}{\sum\limits_{j \in \mathcal{L}_i} \frac{1}{M_j} \sum\limits_{u \in \mathcal{U}_j} \log_2\left(1+\gamma_u^{\text{IB-VL}}\right) + \log_2(1+\gamma_{\mathrm{b}_i})}, \quad \forall i \in \mathcal{T}_1 \tag{31}$$

where $\mathcal{L}_i = \{i, 2i+5, 2i+6\}$ $\forall i \in \mathcal{T}_1$. The minimum value for δ is obtained by taking the maximum sum rate over the six possible triples on the RHS of (31), corresponding to the six backhaul branches. The value of δ is fixed to be:

$$\delta = \frac{\log_2(1+\gamma_{\mathrm{b}_1})}{\max\limits_i \left[\sum\limits_{j \in \mathcal{L}_i} \frac{1}{M_j} \sum\limits_{u \in \mathcal{U}_j} \log_2\left(1+\gamma_u^{\text{IB-VL}}\right)\right] + \log_2(1+\gamma_{\mathrm{b}_1})}. \tag{32}$$

Based on (32), the sum rate of UEs for BS_i, $\forall i \in \mathcal{T}_1 \cup \mathcal{T}_2$, is readily given by (21).

Note that the number of orthogonal resources in this work (i.e., sub-bands) is always two, unlike the case in [36] where the number of orthogonal resources is equal to the number of hops in the network (i.e., half-duplex). In particular, there are only two orthogonal sub-bands for a two-tier network in which three hops are involved for downlink transmission in the second tier.

D. IR Backhaul

Under the assumption of a single IR wavelength being fully reused over all the backhaul links, the sum rates in (29) and (30) for the FR-VL case apply to the IR case, $\mathcal{R}_i^{\text{IR}}$, upon substituting $\gamma_u^{\text{FR-VL}}$ with γ_u^{IR}.

V. Power Control for Wireless Backhaul System

A power optimization framework is presented for wireless optical backhaul systems discussed in Sections III and IV. This is particularly motivated by the fact that backhaul LEDs do not need to provide illumination for the environment, and their optical power can therefore be minimized to enhance the power efficiency. However, reducing the power in the backhaul links adversely affects their capacity, and thus the network performance may be compromised. Finding the minimum power for the backhaul system while maintaining the network performance at a desired level is formulated as an optimization problem. Note that P_{a} is already fixed. As a result, the minimization of P_{b_j} is equivalent to the minimization of $K_j = \frac{P_{\mathrm{b}_j}}{P_{\mathrm{a}}}$. Due to eye safety considerations, the allowed peak power for all wireless optical backhaul systems is limited

to be no more than the power of the access system, as the backhaul LEDs may have narrow emission semi-angles. This means $P_{\mathrm{b}_j} \leq P_{\mathrm{a}}$, and hence $0 < K_j \leq 1\ \forall j$. Note that $K_j = 1$ represents the case where no power control is applied to b_j.

In order to adjust the backhaul power, the network controller requires the instantaneous channel state information for each UE individually. However, for large networks with a large number of UEs, fulfilling such a requirement is cumbersome and practically infeasible. Hence, a scenario in which every BS experiences the highest sum rate from the associated UEs is considered, implying the highest load on the backhaul system. In a given attocell, the maximum achievable rate coincides with the unique point where the peak SINR occurs. Obviously, the sum rate of multiple UEs all of which are colocated at such a point is equal to the achievable rate of a single UE located at the same point, assuming a uniform bandwidth allocation to UEs. Therefore, it is sufficient to focus on the point that corresponds to the peak SINR for the purpose of optimization, and the UE index u is dropped. Although the described scenario might be the worst case, the advantages include: 1) there is no need for the knowledge of the instantaneous downlink channel; 2) the power optimization is done only once for a given network configuration.

In the following, the backhaul power optimization is presented first for a one-tier network and then for a two-tier network. To elaborate, let z_i represent an arbitrary point within the attocell of BS_i with γ_i denoting the downlink SINR at z_i and let $z_{i,\max} = (r_{i,\max}, \theta_{i,\max})$ be the point of the maximum downlink SINR.

TABLE II
SYSTEM PARAMETERS

Parameter	Symbol	Value
Downlink LED Optical Power	P_{opt}	10 W
Downlink LED Semi-Angle	Φ_{a}	40°
Vertical Separation	h	2.25 m
Hexagonal Cell Radius	R	2.5 m
Total VLC Bandwidth	B	20 MHz
IFFT/FFT Length	N	1024
Noise Power Spectral Density	N_0	10^{-21} A^2/Hz
Receiver Field of View	Ψ_{a}, Ψ_{b}	85°
PD Effective Area	A_{PD}	10^{-4} m^2
PD Responsivity	R_{PD}	0.6 A/W
DC Bias Scaling Factor	α	3

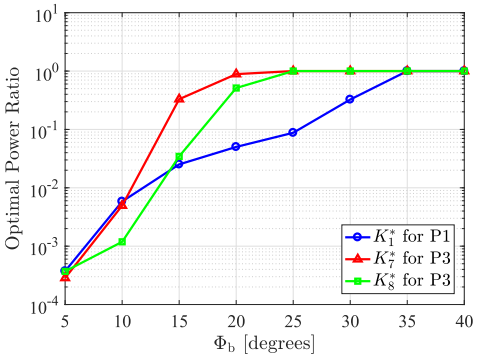

Fig. 5. Optimal power ratios K_1^* for the one-tier FR-VL network, and K_7^* and K_8^* for the two-tier FR-VL network with respect to Φ_{b}.

A. One-Tier Network

To avoid restricting the achievable rate in the downlink, an adequate capacity is required for the backhaul system. For a one-tier network, the backhaul-access rate constraint is:

$$\mathcal{R}_{\mathrm{b}_1} \geq \mathcal{R}_{\mathrm{a}_1}. \tag{33}$$

1) FR-VL Backhaul: The optimization problem is stated as follows:

$$\begin{aligned} \mathrm{P1}: \ & \underset{K_1}{\text{minimize}}\ K_1 \\ & \text{subject to } \log\left(1+\gamma_{\mathrm{b}_1}\right) - \log\left(1+\gamma_1^{\text{FR-VL}}\right) \geq 0, \\ & \qquad 0 < K_1 \leq 1. \end{aligned} \tag{34}$$

The first constraint is due to (33). The second constraint is to limit the backhaul power to be always less than or equal to the access power. The first constraint can be equivalently written as $\gamma_{\mathrm{b}_1} \geq \gamma_1^{\text{FR-VL}}$. Using (9)–(13) for $i = 1$ in place of $\gamma_1^{\text{FR-VL}}$, and solving the inequality for K_1, one obtains:

$$K_1 \geq K_{1,\min}, \tag{35}$$

where $K_{1,\min}$ is derived in closed form:

$$\begin{aligned} & K_{1,\min} \\ & = \frac{\mathcal{S}(z_1)}{2\mathcal{F}_1(z_1;\mathcal{Q}_1)}\left[-\frac{\mathcal{F}_{\mathrm{ICI}}(z_1)+\Omega}{\mathcal{S}(z_1)} + 2\left(\frac{1}{4}\right)^{\ell}\right. \\ & \left. + \sqrt{\left(\frac{\mathcal{F}_{\mathrm{ICI}}(z_1)+\Omega}{\mathcal{S}(z_1)} - 2\left(\frac{1}{4}\right)^{\ell}\right)^2 + \frac{4\mathcal{F}_1(z_1;\mathcal{Q}_1)}{\mathcal{S}(z_1)\gamma_{\mathrm{b}}}}\right]. \end{aligned} \tag{36}$$

Note that $K_{1,\min}$ is expressed at $z_1 = (r_1, \theta_1)$ which can be anywhere within the attocell of BS_1. At the same time, finding exact coordinates of $z_{1,\max}$ depends on the value of K_1. One can jointly find the values of $K_{1,\min}$ and $z_{1,\max}$ by using (36) and maximizing $\gamma_1^{\text{FR-VL}}$ given by (9), in a recursive manner. For infinite size attocell networks, the received SINR peaks exactly at the center of each attocell [7]. It might slightly deviate from the center due to the finite network deployment and the backhaul interference effect. The approximation $z_{1,\max} \approx (0,0)$ is used for simplicity. The solution to P1 can be written in the form:

$$K_1^* = \min[K_{1,\min}, 1]. \tag{37}$$

Numerical results are mainly presented in terms of the backhaul LED semi-angle given a fixed configuration for the downlink system. In optical attocell networks, the downlink parameters such as the LED semi-angle, cell coverage radius

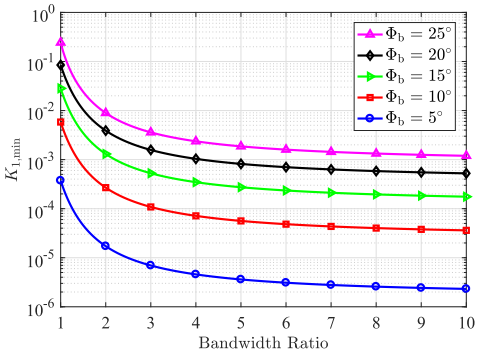

Fig. 6. The minimum power ratio $K_{1,\min}$ against the bandwidth ratio $\frac{B_b}{B_a}$ for the one-tier network with IR backhaul.

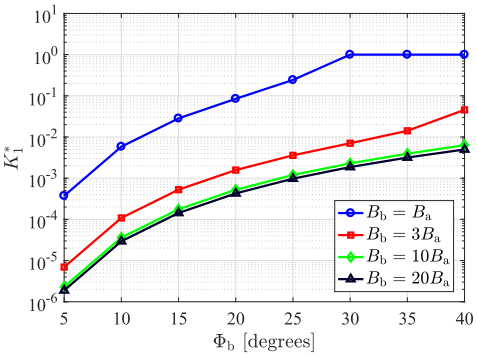

Fig. 7. Optimal power ratio K_1^* for the one-tier network with IR backhaul versus Φ_b for different values of B_b.

and vertical separation are essentially configured to meet the requirements for illumination and SINR quality [7]. Table II lists the system parameters used for simulations.

Fig. 5 shows the optimal solution K_1^* to P1 against Φ_b. It can be observed that by increasing Φ_b, the value of K_1^* is saturated at unity for $\Phi_b \geq 35°$. The value of K_1^* stays below 0.1 for $\Phi_b \leq 25°$. In this case, the power allocated to the backhaul links can be less than one tenth of the downlink power which is a remarkable gain for power efficiency of the FR-VL backhaul system.

2) IR Backhaul and Power-Bandwidth Tradeoff: The bandwidth of the IR system is taken as a variable. More specifically, the desired variable is defined as the ratio of the bandwidth of the backhaul system to that of the downlink system, i.e., $\frac{B_b}{B_a}$. The optimization problem statement is similar to the FR-VL case and is omitted to avoid duplication. The minimum power ratio $K_{1,\min}$ satisfies the constraint in (33), and it can be derived by substituting $\mathcal{R}_{b_1} = \xi B_b \log_2(1+\gamma_{b_1})$ and $\mathcal{R}_{a_1} = \xi B_a \log_2\left(1+\gamma_1^{\text{IR}}\right)$ into (33), which gives:

$$K_{1,\min} = \frac{\left[\left(\left(1+\gamma_1^{\text{IR}}\right)^{\frac{B_a}{B_b}} - 1\right)^{-1} - 2\left(\frac{1}{4}\right)^{\ell}\right]^{-1}}{\gamma_b}. \quad (38)$$

Fig. 6 presents $K_{1,\min}$ as a function of $\frac{B_b}{B_a}$ for different values of Φ_b. A tradeoff is observed between the minimum power ratio and the required bandwidth ratio. The tradeoff is improved by focusing the light beam in the backhaul links. For $\frac{B_b}{B_a} = 1$, $K_{1,\min} < 1$ for all considered values of Φ_b. Fig. 7 shows the optimal power ratio, defined as $K_1^* = [K_{1,\min}, 1]$, with respect to Φ_b for different values of B_b. It can be seen that the optimal power ratio is an increasing function of Φ_b. Also, it can be observed that increasing B_b provides a higher improvement for the optimal power ratio in lower bandwidths. For example, consider increasing B_b from B_a to $3B_a$ and that from $10B_a$ to $20B_a$. The justification is that by increasing B_b, the reduction rate of $K_{1,\min}$ diminishes for higher values of the bandwidth according to Fig. 6.

B. Two-Tier Network

For a two-tier network, there are three backhaul-access rate constraints of:

$$\mathcal{R}_{b_1} \geq \mathcal{R}_{a_1} + \mathcal{R}_{a_7} + \mathcal{R}_{a_8}, \quad (39)$$
$$\mathcal{R}_{b_7} \geq \mathcal{R}_{a_7}, \quad (40)$$
$$\mathcal{R}_{b_8} \geq \mathcal{R}_{a_8}. \quad (41)$$

Among (39)–(41), (39) is the dominant constraint, meaning that the capacity of b_1 has to be sufficiently high to support the aggregate rate demanded by BS_1, BS_7 and BS_8. Otherwise, the limited capacity of b_1 turns into a backhaul bottleneck.

1) FR-VL Backhaul: The optimization problem is stated as follows:

$$\begin{aligned} \text{P2}: \underset{\{K_1,K_7,K_8\}}{\text{minimize}}\ & K_{\text{sum}} = \sum_{j=1,7,8} K_j \\ \text{subject to}\ & g_1(K_1,K_7,K_8) \geq 0, \\ & \log\left(1+\gamma_{b_7}\right) - \log\left(1+\gamma_7^{\text{FR-VL}}\right) \geq 0, \\ & \log\left(1+\gamma_{b_8}\right) - \log\left(1+\gamma_8^{\text{FR-VL}}\right) \geq 0, \\ & 0 < K_j \leq 1. \end{aligned} \quad (42)$$

The objective is to minimize the total power allocated to each backhaul branch including three backhaul links. The first three constraints are adopted from (39)–(41). The function g_1 in the first constraint is given by:

$$g_1(K_1,K_7,K_8) = \log\left(1+\gamma_{b_1}\right) - \sum_{i=1,7,8} \log\left(1+\gamma_i^{\text{FR-VL}}\right). \quad (43)$$

An instant illustration of the admissible region defined by the first three constraints in (42) helps to gain insight on the solution space for P2. To this end, note that the function g_1 in (43) is monotonically increasing in the direction of K_1. It is shown in Appendix B that the partial derivative of g_1 with respect to K_1 is strictly positive. Therefore, one can rearrange the first constraint in (42) and write it as:

$$K_1 \geq K_{1,\min}(K_7,K_8). \quad (44)$$

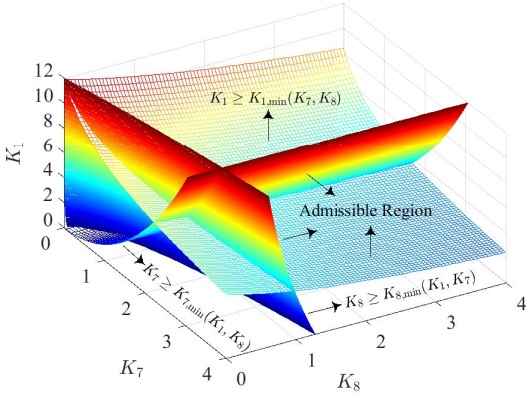

Fig. 8. An instant illustration of the admissible region for P2 based on the first three constraints for $\Phi_{\rm b} = 20°$.

In a similar way, the following alternative forms are obtained for the second and the third constraints in (42), respectively:

$$K_7 \geq K_{7,\min}(K_1, K_8), \tag{45}$$

$$K_8 \geq K_{8,\min}(K_1, K_7), \tag{46}$$

where $K_{7,\min}(K_1, K_8)$ and $K_{8,\min}(K_1, K_7)$ are derived in closed from in (47) and (48), shown at the bottom of the page, respectively. However, $K_{1,\min}$ in (44) cannot be explicitly expressed in terms of K_7 and K_8, as the equation $g_1(K_1, K_7, K_8) = 0$ is non-resolvable for K_1. The Newton-Raphson method is used to evaluate $K_{1,\min}(K_7, K_8)$ given the values of K_7 and K_8, according to the following iterative rule:

$$K_{1,\min}^{(n)} = K_{1,\min}^{(n-1)} - \frac{g_1(K_1, K_7, K_8)}{\frac{\partial g_1}{\partial K_1}}\bigg|_{K_1 = K_{1,\min}^{(n-1)}}, \tag{49}$$

where the superscript n indicates the iteration number. Fig. 8 illustrates the boundary surfaces for (44), (45) and (46), for $\Phi_{\rm b} = 20°$. It is observed that the boundary surface of $K_{1,\min}(K_7, K_8)$ stands beyond the allowed level of $K_1 = 1$. Moreover, when considering the three boundaries, their admissible region has no intersection with the unit cube defined by the last constraint in (42). This reveals a fundamental design challenge for the FR-VL backhaul system since the power in the backhaul links is not practically allowed to exceed the downlink power, and thus the finite capacity of b_i, $i \in \mathcal{T}_1$, determines the upper limit of the downlink data rate in the first and the second tiers. In fact, the feasible set of P2 is empty for most practical cases. To verify this observation, the feasibility of the constraint in (44) has to be examined analytically. However, the function $K_{1,\min}(K_7, K_8)$ is not available in closed form. Instead, an asymptotic bound is derived for $K_{1,\min}(K_7, K_8)$ for small values of $\Phi_{\rm b}$ in Appendix C. This bound represents the best scenario under which the backhaul links attain a high capacity by means of focusing the light emission pattern. In practice, this can be realized by using appropriate optical lenses to collimate the LED light in the backhaul links. Based on (64), and using the system parameters in Table II, it can be verified that $K_{1,\min} \gg 1$. For example, $K_{1,\min} \approx 480$ for $\Phi_{\rm b} = 5°$. To move on further, the first constraint is relaxed by fixing K_1 at $K_1 = 1$, which is the maximum possible value for K_1. One can continue to minimize K_7 and K_8 with the new problem stated as follows:

$$\begin{aligned} \mathrm{P3}: \ & \underset{\{K_7, K_8\}}{\text{minimize}} \ \sum_{j=7,8} K_j \\ & \text{subject to } K_7 \geq K_{7,\min}(K_8), \\ & \qquad K_8 \geq K_{8,\min}(K_7), \\ & \qquad 0 < K_j \leq 1. \end{aligned} \tag{50}$$

Fig. 9 illustrates the admissible region for P3 for $\Phi_{\rm b} = 20°$ on the K_7-K_8 plane, based on the boundaries given by (47) and (48) for $K_1 = 1$. It can be verified that the boundary curves $K_{7,\min}(K_8)$ and $K_{8,\min}(K_7)$ are monotonically increasing for $K_7 > 0$ and $K_8 > 0$. They coincide at the

$$\begin{aligned} K_{7,\min}(K_1, K_8) = \frac{\mathcal{S}(z_7)}{2\mathcal{F}_2(z_7; \mathcal{O}_7)} \Bigg[& - \frac{K_1\mathcal{F}_1(z_7; \mathcal{Q}_7) + K_8\mathcal{F}_2(z_7; \mathcal{E}_7) + \mathcal{F}_{\rm ICI}(z_7) + \Omega}{\mathcal{S}(z_7)} \\ & + \Bigg(\left(\frac{K_1\mathcal{F}_1(z_7; \mathcal{Q}_7) + K_8\mathcal{F}_2(z_7; \mathcal{E}_7) + \mathcal{F}_{\rm ICI}(z_7) + \Omega}{\mathcal{S}(z_7)} \right)^2 \\ & + \frac{4\mathcal{F}_2(z_7; \mathcal{O}_7)}{\mathcal{S}(z_7)} \left(\frac{2}{9} \left(\frac{3}{4} \right)^{\ell+1} K_1 + 5 \left(\frac{1}{4} \right)^{\ell+1} K_8 + \frac{1}{\gamma_{\rm b}} \right) \Bigg)^{\frac{1}{2}} \Bigg]. \end{aligned} \tag{47}$$

$$\begin{aligned} K_{8,\min}(K_1, K_7) = \frac{\mathcal{S}(z_8)}{2\mathcal{F}_2(z_8; \mathcal{E}_8)} \Bigg[& - \frac{K_1\mathcal{F}_1(z_8; \mathcal{Q}_8) + K_7\mathcal{F}_2(z_8; \mathcal{O}_8) + \mathcal{F}_{\rm ICI}(z_8) + \Omega}{\mathcal{S}(z_8)} \\ & + \Bigg(\left(\frac{K_1\mathcal{F}_1(z_8; \mathcal{Q}_8) + K_7\mathcal{F}_2(z_8; \mathcal{O}_8) + \mathcal{F}_{\rm ICI}(z_8) + \Omega}{\mathcal{S}(z_8)} \right)^2 \\ & + \frac{4\mathcal{F}_2(z_8; \mathcal{E}_8)}{\mathcal{S}(z_8)} \left(\left[\left(\frac{1}{4} \right)^{\ell} + \frac{1}{9} \left(\frac{3}{4} \right)^{\ell+1} + \frac{25}{49} \left(\frac{1}{28} \right)^{\ell+1} \right] K_7 + \frac{1}{\gamma_{\rm b}} \right) \Bigg)^{\frac{1}{2}} \Bigg]. \end{aligned} \tag{48}$$

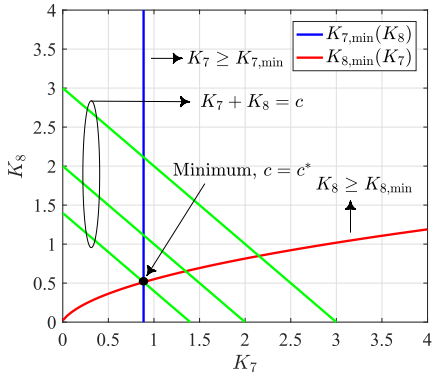

Fig. 9. An instant illustration of the admissible region for P3 for $\Phi_{\rm b} = 20°$. The objective function is shown as the family of lines $K_7 + K_8 = c$ for three values of c. The minimum of the objective function is indicated by $c = c^*$.

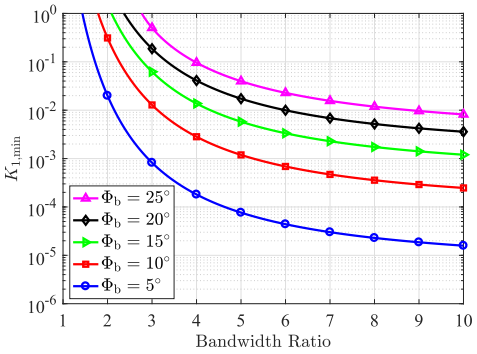

Fig. 10. The tradeoff between the minimum power ratio $K_{1,\min}$ and the bandwidth ratio $\frac{B_{\rm b}}{B_{\rm a}}$ for the two-tier network with IR backhaul.

unique intersection point represented by $\left(K^{\dagger}_{7,\min}, K^{\dagger}_{8,\min}\right)$ in the positive quadrant $\mathbb{R}^2_+$, which, in fact, is the minimum element of the feasible set. This is proved by using the aforementioned property of the boundary curves; see Appendix D. The projections of the objective function onto the K_7-K_8 plane are the family of lines $K_7 + K_8 = c$ for $c \geq 0$, as shown for different values of c in Fig. 9. By decreasing c, the minimum value of the objective function occurs for $c = c^*$ at the intersection point. The solution to P3 can be written as:

$$(K^*_7, K^*_8) = \left(\min\left[K^{\dagger}_{7,\min}, 1\right], \min\left[K^{\dagger}_{8,\min}, 1\right]\right). \quad (51)$$

Referring to Fig. 5, the optimal solutions (K^*_7, K^*_8) to P3 against $\Phi_{\rm b}$ are shown. It can be observed that by increasing $\Phi_{\rm b}$, the value of K^*_1 is saturated at unity for $\Phi_{\rm b} \geq 35°$. It is observed that for $\Phi_{\rm b} \leq 20°$, both K^*_7 and K^*_8 are less than one. The power minimization for the FR-VL backhaul system in the two-tier case encountered a fundamental limitation due to the inadequate capacity of the bottleneck backhaul link even when using a directive light beam. This challenge is addressed by using the IR band for backhauling.

2) IR Backhaul and Power-Bandwidth Tradeoff: Different from the FR-VL case, for the IR case, the underlying optimization problem for a two-tier network can be solved. The reason for this is the downlink SINR $\gamma^{\rm IR}_1$ does not depend on the power ratios unlike in the FR-VL case. Therefore, $\gamma^{\rm IR}_1$ is decoupled from $\gamma_{{\rm b}_1}$, and this causes the boundary surface defined by (39), i.e., $K_{1,\min}(K_7, K_8)$, to be a flat plane. By considering the other two planes defined by (40) and (41), i.e., $K_{7,\min}(K_1, K_8)$ and $K_{8,\min}(K_1, K_7)$, the solution is at the vertex of the admissible region, which is the intersection of the three planes. Based on (39), $K_{1,\min}$ is derived in (52), shown at the bottom of the next page. Based on the other two constraints in (40) and (41), and by using (52), the minimum power ratios $K_{7,\min}$ and $K_{8,\min}$ are derived in (53) and (54), shown at the bottom of the next page, respectively. Among the three power ratios of $K_{1,\min}$, $K_{7,\min}$ and $K_{8,\min}$, $K_{1,\min}$ introduces the most challenging tradeoff as it represents the bottleneck backhaul link.

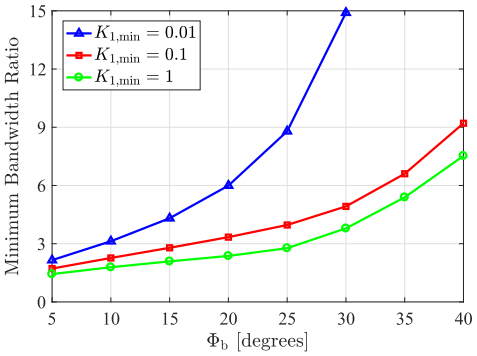

Fig. 11. The minimum bandwidth ratio $\frac{B_{\rm b}}{B_{\rm a}}\big|_{\min}$ against $\Phi_{\rm b}$ for the two-tier network with IR backhaul for different values of $K_{1,\min}$.

Fig. 10 demonstrates the tradeoff between $K_{1,\min}$ and $\frac{B_{\rm b}}{B_{\rm a}}$ for the same set of values for $\Phi_{\rm b}$ as used in Fig. 6. Compared with Fig. 6, the tradeoff curves are shifted to the right. In particular, so as to achieve $K_{1,\min} < 1$, a bandwidth ratio of $\frac{B_{\rm b}}{B_{\rm a}} > 1$ is required even in the case where $\Phi_{\rm b}$ is as small as $5°$. As a design guideline, it is useful to investigate how much bandwidth is needed for the IR backhaul system to ensure a certain minimum power level for the bottleneck backhaul link. This can be acquired using Fig. 10. For instance, to allow the power ratio of the bottleneck backhaul link to be equal to $K_{1,\min} = 0.01$ for $\Phi_{\rm b} = 5°$, a bandwidth ratio no less than $\frac{B_{\rm b}}{B_{\rm a}} = 2.1$ is needed. The minimum bandwidth ratio denoted by $\frac{B_{\rm b}}{B_{\rm a}}\big|_{\min}$ is formally presented in Fig. 11 as a function of $\Phi_{\rm b}$ for different values of $K_{1,\min}$. It can be observed that $\frac{B_{\rm b}}{B_{\rm a}}\big|_{\min}$ is rising with increase in $\Phi_{\rm b}$. The case of $K_{1,\min} = 1$ gives the lower bound for the minimum bandwidth ratio. For $\Phi_{\rm b} = 20°$, $\frac{B_{\rm b}}{B_{\rm a}}\big|_{\min} = 6, 3.3, 2.4$ for $K_{1,\min} = 0.01, 0.1, 1$.

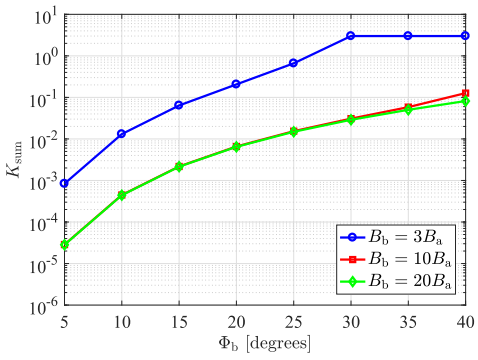

Fig. 12. Optimal sum power ratio $K_{\rm sum} = K_1^* + K_7^* + K_8^*$ for the two-tier network with IR backhaul versus $\Phi_{\rm b}$ for different values of $B_{\rm b}$.

Fig. 12 presents the optimal sum power ratio defined as $K_{\rm sum} = K_1^* + K_7^* + K_8^*$ against $\Phi_{\rm b}$ for different values of $B_{\rm b}$, where $K_j^* = \min[K_{j,\min}, 1]$ for $j = 1, 7, 8$. Note that the maximum value of $K_{\rm sum}$ is exactly equal to 3, which can be seen in the case of $B_{\rm b} = 3B_{\rm a}$ in Fig. 12. It can be observed that by further increasing the bandwidth after $B_{\rm b} = 10B_{\rm a}$, there is a negligible change in $K_{\rm sum}$. This can be explained as the values of K_j^* are effectively flattened for $B_{\rm b} \geq 10B_{\rm a}$.

Next, simulation results are presented for the overall average sum rate performance of one-tier and two-tier optical attocell networks using FR-VL, IB-VL and IR backhaul systems based on the sum rate analysis and the backhaul power optimization presented in Sections IV and V. In addition, a UB network is considered as the baseline scenario in which every single BS is individually connected to the core network using a high capacity wired backhaul link. Simulations are conducted based on Monte Carlo averaging over a large number of random realizations for the distribution of UEs in the network, using the parameters given in Table II. To make a fair comparison between a one-tier and a two-tier network, the average UE density (i.e., the average number of UEs per cell) is fixed, by considering $M = 15$ and $M = 40$ for one-tier and two-tier cases, respectively. For FR-VL and IR backhaul systems, both cases including with and without power control are studied using various combinations of the power ratios to exemplify the effect of power control on the network performance. Note that the optimization objective is the sum power of the backhaul system and therefore it does not necessarily maximize the sum rate performance. However, this may happen in some cases as an extra benefit.

C. Average Sum Rate Performance

1) One-Tier Network: Fig. 13 demonstrates the average performance of the one-tier optical attocell network. First, the focus is on FR-VL and IB-VL backhaul systems. It is observed that general trends for both FR-VL and IB-VL systems are monotonically decreasing with respect to $\Phi_{\rm b}$. For FR-VL, the reason is that by widening the light beam, the backhaul interference on the downlink is increased and at the same time, the SINR of the backhaul links is reduced. For IB-VL, on the other hand, an increase in $\Phi_{\rm b}$ causes the sub-band ratio δ to decrease because of the lower SINR of

$$K_{1,\min} = \left[\prod_{i=7,8} \left[\left(1+\gamma_i^{\rm IR}\right)^{\frac{B_{\rm a}}{B_{\rm b}}} - 1 \right]^{-1} + \left(\frac{1}{4}\right)^{\ell+1} \left[\left(1+\gamma_8^{\rm IR}\right)^{\frac{B_{\rm a}}{B_{\rm b}}} - 1 \right]^{-1} - 5\left(\frac{1}{4}\right)^{\ell+1} \left[\frac{3}{4}\left(\frac{1}{4}\right)^{\ell} + \frac{1}{9}\left(\frac{3}{4}\right)^{\ell+1} + \frac{25}{49}\left(\frac{1}{28}\right)^{\ell+1} \right] \right] \gamma_{\rm b}^{-1}\Delta^{-1}, \tag{52}$$

$$K_{7,\min} = \left[\left(\left[\prod_{i=1,7,8} \left(1+\gamma_i^{\rm IR}\right)^{\frac{B_{\rm a}}{B_{\rm b}}} - 1 \right]^{-1} - 2\left(\frac{1}{4}\right)^{\ell} \right) \left(\left[\left(1+\gamma_8^{\rm IR}\right)^{\frac{B_{\rm a}}{B_{\rm b}}} - 1 \right]^{-1} + 5\left(\frac{1}{4}\right)^{\ell+1} \right) + \frac{2}{9}\left(\frac{3}{4}\right)^{\ell+1} \left[\left(1+\gamma_8^{\rm IR}\right)^{\frac{B_{\rm a}}{B_{\rm b}}} - 1 \right]^{-1} \right] \gamma_{\rm b}^{-1}\Delta^{-1}, \tag{53}$$

$$K_{8,\min} = \left[\left(\left[\prod_{i=1,7,8} \left(1+\gamma_i^{\rm IR}\right)^{\frac{B_{\rm a}}{B_{\rm b}}} - 1 \right]^{-1} - 2\left(\frac{1}{4}\right)^{\ell} \right) \left(\left[\left(1+\gamma_7^{\rm IR}\right)^{\frac{B_{\rm a}}{B_{\rm b}}} - 1 \right]^{-1} + \left(\frac{1}{4}\right)^{\ell} + \frac{1}{9}\left(\frac{3}{4}\right)^{\ell+1} + \frac{25}{49}\left(\frac{1}{28}\right)^{\ell+1} \right) + \frac{2}{9}\left(\frac{3}{4}\right)^{\ell+1} \left[\frac{3}{4}\left(\frac{1}{4}\right)^{\ell} + \frac{1}{9}\left(\frac{3}{4}\right)^{\ell+1} + \frac{25}{49}\left(\frac{1}{28}\right)^{\ell+1} \right] \right] \gamma_{\rm b}^{-1}\Delta^{-1}, \tag{54}$$

$$\Delta = \left(\prod_{i=7,8} \left[\left(1+\gamma_i^{\rm IR}\right)^{\frac{B_{\rm a}}{B_{\rm b}}} - 1 \right]^{-1} - 5\left(\frac{1}{4}\right)^{\ell+1} \left[\left(\frac{1}{4}\right)^{\ell} + \frac{1}{9}\left(\frac{3}{4}\right)^{\ell+1} + \frac{25}{49}\left(\frac{1}{28}\right)^{\ell+1} \right] \right) \times \left(\left[\prod_{i=1,7,8} \left(1+\gamma_i^{\rm IR}\right)^{\frac{B_{\rm a}}{B_{\rm b}}} - 1 \right]^{-1} - 2\left(\frac{1}{4}\right)^{\ell} \right) - \frac{2}{9}\left(\frac{3}{16}\right)^{\ell+1} \left[\left(1+\gamma_8^{\rm IR}\right)^{\frac{B_{\rm a}}{B_{\rm b}}} - 1 \right]^{-1}. \tag{55}$$

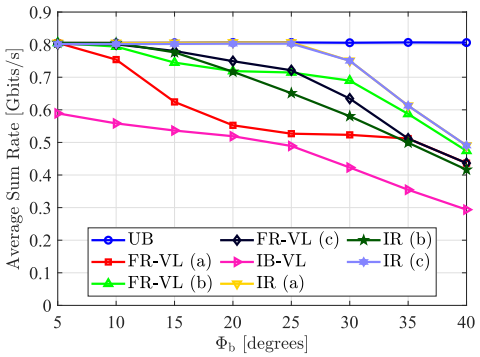

Fig. 13. Average sum rate performance of the one-tier optical attocell network using FR-VL, IB-VL and IR backhaul systems as a function of Φ_b. For FR-VL (a) $K_1 = 1$; (b) $K_1 = 0.1$; (c) $K_1 = K_1^*$. For IR (a) $K_1 = 1$; (b) $K_1 = 0.01$; and (c) $K_1 = K_1^*$. For IR backhaul, $B_b = B_a$.

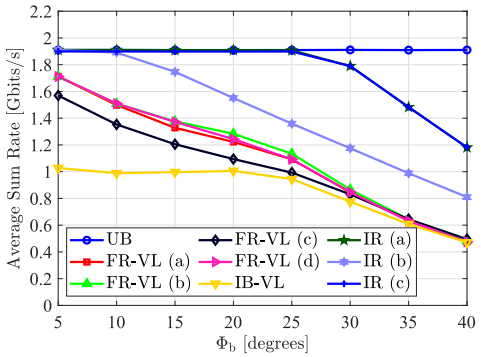

Fig. 14. Average sum rate performance of the two-tier optical attocell network using FR-VL, IB-VL and IR backhaul systems as a function of Φ_b. For FR-VL case (a) $K_1 = K_7 = K_8 = 1$; (b) $K_1 = 1$, and $K_7 = K_8 = 0.1$; (c) $K_1 = K_7 = K_8 = 0.1$; and (d) $K_1 = 1$, and $(K_7, K_8) = (K_7^*, K_8^*)$. For IR case (a) $K_1 = K_7 = K_8 = 1$; (b) $K_1 = K_7 = K_8 = 0.01$; and (c) $K_j = K_j^*$ for $j = 1, 7, 8$. For IR backhaul, $B_b = 3B_a$.

the backhaul links. This has suppressed the overall performance of the first tier since it is directly proportional to δ according to (21). Furthermore, it is observed that FR-VL outperforms IB-VL throughout the entire range of Φ_b regardless of the value of K_1, in spite of the fact that FR-VL causes a higher interference. This is achieved as a result of a better utilization of the bandwidth. For $\Phi_b = 5°$, the performance of the FR-VL network reaches the upper limit of 806 Mbits/s offered by the UB network. This is attributed in part to a substantial reduction in the backhaul interference for small values of Φ_b, in line with Theorem 1.

Fig. 13 shows the performance of FR-VL and IR backhaul systems including power control. For FR-VL, by comparing the cases (a) and (b), it can be observed that the performance is significantly improved when the backhaul power is reduced by a factor of 10. The improvement is up to 188 Mbits/s for moderate values of Φ_b. This is primarily because by reducing the backhaul power, the adverse effect of backhaul interference is alleviated. In comparison to the case (b), the FR-VL case (c) that uses the optimal power ratio achieves a better performance until $\Phi_b = 25°$, at which $K_1^* = 0.1$. Note that $K_{1,\min} > 0.1$ for $\Phi_b > 25°$; see Fig. 5. In the case of IR, the bandwidth ratio is equal to one. Fig. 13 shows that IR backhauling performs near the UB limit especially for the cases (a) and (c) which correspond to $K_1 = 1$ and $K_1 = K_1^*$, for small to moderate values of Φ_b. This indicates that the power efficiency of the IR backhaul system can be remarkably improved by using the minimum power control coefficients given by (52), (53) and (54), depending on the value of Φ_b. This gain is attained while preserving the average sum rate performance identical to the case when using the full power for the IR backhaul system. In the IR case (b), where the power of the backhaul system is reduced by a factor of 100, no loss in performance is observed for $\Phi_b \leq 10°$, and the extent of performance loss is still sustainable for moderate to large values of Φ_b.

2) Two-Tier Network: Fig. 14 demonstrates the average sum rate performance of the two-tier optical attocell network. The UB network gives the constant upper limit of 1.91 Gbits/s for the network performance. In addition, the IB-VL network globally has the worst performance. Among the FR-VL cases, the case (c) using $K_1 = K_7 = K_8 = 0.1$ has the lowest performance. The other three cases take the same value of $K_1 = 1$. The low performance in the case (c) is due to a ten times reduction in the power of the bottleneck backhaul link, which directly affects the sum rate performance of the network. The performance of the case (d) using the optimal power ratios of (K_7^*, K_8^*) is bounded from below by that of the case (a) and from above by that of the case (b), where (a) and (b) correspond to $K_7 = K_8 = 1$ and $K_7 = K_8 = 0.1$. The cases (a), (b) and (d) perform slightly better than the case (c). Furthermore, in the case of IR, a bandwidth ratio of three is used. It is evident that the performance of the case (c) using the minimized power ratios perfectly matches with the case (a) that uses the full power for the IR backhaul system, though using the minimum sum power. Likewise, the power of all the backhaul links can be reduced according to the value of Φ_b without degrading the network performance. This is achieved by choosing a sufficient bandwidth for the IR backhaul system, i.e., $B_b = 3B_a$.

VI. Conclusions

In this paper, a novel wireless backhaul solution is proposed for indoor optical attocell networks by which the BSs are connected to the gateway via multi-hop wireless optical links. For both FR-VL and IB-VL backhaul systems, the downlink performance depends upon the directivity of the light beam in the backhaul links. A better performance is achieved for a smaller value of Φ_b. In addition, FR-VL gives a significantly better performance than IB-VL, and it enables the network to attain the performance of a benchmark UB network particularly for a one-tier deployment. Following a power optimization for the backhaul system, the results suggest that FR-VL is not an appropriate option for network deployments of more than one tier. Alternatively, the migration of wireless optical

backhauling to the IR band is proposed. In this case, after establishing a power-bandwidth tradeoff analysis for a two-tier network, IR backhauling shows the potential that it does not only outperform FR-VL backhauling but its performance is closely matched to that of the UB network in terms of the network sum rate, when using a properly designed divergence angle for the light beam in the backhaul links. For the IR backhaul system, given a modulation bandwidth of only three times that of the downlink VLC system, the backhaul transmission power can be made 100 times lower than the full power operation without influencing the network performance. This is a remarkable gain for power efficiency. Future directions include but are not limited to: 1) an investigation into the effect of imperfect alignment for an aimed wireless optical backhaul link on the overall network performance; 2) a study of the scaling laws of the presented power-bandwidth tradeoff for the design of wireless optical backhaul systems applied to multi-tier networks; and 3) an extension to other network deployment models.

Appendix A
Proof of Theorem 1

The analysis is performed for the limit $\ell \to \infty$ which is equivalent to $\Phi_{\rm b} \to 0$. Based on (13) and (28), a unified expression is obtained for the backhaul interference effect as follows:

$$\mathcal{F}_{\rm BI}(z_u) = \frac{(\ell+1)^2}{(m+1)^2 h^{2m}} \sum_{j\in\mathcal{Q}_i} \frac{K_j r_s^{2\ell}(z_u)\cos^{2\ell}\left(\theta_s - \Theta_{{\rm b}_j}\right)}{\left(r_s^2(z_u)+h^2\right)^{\ell+3}}. \tag{56}$$

Rearranging (56), and taking the limit $\ell \to \infty$, the asymptotic backhaul interference effect can be evaluated as:

$$\lim_{\ell\to\infty} \mathcal{F}_{\rm BI}(z_u) = \frac{1}{(m+1)^2 h^{2m}\left(r_s^2+h^2\right)^3} \times \lim_{\ell\to\infty} \sum_{j\in\mathcal{Q}_i} K_j(\ell+1)^2 \left[\frac{r_s^2\cos^2\left(\theta_s-\Theta_{{\rm b}_j}\right)}{r_s^2+h^2}\right]^{\ell}. \tag{57}$$

In (57), the fraction inside the bracket is bounded as follows:

$$0 \le \frac{r_s^2\cos^2\left(\theta_s-\Theta_{{\rm b}_j}\right)}{r_s^2+h^2} < 1. \tag{58}$$

Using (58), the limit of the two product terms that depend on ℓ under the summation in (57) can be calculated as:

$$\lim_{\ell\to\infty} (\ell+1)^2 \left[\frac{r_s^2\cos^2\left(\theta_s-\Theta_{{\rm b}_j}\right)}{r_s^2+h^2}\right]^{\ell} = 0, \tag{59}$$

because, as $\ell \to \infty$, the term $[\ ]^{\ell}$ decays much faster than the term $(\ell+1)^2$ grows. Considering that K_j is a finite value under the summation in (57), substituting (59) into (57) yields:

$$\lim_{\ell\to\infty} \mathcal{F}_{\rm BI}(z_u) = 0, \quad \forall u, \tag{60}$$

hence the proof is complete.

Appendix B
Monotonicity of $g_1(K_1, K_7, K_8)$ in K_1

By taking the partial derivative of g_1 in (43) with respect to K_1, one can verify that:

$$\frac{\partial g_1}{\partial K_1} = \frac{\frac{\partial \gamma_{{\rm b}_1}}{\partial K_1}}{1+\gamma_{{\rm b}_1}} - \sum_{i=1,7,8} \frac{\frac{\partial \gamma_i^{\text{FR-VL}}}{\partial K_1}}{1+\gamma_i^{\text{FR-VL}}} > 0, \tag{61}$$

because:

$$\frac{\partial \gamma_{{\rm b}_1}}{\partial K_1} = \frac{\left(\frac{1}{4}\right)^{\ell+1} K_7 + \frac{1}{\gamma_{\rm b}}}{\left[2\left(\frac{1}{4}\right)^{\ell} K_1 + \left(\frac{1}{4}\right)^{\ell+1} K_7 + \frac{1}{\gamma_{\rm b}}\right]^2} > 0, \tag{62}$$

and the partial derivative of $\gamma_i^{\text{FR-VL}}$ with respect to K_1 is always negative as in (63), shown at the bottom of the page. To derive (62) and (63), respectively, (25) and (9) are used.

Appendix C
A Remark on the Constraint in (44)

For sufficiently small values of $\Phi_{\rm b}$, according to Theorem 1, the backhaul interference effect tends to zero and $\mathcal{F}_{\rm BI}(z_i) \approx 0$, $\forall i$, taking into account the last constraint of P2, $0 < K_j \le 1$ for $j = 1, 7, 8$. In such a case, $\gamma_i^{\text{FR-VL}}$ in (9) can be tightly approximated by $\gamma_i^{\text{FR-VL}} \approx \frac{\mathcal{S}(z_i)}{\mathcal{F}_{\rm ICI}(z_i)+\Omega}$, which is independent of K_1, K_7 and K_8. In addition, provided that the optical power is concentrated within the backhaul links, the cross-coupling interference among them is insignificant. Thus, $\gamma_{{\rm b}_1}$ in (25) reduces to $\gamma_{{\rm b}_1} \approx K_1\gamma_{\rm b}$ and, by using (43), (44) simplifies to:

$$K_1 \ge \frac{\prod_{i=1,7,8}\left(1+\gamma_i^{\text{FR-VL}}\right)-1}{\gamma_{\rm b}} \ge \frac{\prod_{i=1,7,8}\gamma_i^{\text{FR-VL}}}{\gamma_{\rm b}}. \tag{64}$$

The second inequality is due to $\gamma_i^{\text{FR-VL}} \gg 1$, which typically holds at the center of an attocell and the optimization is based on the downlink SINR at the center of attocells. The RHS of (64) is an asymptotic bound for $K_{1,\min}(K_7, K_8)$ in (44).

Appendix D
Minimum Element of the Feasible Set for P3

Let $K_7 = K_{7,\min}(K_8)$ and $K_8 = K_{8,\min}(K_7)$ be replaced by $x = g(y)$ and $y = f(x)$, respectively, and let (x_0, y_0) be their intersection point, to simplify notation. The feasible set can be expressed as:

$$\mathcal{D} = \left\{(x,y) \in \mathbb{R}_+^2 \middle| x \ge g(y), y \ge f(x)\right\}. \tag{65}$$

As a geometric description, to say that (x_0, y_0) is the minimum element of $\mathcal{D}$ means that all other points of $\mathcal{D}$ lie to the right and above the point (x_0, y_0). More precisely, the objective is to prove that $(x_0, y_0) \preceq (x, y)$, $\forall (x, y) \in \mathcal{D}$, where $\preceq$ is induced by the positive quadrant $\mathbb{R}_+^2$ [39]. To this end, since f and g in (65) are increasing with respect to their arguments,

$$\frac{\partial \gamma_i^{\text{FR-VL}}}{\partial K_1} = -\frac{\mathcal{F}_1(z_i;\mathcal{Q}_i)\mathcal{S}(z_i)}{\left[K_1\mathcal{F}_1(z_i;\mathcal{Q}_i) + K_7\mathcal{F}_2(z_i;\mathcal{O}_i) + K_8\mathcal{F}_2(z_i;\mathcal{E}_i) + \mathcal{F}_{\rm ICI}(z_i) + \Omega\right]^2} < 0, \tag{63}$$

by jointly expanding the conditions $x \geq g(y)$ and $y \geq f(x)$, one arrives at:

$$\begin{cases} x \geq g(y) \geq g(y_0) = x_0, \\ y \geq f(x) \geq f(x_0) = y_0, \end{cases} \tag{66}$$

which is what was to be shown.

REFERENCES

[1] M. Figueiredo, L. N. Alves, and C. Ribeiro, "Lighting the wireless world: The promise and challenges of visible light communication," *IEEE Consum. Electron. Mag.*, vol. 6, no. 4, pp. 28–37, Oct. 2017.

[2] "Cisco visual networking index: Global mobile data traffic forecast update, 2016–2021," Cisco, San Jose, CA, USA, White Paper 1454457600805266, Mar. 2017. [Online]. Available: https://www.cisco.com/c/en/us/solutions/collateral/service-provider/visual-networking-index-vni/mobile-white-paper-c11-520862.html?dtid=osscdc000283

[3] H. Burchardt, N. Serafimovski, D. Tsonev, S. Videv, and H. Haas, "VLC: Beyond point-to-point communication," *IEEE Commun. Mag.*, vol. 52, no. 7, pp. 98–105, Jul. 2014.

[4] H. Haas, L. Yin, Y. Wang, and C. Chen, "What is LiFi?" *J. Lightw. Technol.*, vol. 34, no. 6, pp. 1533–1544, Mar. 15, 2016.

[5] C.-X. Wang *et al.*, "Cellular architecture and key technologies for 5G wireless communication networks," *IEEE Commun. Mag.*, vol. 52, no. 2, pp. 122–130, Feb. 2014.

[6] V. Chandrasekhar, J. G. Andrews, and A. Gatherer, "Femtocell networks: A survey," *IEEE Commun. Mag.*, vol. 46, no. 9, pp. 59–67, Sep. 2008.

[7] C. Chen, D. A. Basnayaka, and H. Haas, "Downlink performance of optical attocell networks," *J. Lightw. Technol.*, vol. 34, no. 1, pp. 137–156, Jan. 1, 2016.

[8] I. Stefan, H. Burchardt, and H. Haas, "Area spectral efficiency performance comparison between VLC and RF femtocell networks," in *Proc. IEEE Int. Conf. Commun.*, Jun. 2013, pp. 3825–3829.

[9] D. J. F. Barros, S. K. Wilson, and J. M. Kahn, "Comparison of orthogonal frequency-division multiplexing and pulse-amplitude modulation in indoor optical wireless links," *IEEE Trans. Commun.*, vol. 60, no. 1, pp. 153–163, Jan. 2012.

[10] D. Tsonev, S. Videv, and H. Haas, "Unlocking spectral efficiency in intensity modulation and direct detection systems," *IEEE J. Sel. Areas Commun.*, vol. 33, no. 9, pp. 1758–1770, Sep. 2015.

[11] C. Chen, S. Videv, D. Tsonev, and H. Haas, "Fractional frequency reuse in DCO-OFDM-based optical attocell networks," *J. Lightw. Technol.*, vol. 33, no. 19, pp. 3986–4000, Oct. 1, 2015.

[12] S. Chia, M. Gasparroni, and P. Brick, "The next challenge for cellular networks: Backhaul," *IEEE Microw. Mag.*, vol. 10, no. 5, pp. 54–66, Aug. 2009.

[13] K. Chandra, R. V. Prasad, and I. Niemegeers, "An architectural framework for 5G indoor communications," in *Proc. Int. Wireless Commun. Mobile Comput. Conf. (IWCMC)*, Aug. 2015, pp. 1144–1149.

[14] X. Li, F. Jin, R. Zhang, J. Wang, Z. Xu, and L. Hanzo, "Users first: User-centric cluster formation for interference-mitigation in visible-light networks," *IEEE Trans. Wireless Commun.*, vol. 15, no. 1, pp. 39–53, Jan. 2016.

[15] Z. Huang and Y. Ji, "Efficient user access and lamp selection in LED-based visible light communication network," *Chin. Opt. Lett.*, vol. 10, no. 5, p. 050602, May 2012.

[16] H. Ma, L. Lampe, and S. Hranilovic, "Coordinated broadcasting for multiuser indoor visible light communication systems," *IEEE Trans. Commun.*, vol. 63, no. 9, pp. 3313–3324, Sep. 2015.

[17] T. Komine and M. Nakagawa, "Integrated system of white LED visible-light communication and power-line communication," *IEEE Trans. Consum. Electron.*, vol. 49, no. 1, pp. 71–79, Feb. 2003.

[18] J. Song, W. Ding, F. Yang, H. Yang, B. Yu, and H. Zhang, "An indoor broadband broadcasting system based on PLC and VLC," *IEEE Trans. Broadcast.*, vol. 61, no. 2, pp. 299–308, Jun. 2015.

[19] H. Ma, L. Lampe, and S. Hranilovic, "Hybrid visible light and power line communication for indoor multiuser downlink," *IEEE/OSA J. Opt. Commun. Netw.*, vol. 9, no. 8, pp. 635–647, Aug. 2017.

[20] P. Mark, "Ethernet over light," M.S. thesis, Dept. Elect. Comput. Eng., Univ. British Columbia, Vancouver, BC, Canada, Dec. 2014.

[21] F. Delgado, I. Quintana, J. Rufo, J. A. Rabadan, C. Quintana, and R. Perez-Jimenez, "Design and implementation of an Ethernet-VLC interface for broadcast transmissions," *IEEE Commun. Lett.*, vol. 14, no. 12, pp. 1089–1091, Dec. 2010.

[22] Y. Wang, N. Chi, Y. Wang, L. Tao, and J. Shi, "Network architecture of a high-speed visible light communication local area network," *IEEE Photon. Technol. Lett.*, vol. 27, no. 2, pp. 197–200, Jan. 15, 2015.

[23] C.-W. Chow, C.-H. Yeh, Y. Liu, C.-W. Hsu, and J.-Y. Sung, "Network architecture of bidirectional visible light communication and passive optical network," *IEEE Photon. J.*, vol. 8, no. 3, pp. 1–7, Jun. 2016.

[24] H. Kazemi, M. Safari, and H. Haas, "A wireless backhaul solution using visible light communication for indoor Li-Fi attocell networks," in *Proc. IEEE Int. Conf. Commun. (ICC)*, May 2017, pp. 1–7.

[25] H. Kazemi and H. Haas, "Downlink cooperation with fractional frequency reuse in DCO-OFDMA optical attocell networks," in *Proc. IEEE Int. Conf. Commun. (ICC)*, May 2016, pp. 1–6.

[26] H. Kazemi, M. Safari, and H. Haas, "Spectral efficient cooperative downlink transmission schemes for DCO-OFDM-based optical attocell networks," in *Proc. IEEE 84th Veh. Technol. Conf. (VTC Fall)*, Sep. 2016, pp. 1–6.

[27] J. M. Kahn and J. R. Barry, "Wireless infrared communications," *Proc. IEEE*, vol. 85, no. 2, pp. 265–298, Feb. 1997.

[28] S. Shao *et al.*, "Design and analysis of a visible-light-communication enhanced WiFi system," *IEEE/OSA J. Opt. Commun. Netw.*, vol. 7, no. 10, pp. 960–973, Oct. 2015.

[29] D. Tsonev *et al.*, "Brien, "A 3-Gb/s single-LED OFDM-based wireless VLC link using a gallium nitride μLED," *IEEE Photon. Technol. Lett.*, vol. 26, no. 7, pp. 637–640, Apr. 1, 2014.

[30] *Light Lighting—Lighting Work Places. Part I: Indoor Work Places*, document BS EN 12464-1, British Standards Institution, 2011.

[31] J. N. Laneman, D. N. C. Tse, and G. W. Wornell, "Cooperative diversity in wireless networks: Efficient protocols and outage behavior," *IEEE Trans. Inf. Theory*, vol. 50, no. 12, pp. 3062–3080, Dec. 2004.

[32] O. Narmanlioglu, R. C. Kizilirmak, F. Miramirkhani, and M. Uysal, "Cooperative visible light communications with full-duplex relaying," *IEEE Photon. J.*, vol. 9, no. 3, pp. 1–11, Jun. 2017.

[33] C. H. Chen *et al.*, "GHz bandwidth GaAs light-emitting diodes," *Appl. Phys. Lett.*, vol. 74, no. 21, pp. 3140–3142, May 1999.

[34] E. F. Schubert, *Light-Emitting Diodes*, 2nd ed. Cambridge, U.K.: Cambridge Univ. Press, 2006.

[35] S. Dimitrov, S. Sinanovic, and H. Haas, "Clipping noise in OFDM-based optical wireless communication systems," *IEEE Trans. Commun.*, vol. 60, no. 4, pp. 1072–1081, Apr. 2012.

[36] O. Oyman and S. Sandhu, "A Shannon-theoretic perspective on fading multihop networks," in *Proc. 40th Annu. Conf. Inf. Sci. Syst. (CISS)*, Mar. 2006, pp. 525–530.

[37] S. Lu, V. Bharghavan, and R. Srikant, "Fair scheduling in wireless packet networks," *IEEE/ACM Trans. Netw.*, vol. 7, no. 4, pp. 473–489, Aug. 1999.

[38] T. M. Cover and A. A. El Gamal, "Capacity theorems for the relay channel," *IEEE Trans. Inf. Theory*, vol. 25, no. 5, pp. 572–584, Sep. 1979.

[39] S. Boyd and L. Vandenberghe, *Convex Optimization*. Cambridge, U.K.: Cambridge Univ. Press, Mar. 2004.

Hossein Kazemi (S'16) received the M.Sc. degree in electrical engineering (with a specialty in microelectronic circuits) from the Sharif University of Technology, Tehran, Iran, in 2011, and the M.Sc. degree (Hons.) in electrical engineering, with a focus in communication systems, from Özyeğin University, Istanbul, Turkey, in 2014. He is currently pursuing the Ph.D. degree in electrical engineering with the Institute for Digital Communications, University of Edinburgh, Edinburgh, U.K. His main research interests include wireless optical communications and networks.

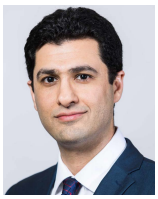

Majid Safari (S'08–M'11) received his Ph.D. degree in Electrical and Computer Engineering from the University of Waterloo, Canada in 2011. He also received his B.Sc. degree in Electrical and Computer Engineering from the University of Tehran, Iran, in 2003, M.Sc. degree in Electrical Engineering from Sharif University of Technology, Iran, in 2005. He is currently an assistant professor in the Institute for Digital Communications at the University of Edinburgh. Before joining Edinburgh in 2013, he held postdoctoral fellowship at McMaster University, Canada. Dr. Safari is currently an associate editor of IEEE COMMUNICATION LETTERS. His main research interest is the application of information theory and signal processing in optical communications including fiber-optic communication, free-space optical communication, visible light communication, and quantum communication.

Harald Haas (S'98–A'00–M'03–SM'16–F'17) received the Ph.D. degree from the University of Edinburgh in 2001. He currently holds the Chair of the Mobile Communications at the University of Edinburgh. He is the Initiator, Co-Founder, and the Chief Scientific Officer of pureLiFi Ltd., and the Director of the LiFi Research and Development Center, University of Edinburgh. He has authored 400 conference and journal papers, including a paper in *Science* and has co-authored the book *Principles of LED Light Communications Towards Networked Li-Fi* (Cambridge University Press, 2015). His main research interests are in optical wireless communications, hybrid optical wireless and RF communications, spatial modulation, and interference coordination in wireless networks. He first introduced and coined spatial modulation and LiFi. LiFi was listed among the 50 best inventions in *TIME* Magazine in 2011. He was an invited speaker at TED Global 2011, and his talk on "Wireless Data from Every Light Bulb" has been watched online over 2.4 million times. He gave a second TED Global lecture on the use of solar cells as LiFi data detectors and energy harvesters in 2015. This has been viewed online over 1.8 million times. He was elected as a fellow of the Royal Society of Edinburgh in 2017. In 2012 and 2017, he was a recipient of the prestigious Established Career Fellowship from the Engineering and Physical Sciences Research Council (EPSRC) within Information and Communications Technology in U.K. In 2014, he was selected by EPSRC as one of the ten Recognizing Inspirational Scientists and Engineers (RISE) Leaders in the U.K. He was a co-recipient of the EURASIP Best Paper Award of the *Journal on Wireless Communications and Networking* in 2015, and a co-recipient of the Jack Neubauer Memorial Award of the IEEE Vehicular Technology Society. In 2016, he received the Outstanding Achievement Award from the International Solid State Lighting Alliance. He was a co-recipient of the Best Paper Awards at the VTC-Fall 2013, VTC-Spring 2015, ICC 2016, and ICC 2017. He is an Editor of the IEEE TRANSACTIONS ON COMMUNICATIONS and the IEEE JOURNAL OF LIGHTWAVE TECHNOLOGIES.

Bibliography

[1] "Cree extends groundbreaking OSQ Series to deliver 58 percent efficacy increase and new higher output luminaire," Cree Inc. Technical Report, 24 May 2016.

[2] "Energy savings forecast of solid-state lighting in general illumination applications." U.S. Department of Energy. Technical Report, Aug. 2014.

[3] "Cisco Visual Networking Index: Forecast and Trends, 2017–2022," Cisco White Paper, Nov. 2018.

[4] M. Figueiredo, L. N. Alves, and C. Ribeiro, "Lighting the Wireless World: The Promise and Challenges of Visible Light Communication," *IEEE Consum. Electron. Mag.*, vol. 6, no. 4, pp. 28–37, Oct. 2017.

[5] A. G. Bell, "Selenium and the Photophone," *Nature*, vol. 22, no. 569, p. 500503, Sep. 1880.

[6] "IEEE Standard for Local and Metropolitan Area Networks–Part 15.7: Short-Range Wireless Optical Communication Using Visible Light," *IEEE Std 802.15.7-2011*, pp. 1–309, Sep. 2011.

[7] G. Cossu, A. M. Khalid, P. Choudhury, R. Corsini, and E. Ciaramella, "3.4 Gbit/s visible optical wireless transmission based on RGB LED," *Opt. Express*, vol. 20, no. 26, pp. B501–B506, Dec 2012.

[8] D. Tsonev, H. Chun, S. Rajbhandari, J. J. D. McKendry, S. Videv, E. Gu, M. Haji, S. Watson, A. E. Kelly, G. Faulkner, M. D. Dawson, H. Haas, and D. O'Brien, "A 3-Gb/s Single-LED OFDM-Based Wireless VLC Link Using a Gallium Nitride μLED," *IEEE Photon. Technol. Lett.*, vol. 26, no. 7, pp. 637–640, Apr. 2014.

[9] H. Burchardt, N. Serafimovski, D. Tsonev, S. Videv, and H. Haas, "VLC: Beyond Point-to-Point Communication," *IEEE Commun. Mag.*, vol. 52, no. 7, pp. 98–105, Jul. 2014.

[10] H. Haas, L. Yin, Y. Wang, and C. Chen, "What is LiFi?" *IEEE/OSA J. Lightw. Technol.*, vol. 34, no. 6, pp. 1533–1544, Mar. 2016.

[11] C. X. Wang, F. Haider, X. Gao, X. H. You, Y. Yang, D. Yuan, H. M. Aggoune, H. Haas, S. Fletcher, and E. Hepsaydir, "Cellular Architecture and Key Technologies for 5G Wireless Communication Networks," *IEEE Commun. Mag.*, vol. 52, no. 2, pp. 122–130, Feb. 2014.

[12] V. Chandrasekhar, J. G. Andrews, and A. Gatherer, "Femtocell Networks: A Survey," *IEEE Commun. Mag.*, vol. 46, no. 9, pp. 59–67, Sep. 2008.

[13] M. Ayyash, H. Elgala, A. Khreishah, V. Jungnickel, T. Little, S. Shao, M. Rahaim, D. Schulz, J. Hilt, and R. Freund, "Coexistence of WiFi and LiFi Toward 5G: Concepts, Opportunities, and Challenges," *IEEE Commun. Mag.*, vol. 54, no. 2, pp. 64–71, Feb. 2016.

[14] A. Goldsmith, *Wireless Communications*. Cambridge University Press, 2005.

[15] M.-S. Alouini and A. J. Goldsmith, "Area Spectral Efficiency of Cellular Mobile Radio Systems," *IEEE Trans. Veh. Technol.*, vol. 48, no. 4, pp. 1047–1066, Jul. 1999.

[16] C. Chen, D. A. Basnayaka, and H. Haas, "Downlink Performance of Optical Attocell Networks," *IEEE/OSA J. Lightw. Technol.*, vol. 34, no. 1, pp. 137–156, Jan. 2016.

[17] I. Stefan, H. Burchardt, and H. Haas, "Area Spectral Efficiency Performance Comparison between VLC and RF Femtocell Networks," pp. 3825–3829, Jun. 2013.

[18] S. Chia, M. Gasparroni, and P. Brick, "The Next Challenge for Cellular Networks: Backhaul," *IEEE Microw. Mag.*, vol. 10, no. 5, pp. 54–66, Aug. 2009.

[19] X. Ge, H. Cheng, M. Guizani, and T. Han, "5G Wireless Backhaul Networks: Challenges and Research Advances," *IEEE Netw.*, vol. 28, no. 6, pp. 6–11, Nov. 2014.

[20] T. Koonen, "Fiber to the Home/Fiber to the Premises: What, Where, and When?" *Proc. IEEE*, vol. 94, no. 5, pp. 911–934, May 2006.

[21] C. Dehos, J. L. Gonzalez, A. D. Domenico, D. Ktnas, and L. Dussopt, "Millimeter-Wave Access and Backhauling: The Solution to the Exponential Data Traffic Increase in 5G Mobile Communications Systems?" *IEEE Commun. Mag.*, vol. 52, no. 9, pp. 88–95, Sep. 2014.

[22] K. Chandra, R. V. Prasad, and I. Niemegeers, "An Architectural Framework for 5G Indoor Communications," in *Proc. Int. Wireless Commun. Mobile Comput. Conf. (IWCMC)*, Aug. 2015, pp. 1144–1149.

[23] M. Timmers, M. Guenach, C. Nuzman, and J. Maes, "G.fast: Evolving the Copper Access Network," *IEEE Commun. Mag.*, vol. 51, no. 8, pp. 74–79, Aug. 2013.

[24] W. Ni, R. P. Liu, I. B. Collings, and X. Wang, "Indoor Cooperative Small Cells over Ethernet," *IEEE Commun. Mag.*, vol. 51, no. 9, pp. 100–107, Sep. 2013.

[25] A. Papaioannou and F. Pavlidou, "Evaluation of Power Line Communication Equipment in Home Networks," *IEEE Sensors J.*, vol. 3, no. 3, pp. 288–294, Sep. 2009.

[26] D. Astely, E. Dahlman, A. Furuskär, Y. Jading, M. Lindström, and S. Parkvall, "LTE: The Evolution of Mobile Broadband," *IEEE Commun. Mag.*, vol. 47, no. 4, pp. 44–51, Apr. 2009.

[27] U. Siddique, H. Tabassum, E. Hossain, and D. I. Kim, "Wireless Backhauling of 5G Small Cells: Challenges and Solution Approaches," *IEEE Wireless Commun.*, vol. 22, no. 5, pp. 22–31, Oct. 2015.

[28] D. Kedar and S. Arnon, "Urban Optical Wireless Communication Networks: The Main Challenges and Possible Solutions," *IEEE Commun. Mag.*, vol. 42, no. 5, pp. S2–S7, May 2004.

[29] I. I. Kim and E. J. Korevaar, "Availability of Free-Space Optics (FSO) and Hybrid FSO/RF Systems," *Proc. SPIE*, vol. 4530, Nov. 2001.

[30] H. Kazemi, M. Safari, and H. Haas, "A Wireless Backhaul Solution Using Visible Light Communication for Indoor Li-Fi Attocell Networks," in *Proc. IEEE Int. Conf. Commun. (ICC)*, May 2017, pp. 1–7.

[31] ——, "A Wireless Optical Backhaul Solution for Optical Attocell Networks," *IEEE Trans. Wireless Commun.*, vol. 18, no. 2, pp. 807–823, Feb. 2019.

[32] ——, "Bandwidth Scheduling and Power Control for Wireless Backhauling in Optical Attocell Networks," in *Proc. IEEE Global Commun. Conf. (GLOBECOM)*, Dec. 2018, pp. 1–7.

[33] H. Kazemi and H. Haas, "Downlink Cooperation with Fractional Frequency Reuse in DCO-OFDMA Optical Attocell Networks," in *Proc. IEEE Int. Conf. Commun. (ICC)*, May 2016.

[34] H. Kazemi, M. Safari, and H. Haas, "Spectral Efficient Cooperative Downlink Transmission Schemes for DCO-OFDM-Based Optical Attocell Networks," in *Proc. IEEE 84th Veh. Technol. Conf. (VTC Fall)*, Sep. 2016.

[35] T. Komine and M. Nakagawa, "Integrated System of White LED Visible-Light Communication and Power-Line Communication," *IEEE Trans. Consum. Electron.*, vol. 49, no. 1, pp. 71–79, Feb. 2003.

[36] T. Komine, S. Haruyama, and M. Nakagawa, "Performance Evaluation of Narrowband OFDM on Integrated System of Power Line Communication and Visible Light Wireless Communication," in *Proc. IEEE 1st Int. Symp. Wireless Pervasive Comput.*, Jan. 2006.

[37] J. Song, W. Ding, F. Yang, H. Yang, B. Yu, and H. Zhang, "An Indoor Broadband Broadcasting System Based on PLC and VLC," *IEEE Trans. Broadcast.*, vol. 61, no. 2, pp. 299–308, Jun. 2015.

[38] H. Ma, L. Lampe, and S. Hranilovic, "Hybrid Visible Light and Power Line Communication for Indoor Multiuser Downlink," *IEEE/OSA J. Opt. Commun. Netw.*, vol. 9, no. 8, pp. 635–647, Aug. 2017.

[39] P. Mark, "Ethernet over Light," Master's thesis, University of British Columbia, Dec. 2014.

[40] F. Delgado, I. Quintana, J. Rufo, J. A. Rabadan, C. Quintana, and R. Perez-Jimenez, "Design and Implementation of an Ethernet-VLC Interface for Broadcast Transmissions," *IEEE Commun. Lett.*, vol. 14, no. 12, pp. 1089–1091, Dec. 2010.

[41] Y. Wang, N. Chi, Y. Wang, L. Tao, and J. Shi, "Network Architecture of a High-Speed Visible Light Communication Local Area Network," *IEEE Photon. Technol. Lett.*, vol. 27, no. 2, pp. 197–200, Jan. 2015.

[42] C. W. Chow, C. H. Yeh, Y. Liu, C. W. Hsu, and J. Y. Sung, "Network Architecture of Bidirectional Visible Light Communication and Passive Optical Network," *IEEE Photon. J.*, vol. 8, no. 3, pp. 1–7, Jun. 2016.

[43] Y. Wang, J. Shi, C. Yang, Y. Wang, and N. Chi, "Integrated 10 Gb/s multilevel multiband passive optical network and 500 Mb/s indoor visible light communication system based on Nyquist single carrier frequency domain equalization modulation," *Opt. Lett.*, vol. 39, no. 9, pp. 2576–2579, May 2014.

[44] C. Chen, S. Videv, D. Tsonev, and H. Haas, "Fractional Frequency Reuse in DCO-OFDM-Based Optical Attocell Networks," *IEEE/OSA J. Lightw. Technol.*, vol. 33, no. 19, pp. 3986–4000, Oct. 2015.

[45] X. Li, F. Jin, R. Zhang, J. Wang, Z. Xu, and L. Hanzo, "Users First: User-Centric Cluster Formation for Interference-Mitigation in Visible-Light Networks," *IEEE Trans. Wireless Commun.*, vol. 15, no. 1, pp. 39–53, Jan. 2016.

[46] Z. Huang and Y. Ji, "Efficient user access and lamp selection in LED-based visible light communication network," *Chin. Opt. Lett.*, vol. 10, no. 5, p. 050602, May 2012.

[47] H. Ma, L. Lampe, and S. Hranilovic, "Coordinated Broadcasting for Multiuser Indoor Visible Light Communication Systems," *IEEE Trans. Commun.*, vol. 63, no. 9, 2015.

[48] R. Kizilirmak, O. Narmanlioglu, and M. Uysal, "Relay-Assisted OFDM-Based Visible Light Communications," *IEEE Trans. Commun.*, vol. 63, no. 10, pp. 3765–3778, Oct. 2015.

[49] M. Kashef, M. Abdallah, K. Qaraqe, H. Haas, and M. Uysal, "Coordinated Interference Management for Visible Light Communication Systems," *IEEE/OSA J. Opt. Commun. Netw.*, vol. 7, no. 11, pp. 1098–1108, Nov. 2015.

[50] C. Chen, D. Tsonev, and H. Haas, "Joint Transmission in Indoor Visible Light Communication Downlink Cellular Networks," in *Proc. IEEE Globecom Workshops*, Dec. 2013, pp. 1127–1132.

[51] C. Chen and H. Haas, "Performance Evaluation of Downlink Cooperative Multipoint Joint Transmission in LiFi Systems," in *Proc. IEEE Globecom Workshops (GC Wkshps)*, Dec 2017, pp. 1–6.

[52] J. Grubor, S. Randel, K. D. Langer, and J. W. Walewski, "Broadband Information Broadcasting Using LED-Based Interior Lighting," *IEEE/OSA J. Lightw. Technol.*, vol. 26, no. 24, pp. 3883–3892, Dec. 2008.

[53] S. Dimitrov and H. Haas, *Principles of LED Light Communication Towards Networked Li-Fi*. Cambridge University Press, Mar. 2015.

[54] J. M. Kahn and J. R. Barry, "Wireless Infrared Communications," *Proc. IEEE*, vol. 85, no. 2, pp. 265–298, Feb. 1997.

[55] S. Shao, A. Khreishah, M. Ayyash, M. B. Rahaim, H. Elgala, V. Jungnickel, D. Schulz, T. D. C. Little, J. Hilt, and R. Freund, "Design and Analysis of a Visible-Light-Communication Enhanced WiFi System," *IEEE/OSA J. Opt. Commun. Netw.*, vol. 7, no. 10, pp. 960–973, Oct. 2015.

[56] S. Shao, A. Khreishah, M. B. Rahaim, H. Elgala, M. Ayyash, T. D. C. Little, and J. Wu, "An Indoor Hybrid WiFi-VLC Internet Access System," in *Proc. IEEE 11th Int. Conf. Mobile Ad Hoc Sensor Syst.*, Oct. 2014, pp. 569–574.

[57] J. M. Kahn, W. J. Krause, and J. B. Carruthers, "Experimental Characterization of Non-Directed Indoor Infrared Channels," *IEEE Trans. Commun.*, vol. 43, no. 2/3/4, pp. 1613–1623, Feb. 1995.

[58] J. R. Barry, J. M. Kahn, W. J. Krause, E. A. Lee, and D. G. Messerschmitt, "Simulation of Multipath Impulse Response for Indoor Wireless Optical Channels," *IEEE J. Sel. Areas Commun.*, vol. 11, no. 3, pp. 367–379, Apr. 1993.

[59] J. B. Carruthers and J. M. Kahn, "Modeling of Nondirected Wireless Infrared Channels," *IEEE Trans. Commun.*, vol. 45, no. 10, pp. 1260–1268, Oct. 1997.

[60] V. Jungnickel, V. Pohl, S. Nonnig, and C. von Helmolt, "A Physical Model of the Wireless Infrared Communication Channel," *IEEE J. Sel. Areas Commun.*, vol. 20, no. 3, pp. 631–640, Apr. 2002.

[61] J. B. Carruthers and S. M. Carroll, "Statistical impulse response models for indoor optical wireless channels," *Int. J. Commun. Syst.*, vol. 18, no. 3, pp. 267–284, Mar. 2005.

[62] K. Lee, H. Park, and J. R. Barry, "Indoor Channel Characteristics for Visible Light Communications," *IEEE Commun. Lett.*, vol. 15, no. 2, pp. 217–219, Feb. 2011.

[63] T. Komine and M. Nakagawa, "Fundamental Analysis for Visible-Light Communication System using LED Lights," *IEEE Trans. Consum. Electron.*, vol. 50, no. 1, pp. 100–107, Feb. 2004.

[64] J. Ding, Z. Huang, and Y. Ji, "Independent reflecting element interaction characterization for indoor visible light communication based on new generation lighting," *Chin. Opt. Lett.*, vol. 8, no. 12, pp. 1182–1186, Dec. 2010.

[65] H. Schulze, "Frequency-Domain Simulation of the Indoor Wireless Optical Communication Channel," *IEEE Trans. Commun.*, vol. 64, no. 6, pp. 2551–2562, Jun. 2016.

[66] C. Chen, D. A. Basnayaka, X. Wu, and H. Haas, "Efficient Analytical Calculation of Non-Line-of-Sight Channel Impulse Response in Visible Light Communications," *IEEE/OSA J. Lightw. Technol.*, vol. 36, no. 9, pp. 1666–1682, May 2018.

[67] J. Vucic, C. Kottke, S. Nerreter, K. D. Langer, and J. W. Walewski, "513 Mbit/s Visible Light Communications Link Based on DMT-Modulation of a White LED," *IEEE/OSA J. Lightw. Technol.*, vol. 28, no. 24, pp. 3512–3518, Dec. 2010.

[68] E. F. Schubert, *Light-Emitting Diodes*, 2nd ed. Cambridge University Press, 2006.

[69] A. M. Khalid, G. Cossu, R. Corsini, P. Choudhury, and E. Ciaramella, "1-Gb/s Transmission Over a Phosphorescent White LED by Using Rate-Adaptive Discrete Multitone Modulation," *IEEE Photon. J.*, vol. 4, no. 5, pp. 1465–1473, Oct. 2012.

[70] T. Komine, J. H. Lee, S. Haruyama, and M. Nakagawa, "Adaptive Equalization System for Visible Light Wireless Communication Utilizing Multiple White LED Lighting Equipment," *IEEE Trans. Wireless Commun.*, vol. 8, no. 6, pp. 2892–2900, Jun. 2009.

[71] H. L. Minh, D. O'Brien, G. Faulkner, L. Zeng, K. Lee, D. Jung, Y. Oh, and E. T. Won, "100-Mb/s NRZ Visible Light Communications Using a Postequalized White LED," *IEEE Photon. Technol. Lett.*, vol. 21, no. 15, pp. 1063–1065, Aug. 2009.

[72] L. Zeng, D. C. O'Brien, H. L. Minh, G. E. Faulkner, K. Lee, D. Jung, Y. Oh, and E. T. Won, "High Data Rate Multiple Input Multiple Output (MIMO) Optical Wireless Communications Using White LED Lighting," *IEEE J. Sel. Areas Commun.*, vol. 27, no. 9, pp. 1654–1662, Dec. 2009.

[73] T. Fath and H. Haas, "Performance Comparison of MIMO Techniques for Optical Wireless Communications in Indoor Environments," *IEEE Trans. Commun.*, vol. 61, no. 2, pp. 733–742, Feb. 2013.

[74] Y. Hong, T. Wu, and L. Chen, "On the Performance of Adaptive MIMO-OFDM Indoor Visible Light Communications," vol. 28, no. 8, pp. 907–910, Apr. 2016.

[75] L. Wu, Z. Zhang, J. Dang, and H. Liu, "Adaptive Modulation Schemes for Visible Light Communications," *IEEE/OSA J. Lightw. Technol.*, vol. 33, no. 1, pp. 117–125, Jan. 2015.

[76] R. X. G. Ferreira, E. Xie, J. J. D. McKendry, S. Rajbhandari, H. Chun, G. Faulkner, S. Watson, A. E. Kelly, E. Gu, R. V. Penty, I. H. White, D. C. O'Brien, and M. D. Dawson, "High Bandwidth GaN-Based Micro-LEDs for Multi-Gb/s Visible Light Communications," *IEEE Photon. Technol. Lett.*, vol. 28, no. 19, pp. 2023–2026, Oct. 2016.

[77] M. F. Leitao, J. M. M. Santos, B. Guilhabert, S. Watson, A. E. Kelly, M. S. Islim, H. Haas, M. D. Dawson, and N. Laurand, "Gb/s Visible Light Communications With Colloidal Quantum Dot Color Converters," *IEEE J. Sel. Areas Commun.*, vol. 23, no. 5, pp. 1–10, Sep. 2017.

[78] M. S. Islim, R. X. Ferreira, X. He, E. Xie, S. Videv, S. Viola, S. Watson, N. Bamiedakis, R. V. Penty, I. H. White, A. E. Kelly, E. Gu, H. Haas, and M. D. Dawson, "Towards 10 Gb/s orthogonal frequency division multiplexing-based visible light communication using a GaN violet micro-LED," *Photon. Res.*, vol. 5, no. 2, pp. A35–A43, Apr. 2017.

[79] J. Armstrong, "OFDM for Optical Communications," *IEEE/OSA J. Lightw. Technol.*, vol. 27, no. 3, pp. 189–204, Feb. 2009.

[80] F. Xiong, *Digital Modulation Techniques*. Artech House, 2006.

[81] H. Elgala, R. Mesleh, and H. Haas, "Practical Considerations for Indoor Wireless Optical System Implementation using OFDM," in *Proc. 10th Int. Conf. Telecommun. (ConTEL)*, Jun. 2009, pp. 25–29.

[82] S. Dimitrov, S. Sinanovic, and H. Haas, "Signal Shaping and Modulation for Optical Wireless Communication," *IEEE/OSA J. Lightw. Technol.*, vol. 30, no. 9, pp. 1319–1328, May 2012.

[83] Y. Wang, X. Wu, and H. Haas, "Resource Allocation in LiFi OFDMA Systems," in *Proc. IEEE Global Commun. Conf. (GLOBECOM)*, Dec. 2017, pp. 1–6.

[84] J. B. Carruthers and J. M. Kahn, "Multiple-Subcarrier Modulation for Nondirected Wireless Infrared communication," *IEEE J. Sel. Areas Commun.*, vol. 14, no. 3, pp. 538–546, Apr. 1996.

[85] O. Gonzalez, R. Perez-Jimenez, S. Rodriguez, J. Rabadan, and A. Ayala, "OFDM over indoor wireless optical channel," *IEE Proceedings - Optoelectronics*, vol. 152, no. 4, pp. 199–204, Aug. 2005.

[86] ——, "Adaptive OFDM system for communications over the indoor wireless optical channel," *IEE Proceedings - Optoelectronics*, vol. 153, no. 4, pp. 139–144, Aug. 2006.

[87] J. Armstrong and A. J. Lowery, "Power efficient optical OFDM," *IET Electron. Lett.*, vol. 42, no. 6, pp. 370–372, Mar. 2006.

[88] J. Armstrong and B. J. C. Schmidt, "Comparison of Asymmetrically Clipped Optical OFDM and DC-Biased Optical OFDM in AWGN," *IEEE Commun. Lett.*, vol. 12, no. 5, pp. 343–345, May 2008.

[89] H. Elgala and T. D. C. Little, "SEE-OFDM: Spectral and Energy Efficient OFDM for Optical IM/DD Systems," in *Proc. IEEE 25th Int. Symp. Pers. Indoor Mobile Radio Commun. (PIMRC)*, Sep. 2014, pp. 851–855.

[90] ——, "P-OFDM: Spectrally Efficient Unipolar OFDM," in *Proc. Opt. Fiber Commun. Conf. (OFC)*, Mar. 2014, p. Th3G.7.

[91] D. Tsonev, S. Videv, and H. Haas, "Unlocking Spectral Efficiency in Intensity Modulation and Direct Detection Systems," *IEEE J. Sel. Areas Commun.*, vol. 33, no. 9, pp. 1758–1770, Sep. 2015.

[92] S. Mazahir, A. Chaaban, H. Elgala, and M. Alouini, "Effective Information Rates of Single-Carrier and Multi-Carrier Modulation Schemes for Bandwidth Constrained IM/DD Systems," in *Proc. IEEE Int. Conf. Commun. (ICC)*, May 2017, pp. 1–6.

[93] S. Dimitrov and H. Haas, "Information Rate of OFDM-Based Optical Wireless Communication Systems With Nonlinear Distortion," *IEEE/OSA J. Lightw. Technol.*, vol. 31, no. 6, pp. 918–929, Mar. 2013.

[94] A. R. S. Bahai, B. R. Saltzberg, and M. Ergen, *Multi-Carrier Digital Communications: Theory and Applications of OFDM*, 2nd ed. Springer, 2004.

[95] A. J. Goldsmith and S.-G. Chua, "Variable-Rate Variable-Power MQAM for Fading Channels," *IEEE Trans. Commun.*, vol. 45, no. 10, pp. 1218–1230, Oct. 1997.

[96] D. Dardari, V. Tralli, and A. Vaccari, "A Theoretical Characterization of Nonlinear Distortion Effects in OFDM Systems," *IEEE Trans. Commun.*, vol. 48, no. 10, pp. 1755–1764, Oct. 2000.

[97] H. Elgala, R. Mesleh, and H. Haas, "Non-linearity effects and predistortion in optical OFDM wireless transmission using LEDs," *Inderscience Int. J. Ultra Wideband Commun. Syst.*, vol. 1, no. 2, pp. 143–150, Aug. 2009.

[98] S. Dimitrov, S. Sinanovic, and H. Haas, "Clipping Noise in OFDM-Based Optical Wireless Communication Systems," *IEEE Trans. Commun.*, vol. 60, no. 4, pp. 1072–1081, Apr. 2012.

[99] J. Wang, Q. Hu, J. Wang, M. Chen, and J. Wang, "Tight Bounds on Channel Capacity for Dimmable Visible Light Communications," *IEEE/OSA J. Lightw. Technol.*, vol. 31, no. 23, pp. 3771–3779, Dec. 2013.

[100] R. Jiang, Z. Wang, Q. Wang, and L. Dai, "A Tight Upper Bound on Channel Capacity for Visible Light Communications," *IEEE Commun. Lett.*, vol. 20, no. 1, pp. 97–100, Jan. 2016.

[101] J. G. Proakis and M. Salehi, *Digital Communications*, 5th ed. McGraw-Hill, 2008.

[102] J. N. Laneman, D. N. C. Tse, and G. W. Wornell, "Cooperative Diversity in Wireless Networks: Efficient Protocols and Outage Behavior," *IEEE Trans. Inf. Theory*, vol. 50, no. 12, pp. 3062–3080, Dec. 2004.

[103] O. Narmanlioglu, R. C. Kizilirmak, F. Miramirkhani, and M. Uysal, "Cooperative Visible Light Communications With Full-Duplex Relaying," *IEEE Photon. J.*, vol. 9, no. 3, pp. 1–11, Jun. 2017.

[104] C. H. Chen, M. Hargis, J. M. Woodall, M. R. Melloch, J. S. Reynolds, E. Yablonovitch, and W. Wang, "GHz bandwidth GaAs light-emitting diodes," *Appl. Phys. Lett.*, vol. 74, no. 21, pp. 3140–3142, May 1999.

[105] J. G. Proakis and M. Salehi, *Communication Systems Engineering*, 2nd ed. Prentice-Hall, 2002.

[106] O. Oyman and S. Sandhu, "A Shannon-Theoretic Perspective on Fading Multihop Networks," in *Proc. 40th Annual Conf. Inf. Sci. Sys. (CISS)*, Mar. 2006, pp. 525–530.

[107] S. Lu, V. Bharghavan, and R. Srikant, "Fair Scheduling in Wireless Packet Networks," *IEEE/ACM Trans. Netw.*, vol. 7, no. 4, pp. 473–489, Aug. 1999.

[108] T. Cover and A. E. Gamal, "Capacity Theorems for the Relay Channel," *IEEE Trans. Inf. Theory*, vol. 25, no. 5, pp. 572–584, Sep. 1979.

[109] C. E. Shannon, "Communication in the Presence of Noise," *Proc. IEEE*, vol. 86, no. 2, pp. 447–457, Feb. 1998.

[110] B. Almeroth, A. J. Fehske, G. Fettweis, and E. Zimmermann, "Analytical Interference Models for the Downlink of a Cellular Mobile Network," in *Proc. IEEE GLOBECOM Workshops (GC Wkshps)*, Dec. 2011, pp. 739–743.

[111] M. Vallentin, *Probability and Statistics Cookbook*, Dec. 2017, Version 0.2.6. [Online]. Available: http://statistics.zone/

[112] J. Mo and J. Walrand, "Fair End-to-End Window-Based Congestion Control," *IEEE/ACM Trans. Netw.*, vol. 8, no. 5, pp. 556–567, Oct. 2000.

[113] S. Boyd and L. Vandenberghe, *Convex Optimization*. Cambridge University Press, Mar. 2004.

[114] D. P. Bertsekas, *Nonlinear Programming*, 3rd ed. Athena Scientific, 2016.

[115] S. Boyd, "Subgradient Methods," Lecture Notes for EE364b, Stanford University, May 2014.

[116] E. K. P. Chong and S. H. Zak, *An Introduction to Optimization*, 4th ed. Wiley-Interscience Publication, Feb. 2013.

[117] M. D. Soltani, X. Wu, M. Safari, and H. Haas, "Bidirectional User Throughput Maximization Based on Feedback Reduction in LiFi Networks," *IEEE Trans. Commun.*, vol. 66, no. 7, pp. 3172–3186, Jul. 2018.

[118] T. Novlan, J. G. Andrews, I. Sohn, R. K. Ganti, and A. Ghosh, "Comparison of Fractional Frequency Reuse Approaches in the OFDMA Cellular Downlink," in *Proc. IEEE Global Commun. Conf. (GLOBECOM)*, Dec. 2010, pp. 1–5.

[119] T. D. Novlan, R. K. Ganti, A. Ghosh, and J. G. Andrews, "Analytical Evaluation of Fractional Frequency Reuse for OFDMA Cellular Networks," *IEEE Trans. Wireless Commun.*, vol. 10, no. 12, pp. 4294–4305, Dec. 2011.

[120] C. Chen, N. Serafimovski, and H. Haas, "Fractional Frequency Reuse in Optical Wireless Cellular Networks," in *Proc. IEEE 24th Int. Symp. Pers. Indoor Mobile Radio Commun. (PIMRC)*, Sep. 2013, pp. 3594–3598.

[121] R. U. Nabar, H. Bolcskei, and F. W. Kneubuhler, "Fading Relay Channels: Performance Limits and Space-Time Signal Design," *IEEE J. Sel. Areas Commun.*, vol. 22, no. 6, pp. 1099–1109, Aug. 2004.

[122] D. Tse and P. Viswanath, *Fundamentals of Wireless Communication*. Cambridge University Press, 2005.